SYNTHESIS AND CHARACTERIZATION OF FUNCTIONAL MESOSTRUCTURES
USING COLLOIDAL CRYSTAL TEMPLATING

BY

YUN-JU LEE

B.S., Massachusetts Institute of Technology, 1999

DISSERTATION

Submitted in partial fulfillment of the requirements
for the degree of Doctor of Philosophy in Materials Science and Engineering
in the Graduate College of the
University of Illinois at Urbana-Champaign, 2004

Urbana, Illinois

ABSTRACT

Functional 3-D periodic mesostructures were synthesized via colloidal crystal templating, and their chemical, physical, and optical properties were characterized. By forming colloidal crystals through self-organization, infiltrating the interstitial space with functional materials, and then removing the templates by chemical etching, inverse opal mesostructures with characteristic distances on the order of optical wavelengths were generated from conducting polymers, hydrogels, and metals. These active mesostructures allow tuning of properties such as Bragg diffraction, potentially enabling applications as electrochemical elements, sensors, flow control devices, and novel photonic band gap materials.

Inverse opal conducting polymer films were fabricated by electropolymerization. The templated films exhibited a compact morphology and larger electrochemical response from cyclic voltammetry. They also displayed shifts in Bragg diffraction, possibly due to changes in interchain spacing and refractive index during redox cycling.

Inverse opal hydrogels were templated using free radical photopolymerization. By copolymerizing appropriate functional groups, mechanically robust thin films were synthesized that exhibit reversible shifts in Bragg diffraction based on changes in solvent, pH, ionic strength, crosslink density, and glucose concentration, caused by the expansion and contraction of the hydrogel film due to changes in the local chemical potential. The kinetics of the diffraction response was also studied and found to be diffusion limited. The diffraction response of the inverse opal hydrogels were correlated to the deformations of their mesostructure directly observed using multiphoton fluorescence microscopy. Reconstruction of the pore mesostructure revealed that the hydrogel swelled

primarily in the sample normal direction, with a significant shrinkage and deformation of the face centered cubic pores, consistent with predictions from scalar wave approximation. The results compared well with finite element modeling and indicated a change in crystallographic symmetry during hydrogel swelling.

Inverse opal metallic films of nickel, copper, and gold were fabricated via electrodeposition. Chemical etching of templated nickel films after electrodeposition were found to affect their optical properties, possibly enabling novel mesostructures that exhibit selective absorption and emission.

By using colloidal crystal templating, tunable photonic mesostructures were synthesized and characterized. With direct observation of the mesostructure evolution through fluorescence microscopy and computational modeling of the physical and optical response, the relationship between the structure and properties of colloidal crystal templated functional 3-D materials was elucidated.

To my parents, Chien-Feng Lee and Mei-Chu Lee

TABLE OF CONTENTS

LIST OF FIGURES

LIST OF TABLES

LIST OF SYMBOLS

Chapter 1

a	lattice parameter
c	speed of light in vacuum
D	diameter
k	wavevector
n	refractive index
n_i	refractive index of component i
δ	refractive index contrast
ϕ_i	volume fraction of component i
λ	wavelength
ψ	angle between incident beam and sample normal
ω	angular frequency

Chapter 2

D	diameter
E^0	standard reduction potential
E_a	anodic peak potential
E_c	cathodic peak potential
I_a	anodic peak current
I_c	cathodic peak current
ΔE	separation between peak potentials

Chapter 3

D	diameter
D_{app}	apparent diffusivity
D_0	diffusivity of analyte in water
C	concentration of monovalent salt
c_a	concentration of mobile anions in the hydrogel phase
C_a	concentration of mobile anions inside in the bulk solution
c_c	concentration of mobile cations in the hydrogel phase
C_c	concentration of mobile cations in bulk solution
c_p	concentration of immobile ionizable groups on hydrogel
d	characteristic interlayer distance
d_0	characteristic interlayer distance of the compact hydrogel
d/d_0	swelling ratio
I	ionic strength
I_b	diffraction peak intensity
K_a	acid dissociation constant
K_4	equilibrium binding constant between glucose and phenylboronic acid
l_0	thickness of the hydrogel for the rate-limiting diffusion process
m	order of diffraction
n_{aq}	refractive index of the aqueous solution phase

n_i	refractive index of component i
n_{gel}	refractive index of the hydrogel phase
T_g	glass transition temperature
α	angle of diffraction
φ_{aq}	volume fraction of the aqueous solution phase
φ_i	volume fraction of component i
φ_{gel}	volume fraction of the hydrogel phase
λ_b	diffraction wavelength
λ_{b0}	diffraction wavelength of the compact hydrogel
λ_b/λ_{b0}	spectroscopic swelling ratio
λ_{bf}	diffraction wavelength at time = 0
λ_{bi}	diffraction wavelength at time = τ
λ_G	diffraction grating pitch
μ_0	chemical potential of the bulk solution
μ_{gel}	chemical potential of the hydrogel phase
τ	equilibration time for diffraction response
$\Delta V/V_0$	dimensionless change in volume

Chapter 4

a	number of photons per excitation process
D	diameter
d	characteristic interlayer distance
d_0	characteristic interlayer distance of the compact hydrogel
d/d_0	normalized interlayer distance
I_b	diffraction peak intensity
N	number of dye molecules excited by light
n	refractive index
P	*incident light power*
λ_b	diffraction wavelength
λ_{b0}	diffraction wavelength of the compact hydrogel
λ_b/λ_{b0}	spectroscopic swelling ratio

Chapter 5

A_b	peak asymmetry
d_c	diameter of a cone of focused light at h away from focal point
h	height of a cone of focused light
I	reflected light intensity
I_0	incident light intensity
I_b	diffraction peak intensity
I_{bg}	background intensity
r	reflectance at given ψ
R	total reflectance integrated over solid angle
Φ	total light flux integrated over solid angle

λ_b	diffraction wavelength
λ_{max}	wavelength at half maximum on longer wavelength peak shoulder
ψ	angle between incident beam and sample normal
ψ_{max}	maximum half-angle for a cone of focused light
ϕ	polar angle
θ	azimuth (longitude)
Ω	solid angle

Chapter 6

c	velocity of light in vacuum
D	diameter
F	focal length
h	Planck's constant
T	temperature
T_m	melting temperature
ΔE	Energy separation between interference fringe maxima
ε	emissivity of the blackbody
σ	Stefan-Boltzmann constant
Φ	flux of blackbody radiation
λ	wavelength
λ_{max}	wavelength of maximum blackbody radiation

LIST OF ABBREVIATIONS

AA	acrylic acid
AEMA	2-aminoethylmethacrylate hydrochloride
APBA	3-acrylamidophenylboronic acid
BAC	N,N'-bis(acryloyl)cystamine
CC	colloidal crystal
CHES	2-(cyclohexylamino)ethanesulfonic acid
cPBG	complete photonic band gap
CV	cyclic voltammetry
CVD	chemical vapor deposition
DI	deionized
DMAEMA	2-(dimethylamino)ethyl methacrylate
EDC	1-ethyl-3-(3-dimethylaminopropyl)-carbodiimide
EGDM	ethylene glycol dimethacrylate
FCC	face centered cubic
FRAP	fluorescence recovery after photobleaching
FT-IR	Fourier transform infrared
HCP	hexagonal close packed
HEMA	2-hydroxyethyl methacrylate
ITO	indium tin oxide
KKR	Korringa-Kohn-Rostoker
LSCM	laser scanning confocal microscope
MPMS	methacryloxypropyltrimethoxysilane
NA	numerical aperture
NHE	normal hydrogen electrode
NMR	nuclear magnetic resonance
OTS	octadecyltrichlorosilane
PC	photonic crystal
PCCA	polymerized colloidal crystal array
PBG	photonic band gap
PDMS	polydimethylsiloxane
PEDOT	polyethylenedioxythiophene
pPBG	partial photonic band gap
PPV	polyphenylenevinylene
PPy	polypyrrole
PS	polystyrene
PSS	polystyrenesulfonate
RhoB	Rhodamine B
RhoB-ITN	Rhodamine B isothiocyanate
SEM	scanning electron microscope/micrograph
SWA	scalar wave approximation
TEAHFP	tetraethylammonium hexafluorophosphate
TMM	transfer matrix method

CHAPTER 1

INTRODUCTION

1.1 Photonic Crystals (PCs)

1.1.1 Background

A photonic crystal (PC) is a mesostructure with periodic modulation of refractive index (n) similar to the wavelength of the incident light.[1-3] The translational symmetry of a PC makes it analogous to an atomic crystal, although the length scale of a PC is larger by a factor of ~ 1000. Just as an atomic crystal causes x-ray diffraction due to coherent scattering by the electrons, a PC interacts strongly with visible and IR light. In the case of a PC, the modulation in n leads to strong coherent scattering of light, and a partial photonic band gap (pPBG) develops, where light with a specific wavelength and direction cannot propagate within the PC. With the appropriate crystal symmetry, lattice parameter (a), and refractive index contrast (δ), where δ is the refractive index ratio between the high n and low n material, a complete photonic band gap (cPBG) may develop, where light propagation is forbidden for all angles. The main thrust of current research has focused on the fabrication of PCs with a high δ to form a cPBG.[4-8] In addition, by introducing well-defined defects into a photonic band gap (PBG) material, the propagation of light will be limited to within the defects. Such mesostructures may enable devices such as photonic waveguides,[5,9] compact high quality factor cavities,[10-12], tunable light emitters,[13] and all-optical circuits.[2] Low δ periodic mesostructures consisting of materials that exhibit shifts in a and n are interesting in their own right, because such tunable PCs exhibit shifts in Bragg diffraction and other optical properties that may be incorporated into applications such as chemical and biological

sensing,[14-21] electrochemical and microfluidic devices,[21-23] and photonic switching.[24,25]

1.1.2 Photonic Band Structure

Calculation of the photonic band structures for PCs will only be briefly described here; see the references for a much more rigorous and complete discussion.[1-3,26] Essentially, a photonic band diagram describes the propagation of electromagnetic radiation of specific wavevectors inside the photonic crystal. In the first step, the propagating direction of the electromagnetic radiation inside a PC with a certain crystallographic symmetry is defined in terms of its reciprocal lattice. The Wigner-Seitz cell of the reciprocal lattice, which bisects the center of the reciprocal lattice from its nearest neighbors, is also known as the first Brillouin zone. An example of the Bravais (real-space) lattice for a face centered cubic (FCC) crystal and its corresponding reciprocal lattice and Brillouin zone is shown in Figure 1.1.[27] The high-symmetry points in the Brillouin zone are assigned letters, with Γ being the center of the Brillouin zone. In the reciprocal space, the propagating light defined by its wavevector $k = 2\pi / \lambda$, where λ is the wavelength of the light. According to Bloch theory, all wavevectors falling can be translated back to the first Brillouin zone using the basis vectors of the reciprocal lattice,[26] greatly simplifying the calculation of light propagation inside PCs.
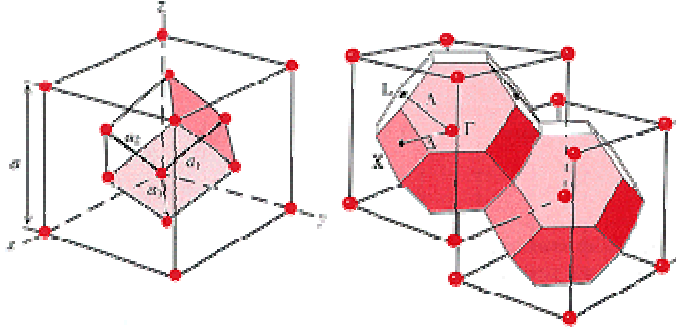
Figure 1.1: Bravais lattice (left) and reciprocal lattice (right) of a face centered cubic crystal. The Brillouin zone of the reciprocal lattice is shown as the shaded polygon with high symmetry points in Greek letters.[27] Note that the FCC[111] direction corresponds to the ΓL direction in the reciprocal lattice.

When the photon travels through an uniform medium with refractive index *n*, the relationship between its angular frequency *ω* and its wavevector *k* is defined by the simple dispersion relation *ω = ck / n*,[26] where *c* is the speed of light in vacuum. In other words, the frequency of the propagating photon is a linear function of its wavevector, and inversely proportional to *n* of the propagating medium. However, in a PC with a periodic variation in refractive index, the relationship between *ω* and *k* is determined by solving the Maxwell's equations, which can be simplified to:[3]

$$\nabla \times \left[\frac{1}{\varepsilon(r)} \nabla \times H(r) \right] = \frac{\omega^2}{c^2} H(r) \tag{1.1}$$

where *H(r)* is the spatially varying magnetic field of the propagating photon and *ε(r)* is the periodically varying dielectric constant. The answers to this equation are a series of functions in the form of *ω(k)*, showing all possible propagating frequencies for the given wavevector. The full photonic band structure is generated by solving Equation 1.1 for a series of wavevectors spanning the high symmetry points of the Brillouin zone, and the plotting the resulting *ω(k)* relations, with the individual wavevectors as the x-axis, and the normalized frequency (*a/λ = (ωa) / (2πc)*) as the y-axis. An example photonic band

3

diagram for a polystyrene colloidal crystal in air (δ = 1.592) is plotted in Figure 1.2. The most salient features are the diagonal lines representing the propagation of waves of given frequencies with slopes equal to the group velocity of the wave, and the regions with gaps, representing forbidden propagation of given frequencies. From the photonic band diagram, it can be seen that the polystyrene (PS) colloidal crystal (CC) has an incomplete photonic band gap in the ΓL direction at a/λ = 0.606, corresponding to the strong Bragg diffraction of light from the FCC(111) planes.
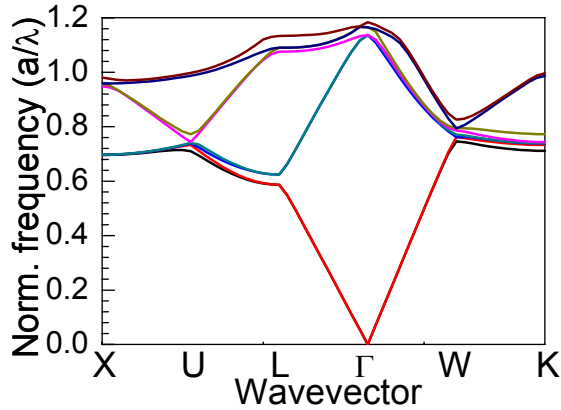
Figure 1.2: Photonic band structure of a polystyrene colloidal crystal in air. A partial photonic band gap is visible at a normalized frequency of 0.606 between the second and third bands in the ΓL direction, corresponding to Bragg diffraction from FCC(111) planes. This photonic band diagram was calculated by the plane wave expansion method.[28]

Photonic band structures are especially useful for quantifying the properties of PCs with high δ, such as the width of potential cPBGs and the propagation direction of light in a medium with highly anisotropic refractive index. However, for PCs with relatively low δ such as colloidal crystals or polymeric mesostructures templated from colloidal crystals, a strong Bragg diffraction peak due to the constructive interference of light reflected from different layers in the PC represents the major optical feature. In this situation, the wavelength corresponding to the diffraction peak (λ_b) can be predicted

using the Bragg equation by approximating the PC as a material with an effective refractive index (n_{eff}):

$$\lambda_b = 2n_{eff}d = \frac{2\sqrt{3}}{3}\left(\sum_i n_i^2\phi_i - \sin^2\psi\right)^{1/2} a \qquad (1.2)$$

where d is the characteristic interlayer distance, n_i and ϕ_i are, respectively, the refractive index and the volume fraction of each component phase, ψ is the angle between the incident beam and the sample normal, and a is the FCC lattice constant.[29,30] For touching spheres with diameter D, $a = \sqrt{2}D$. As we demonstrate in future chapters, Equation 1.2 accrately predicts the diffraction wavelengths of PS CCs and CC templated materials.

1.1.3 Dimensionality of Photonic Crystals

PCs are often divided into three functional categories based on the dimensionality of refractive index modulation, which differ on their ease of fabrication and the type of PBG behavior that can be achieved (see [3] for a recent review on the fabrication of PCs). 1-D PCs are in general quite easy to manufacture and often exhibit a pPBG over a wide range of optical wavelengths for relatively small δ values. For example, planar dielectric stacks of (most commonly) silica and titania are often used as highly reflective mirrors, anti-reflection coatings, and laser filters. Typically, 1-D photonic crystals are fabricated using a multistep evaporation process. Novel methods for creating 1-D PCs include electrical switching of cholesteric liquid crystals, layer-by-layer adsorption of polyelectrolytes, and electrochemical etching of Si wafers.[3] However, it is impossible to realize a 1-D PC with cPBG using readily available materials in the visible and near-infrared wavelengths.[1]

2-D and 3-D PCs are more difficult to fabricate, but their highly anisotropic dispersion surfaces may offer new optical properties such as cPBG, highly nonlinear optical effects,[31] enhanced selective absorption and emission due to low group velocity,[1] and superprism phenomena.[32-34] 2-D PCs can be fabricated with standard semiconductor lithographic techniques, which is especially convenient in generating periodic mesostructure out of Si, an excellent material for PCs due to its high n and transparency in the optical communications wavelengths (~ 1.5 μm). Unlike 1-D PCs, these 2-D PC slabs have demonstrated a cPBG for polarized light.[2] Simple modifications in the lithography procedure have successfully incorporated defects of arbitrary sizes and shapes at specific locations within 2-D PCs, and have led to devices such as waveguides and cavities[9] that may form the basis of photonic circuits. 2-D PCs can also exhibit highly anisotropic dispersion surfaces so that the propagation of light inside the PCs depends strongly on parameters such as the incident angle and frequency, leading to the so-called superprism effect.[33,35,36] Photonic crystal fibers, which behave as a composite of 1-D and 2-D PCs, can be made by drawing a bundle of hollow glass tubes until the diameter of each glass tube decreases to optical wavelengths.[37] By using more exotic materials with high n, the resulting PC may exhibit superior optical properties such as a large PBG and waveguide behavior.[38-40]

3-D PCs, where the refractive index modulation occurs in three spatial dimensions, can be fabricated through two general mechanisms: a layer-by-layer process or a self-assembly process. In the layer-by-layer process, the standard semiconductor lithography is applied sequentially on a substrate to build up sections of pseudo 2-D PCs into 3-D mesostructures. As was the case in the 2-D process, the precise incorporation of

arbitrary defects can be easily accomplished. However, due to its multistep nature, the layer-by-layer process can sometimes be labor-intensive and technically challenging. For example, 3-D PCs from the Noda group are generally fabricated using the wafer fusion process.[41] In this process, several 2-D PCs are first patterned onto semiconductor wafers using lithography. Then, the PCs are brought into close contact against each other by pressing together the two wafers, and the unpatterned regions of one wafer is completely etched. To make a multilayered 3-D PC, the wafer fusion process must be repeated several times. In addition, to maintain the proper crystallographic symmetry, the different layers must be carefully aligned to obtain the proper registration. In a different variation of the layer-by-layer process, materials of the appropriate refractive index are deposited on the substrate via techniques such as chemical vapor deposition (CVD) and then patterned by etching. Through the appropriate use of an etch stop, a smooth surface can be generated on top of the patterned region which allows further deposition and etching. Using this procedure, 3-D PCs of dielectric materials[5] and metals[42] have been successfully manufactured and characterized.

In traditional photolithography, a photoresist is chemically converted by the exposure to light through a photomask, and either the exposed or unexposed region is dissolved to yield a pattern standing on a substrate. However, it is well known that light propagating from different directions can generate an interference pattern with well-defined spatial modulation in light intensity. Through careful control of the wavelength, phase, direction, and power of four laser beams, a 3-D hologram with ordered maxima and minima can be created. In holographic lithography, a photoresist is exposed to this interference pattern and then developed, yielding a 3-D PC with the same

crystallographic symmetry as the interference pattern, as demonstrated by several research groups.[43,44] Holographic lithography is an attractive process for fabricating 3-D PCs for two main reasons. First, because the resulting PC is patterned by the exposure to a 3-D hologram, the mesostructure should exhibit excellent long-range periodicity, which is critical to the photonic band structure of the PC. Second, by adjusting the aforementioned exposure parameters of the laser beams, 3-D PCs with different lattice constants and symmetries can be created in a one step process.[43] A current limitation of holographic lithography is that the commercially available polymeric photoresists, which generates 3-D PCs with the optimal spatial resolution, do not possess sufficient refractive index contrast with air to exhibit a cPBG. In addition, the incorporation of defects at arbitrary positions requires additional steps after the PC fabrication and has not yet been demonstrated. Much research effort is now underway to create 3-D PBG materials through holographic lithography.

3-D PCs can also be fabricated by the self-assembly of smaller building blocks into a periodic mesostructure. Due to the size scale (hundreds of nanometers to tens of microns) and long range translational order that are needed to create PCs at visible and infrared wavelengths, colloidal crystals consisting of close-packed monodisperse particles are utilized to create 3-D PCs by self-assembly. Most commonly, CCs are formed from charge-stabilized suspensions of silica or polystyrene colloids. CCs typically adopt a face centered cubic (FCC) crystallographic symmetry instead of the closely related hexagonal close packed (HCP) symmetry, primarily because the the second nearest neighbors are slightly farther away in the FCC symmetry, minimizing the repulsive interactions between particles and also the hydrodynamic interactions between

8

colloids during self-assembly. The various self-assembly techniques for creating CCs were reviewed by Xia and co-workers,[45] and will be discussed in detail in a later section.

The nature of the self-assembly process imposes limitations on the types of 3-D PCs that can be generated using CCs. As mentioned previously, the FCC symmetry is almost always adopted by CCs because it is the most stable configuration. In fact, at the time of this writing, the synthesis of CCs in air with large domains of non-FCC packing (e. g. diamond cubic) requires the mechanical manipulation of individual particles into the correct spatial position.[46,47] Compared with the lithographic process, the incorporation of defects inside self-assembled PCs necessitates additional steps, such as two-photon polymerization of monomers infiltrated inside CCs to generate potential waveguide structures.[48]

Another major issue in the utilization of CCs as 3-D PCs with cPBG is that CCs of silica or PS in air do not possess sufficient refractive index contrast.[49] Therefore, CCs are generally utilized as templates for the growth of high n materials in the voids between the colloids to fabricate inverse opal PCs. For example, Blanco and co-workers fabricated inverse opal Si PCs by first forming silica CCs.[7] Si was then deposited inside the CCs by CVD, and the CC template was removed by etching with hydrofluoric acid. The resulting mesostructure showed the growth of a shell of Si around the CC template with clear FCC symmetry (Fig 1.3a and 1.3b). In addition, near-IR spectroscopy in the FCC[111] direction revealed high reflectance between 1.4 and 1.5 μm and a Bragg diffraction peak at 2.5 μm (Fig. 1.3c), in excellent agreement with theoretical calculations, which predicted a cPBG at $a/\lambda = 0.83$ and a pPBG along ΓL at $a/\lambda = 0.5$

9

(Fig. 1.3d). A thicker film of inverse opal Si in air fabricated using a similar technique exhibited near-unity reflectance at the same normalized frequency.[8] More recently, Garcia-Santamaria and co-workers demonstrated that by varying the thickness of the Si shell grown around the CC template during of the CVD process, the width and intensity of the reflectance peak for the inverse opal Si can be varied due to the corresponding changes in the photonic band structure.[50] Moreover, using a multistep CVD process, multilayers of Si, silica, and Ge can be synthesized around the CC template to further tailor the PBG.[50]
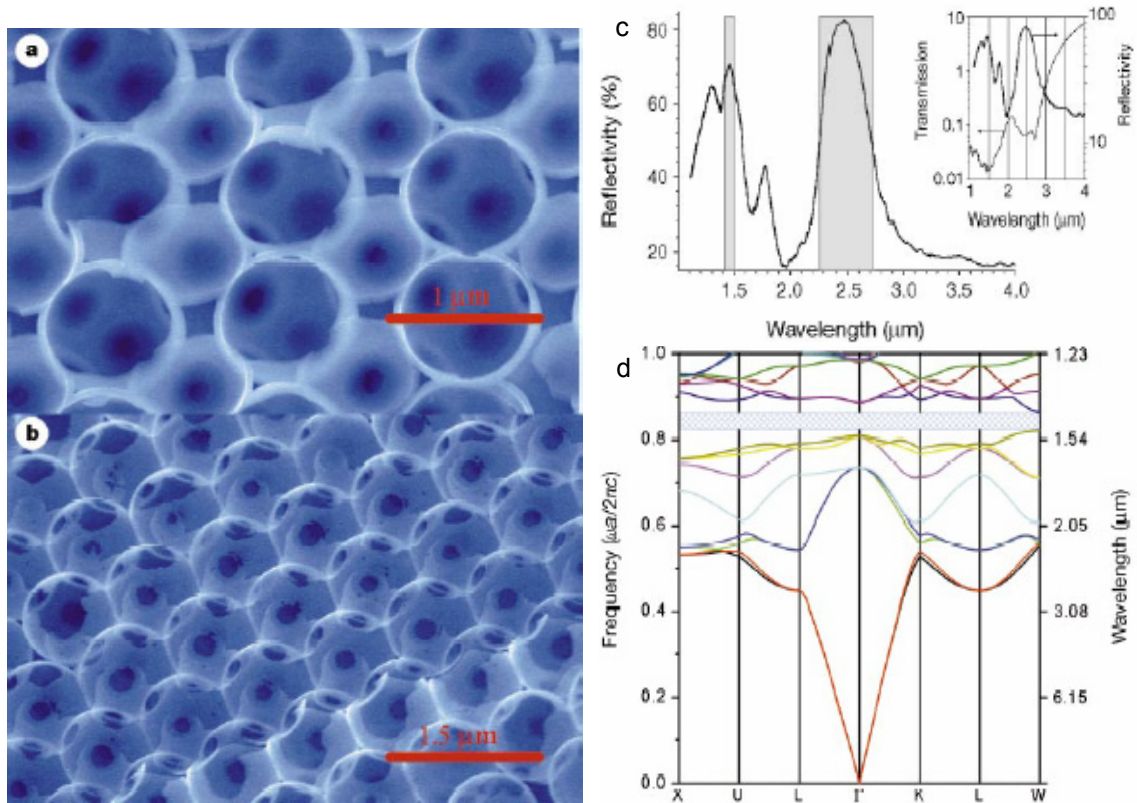
Figure 1.3: 3-D PC of Si forming by CC templating, showing a cPBG between 1.4 μm and 1.5 μm. (a) SEM of the FCC[100] facet. (b) SEM of the FCC[111] facet. (c) Reflectance spectra in the FCC[111] direction, showing the cPBG and the first order diffraction peak at 2.5 μm. (d) Calculated photonic band structure. Data adapted from Blanco and co-workers.[7]

Finally, experiments first reported by the Asher group showed that 3-D PCs based on CCs can exhibit photonic response without a cPBG.[51] They fabricated polymerized

10

colloidal crystal arrays (PCCAs) by lightly crosslinking highly charged CCs in water with dilute solutions of hydrogels functionalized with certain responsive groups. When the hydrogels expand or contract under a specific stimulus, the distances between the colloids also increase or decrease uniformly, leading to the Bragg diffraction of different wavelengths of light. For example, if the hydrogel was functionalized with crown ethers that bind to Pb^{2+} ions, the PCCA exhibited a red shift in diffraction as the Pb^{2+} concentration was increased, due to the ionization of the hydrogel with the Pb^{2+} (Fig. 1.4a). Similarly, a hydrogel functionalized with the enzyme glucose oxidase exhibited a red shift in diffraction in the presence of glucose and oxygen (Fig. 1.4b). It should be noted that the hydrogel swelling did not correspond to a change in the photonic band structure. Instead, the expansion of the functionalized hydrogel increased the lattice constant a of the 3-D PC, causing the pPBG to shift to a longer wavelength. The photonic response of functionalized hydrogels templated inside 3-D PCs will be further discussed in Chapter 3.
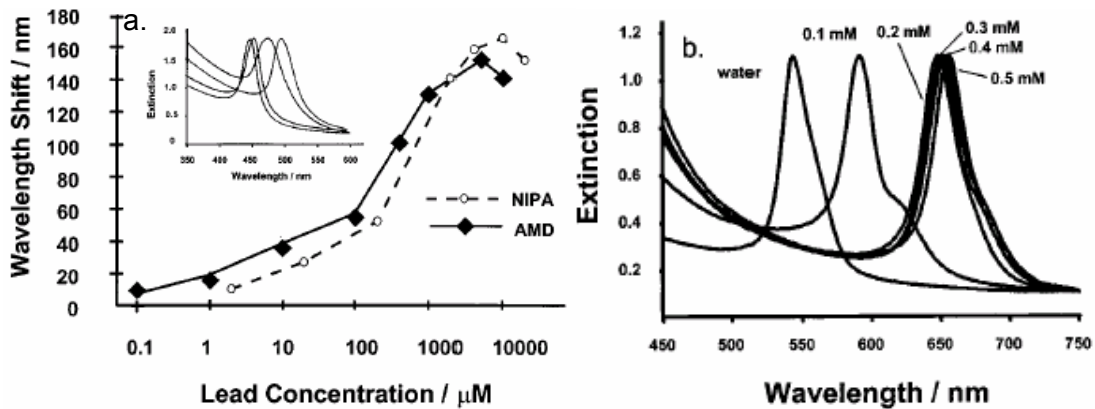
Figure 1.4: 3-D PCCAs of functionalized hydrogels formed by CC templating, showing tunable Bragg diffraction due to hydrogel deformation. (a) Crown ether-functionalized PCCA, showing a red shift in diffraction to Pb^{2+} concentration. (b) Glucose oxidase-functionalized PCCA, showing a red shift in diffraction to glucose concentration. Data adapted from Holtz and co-workers.[15]

1.1.4 Incorporation of Defects

As mentioned previously, incorporation defects into a PC containing a cPBG is of central interest in the production of all-optical circuits because such defects generate states for the propagation of photons inside the PC.   Unlike an optical fiber, which transmits photons by total internal reflection, a PC with incorporated defects may allow the conduction of light around sharp bends and through arbitrary geometry on the micron scale, therefore enabling the production of optical processors similar to the current integrated circuits for electrons.   The defect can be generated by add/removing a structural element in the PC, locally changing the refractive index, or modifying the size of the element.   The incorporation of point defects may also create PCs with useful optical properties.   Since the a point defect forces the localization of light into the defect region,[52,53] the incorporation of point defects into PCs may enable applications where very high populations of photons is desirable, such as highly efficient emitters and compact lasers.   The point defect may also act as an optical cavity, so that at the resonant frequency, the emitted light intensity from the point defect becomes significantly enhanced, appearing as a sharp peak in the emission spectra.   The degree of the light localization by a point defect is often defined in terms of its quality factor $Q = \omega / \Delta\omega$, where ω is the frequency of the emission maximum and $\Delta\omega$ is the width of the corresponding peak.[26]

The effects of point and line defects of the optical properties of PCs was elegantly demonstrated by Noda and co-workers, who fabricated a 2-D PC consisting of air holes in InGaAsP using lithography, which exhibited a cPBG at ~ 1.5 μm.[9]   The triangular array of air holes contained a lattice constant a of 0.42 μm, with a radius $0.29a$.   They

incorporated a line defect of a single row of missing air holes through the PC as the waveguide (Fig. 1.5a), and introduced two point defect of air holes in the vicinity of the waveguide with radii of 0.56a and 0.58a (Fig. 1.5c). First, they demonstrated the successful transmission of IR light through the waveguide feature, as shown by the IR micrographs in Figure 1.5b. Second, through careful control of the size and position of the two point defects, they showed that these optical microcavities coupled the light input from the waveguide and emitted at different normalized frequencies, with $Q \sim 400$. Thus, through precise defect engineering, a compact add-drop filter of desired optical frequencies can be fabricated inside PCs. Subsequently, Ogawa and co-workers fabricated 3-D woodpile PCs of 8 layers of GaAs rods in air sandwiching a single layer of InGaAsP emitter. By careful tailoring of the size and shape of a single dielectric point defect in the emitter layer, features in emission spectra of the 3-D PC can shift by nearly 200 nm from the typical emission wavelength of 1.55 μm.[13] Very recently, Qi and co-workers used a multistep e-beam lithography process to fabricate a layered 3-D PC of Si in air containing isolated dielectric point defects of unetched Si (Fig. 1.6a-c). When examined under IR spectroscopy, the 3-D PC exhibited low transmission between 1.2 μm to 1.6 μm due to the cPBG, with the exception of transmission peaks at 1.3 μm and 1.5 μm from the multiple resonance modes of the point defects, albeit with a low Q of ~ 25 (Fig. 1.6d).
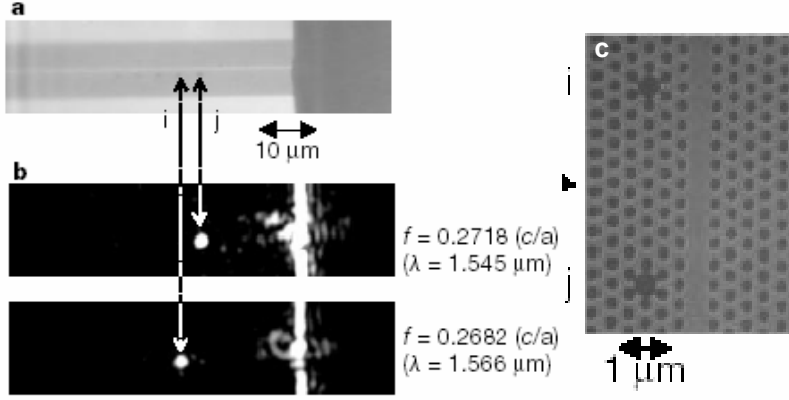
Figure 1.5: A waveguide with add/drop filter capability embedded in a 2-D PC of air holes in InGaAsP. (a) Low magnification SEM of the 2-D PC, containing a line defect of unpatterned InGaAsP acting as a waveguide, as well as two point defects (points i and j) three lattice constants away from the waveguide. (b) Infrared micrographs of the 2-D PC, showing the guiding of infrared right through the line defect (bright line), as well as emission of two different wavelengths of light from the two point defects (bright points), due to the different resonance frequencies of the microcavity. (c) High magnification SEM of the 2-D PC, showing the two point defects (microcavities) lying adjacent to the line defect (waveguide). The different sizes of air hole in point i and j directly caused the variation in its resonant frequency. Data adapted from Noda and co-workers.[9]
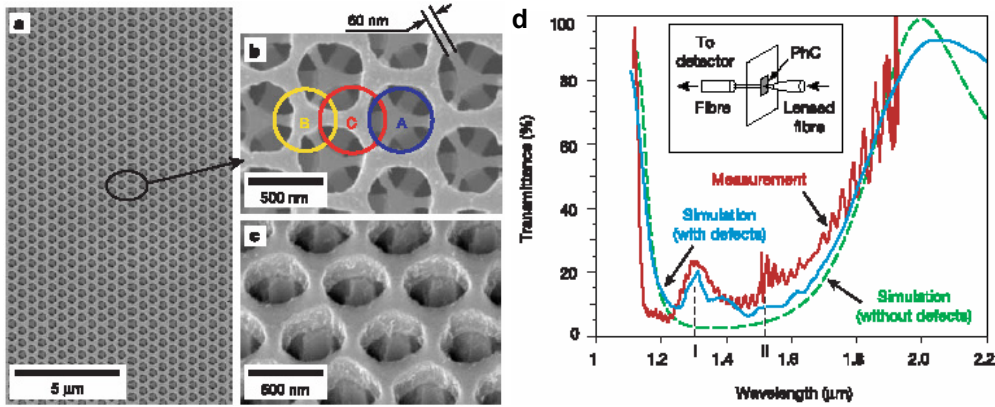
Figure 1.6: A 3-D layered PC of Si in air containing isolated air point defects. (a) Low magnification SEM of the 3-D PC, showing a mesostructure of air holes surrounded by Si. (b) High magnification view of the 3-D PC, showing the connecting elements between layers. Note the symmetry is not FCC. (c) High magnification tilted view of the 3-D PC. (d) Transmission spectra of the 3-D PC, showing nearly zero transmission from 1.2 μm to 1.6 μm due to the cPBG, except for peaks at 1.3 μm and 1.5 μm, the resonance wavelengths of the point defects. The experimental data (red) agreed very well with finite element time domain simulations (blue). Data adapted from Qi and co-workers.[12]

14

1.1.5 Group Velocity Anomaly and Anomalous Dispersion

Even without a cPBG, PCs (especially 2-D and 3-D PCs) can still exhibit interesting optical phenomena; two of the most promising research areas are group velocity anomaly and anomalous dispersion. Due to the refractive index contrast, light of a certain frequency and propagation direction may strongly interact with the PC. The long interaction time between PC and light manifests itself as a small group velocity v_g, and since $v_g = (d\omega/dk)$, such strong interactions correspond to small slopes for the propagation curves in the photonic band structure. This group velocity anomaly may be utilized to enhance stimulated emission, cause sum-frequency generation, increase light absorption, and induce other phenomena.[1] An interesting example of the group velocity anomaly was reported by Fleming and co-workers at Sandia, who fabricated 3-D woodpile PCs of tungsten rods in air with a of ~ 1.5 μm using multistep lithography (Fig. 1.7a).[42,54] They found that while these 3-D PCs exhibited high reflectivity at mid-IR wavelengths (> 8 μm) characteristic of metal films, they also showed strong absorption of specific wavelengths of light at near-IR wavelengths (1.5 μm to 5 μm) with bandwidths of ~ 200 nm.[42] The wavelengths of maximum absorption corresponded very well to the calculated frequencies with flat photonic bands and high photon-PC interaction, suggesting that the enhanced absorption may be due to the group velocity anomaly. In addition, since blackbody radiation and absorption in metals originates from the same process, the Sandia group have demonstrated that the metallodielectric PCs, when heated to high temperatures (~ 1000 K), exhibit an emission spectra with peaks at the wavelengths of enhanced absorption. These peaks exhibited much narrower bandwidths compared to the blackbody emission spectra of unstructured metal films and radiated at a

flux that is five times higher for a given wavelength (Fig. 1.7b), which they successfully used to power a photovoltaic cell.[54] Thus, even for frequencies without a cPBG, a PC can still exhibit interesting optical behavior.
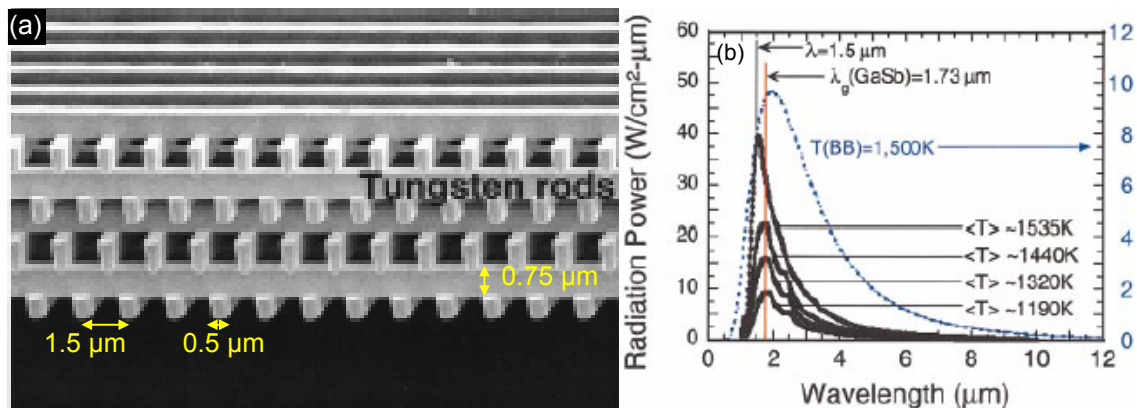
Figure 1.7: A 3-D woodpile PC of W rods in air fabricated by lithography. (a) SEM of the metallodielectric PC, showing a woodpile structure with a lattice constant of ~ 1.5 μm. (b) Blackbody radiation of a similar PC in vacuum at different temperatures, showing a narrow emission spectra with an enhanced light flux at 1.8 μm. Data adapted from Lin and co-workers.[54]

2-D and 3-D PCs also may exhibit anomalous dispersion of light due to their highly anisotropic photonic band structures. When light travels from one isotropic medium to another isotropic medium with a different n, it is refracted following Snell's law, which can be visualized in wavevector space following the conservation of the component of the light wavevector parallel to the interface, with an equifrequency surface that is circular in shape.[26] However, in a PC, the equifrequency surface can be very anisotropic, and the refractive index can very greatly depending on the propagating direction or frequency of light. Thus, a small variation in either parameter can lead to a dramatic and often unexpected change in light refraction inside the PC, a process that is called anomalous dispersion or superprism effect. As an example, Kosaka and co-workers fabricated a honeycomb-shaped pseudo 3-D PC of Si in silica using multistep lithography (Fig. 1.8a). When a 956 nm laser is coupled into the side of the PC, they

found that the propagation direction of light inside the PC varied strongly as a function of its incident angle when $a/\lambda = 0.33$. For example, a 14° change in the incident angle caused a 140° change in the propagation angle inside the PC (Fig. 1.8b). They attributed this anomalous dispersion behavior to the highly anisotropic equifrequency surface of the PC as a function of wavevector at the specific normalized frequency. Using similar PCs, they have also demonstrated anomalous dispersion based on variations in the incident beam wavelength,[35] as well as collimation and divergence of light propagating inside the PC.[36] More recently, Wu and Krauss utilized the superprism effect of a 2-D PC to fabricate wave division multiplexing devices by splitting an optical signal of ~ 30 nm in bandwidth into several distinct beams propagating at different angles within the PC based on their wavelength.[33] Theoretical calculations on a 3-D PC with low δ (inverse opal of PS in air) have also predicted anomalous dispersion with the possibility of negative refractive index,[34] although the predictions have not yet been experimentally verified. In summary, through better understanding of the parameters during their synthesis, PCs promise to bring on a rich variety of new optical phenomena that may one day allow the manipulation of photons in a similar fashion as the electronics are being used today, leading to many potential applications.
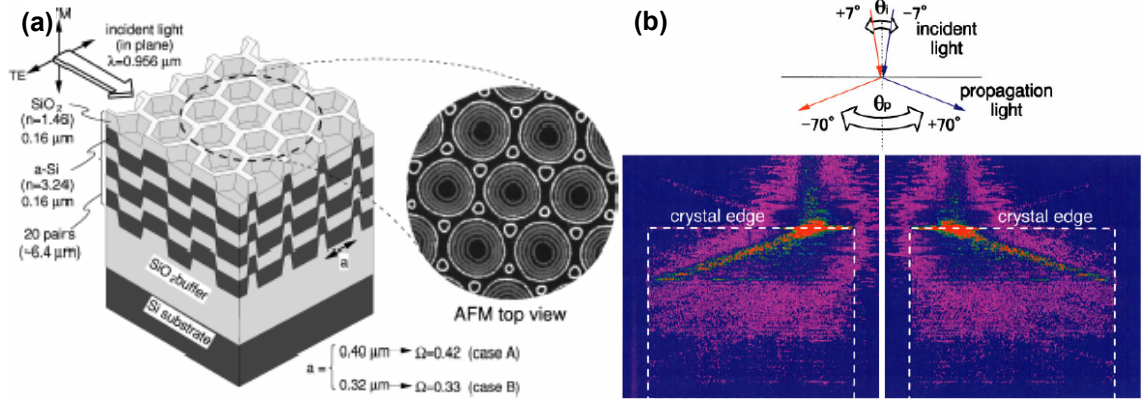
Figure 1.8: A pseudo 3-D PC of Si in silica exhibiting anomalous dispersion. (a) Schematic of the 3-D PC fabricated through lithography. (b) Optical micrographs of the propagation of a 956 nm laser ($a/\lambda = 0.33$) through the PC. A 14° change in the incident angle caused a 140° change in the propagation direction. The PC size is 500 μm x 500 μm. Data adapted from Kosaka and co-workers.[32]

1.2 Colloidal Crystals (CCs)

1.2.1 Fabrication of Colloidal Crystals

Since suspensions of monodisperse silica and PS colloids are commercially available, only the process of CC formation will be described here. CCs can be self-assembled from suspensions of colloids through several general techniques, all of which involve a combination of charge stabilization, hydrodynamic forces, and capillary forces during drying to induce the colloids to pack into an ordered array. A schematic diagram of four CC assembly techniques that we utilized is shown in Figure 1.9.
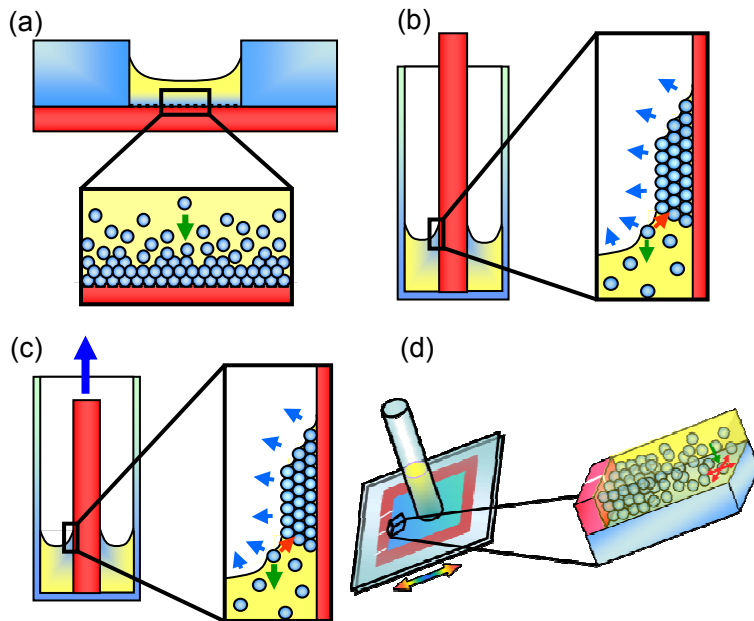
Figure 1.9: Schematic diagrams of four techniques for fabricating colloidal crystals. (a) Sedimentation. (b) Evaporation. (c) Dip coating. (d) Sonication-assisted flow cell.

Sedimentation is probably the most frequently used technique for CC fabrication,[55] since it is easy to set up and is conceptually simple. The density difference between the colloids and the surrounding liquid causes the colloids to settle on the substrate due to gravity, where the interactions between particles cause the formation of an ordered array of CC. However, there are several shortcomings to the sedimentation method. First, since the sedimentation rate of the colloids is dependent on their diameter and the density difference versus the solvent, the time required for full sedimentation may be quite long, especially for systems with a small difference in density, such as PS colloids (1.05 g/cm^3) in water (1 g/cm^3). Second, it is not easy to directly control the thickness of the CC formed, which is important for quantifying the Bragg diffraction intensity of a CC. Third, to obtain a CC in air, the liquid must be removed by evaporation. Unfortunately, since the outside edges of the CC tend to dry first, evaporation drives the colloids from the center of the CC toward the edges, further

decreasing the uniformity of CC thickness. Due to these complicating factors, we fabricated CCs by sedimentation for only some of our initial experiments on conducting polymers (Chapter 2).

In the evaporation method (Fig. 1.9b), a hydrophilic substrate is submerged in a suspension of colloids, and the liquid is allowed to evaporate at room temperature or at an elevated temperature inside a heating bath. The evaporation of liquid induces a flux of colloids to the drying front, where hydrodynamic interactions order the colloids into a close-packed structure, generally FCC. Using this technique, several groups have reported the fabrication of dried CCs with predictable thickness and excellent order, with crack free domains up to hundreds of microns.[8,56,57] One major advantage we have discovered with the evaporation technique is the fact that, because the colloids are constantly swept toward the drying front (which forms a more or less horizontal line), the orientation of the CC remains largely unchanged throughout most of the sample when observed under a microscope. In other words, the CC appears to be composed of a single domain that is separated only by the drying cracks. However, since the flux of colloids to the drying front depends on the rate of evaporation, variation in ambient conditions such as temperature and relative humidity (if drying from an aqueous suspension) may change the thickness and order of the deposited CC. We have also found that the driving force for packing due to evaporation is offset by gravity; in fact, experiments conducted at 45 °C did not induce CC formation from aqueous suspensions of PS colloids if $D > 1.5$ μm. Finally, as mentioned by previous reports,[56,57] we discovered that the number of colloidal layers in a CC formed by the evaporation was roughly inversely proportional to D. Therefore, it was almost impossible to form thick CCs of > 20 layers for $D > 1$ μm.

Nevertheless, we have successfully used evaporation to deposit polystyrene CCs on electrically conductive indium tin oxide (ITO) and modified gold substrates for the electrodeposition of metals through the CC templates (Chapter 6).

Dip coating is a variation on the evaporation technique where the substrate is withdrawn from the colloidal suspension at a constant rate as evaporation takes place (Fig. 1.9c).[30] The relatively slow withdraw rate (0.2 μm/s) allows thin CCs of ~ 30 layers to be formed from a 2% v/v suspension of small polystyrene colloids ($D = 244$ nm) in water, which were used to quantify the effect of the light numerical aperture on the Bragg diffraction of CCs (Chapter 5). Issues with the dip coating process are similar to those of the evaporation technique.

We found the sonication-assisted flow cell technique to be a versatile method for fabricating CCs of uniform thickness and good crystallinity from different types of colloidal suspensions. In this method, the colloidal suspension is introduced into a flow cell from a reservoir, and the evaporation of the solvent from the sides of the flow cell under damped sonication causes the self-organization of colloids into a close-packed structure (Fig. 1.9d).[58] Because the thickness of the flow cell is controlled by the gasket thickness, the CCs formed using the sonication-assisted flow cell method exhibited a uniform thickness that is reproducible across many samples. In addition, the geometry of the flow cell allows for the packing of monodisperse colloidal suspensions with many D values (we have tried D ranging from 170 nm to 10 μm). Finally, the flow cell geometry facilitates the infiltration of dried CCs with acrylated monomers and their subsequent polymerization to CC templated hydrogel films of controlled thickness (Chapters 3 and 4). However, because the reservoir is positioned at the center of the flow

cell, CCs dried from the flow cell generally exhibited drying cracks that radiated outward from the reservoir region to the outside edges of the flow cell. The orientation of the CC from different spots on the sample also varied, suggesting that the CC is not single domain. Fortunately, since the characteristic spacing between layers of colloids is not strongly influenced by the existence of multiple domains, the inverse opal hydrogels polymerized inside these CCs still exhibited strong Bragg diffraction of light that can be tuned through hydrogel deformation.

1.2.2 Colloidal Crystal Templating

Using the techniques mentioned above, high quality CCs can be fabricated from commercially available suspensions of monodisperse silica and PS colloids on a variety of substrates. However, due to the relatively low n values of silica and PS, and the rigidity of these materials, the CCs typically exhibit only a pPBG corresponding to Bragg diffraction from the FCC(111) layers when probed in the sample normal direction. Thus, the fabrication of 3-D PCs from a CC generally involves using the CC as a template for the infiltration of another material. After the infiltration process is complete, the CC template is typically removed, leaving a negative replica with an inverse opal mesostructure (Fig. 1.10). Assuming that the CC template can withstand the processing conditions required for the infiltration of the second material, 3-D PCs of any material can be created using CC templating. In fact, CC templating is critical for the fabrication of FCC PCs with a cPBG since theoretical calculations predicted that an inverse opal mesostructure of a low n material surrounded by a high n material, and not vice versa, exhibited a cPBG,[49] a result that is now supported by experimental observations.[7,8] CC templating is also useful for the generation of functional low n materials that may

alter their refractive index, dimensions, morphologies, and other properties depending on the environmental conditions. As we will show, these functional inverse opal mesostructures exhibited a tunable photonic response that is closely related to the changes in their physical dimensions and optical properties.
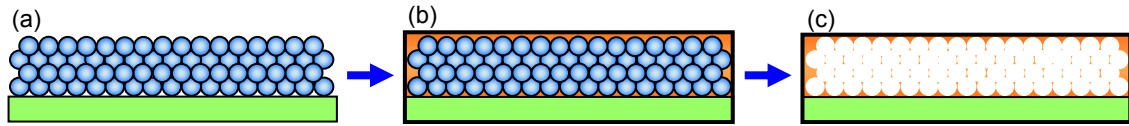
Figure 1.10: Schematic of colloidal crystal templating. (a) Colloidal crystal fabrication. (b) Infiltration with another material. (c) Removal of colloidal crystal template.

An experimental concern that currently degrades the photonic properties CC templated PCs is the existence of defects inherent to the CC templates. Because the colloidal building blocks are never perfectly monodisperse, and because the self-assembly process deals with interactions between many colloids, isolated defects such as vacancies and stacking faults are unavoidable. Moreover, since charge-stabilized colloids are separated by a thin layer of liquid (generally water), the shrinking of the lattice constant that occurs during drying creates cracks even in the most ordered CCs. A recent report has predicted that defects in real CCs cause scattering of light in a cone around the expected propagation direction,[59] so that light propagating in a CC-templated PC will also be scattered. Thus, for subtle effects such as group velocity anomaly and anomalous dispersion, where the interaction of light with the PC is very sensitive to the propagation direction, the defect-induced scattering may weaken the resulting response or mask it altogether. As another example, it is easy to envision that the Q value for an optical resonance cavity will be significantly depressed if there are local variations in the cavity dimensions due to defects in the template. Clearly, synthesizing defect-free CC templates is an important issue for CC templating to become a viable alternative to semiconductor

lithography for the fabrication of 3-D PCs with a full array of photonic properties. Some interesting progress is being made on this front,[60,61] but is beyond the scope of this report. Instead, we will examine the basic optical properties of CC templated 3-D PCs, and quantify the effect of template defects on these properties.

CHAPTER 2

CC TEMPLATING OF CONDUCTING POLYMERS

2.1 Introduction

Since their initial discovery in 1979,[62] conducting polymers have been studied for a variety of applications due to their combination of electrical conductivity, mechanical flexibility, and in some cases switchable electronic and optical properties. A partial list of the potential applications includes mechanical actuators,[63,64] transistors for plastic electronics,[65,66] electrochromic materials,[67] and electrochemical sensors.[68,69] Most conducting polymers switch between an electrically conductive state and insulating state by changing their oxidation state, which involves a change in the formal charge on the polymer backbone. As a result, the intercalation and de-intercalation of counter ions which maintain charge neutrality often controls the performance of devices made from conducting polymers. If a conducting polymer can be made as a mesoporous material, where the pores are accessible to the bulk electrolyte solution containing the counter ions, then the equilibration time after switching for the conducting polymer should decrease, leading to improved device performance.

Many methods have been utilized to generate mesoporous conducting polymers, and some of these mesostructures exhibited superior electrochemical properties. Ghosh and Inganas solution casted polyethylenedioxythiophene-polystyrenesulfonate (PEDOT-PSS) conducting polymer-polyelectrolyte blends in the presence of divalent cations such as Mg^{2+} to produce a highly porous film due to chelation of PSS by the cations.[70] In cyclic voltammetry, the porous PEDOT-PSS exhibited higher peak currents during oxidation and reduction compared with control films cast in the absence of the divalent

cations, indicating that the porous PEDOT-PSS switched between the oxidized and reduced state much more quickly than the unstructured film. In addition, the total charge response of the porous film, which was calculated by integrating the current response in cyclic voltammetry with respect to the elapsed time, was a order of magnitude higher than the control film, again suggesting that there was an increase in surface area and/or counter ion diffusion in the porous PEDOT-PSS.[70] Hughes and co-workers found a similar enhancement in electrochemical response when a polypyrrole (PPy) film was electropolymerized in the presence of modified anionic carbon nanotubes and smaller negative counter ions.[71] They attributed the increased response to enhanced diffusion of small counter ions around the bulky carbon nanotubes. In another method, electropolymerization of PEDOT inside lyotropic liquid crystals generated nanostructured conducing polymer films templated by the morphology of the lyotropic liquid crystal, as shown by the birefringence of templated PEDOT under polarized light microscopy.[72] Finally, we should note that conducting polymer films synthesized through electropolymerization and other methods where the conducting polymer is charged will usually be porous, since counter ions must intercalate between the polymer backbones sometime during the polymerization process. Unfortunately, such pores are generally small (on the order of nanometers) and randomly distributed, and their contribution to the electrochemical properties of the conducting polymer film is not easily determined.

CC templating is an attractive method for fabricating mesoporous conducting polymers with controlled porosity which is easily accessible to the bulk solution due to their large size. In addition, the electrochemical switching of the optical properties of

conducting polymers may enable another way of tuning the Bragg diffraction of the periodically ordered mesostructures. Several groups have demonstrated the electropolymerization of PPy and polythiophenes inside PS or silica CCs, followed by optional etching of the CC template.[22,23,73] In UV-visible-near IR transmission spectroscopy, inverse opal conducting polymers exhibited a sharp dip in transmission corresponding to Bragg diffraction of the CC templated mesostructure, in addition to the features due to optical absorption by the conducting polymer.[22] Caruso and co-workers also immobilized enzymes on inverse opal PPy films and demonstrated that the mesostructured film can potentiometrically sense biomolecules with high sensitivity, due to the large surface area and continuous conductive mesostructure of inverse opal PPy.[23] Yoshino and co-workers infiltrated silica CCs with molten polythiophene and demonstrated that the resulting composite exhibited a Bragg diffraction peak that can be shifted by ~ 1% by heating the sample, taking advantage of change in refractive index of conducting polymers as a function of temperature (thermochromic effect).[74,75] Finally, Deutsch and co-workers synthesized a light emitting conducting polymer, polyphenylenevinylene (PPV), inside a silica CC by thermal conversion of a precursor salt, p-xylylenebis-(tetrahydrothiophenium chloride), and showed that the resulting PPV-CC exhibited a dip in photoluminescence corresponding to the band gap of the CC template.[76] As of the time of this writing, no detailed studies of the electrochemical switching of the Bragg response of inverse opal conducting polymers, or of the effect of CC templating on the transport properties of conducting polymers, have been published.

2.2 Synthesis

2.2.1 Colloidal Crystal Formation

The CC templates were fabricated on two kinds of conducting electrodes via evaporative techniques. For PPy, a glassy carbon voltammetry electrode (MF-2012, Bioanalytical Systems) with a diameter of 3 mm was used as the substrate due to published reports demonstrating good adhesion between glassy carbon and PPy.[64,77] First, the glassy carbon electrode was polished using an aqueous suspension of alumina particles (D = 50 nm, Buehler). The electrode, with the exposed glassy carbon sitting horizontally, was then placed inside an oven (Precision Vacuum Model 19) set at 80 °C. 3.27 μL of a 4% v/v PS colloidal suspension in water (Interfacial Dynamics) was dropped on the surface of the electrode, and the CC formed in about 3 minutes. The self assembly process also lightly sintered the colloids and improved the mechanical stability. We fabricated CCs of two different diameters (D = 500 nm and D = 244 nm). The CC templates visibly opalescent, indicating that they are moderately ordered.

For PEDOT, we fabricated PS CCs by evaporation on a horizontal slide of indium tin oxide (ITO) (thickness = 100 nm, Delta Technologies) sputtered on glass, with the CC area defined by a PDMS gasket. The PDMS gasket was made by placing a rectangular rod of stainless steel with the square cross section (12.5 mm x 12.5 mm) flush against a Si(111) wafer, and then putting the assembly inside a PS Petri dish. The PDMS prepolymer (Sylgard 184, Dow Corning) was first degassed in a vacuum oven and then poured around the stainless steel rod/Si wafer assembly. The PDMS was cured in an oven at 70 °C for 24 h, and the rod and wafer were carefully removed from the PDMS to form the gasket with a thickness of approximately 1 cm. The 25 mm x 25 mm ITO was

cleaned in 20% v/v ethanolamine in water at 80 °C for 30 minutes with gentle stirring, followed by rinsing with DI water and drying under a N_2 stream. We then pressed the PDMS gasket against the cleaned ITO to form a well, which was placed horizontally on the leveling stage inside a plastic dessicator. 360 μL of a 1.33% v/v suspension of PS colloidal suspension in water (D = 466 nm) was injected into the well and allowed to dry completely over ~ 2-3 days. The resulting CC diffracted light, especially near the edges of the well.

2.2.2 Electrochemical Cell Fabrication

For the electropolymerization and electrochemical characterization of PPy, we fabricated a basic three-electrode cell using a black polyethylene photographic film container (Fuji Films). Three holes of different diameters were drilled on the lid of the container: a 6 mm hole for the working electrode (CC on glassy carbon), a 6.5 mm hole for the counter electrode (Cu mesh) during electropolymerization or the reference electrode (0.1M Ag/Ag$^+$ in acetonitrile) during electrochemical characterization, and a 2 mm hole for the counter electrode (Pt flag, area = 1 cm^2). The distance between the working and counter electrode during electropolymerization was 3 cm.

For the electropolymerization and electrochemical characterization of PEDOT, a wide mouthed glass vial (Fisher) was used to hold the electrolyte solutions, since the seal between PDMS and ITO leaked when the monomer solution was injected into the well. The CC on ITO was used as the working electrode, while a Pt wire (D = 500 μm) was used as the counter electrode. The separation between the working and counter electrodes was ~ 2 cm. We used an aqueous Ag/AgCl reference electrode with a standard

reduction potential E^0 of 0.197 V vs. normal hydrogen electrode (NHE) (Bioanalytical Systems) for all PEDOT experiments.

2.2.3 Electropolymerization of Conducting Polymers

2.2.3.1 Polypyrrole (PPy)

Pyrrole (Acros), propylene carbonate (Acros), tetraethylammonium hexafluorophosphate (Alfa Aesar), and acetonitrile (Acros) were used as received. We mixed pyrrole (84 μL), water (200 μL), tetraethylammonium hexafluorophosphate (0.275 g), and propylene carbonate (23.738 g) to make 20 mL of the monomer solution, following published procedures.[64,77] We then degassed the pyrrole monomer solution by bubbling N_2 and transferred the solution into a glove box (mBraun) operating in an Ar atmosphere. We injected the monomer solution into the electrochemical cell, and then submerged into solution the CC/glassy carbon working electrode and a counter electrode consisting of a 50 mesh Cu gauze (Alfa Aesar) rolled into a cylinder (D = 6 mm). We then electropolymerized PPy on the working electrode under galvanostatic conditions with an anodic current density of -0.125 mA/cm^2 and gentle Ar sparging, using a commercial potentiostat/galvanostat (Princeton Applied Research Model 263A). A total charge density of 1.193 C/cm^2 was consumed during electropolymerization, corresponding to a thickness of ~ 10 μm for the inverse opal PPy film assuming a coulombic efficiency of 100%. After electropolymerization, the CC template was etched by placing the PPy film in $CHCl_3$ for 18 h.

2.2.3.2 Polyethylenedioxythiophene (PEDOT)

Electropolymerization of the templated PEDOT followed published procedures.[78,79] Ethylenedioxythiophene (Bayer), sodium dodecyl sulfate (Acros),

and LiClO$_4$ (Acros) were used as received. We prepared the monomer solution by mixing ethylenedioxythiophene (0.142 g), sodium dodecyl sulfate (0.404 g), and LiClO$_4$ (0.213 g) with water (20 mL), yielding a monomer concentration of 0.05 M. We injected the monomer solution into the cell and submerged the CC/ITO working electrode the Pt wire counter electrode, and the Ag/AgCl reference electrode into the solution. Anodic electropolymerization was performed galvanostatically at a current density of -0.1 mA/cm^2 in atmosphere using the potentiostat/galvanostat. A total charge density of 0.155 C/cm^2 was consumed during electropolymerization, corresponding to an expected PEDOT thickness of ~ 4 μm assuming an inverse FCC structure and a coulombic efficiency of 100%. After electropolymerization, the CC template was etched by placing the PEDOT film in THF for 12 h.

2.3 Characterization

2.3.1 Scanning Electron Microscopy

The mesostructure of the inverse opal PPy and PEDOT films was examined using a scanning electron microscope (Hitachi S-4700), typically under an accelerating voltage of 10kV. Since the as-polymerized PPy and PEDOT are electrically conductive, no metal sputtering was required.

2.3.2 Cyclic Voltammetry

To examine the effect of the dense film morphology and interconnected pore mesostructure on the electron transport properties of conducting polymers, we performed cyclic voltammetry (CV) on three types of PPy films: the CC templated film prior to etching, the CC templated film after etching, and a control film electropolymerized on an electrode without CC. All CV experiments were carried out inside the Ar atmosphere of

the glove box (mBraun). The electrochemical cell used for the electropolymerization was also used for CV. A PPy film electropolymerized on the CV electrode was used as the working electrode. A 0.05 M electrolyte solution was made by mixing tetraethylammonium hexafluorophosphate (0.2752 g, Alfa Aesar) with propylene carbonate (23.728 g, Acros). In addition, a 0.5 M electrolyte solution was prepared by using 10 times the amount of tetraethylammonium hexafluorophosphate (2.752 g). A 0.01 M nonaqueous Ag/Ag$^+$ reference electrode with E^0 = 0.473 V vs. NHE was fabricated by dissolving AgNO$_3$ (0.170 g, Aldrich) in acetonitrile (10 mL, Acros) and filling an empty Ag reference electrode (Bioanalytical Systems) with the solution. A Pt flag with a square area of 1 cm^2 and a pole length of 3 cm was cut from a larger Pt sheet (Alfa Aesar) and used as the counter electrode.

The electrochemical cell was filled either with the 0.5 M or 0.05 M electrolyte solution. PPy film was first rinsed with propylene carbonate to remove any pyrrole monomer and then placed inside the electrochemical cell. We waited 20 minutes before starting CV experiments to allow for the full equilibration of concentrations of hexafluorophosphate and other ions inside the PPy. The Ag/Ag$^+$ reference electrode and the Pt flag counter electrode were also submerged in the electrolyte solution. CV was performed on the Princeton Applied Research 263A potentiostat/galvanostat using commercial software (PowerSuite, Princeton Applied Research). After the electrodes have been connected, the PPy film was first converted to the reduced state by applying a steady state voltage of -1.2 V vs. Ag/Ag$^+$ for 20 minutes. The potential on the working electrode was then linearly swept from -1.2 V vs. Ag/Ag$^+$ to 0.3 V vs. Ag/Ag$^+$ and then back at a scan rate of 1 mV/s, and the current response was plotted at each voltage to

32

yield a cyclic voltammogram. The experiment was then repeated at 2 mV/s, 5 mV/s, 10 mV/s, 20 mV/s, 50 mV/s, 100 mV/s, and 200 mV/s, without any delay time between each scan. For each scan rate, we analyzed only the cyclic voltammogram from the fifth cycle to minimize the effects of transient (nonfaradaic) currents. The PPy film was then removed from the 0.5 M electrolyte solution and rinsed with propylene carbonate, the electrochemical cell was refilled with the 0.05 M electrolyte solution, and the CV experiments were repeated.

2.3.3 Microspectroscopy

The Bragg diffraction of inverse opal PEDOT films at different oxidation states were examined with vis-near IR microspectroscopy, which is described in detail in Chapter 3. Briefly, normal incidence reflectance spectra from a small spatial region of the PEDOT film was collected using an inverted reflection optical microscope (Axiovert 135, Zeiss) coupled to a diffraction grating spectrometer (Control Development, Inc.). The as-polymerized PEDOT sample was dried with an N_2 stream and placed in a PS Petri dish mounted on top of the optical microscope, and the reflectance spectra was collected. 0.1 M $LiClO_4$ (aq.) electrolyte solution was then added to the Petri dish, and the reflectance spectra of PEDOT in aqueous solution was acquired. The sample was then submerged in the electrochemical cell with 0.1 M $LiClO_4$ (aq.), and the PEDOT film was reduced for 110 s at a potential of -0.8 V vs. Ag/AgCl using a Pt wire (Alfa Aesar) as the counter electrode. The reduced film was dried with N_2 and placed in the Petri dish, and the reflectance spectra was collected. Finally, the PEDOT film was reoxidized for 110 s at a potential of 0.6 V vs. Ag/AgCl, placed back in the Petri dish, and characterized. An effort was made to collect the reflectance spectra from the same sampling spot on the

inverse opal PEDOT, although due to the moving of the sample between the Petri dish and the electrochemical cell, the sampling spot probably shifted between microspectroscopy experiments.

2.4 Results and Discussion

2.4.1 Mesostructure of Inverse Opal Conducting Polymers

For both templated PPy and PEDOT, we observed an inverse opal mesostructure consisting of smooth and compact films, similar to previous reports.[22,73] The interconnects between each pore and the three nearest neighbors on the subsequent FCC(111) plane can be easily discerned from the micrographs of the templated PPy (Fig. 2.1b and c) and PEDOT films (Fig. 2.2). In the case of PPy templated with the larger PS colloids (D = 500 nm), the mesopores were rather disordered (Fig. 2.1a), suggesting that the template itself possessed a low degree of order. The nearly complete etching of the CC templates indicates that the colloids were in close contact. The coulombic efficiency for the PPy electrodeposition can be calculated from the thickness of the PPy film in Figure 2.1, which showed a dense film of ~ 1 μm thickness and an inverse opal film of ~ 2 μm thickness. Converting the thickness values to a completely inverse opal film with volume fraction of 0.26 yielded a coulombic efficiency of 0.60. The coulombic efficiency for the PEDOT electropolymerization, calculated from the thickness of the inverse opal film in Figure 2.2 (3 μm), was 0.75.
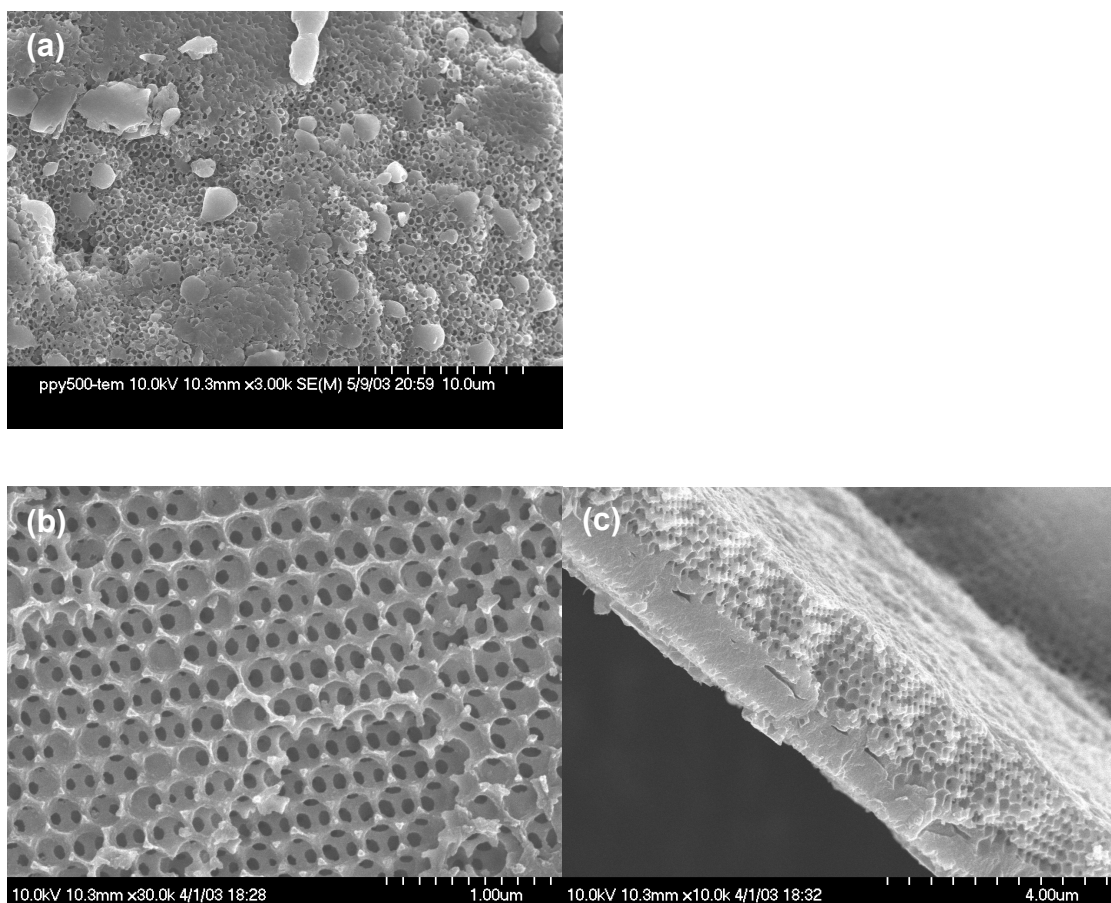
Figure 2.1: SEM of an electropolymerized templated PPy film. (a) *D* = 500 nm, top view, showing a disordered mesoporous morphology due to poor packing of the CC template. (b) *D* = 240 nm, top view, with an inverse opal mesostructure. (b) *D* = 240 nm, side view, showing an ~ 1.5 μm thick untemplated PPy film below the templated region. The colloidal template may have detached during the electrodepostion process.
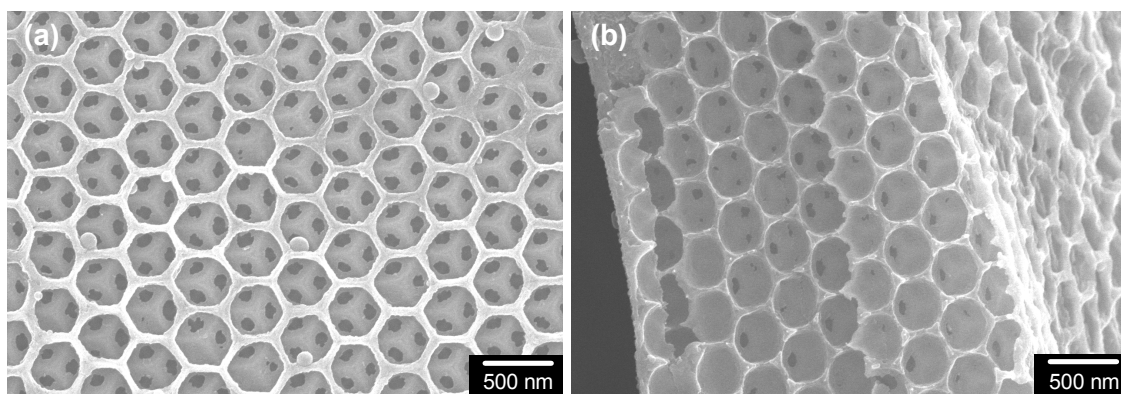
Figure 2.2: SEM of an electropolymerized inverse opal PEDOT film. (a) Top view. (b) Side view.

The morphology of the CC templated conducting polymer films differed significantly from films electropolymerized under the same condition on an untemplated electrode. For example, the untemplated PEDOT film exhibited a high degree of roughness on length scales equal to and larger than the colloidal diameter (Fig. 2.3). The high degree of roughness for the untemplated PEDOT film is consistent with published reports, which showed roughness on the order of hundreds of nm for PEDOT films electrodeposited from similar aqueous micellar monomer solutions.[78] Thus, the CC may be acting as a leveling agent to promote the growth of smooth and compact films inside the template.
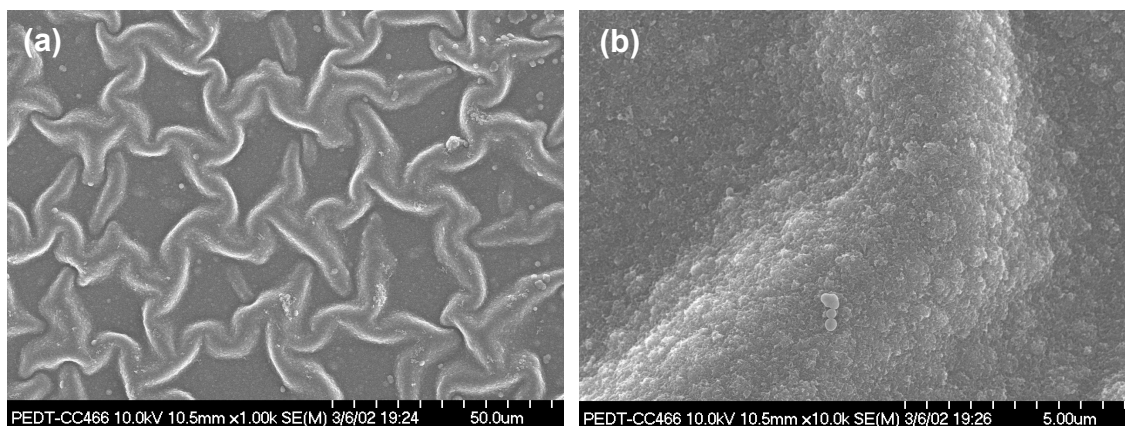
Figure 2.3: SEM of an electropolymerized untemplated PEDOT film, top view. The untemplated PEDOT is significantly rougher than the templated film. (a) Low magnification view. (b) High magnification view.

2.4.2 Electrochemical Properties of PPy and Effect of CC Templating

The CV behavior of the electropolymerized PPy films varied greatly depending on the type of templating (CC vs. random close packed particles), the presence or absence of etching, and the concentration of electrolyte. For the PPy film templated by the 500 nm colloidal aggregate, we found that in 0.05 M electrolyte, the I-V response of the etched film to be lower than the unetched film for scan rates of less than 2 mV/s (Fig.

36

2.4). However, at the scan rate increased, the etched film became more responsive, exhibiting larger anodic and cathodic peak currents (I_a and I_c) as well as total charge transferred, which was calculated by the area under the I-V curve. As the scan rate increased, the separation between the anodic and cathodic peak potentials ($\Delta E = E_a - E_c$) also increased (Fig. 2.4), suggesting that the redox reaction was not fully reversible and that the electron transfer inside the PPy film was relatively slow.[80] Finally, at each scan rate, both E_a and E_c remain the same for the etched and unetched PPy film, indicating that the exposure to $CHCl_3$ during template removal did not chemically modify the conducting polymer.

(a) 500nm PS PPY CV E/UE 1mV/s, .05 M Electrolyte

Current (A)

6.00E-05
4.00E-05
2.00E-05
0.00E+00
-2.00E-05
-4.00E-05
-6.00E-05
-8.00E-05

-1.5   -1   -0.5   0   0.5

I_1_.05_UE
I_1_.05_E

Potential (V)

(b) 500nm PS PPY CV E/UE 2mV/s, .05 M Electrolyte

Current (A)

1.00E-04
5.00E-05
0.00E+00
-5.00E-05
-1.00E-04
-1.50E-04

-1.5   -1   -0.5   0   0.5

I_2_.05_UE
I_2_.05_E

Potential (V)

(c) 500nm PS PPY CV E/UE 5mV/s, .05 M Electrolyte

Current (A)

1.50E-04
1.00E-04
5.00E-05
0.00E+00
-5.00E-05
-1.00E-04
-1.50E-04
-2.00E-04

-1.5   -1   -0.5   0   0.5

I_5_.05_UE
I_5_.05_E

Potential (V)

(d) 500nm PS PPY CV E/UE 10mV/s, .05 M Electrolyte

Current (A)

0.0003
0.0002
0.0001
0
-0.0001
-0.0002
-0.0003

-1.5   -1   -0.5   0   0.5

I_10_.05_UE
I_10_.05_E

Potential (V)

(e) 500nm PS PPY CV E/UE 20mV/s, .05 M Electrolyte

Current (A)

0.0003
0.0002
0.0001
0
-0.0001
-0.0002
-0.0003
-0.0004

-1.5   -1   -0.5   0   0.5

I_20_.05_UE
I_20_.05_E

Potential (V)

Figure 2.4: Cyclic voltammograms of a PPy film electropolymerized inside a colloidal aggregate (D = 500 nm), tested in a 0.05M electrolyte solution. (a) 1 mV/s. (b) 2 mV/s. (c) 5 mV/s. (d) 10 mV/s (e) 20 mV/s. Magenta (blue) curves correspond to etched (unetched) films.

When I_c values for the unetched and etched PPy film were plotted as a function of scan rate, two different power law relationships were extrapolated (Fig 2.5). The stronger dependence of peak current on scan rate for the PPy film after template removal can be explained by the slow electron transfer kinetics inside PPy films. When the response of a

redox active substrate is limited by the diffusion of species to the substrate, the peak current was found to be proportional to the square root of scan rate.[80] At the other extreme, when the electron transfer kinetics of the substrate represented the rate limiting step, the peak current was found to be linearly proportional to the scan rate.[81] At a low electrolyte concentration of 0.05 M, there was an insufficient quantity of counter ions surrounding an untemplated PPy film to maintain charge neutrality during the redox cycle of the conducting polymer film, and thus counter ions must diffuse in from the bulk electrolyte solution, leading to the square root dependence on scan rate (Fig. 2.5, diamonds). However, when the colloidal template was removed, the FCC pores acted as a reservoir of electrolytes, and thus I_c exhibited a greater responsiveness to the scan rate (Fig 2.5, squares), indicating that the response of the etched film has become partially limited by surface diffusion (i.e. slow electron transport kinetics inside the PPy film). The quantitative discrepancy between the experimentally observed exponent (0.63) and the expected value for a surface diffusion limited system (1) may be partially explained by the polymeric nature of the PPy film. For example, when PPy becomes positively charged during oxidation, the intercalation of counter ions into between the PPy chains should be slowed down due to the time required for chain relaxation. As a result, the I-V response of a PPy film to redox cycling would be expected to be slower compared to a simple redox-active electrode.
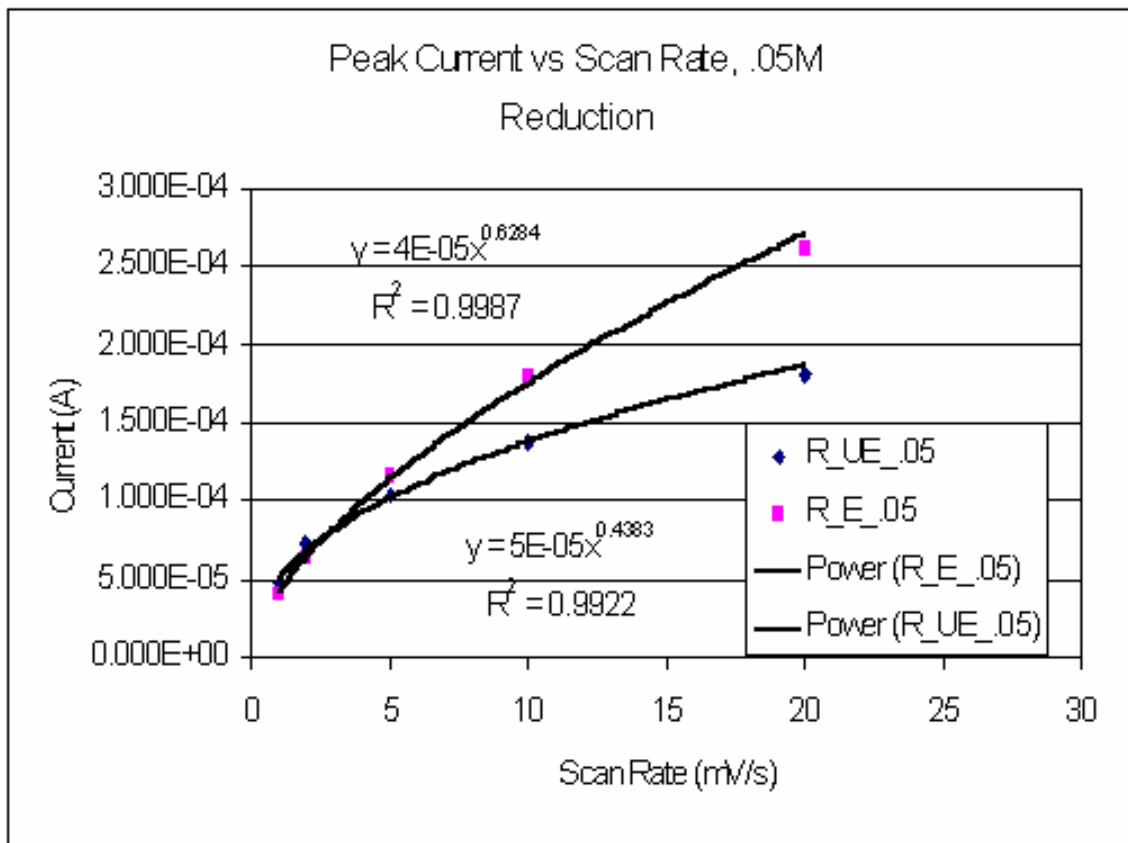
Figure 2.5: Cathodic peak current versus scan rate for the colloidal aggregate templated PPy, tested in a 0.05 M electrolyte solution. The best power law fits for the two trends were also plotted. The fit for the etched film exhibited a higher exponent for the dependence of peak current versus scan rate, indicating that the response of the etched film was partially limited by surface diffusion (i.e. slow electron transport kinetics inside the PPy film), whereas the response of the unetched film was controlled by bulk diffusion of counter ions in/out of the film during oxidation/reduction.

If the CV response of a templated PPy film was limited by a combination of bulk counter ion diffusion and slow electron transport kinetics through the PPy film, then the I-V relationship of a PPy film at high electrolyte concentration should approach the surface diffusion limit as the counter ion diffusion becomes less of an issue. That was indeed the behavior observed for the CV of the PPy film tested in a 0.5M electrolyte solution (Fig. 2.6). With the high electrolyte concentration, the I-V responses for the PPy film before and after etching are similar to each other. For both the etched and unetched film, the dependence of I_c on scan rate followed a power law with an exponent of ~ 0.7

(Fig 2.7). The higher value for the exponent compared with the low concentration electrolyte case (0.63) also supports the hypothesis that the increase in electrolyte concentration shifted the rate limiting mechanism from bulk counter ion diffusion toward electron transfer kinetics in PPy. Interestingly, the magnitude of the current response for 0.5 M electrolyte concentration was higher for the unetched versus etched PPy films (Fig. 2.6, blue versus magenta lines). Such quantitative deviations may be the result of a slight change in the distance between the working and counter electrodes between the two sets of CV experiments, especially in a propylene carbonate based electrolyte that has a high solution electrical resistance.
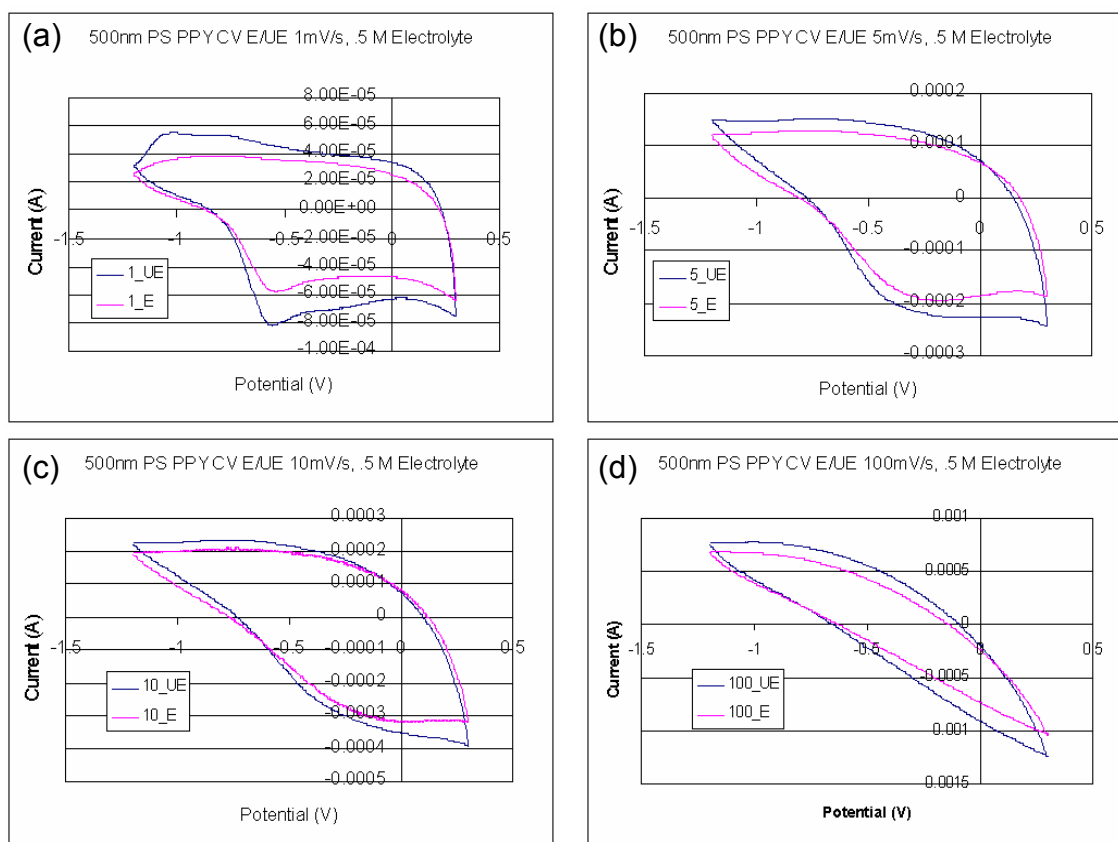
Figure 2.6: Cyclic voltammograms of a PPy film electropolymerized inside a colloidal aggregate (D = 500 nm), tested in a 0.5 M electrolyte solution. (a) 1 mV/s. (b) 5 mV/s. (c) 10 mV/s. (d) 100 mV/s. Magenta (blue) curves correspond to etched (unetched) films.
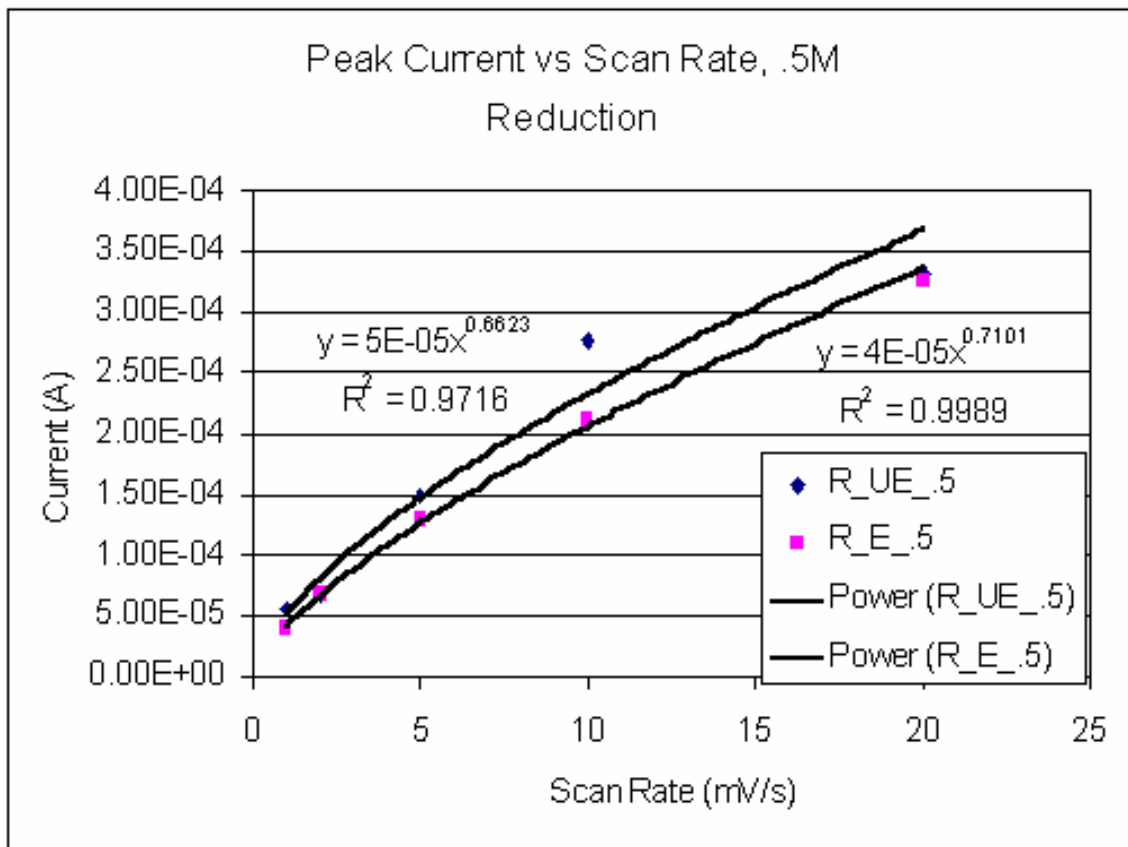
Figure 2.7: Cathodic peak current versus scan rate for the colloidal aggregate templated PPy, tested in a 0.5 M electrolyte solution. The best power law fits for the two trends were also plotted. The exponents for the both etched and unetched PPy film are similar to each other, suggesting that the pores now contain sufficient electrolytes so that counter ion diffusion was no longer the rate limiting mechanism.

PPy film templated by a CC with D = 240 nm, while exhibiting a well ordered inverse opal mesostructure (Fig 2.1b), displayed complicated CV data which suggested possible chemical modification of the film due to contaminants. Representative I-V curves for the CC templated PPy film in 0.05 M electrolyte solution before and after etching are shown in Figure 2.8. Even from visual observation, it is clear that E_a and E_c before and after etching were significantly different (Fig. 2.8). In addition, when I_c was plotted as a function of scan rate for this film, the etched film exhibited a current response that was smaller by a factor of 6 (Fig. 2.9). Discrepancies were also observed in the CV data tested in 0.5 M electrolyte (Fig. 2.10 and 2.11). In contrast to PPy

polymerized inside the colloidal aggregate, the CC templated PPy film exhibited shifts in E_a and E_c at different scan rates, suggesting that contaminants may have chemically damaged the PPy film during electropolymerization and/or characterization. A possible film damage would be consistent with the lower magnitude of current response observred in the CC templated PPy (Fig. 2.9 and 2.11) as compared to the colloidal aggregate templated PPy (Fig. 2.5 and 2.7). Finally, it is also possible that the untemplated PPy that was electropolymerized underneath the inverse opal PPy (Fig. 2.1c) may have complicated the CV response, although one would expect that the presence of a thick untemplated film should serve to make the behavior of the etched and unetched PPy film more similar.
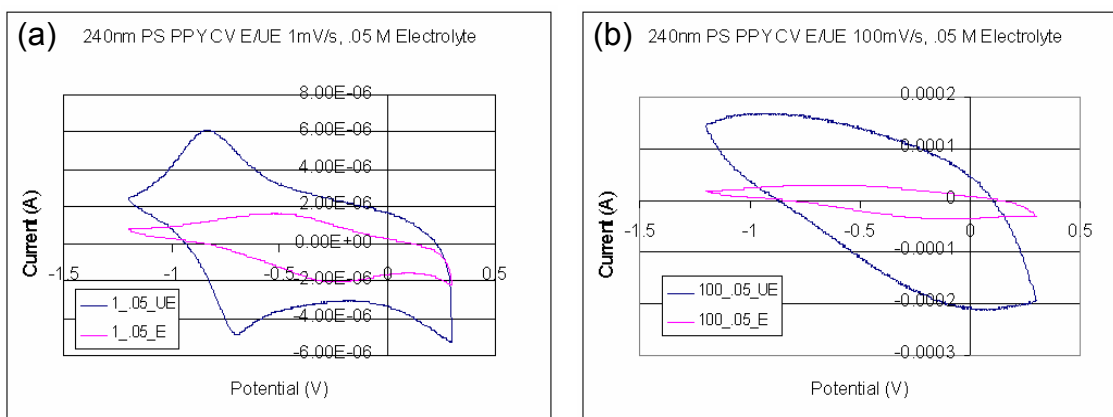
Figure 2.8: Cyclic voltammograms of a PPy film electropolymerized inside a CC (D = 240 nm), tested in a 0.05 M electrolyte solution. (a) 1 mV/s. (b) 100 mV/s. Magenta (blue) curves correspond to etched (unetched) films.
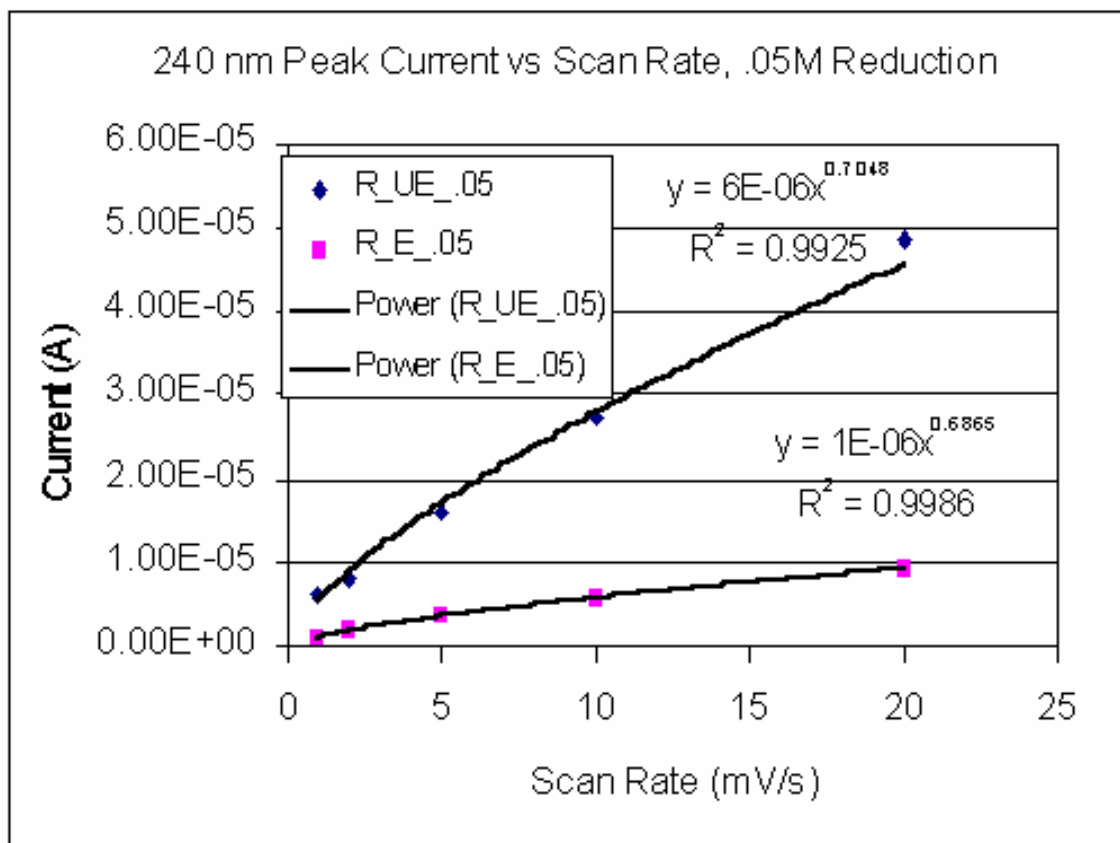
Figure 2.9: Cathodic peak current versus scan rate for the PPy film electropolymerized inside the CC template, tested in a 0.05 M electrolyte solution. The current response for the etched film (squares) is much smaller than for the unetched film (diamonds), which may be caused by inclusion of contaminants.

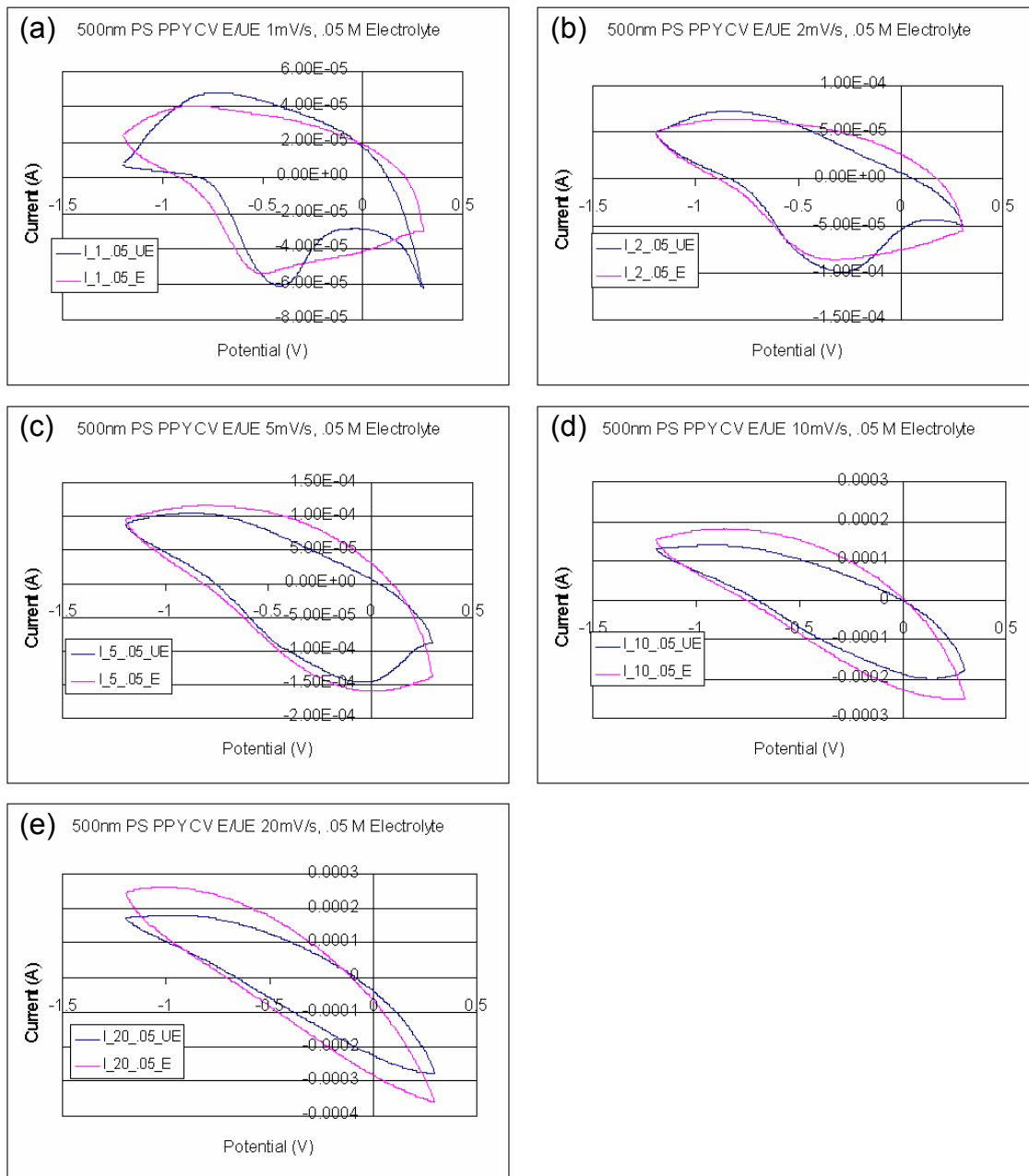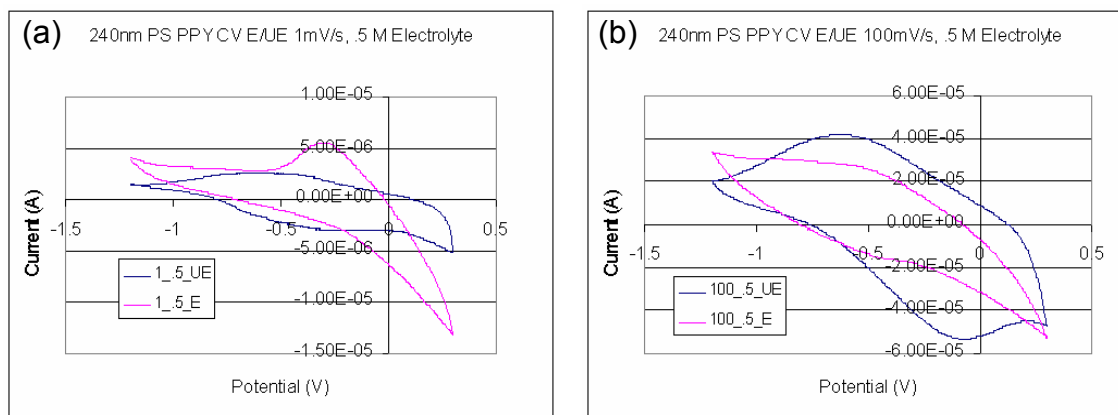**Fig. 2.10:** Cyclic voltammograms of a PPy film electropolymerized inside a CC ($D = 240$ nm), tested in a 0.5 M electrolyte solution. (a) 1 mV/s. (b) 100 mV/s. Magenta (blue) curves correspond to etched (unetched) films.

44

240 nm Peak Current vs Scan Rate, .5M Reduction

$y = 2E\text{-}06x^{0.6191}$

$R^2 = 0.9979$

$y = 6E\text{-}06x^{0.3394}$

$R^2 = 0.984$
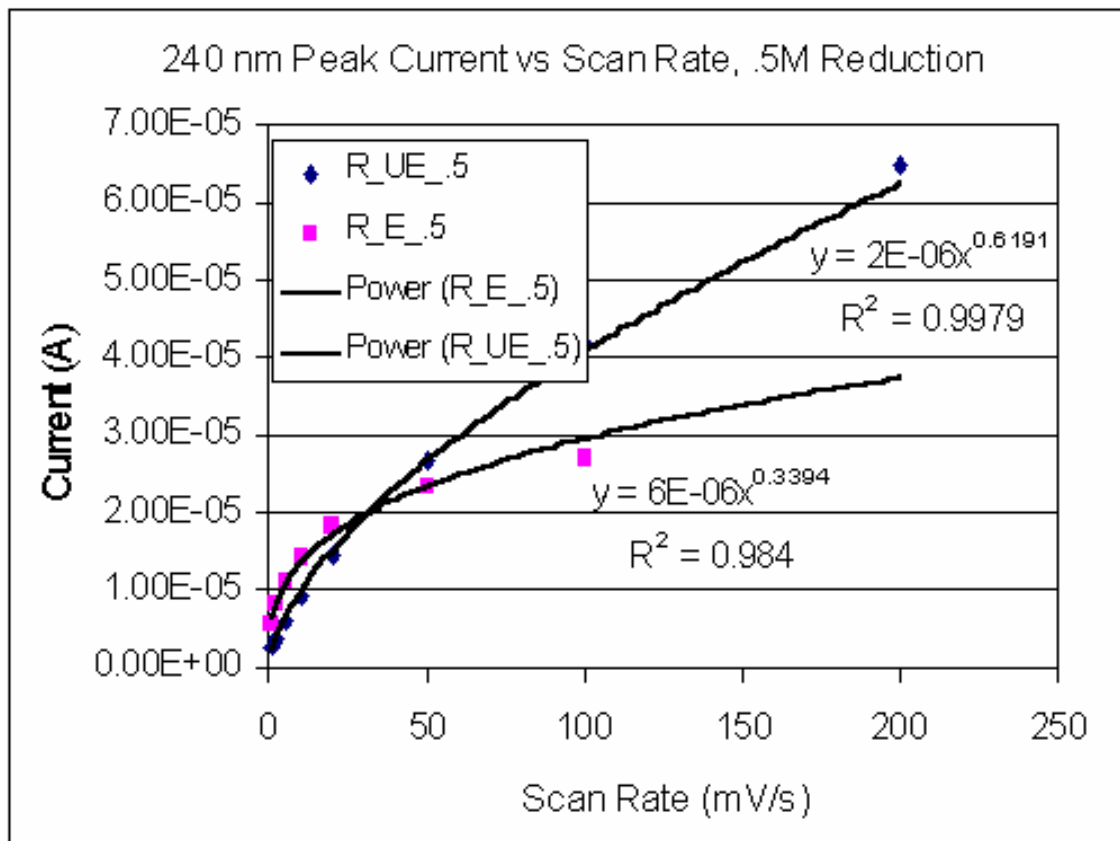
Figure 2.11: Cathodic peak current versus scan rate for the PPy film electropolymerized inside the CC template, tested in a 0.5 M electrolyte solution. A significant discrepancy exists between the responses of the etched (squares) versus unetched (diamonds) film.

2.4.3 Optical Properties of Inverse Opal PEDOT

We chose to test the Bragg diffraction response of inverse opal PEDOT films because PEDOT exhibits favorable optical and chemical properties compared to PPy. Whereas PPy is optical absorbing over the visible and near-IR wavelengths, PEDOT possesses good transparency in its oxidized state.[67] In addition, PEDOT can be polymerized and electrochemically operated in the presence of O_2 and water, which makes it relatively simple to characterize when exposed to air during microspectroscopy. In fact, the favorable combination of properties have resulted in a significant amount of research on the utilization of PEDOT and similar conducting polymers in optically active devices such as electrochromic windows.[67] Using the approximately 8-layer PEDOT

film shown in Fig. 2.2, we found that by stepping the electrochemical potential between 0.6 V and -0.8 V vs. Ag/AgCl, the PEDOT film switched from an oxidized state with a dark blue coloration to a reduced state with a purple coloration, similar to published data.[78,79]

Microspectroscopy of the templated PEDOT film revealed distinct peaks in the reflectance spectra which shifted depending on its oxidation state and surrounding environment (Fig 2.12). The as polymerized inverse opal PEDOT, which was oxidized, exhibited a reflectance peak at 670 nm in air. When the film was submerged in water, the peak red shifted to 830 nm. Finally, after the PEDOT film was reduced and then dried, the peak blue shifted all the way to 590 nm. These shifts are qualitatively consistent with the physical changes in the conducting polymer and/or the environment. For example, replacing air with water should cause a red shift in Bragg diffraction, while electrochemical reduction of PEDOT should cause the film to contract due to deintercalation of negatively charged counter ions, leading to a blue shift in Bragg diffraction. Unfortunately, the observed peak positions do not match well to the values calculated from the Bragg equation (Eq. 1.2). Assuming that the lattice constant increased by 5% in the oxidized cases and that the refractive index of PEDOT equals 1.7, an inverse opal of PEDOT electropolymerized inside a CC with diameter of 466 nm should exhibit peak positions of 977 nm, 1149 nm, and 929 nm respectively. A major complication with the Bragg diffraction of mesostructured conducting polymers during redox cycling arises from the simultaneous deformation of the mesostructure due to counter ion intercalation and potentially large changes in the complex refractive index due to shifts in the absorption spectra. Also, the large optical absorption of conducting

polymers generally leads to inefficient Bragg diffraction, as shown by the small background subtracted peak intensities (2-4%) in Figure 2.12. As we demonstrate in the next chapter, the tunable Bragg response of transparent materials which undergo volumetric changes, e. g. hydrogels, is more readily characterized by microspectroscopy and predicted using Equation 1.2 and other theoretical calculations.
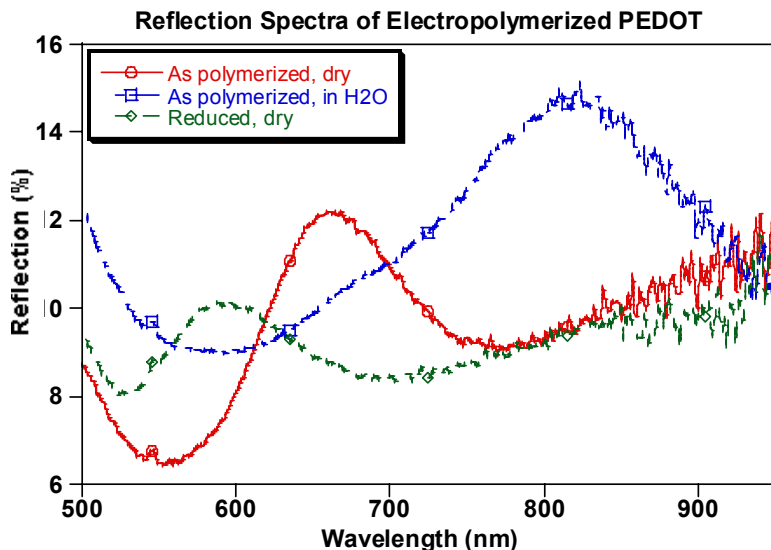
Figure 2.12: Reflectance spectra of a CC templated PEDOT film. The weak diffraction peak shifted depending on the oxidation state of the polymer and on the refractive index of the surrounding medium.

2.5 Summary

Templated films of conducting polymers such as PPy and PEDOT were electropolymerized inside self-assembled colloidal mesostructures. Structural characterization of the templated conducting polymers films after template etching revealed robust inverse opal or inverse random close packed mesostructures depending on the order of the colloidal template. Cyclic voltammetry of PPy films in a template of colloidal aggregates (D = 500 nm) before and after template removal showed that, for a low electrolyte concentration of 0.05 M, the current response of the etched PPy film increased more quickly as a function ofscan rate (power law exponent ~ 0.7) compared to

47

the unetched film (power law exponent ~ 0.5), corresponding to a change from a bulk diffusion limited regime to a partially surface diffusion limited regime. This shift in the rate limiting mechanism is consistent with the greater availability of counter ions due to the larger surface area provided by the templated mesostructure. When the electrolyte concentration was increased to 0.5 M, both the etched and unetched PPy film showed comparable current responses with each other, and the high power law coefficient of 0.7 suggested that, as expected, the CV response of PPy at high ion concentration is no longer diffusion limited. PPy films templated inside a CC (D = 240 nm) displayed inconclusive trends with respect to the scan rate, which may have resulted from contamination. Electropolymerized inverse opal PEDOT films displayed shifts in the reflectance peaks which were qualitatively consistent with the deformation of the conducting polymer and/or changes in the environment. However, the quantitative discrepancy between the observed peak positions and the predictions from Bragg equation suggests that the larger optical absorption and environmental instability of conducting polymers may reduce their applicability as devices with tunable Bragg diffraction.

CHAPTER 3

CC TEMPLATING OF HYDROGELS

Significant components of this chapter were published as "Tunable inverse opal hydrogel pH sensors", Y.-J. Lee and P. V. Braun, *Advanced Materials* **2003**, *15*, 563-566, and "Glucose-sensitive inverse opal hydrogels: analysis of optical diffraction response", Y.-J. Lee, S. A. Pruzinsky, and P. V. Braun, *Langmuir* **2004**, *20*, 3096-3106.

3.1 Introduction

There is a growing interest in the creation of optically active 3-D mesostructured hydrogels for chemical and biological sensing. Hydrogels can be designed to undergo reversible changes in physical dimensions in response to external parameters such as solvent composition,[82,83] temperature,[84,85] pH, ionic strength (*I*),[86] and biomolecule binding[87-90] through functionalization with responsive moieties. Such reversible swelling makes hydrogels excellent candidate materials for optically based sensors when coupled to an appropriate signal transduction mechanism. One possible method takes advantage of optical diffraction of CCs, arising from their 3-D mesostructure with periodicity on the order of the wavelength of visible light. If the periodicity of the colloidal crystal can be imparted to a responsive hydrogel, then the reversible swelling of the hydrogel may change the periodic spacing, resulting in a shift in diffraction wavelength (Fig. 3.1). For example, if a responsive hydrogel is polymerized in the interstitial space of a CC template, the resulting mesostructured hydrogel may form the basis for a sensor based on tunable optical diffraction.
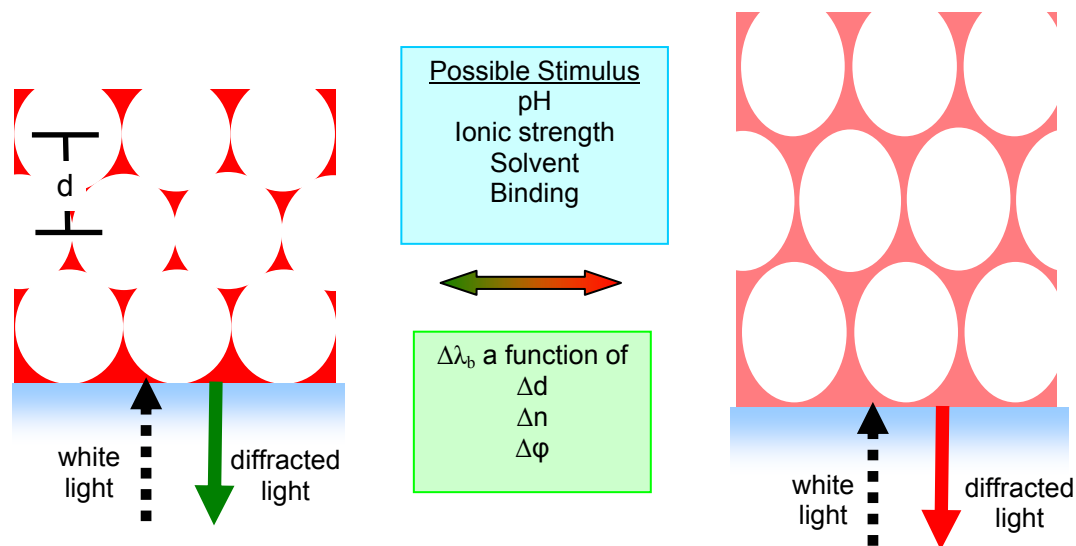
Figure 3.1: Schematic of a sensor with tunable Bragg diffraction, such as a CC-templated hydrogel. When the mesostructure responds to the introduction of a stimulus with volumetric changes, the corresponding change in the characteristic interlayer distance d, the refractive index n, and/or volume fraction φ of the component phases causes a shift in the Bragg condition, leading to reflection of a new wavelength of light (λ_b).

Large area colloidal crystal templates can be formed by self-assembly of monodisperse colloids using techniques including patterned sedimentation,[91] controlled evaporation,[8,56] sonication-assisted packing,[58] formation in a flow cell,[51,92] and other methods.[93] A colloidal crystal formed on a planar substrate usually adapts a FCC structure with the (111) plane parallel to the substrate, and interacts strongly with light following the Bragg equation (Eq. 1.2). Colloidal crystals have been successfully utilized to template the growth of various polymers,[22,73,94-97] including hydrogels.[14-16,92]

It has been known for more than 20 years that hydrogels can undergo significant volumetric transformations when exposed to changes in parameters such as solvent composition, pH/ionic strength, and temperature. The groundbreaking research from Tanaka and co-workers showed that a weakly crosslinked hydrogel polymerized from dilute acrylamide monomer solutions can exhibit a reversible 100 to 1000-fold decrease

in volume when the hydrogel was submerged in mixtures of solvents ranging from pure water to pure acetone.[82,83] They attributed the dramatic volumetric changes to a more positive osmotic pressure experienced by the hydrogel in water due to favorable hydrophilic interactions between acrylamide and water.   They demonstrated that highly charged polyacrylic acid hydrogels converted from polycrylamide by treatment with strong acids were sensitive to changes in pH[82] and ionic strength.[86] The continued (though weaker) expansion of the charged hydrogel even in high ionic strength (> 1 mM) solutions indicated that electrostatic repulsion between the charged polymer chains could no longer adequately explain the response of the hydrogel due to screening. Instead, the major contribution to the volumetric response at high ionic strength was caused by a greater concentration of ions inside the hydrogel phase, leading to an increase in osmotic pressure inside the hydrogel which is also known as the Donnan potential.[98]   The Moore group also utilized the physical transformations of acid-functionalized hydrogels to produce microfludic sensors that also function as valves. Through UV polymerization of mixtures of pH-sensitive monomers such as acrylic acid and structural monomers such as 2-hydroxyethyl methacrylate (HEMA) inside microfluidic channels through photomasks, they fabricated structures including posts[99] and biomimetic valves[100] which can control the flow through the microfluidic channel depending on solution pH, by expansion (blocking the flow) and contraction (allowing the flow). Other researchers discovered that certain hydrogels, most notably PNIPAM in water, underwent large changes in volume when the temperature was varied,[84,85] corresponding to the LCST behavior of aqueous solutions of linear PNIPAM polymers. Other driving forces such as

light exposure[101] and electric fields[102-104] can also be used to induces volumetric changes in appropriately functionalized hydrogels.

Functionalized hydrogels are also good candidates as sensors for biomolecules due in part to their activity and biocompatibility in aqueous environments. For example, hydrogels functionalized with phenylboronic acid and its derivatives are useful materials for the detection and purification of various carbohydrates.[105] Phenylboronic acid is a Lewis acid that reversibly interacts with 1,2-cis diols such as glucose by forming a charged complex (Figure 3.2), where K_a and K_4 are respectively the acid dissociation constant and the equilibrium constant for the binding of glucose to the deprotonated phenylboronic acid. Another equilibrium constant, K_3, exists for the binding of glucose to the uncharged phenylboronic acid, but it is much smaller than K_4.[106]
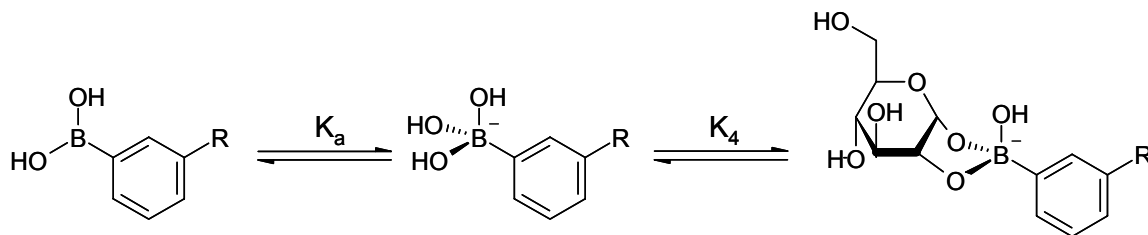
Figure 3.2: Binding equilibrium between glucose and phenylboronic acid group.

Binding with glucose causes the charged complex state to be more thermodynamically favorable; in other words, the pK_a of the phenylboronic acid group decreases when bound to a 1,2-cis diol.[107,108] If the phenylboronic acid is covalently attached to a hydrogel, binding to 1,2-cis diols increases the degree of ionization on the hydrogel and builds up a Donnan potential between the hydrogel phase and the bulk solution phase. The resulting influx of solvent and ions leads to hydrogel swelling, which may be detected as a red shift in optical diffraction in a CC templated hydrogel. The pH of the aqueous solution strongly affects the sensitivity of the functionalized hydrogel to

1,2-cis diols. A higher pH increases the concentration of the deprotonated phenylboronic acid group, which is more sensitive to the analyte due to the larger equilibrium constant, K_4. However, if pH is too high, almost all phenylboronic acid groups become charged, and the additional swelling due to glucose binding becomes negligible. Thus, glucose sensing with phenylboronic acid functionalized hydrogels are typically performed at pH $\sim$ pK$_a$. The pK$_a$ for phenylboronic acid is $\sim$8.8,[109] so a pH between 8.5 and 9.0 is generally used.[20,87] By exploiting the interaction between phenylboronic acids and 1,2-cis diols, Kataoka and co-workers synthesized a phenylboronic acid functionalized hydrogel that swelled as a function of the glucose concentration in the surrounding solution,[87] and when loaded with insulin, released insulin upon exposure to glucose.[110] A similar hydrogel copolymerized from phenylboronic acid and NIPAM was utilized as a separation agent for RNA by binding to the ribose group on the RNA backbone.[111]

The field of responsive CC templated hydrogels is expanding rapidly. The pioneering work of Asher and co-workers is based on functional periodic hydrogels generated through polymerization of acrylamide-based aqueous solutions inside charge-stabilized colloidal crystals,[92] followed by modification of the amide group. Using this technique, they and other groups demonstrated colloidal crystal-hydrogel composites termed polymerized colloidal crystal arrays (PCCAs), which exhibited reversible diffraction shifts due to stimuli such as mechanical force,[92,112] complexion between crown ethers and metal ions,[14,15,113] pH and ionic strength,[16] and carbohydrate binding (including glucose).[15,20,114] The diffraction response of the pH- and ionic strength-sensitive PCCA[16] as well as the carbohydrate-sensitive PCCA[20] was

53

successfully modeled using free energy equations of charged polyelectrolyte networks first described by Flory.[115] Interestingly, the diffraction response of the phenylboronic acid-functionalized PCCA to glucose ceased for ion concentrations of >10 mM, apparently due to the weakening of Donnan potential in high ionic strength solutions.[20] More recently, Asher and co-workers also demonstrated a PCCA which contracted after introduction of glucose due to increased crosslinking caused by the binding of each glucose molecule to two pendant phenylboronic acid groups.[114] Finally, when the CC template was etched away from a PCCA, an ordered array of isolated water-filled pores was generated, and entropic entrapment of macromolecules inside these pores were observed by diffraction and spectral absorption.[116,117]

Other methods can also generate 3-D mesostructured hydrogels using CC templating. An approach involved the synthesis of colloidal particles of the hydrogel poly(N-isopropylacrylamide) (PNIPAM), which were subsequently organized into ordered arrays.[18,118-120] These periodic structures displayed thermally induced shifts in optical diffraction due to LCST behavior. Other groups, including our own, have focused on an inverse opal approach, where a dried colloidal crystal is used to template the polymerization of infiltrated monomer precursors. After polymerization, the colloidal template is removed by chemical etching, yielding a bicontinuous polymer/solvent mesostructure. As an example of this approach, Takeoka and Watanabe polymerized inverse opals consisting of temperature sensitive pNIPAM, which also showed a reversible diffraction shift versus temperature.[121]

There are certain inherent advantages of both the PCCA and inverse opal based sensor designs. Benefits of the PCCA method include rapid formation of the charge

stabilized colloidal crystal and high diffraction intensity due to large single crystal domains, both of which are very significant for applications. However, because the charge stabilized colloidal crystal generally forms only in aqueous solutions of very low ionic strength, the hydrogel chemistry is limited to uncharged systems, and incorporation of charged functional groups into the hydrogel requires a second processing step. In addition, to maintain the stability of the charge stabilized colloidal crystal, the maximum concentration of functional groups that can be introduced may be limited. Finally, the composite PCCA structure does not contain interconnected pores, and thus requires the use of low polymer content hydrogels to allow rapid diffusion of analytes, which may limit the mechanical stability of the hydrogel. Advantages of the inverse opal method include the ability to accommodate a wide variety of functional groups and polymerization techniques, the facile variation of functional group concentration, and the ability to polymerize dense, robust hydrogel structures while potentially maintaining connectivity to the bulk solvent. The disadvantages of the inverse opal method include the generally higher defect density of a dried CC template and possible damage to the hydrogel mesostructure due to the template etching process using either organic solvent (for polymer colloids) or hydrofluoric acid (for silica colloids).

We synthesized 3-D mesostructured hydrogels based on copolymerization of HEMA and various functional groups infiltrated inside CCs, followed by etching of the template. Bragg diffraction from a single or few domains of the inverse opal hydrogels were characterized by collecting their normal incidence reflectance spectra using a microspectrometer consisting of an inverted reflection microscope with output coupled to a fiberoptic spectrometer. We demonstrated the tuning of Bragg diffraction for the

inverse opal hydrogels by introducing specific analyte molecules which causes reversible swelling of the hydrogel network, which changes the characteristic spacing between the FCC(111) layers of pores. Acrylic acid functionalized hydrogel exhibited a red shift in the diffraction peak as the pH was increased.[19] The primary mechanism for the diffraction response was the ioniziation of the hydrogel network, as shown by the effect of solution ionic strength on the magnitude of the diffraction shift. Phenylboronic acid functionalized hydrogel exhibited a red shift as glucose concentration was increased at physiological ionic strength,[21] due to formation of anionic complexes between phenylboronic acid and 1,2-cis-diols. The HEMA inverse opal without any additional functional group exhibited a diffraction response to ethanol and potentially to other alcohols, due to the favorable interactions between HEMA and alcohols. An inverse opal polymerized using N,N'-bis(acryloyl)cystamine (BAC) as the crosslinker demonstrated diffraction tuning in the presence of mild reducing and oxidizing agents caused by the breakage and formation of the disulfide bond on BAC. The kinetics of sensing by the CC templated hydrogels were determined by characterizing the time dependence of the diffraction peak shift and were found to be diffusion limited. Comparison of the magnitude of the peak shift to the relative concentration of the functional group suggested that changes in the FCC lattice constant occurred primarily in the sample normal direction. The diffraction response of the glucose sensitive hydrogel was also compared with theoretical results calculated using scalar wave approximation (SWA)[122] and transfer matrix method (TMM),[123,124] using simple models for the swelling of the mesoporous hydrogel, which indicated that the decrease in the intensity of the red shifted diffraction peak corresponded to swelling of the hydrogel into the FCC

pores. The detailed 3-D swelling behavior was experimentally confirmed using scanning two-photon fluorescence microscopy (Chapter 4).

3.2 Synthesis

3.2.1 Colloidal Crystal Formation

We decided to fabricate PS colloidal crystals using the sonication-assisted packing inside flow cells[58] (Fig. 3.3) for two main reasons. First, the colloidal crystals fabricated inside a flow cell exhibited a uniform thickness defined by the gasket thickness, which was essential for the quantitative study of the Bragg diffraction response of inverse opal mesostructures templated by the CCs. Second, the flow cell geometry minimized the potential problem regarding the formation of thick hydrogel overlayers during the UV polymerization. Instead, the proximity between the CC and the bulk liquid following the disassembly of the flow cell allowed for facile etching of the CC template and potentially fast diffusion of molecules throughout the hydrogel through the etched FCC pores. Using the sonication-assisted flow cell method, we have fabricated many colloidal crystals on a variety of hydrophilic substrates from aqueous suspensions of both PS and silica colloids.
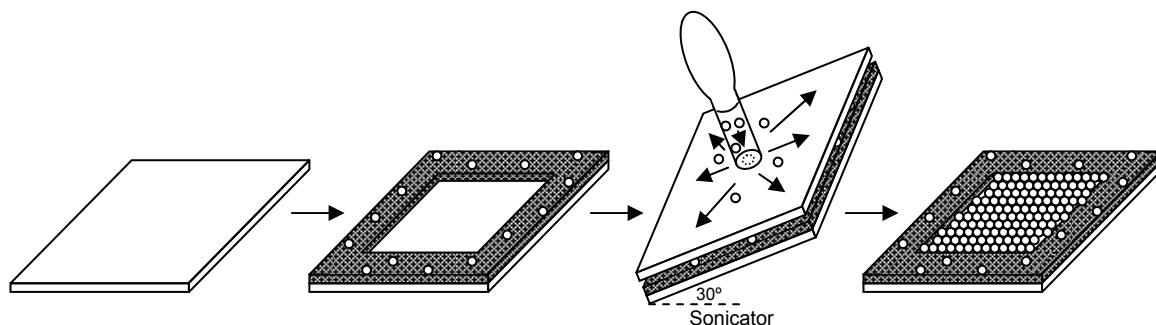
Figure 3.3: Schematic of colloidal crystal formation using the sonication assisted flow cell method. A colloidal suspension was placed inside a reservoir and capped to generate positive pressure. With gentle sonication at an angle, the colloids flow into the space between the substrates as the water exits the flow cell around the submonolayer of colloids (white circles) on the gasket (gray). After drying, the top slide/reservoir was removed, and a dried colloidal crystal of uniform thickness is made.

The substrate materials for the deposition of colloidal crystals were ~ 25 mm x 25 mm pieces cut from standard microscope slides (Fisher). 22 mm x 22 mm cover slips (No. 1, Corning) were sometimes used as the substrates to allow characterization with a laser scanning confocal microscope. 2.5 mm diameter holes were drilled through some of the glass slides using a diamond-tipped drill bit (Micromite Diamond Glass Drill, Lapcraft, Inc.) for use as top slides. All glass parts were then cleaned using a hot piranha solution (H_2SO_4: 30% H_2O_2 (aq.), 3:1 volume ratio) for 30 minutes, rinsed with water, and dried under flowing N_2. Alternatively, the glass pieces can be cleaned by submerging in 5% v/v HF (aq.) for 10 seconds, following by rinsing and drying. Top slides were submerged in 10 mM octadecyltrichlorosilane (OTS, Acros) in hexane for 20 minutes to render them hydrophobic. The OTS treatment ensured that the colloidal crystal preferentially adhered to the substrate, so that the polymerized hydrogel would remain on the substrate as the flow cell was disassembled. We have also used 10 mM (tridecafluoro-1,1,2,2-tetrahydrooctyl)dimethylchlorosilane (Gelest) in toluene for treating the top slides, with similar results to OTS. Substrates were submerged in 10 mM

58

methacryloxypropyltrimethoxysilane (MPMS, Gelest) in acetone for 20 minutes to functionalize the surface with acrylate groups. During UV polymerization of the hydrogel, the acrylate group polymerized into the hydrogel network, leading to a covalent linkage between the substrate and the hydrogel that resisted delamination while the hydrogel swelled. Glass tubes (5 mm ID, 25 mm length) were attached to a top slide via 5 Minute® Epoxy (Devcon, Danvers, MA) to form a reservoir. Gaskets were made by cutting 15 mm x 15 mm square holes inside 25 mm x 25 mm x 12 μm Mylar® films, and cleaned by sonication in ethanol. Each gasket was submerged in a 0.05% v/v PS colloidal suspension (with the same diameter as the CC to be formed) in ethanol for 30 seconds.

A cell was assembled by clamping together a substrate, a colloid decorated gasket, and a top slide/reservoir with binder clips (Fig. 3.3). For fragile substrates such as the cover slips, the flow cell was assembled by clamping together a glass slide, a 25 mm x 25 mm x 12 μm Mylar® film, a cover slip, a colloid decorated gasket, and a top slide/reservoir, so that the film acted as a shock absorber. For each cell, ~ 300 μL of 2% v/v aqueous polystyrene colloidal suspension (Interfacial Dynamics) was injected into the reservoir and capped tightly with a standard rubber pipette bulb. Two strips of duct tape were affixed on top of the sonicator (F530, Fisher) across the two diagonals. Each assembled cell was placed on the edge of a glass Petri dish on top of the tape so that the slide formed a 30º angle to horizontal. After 24 hours of sonication, the cell was removed from the sonicator, excess colloidal suspension was decanted, the rubber bulb was placed back on, and the cell was allowed to dry overnight under an inverted crystallization dish.

3.2.2 Inverse Opal Hydrogel Synthesis

Mixtures of the functional molecules, crosslinker, and photoinitiator were dissolved in the monomer and infiltrated into the dried colloidal crystal template for UV polymerization. The hydrogels were based on 2-hydroxyethyl methacryate (HEMA, Aldrich), and ethylene glycol dimethacrylate (EGDM, Aldrich) and Irgacure® 651 (Ciba) were used as the crosslinker and photoinitiator, respectively. Acrylic acid (AA, Acros), 2-(dimethylamino)ethyl methacrylate (DMAEMA, Acros), 3-acrylamidophenylboronic acid (APBA), and N,N'-bis(acryloyl)cystamine (BAC, Acros) were used as the functional groups. All reagents were used as received, except for APBA, which we synthesized using a simple acid-base coupling process described in the next paragraph. In some cases, water was added to the monomer mixture (up to 20% v/v water) to modify the swelling behavior, but we discovered that water content greater than ~ 40% v/v caused the polymerized hydrogel to collapse once the colloidal crystal was etched, and thus in most cases the monomer mixture did not contain water. Table 3.1 summarizes the compositions of the monomer mixtures used for the detection of various molecules.

Stimulus	Func. Type	HEMA	Func.	x-linker	Init.	Water
		(g, mmol)	(mg, µmol)	(mg, µmol)	(mg, µmol)	(mg, mmol)
pH	5% AA	2.5, 19.2	69.2, 961	25.0, 126	75.0, 288	625, 34.7
	2.5% AA	2.5, 19.2	35.0, 486	25.0, 126	75.0, 288	625, 34.7
	5% DMAEMA	2.5, 19.2	150.9, 960	25.0, 126	75.0, 288	625, 34.7
	5% AA	0.943, 7.25	27.8, 386	10.0, 50.5	21.4, 82.2	0
Glucose	6.25% APBA	0.916, 7.04	90.7, 475	15.0, 75.7	19.7, 75.7	0
	1.25% APBA	0.916, 7.04	18.4, 95.5	15.0, 75.7	19.7, 75.7	0
Ethanol	HEMA	0.499, 3.83	0	7.8, 39.4	9.8, 37.6	0
x-linker	1.6% BAC	0.479, 3.68	15.6, 60.0	3.1, 15.6	9.9, 38.0	0

Table 3.1: Monomer mixture compositions used to polymerize functional hydrogels inside CC templates. Each mixture consists of the structural (nonfunctional) monomer HEMA, the polymerizable functional group, the crosslinker EGDM, the photoinitiator Irgacure® 651, and water (optional).

To make an inverse opal hydrogel, ~ 300 µL of a monomer mixture was pipetted into the injection tube, which was then capped with a pipette bulb. Once the colloidal crystal became translucent, indicating successful infiltration, excess precursors were removed from the injection tube, and the remaining mixture was photopolymerized at 365 nm for 50 minutes using a high intensity UV lamp (B-100A, UVP, Inc.). The two slides were separated and then placed in chloroform for at least 24 hours to fully dissolve the polystyrene colloids. Each inverse opal hydrogel was solvent exchanged by submerging the sample in pure $CHCl_3$ for 30 seconds, in ethanol for 30 seconds, then in water for 30 seconds. The AA-functionalized and APBA-functionalized hydrogels were then placed in an acidic aqueous solution, either 1 mM HCl (aq.) or a buffer solution with a pH of ~ 3, to ensure that it was in its compact state. The DMAEMA-functionalized hydrogel was placed in a phosphate buffer with pH = 9 for storage.

3.2.3 APBA Synthesis

The synthesis of the free radical polymerizable phenylboronic acid APBA was performed in a procedure similar to Kitano and co-workers.[125] 3-aminophenylboronic acid (Acros), NaOH (Acros), and 1-ethyl-3-(3-dimethylaminopropyl)carbodiimide (EDC, Pierce Biotech) were used as received. In a 100 mL round bottom flask, 3-aminophenylboronic acid hemisulfate (1.862 g, 10 mmol) was dissolved in water (30 mL), and the pH of the solution was adjusted to 4.8 by adding NaOH. The flask was stirred in an ice bath, and after temperature equilibration, EDC (2.301 g, 12 mmol) was added, and the pH was again adjusted to 4.8. In another container, acrylic acid (0.868 g, 12 mmol) was dissolved in water (10mL), followed by pH adjustment to 4.8. The acrylic acid solution was then slowly added to the flask, and the mixture was capped with a rubber septum and allowed to stir in an ice bath for one hour. The flask was then removed from the ice bath and left at room temperature overnight. The reaction mixture was extracted with 4x ethyl ether and rotovaped (R-114, Buchi). The resulting oily liquid was mixed with water (30mL) and stirred in the ice bath for 24 hours, leading to precipitation of needlelike crystals. The solid precipitate was collected by filtration (#1, Whatman). FTIR (Nexus 670, Thermo Nicolet) showed absorption maxima at 1340 cm^{-1} (B-O), 1550 cm^{-1} (-CONH-), and 1660 cm^{-1} (-CONH-). ^{1}H NMR spectroscopy in CD$_3$OD was performed in a Varian UNITY 300 NMR spectrometer and showed chemical shifts at $\delta = 5.8$ (1H, CH$_2$=C$\underline{H}$-), $\delta = 6.4$ (2H, C$\underline{H_2}$=CH-) and $\delta = 7.2 - 7.8$ (4H, phenyl). The overall yield was 48%.

3.2.4 Microfluidic Flow Cell Fabrication

We decided to enclose the APBA-functionalized inverse opal hydrogel inside a microfluidic flow cell to facilitate the transport of molecules between the bulk solution and the hydrogel and to better control the concentration of the analyte molecule (glucose) in the solution. The seal of the flow cell consisted of patterned polydimethylsiloxane (PDMS).[126]   A degassed PDMS prepolymer (Sylgard® 184, Dow Corning Co., Midland, MI) was poured over a pre-cleaned 18 mm x 18 mm #1 cover slip placed on top of a standard 2" Si wafer in a polystyrene Petri dish. The prepolymer was cured at 70 °C for 1 hour. The cover slip/Si wafer was detached from the cured PDMS, and a ~3 cm x 3 cm block was cut from the cured polymer to yield PDMS with an indentation of 18 mm x 18 mm x 170 μm at the center. A small hole was bored through the PDMS at one corner of the indentation using a disposable 20-gauge needle polished by 120-grit sand paper to remove the anti-coring tip. A larger hole was bored at the adjacent corner using a similarly polished disposable 16-gauge needle. A ~3 cm long 26 gauge Teflon® tubing ("inlet") was coated on one end with a thin layer of PDMS prepolymer, taking care not to coat the inside of the tube, and was inserted into the small hole until the tip was flush with the indentation. In a similar fashion, a ~20 cm long 20 gauge Teflon® tubing ("outlet") was coated and inserted into the larger hole. The assembled PDMS block was cured at 70 °C for 1 hour to form the seal.

3.2.5 Plasma Etching

A 6.25% APBA hydrogel was polymerized inside a PS CC template. ~ 2μm of the hydrogel and the PS template were removed with oxygen plasma etch in a reactive ion etcher (Plasma-Therm 790) at conditions of 200 W, 30 mTorr, and 20 sccm oxygen

for 5 minutes. The remaining procedure for fabricating an inverse opal hydrogel from the plasma etched sample is identical to section 3.2.2.

3.3 Characterization

3.3.1 Scanning Electron Microscopy

Immediately after template etching, one inverse opal hydrogel was removed from $CHCl_3$, dried in air, and characterized by SEM (Hitachi S-4700 SEM or Philips XL30 ESEM-FEG). A thin layer of gold was sputtered on the samples to prevent charging. Despite their polymeric nature and relatively low crosslink density, the inverse opal hydrogels were resistant to beam damage at acceleration voltages below 10 kV. We also dried several inverse opal hydrogel films from water, but SEM revealed no feature, suggesting that the high surface tension of water may have caused the collapse of the FCC pores during evaporation.

3.3.2 Optical Microscopy

Reflection optical micrographs of the inverse opal hydrogels were collected by a digital camera (Kodak) directly mounted on the reflection optical microscope using an image processing software (Photoshop, Adobe). Digital photographs of the hydrogels were taken using a handheld digital camera (Canon).

3.3.3 Microspectroscopy

We examined the Bragg diffraction response of the inverse opal hydrogels from small sampling regions by coupling the light reflected from the hydrogel via a reflection optical microscope (Axiovert 135, Zeiss) to a diffraction grating spectrometer (Control Development, Inc.).[21]   The schematic diagram of the microspectrometer is shown in Figure 3.4. By limiting the sampling region to micron-sized spots, microspectroscopy

avoids most of the complications arising from the self-organized nature of the colloidal crystal templates, such as crystalline defects and drying cracks. The detector consisted of a 512-element Si photodiode array with a sensitivity range from 300 nm to 1050 nm and a nominal wavelength resolution of ~ 2 nm. The illumination light source was a 100 W tungsten halide lamp, which was powered up for at least 20 minutes prior to data collection to ensure a steady state brightness. Reflectance spectra were usually collected with the 10x, 0.25 NA objective (Zeiss), corresponding to a sampling spot diameter of 16 μm. We adjusted the integration time for data collection so that there was a significant raw data count (~ 40000) for the 16-bit detector. Unless otherwise noted, all spectra were recorded after the equilibration of the diffraction response, denoted by the stabilization of the wavelength of the reflectance peak at a constant value. The kinetic swelling behavior of the hydrogel sensors was determined by collecting reflectance spectra at regular intervals (typically every 10 s), then plotting the peak position as a function of the elapsed time.
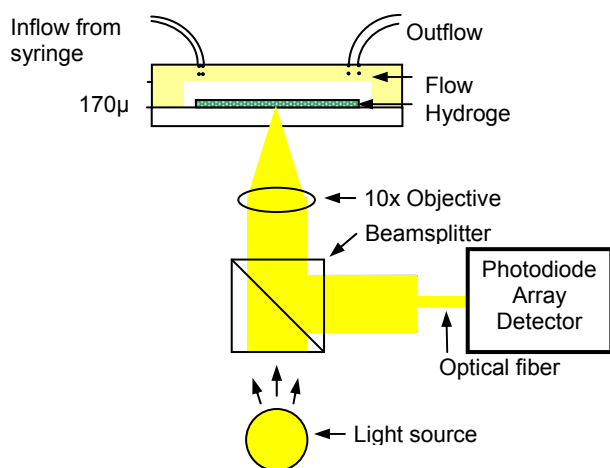
Figure 3.4: Schematic for microspectroscopy of the inverse opal hydrogel sensor in solution. The sample was either submerged in a Petri dish containing the appropriate solution, or inside a flow cell constructed from patterned PDMS and a glass substrate. Light reflected from the sample was collected by the objective and fiberoptically coupled to the spectrophotometer.

3.3.3.1 pH Sensor

For all experiments where aqueous pH buffers were needed, Milli-Q deionized (DI) water (Millipore) was used to make the buffers. pH measurements were taken using a Accumet AR-10 pH meter (Fisher). To test the pH-dependent Bragg diffraction response of the AA-functionalized inverse opal hydrogels, we initially used phosphate pH buffers by mixing 0.1M KH_2PO_4 (aq) (Acros) with different quantities of 0.1M HCl (aq) or 0.1M NaOH (aq), and measuring the resulting pH. This buffer system was used to examine the Bragg response of the AA-functionalized hydrogel samples polymerized with water. Each sample was placed, hydrogel side up, in a polystyrene Petri dish, followed by immersion with buffer. pH was adjusted by removing ~50% of solution from the Petri dish and adding an equal quantity of a new buffer. Reflectance spectra were acquired for 10 s at ~ 400 s after each pH change, and the corresponding pH was measured. All spectra are normalized to a front silvered mirror (Melles Griot) and to air. To determine ionic strength dependence of diffraction, unbuffered 1 mM or 0.01 mM HCl (aq) solution containing 0.3 M KCl was diluted by adding a solution containing the same concentration of HCl with no KCl, and reflectance spectra were collected for 10 s at ~ 400 s after each dilution. For kinetic studies, individual spectra were integrated for 2 s every 10 s.

To examine the pH sensing of a 5% AA hydrogel polymerized without water, we used pH buffers consiting of mixtures of citric acid (Acros) and K_2HPO_4 (Acros) because it allowed precise control of ionic strength over a pH range of 2 to 8 through the addition of KCl (Fisher).[127] Various amounts of 1 M citric acid (aq.), 2 M K_2HPO_4 (aq.) and KCl were mixed and then diluted with water to make 100 mL of 10 mM pH buffers with

I = 150 mM; the exact quantities added are listed in Table 3.2. The placement of the sample and the adjustment of pH using different buffers were performed in the same way as described in the previous paragraph. However, we waited for ~ 30 minutes before acquiring the steady state reflectance spectra to ensure complete equilibration of diffraction response. For kinetics, reflectance spectra were collected every 10 s. The integration time was 1 s for all spectra.

pH	1 M citric acid (mL)	2 M KH_2PO_4 (mL)	KCl (g)
3.0	0.811	0.189	1.058
4.0	0.619	0.381	0.992
4.5	0.550	0.450	0.960
5.0	0.490	0.510	0.931
5.6	0.437	0.563	0.902
6.0	0.375	0.625	0.881
6.6	0.277	0.723	0.847
7.1	0.178	0.822	0.821
8.0	0.028	0.972	0.708

Table 3.2: Amounts of 1 M citric acid (aq.), 2 M KH_2PO_4 (aq.), and KCl mixed with water to make 100 mL of pH buffers with constant ionic strength of 150 mM.

3.3.3.2 Glucose Sensor

2-(cyclohexylamino)ethanesulfonic acid (CHES) (Acros), D(+)-glucose (Acros), and 1,2-cis-cyclohexanediol (Acros) were used as received. For the diffraction response of APBA-functionalized hydrogels to glucose, 75 mM CHES buffer solution (I ~ 150 mM) at pH 9 was made by mixing CHES (1.555 g, 7.5 mmol) and NaCl (0.707 g, 12 mmol) in DI water to make a 50 mL solution, followed by addition of 1 M NaOH (2.502 g) and diluted to 100 mL with DI water. CHES buffer solutions at pH 9.5 and pH 7.4

were made in the same fashion, except the amount of 1 M NaOH was varied. Glucose was then added to yield concentrations ranging from 0.1 mM to 100 mM. For ionic strength tests, pH 9 buffer solutions of 75 mM CHES buffer solution containing 10 mM glucose and 0 to 300 mM NaCl were used. Each buffer was drawn into a disposable syringe. A bottom slide containing the inverse opal hydrogel was removed from storage solution. Excess liquid on the areas not containing the hydrogel was carefully wicked away. The PDMS seal was aligned with the slide by hand, and the edges of the seal and the glass slide were firmly pressed together to form the flow cell. The cell was then manually filled with DI water through the inlet tube. The syringe containing the appropriate buffer solution was placed in a syringe pump (Sage M365, Thermo Electron Co., Beverly, MA) and connected to the flow cell inlet with ~30 cm 26 gauge Teflon® tubing. A solution flow rate of 2.5 μL per second was used during testing, and the reflectance spectra were collected with 1 s integration time and a 10 s interval.

3.3.3.3 Ethanol Sensor

To examine the swelling of the HEMA-only inverse opal hydrogel in the presence of ethanol, the sample was carefully rinsed with DI water and placed in a Petri dish containing 10 mL water. The reflectance spectra were collected with the microspectrometer, and then enough ethanol was added to make a 5% v/v ethanol in water. The process was repeated for 10%, 20%, and 30% v/v ethanol solutions. Some of the solution was removed from the Petri dish, and increasing amounts of water was added to examine the diffraction response when the ethanol concentration was decreased. Finally, we replaced as much of the solution as possible with water to characterize the

response once again at 0% v/v ethanol. The integration time for all reflectance spectra was 1 s, and a 10 s interval was used between spectra collection for kinetics experiments.

3.3.3.4 Crosslinker Sensor

Microspectroscopy of the diffraction tuning BAC-functionalized was accomplished using dithiothreitol (DTT, Acros) as the reducing agent and sodium bromate (Acros) as the oxidizing agent. The as-polymerized hydrogel containing disulfide linkage was placed in a Petri dish with water, and its reflectance spectra after equilibration was collected. The sample was then exposed successively to 1 mM DTT, 1 mM sodium bromate, 100 mM DTT, 100 mM sodium bromate to examine the diffraction response as the disulfide linkage was broken and reformed.

3.3.4 Laser Diffraction

A PS CC with D = 1250 nm and a thickness of 23 um was fabricated using the sonication assisted flow cell method. It was then infiltrated with the HEMA-only hydrogel monomer mixture used for ethanol sensing (Table 3.1), UV-polymerized, and etched in $CHCl_3$ to generate an ethanol sensor with a large lattice constant. The setup for laser diffraction consisted of a continuous wave frequency-doubled Nd:YAG laser at 532 nm (Compass 315M-150, Coherent) mounted horizontally on a optical table. A rectangular glass UV-vis cuvette with dimensions of 3 cm (L) x 1 cm (W) x 4 cm (H) was also mounted on the optical table approximately 1 m away from the laser, with the length of the cuvette perpendicular to the direction of the laser light. A gridded paper was attached to the outside face of the cuvette facing away from the laser using double sided tape, and the laser was turned on. The HEMA-only inverse opal hydrogel was placed in the cuvette with the substrate flush against the front surface of the cuvette and the sample

69

facing away from the laser. The cuvette was then filled with an appropriate liquid. After waiting for ~ 10 minutes, the diffraction pattern projected onto the gridded paper was imaged using a digital camera (Canon). The solution was replaced, and the imaging procedure was repeated to acquire a new equilibrium diffraction pattern. The solutions tested include $CHCl_3$, water, 5% v/v ethanol (aq.), 10% v/v ethanol (aq.), 20% v/v ethanol (aq.), and 30% v/v ethanol (aq.).

3.3.5 Peak Analysis and Simulation

Diffraction wavelength (λ_b), full width at half maximum (FWHM), and peak intensity (I_b) values for the 6.25% APBA inverse opal film during equilibrium and kinetics tests were determined by curve fitting with Origin 7.0 (OriginLab Co., Northampton, MA) using a Pearson VII or a Gaussian fit. The extracted peak parameters at different swelling ratios were compared to the theoretical values calculated using three different models describing the swelling of the hydrogel around the FCC pores to determine if the evolution in the diffraction peak parameters can be described by the deformation of the pores.

In the scalar wave approximation (SWA) method, the full Maxwell equations are approximated by scalar equivalents; one such approximation for the FCC photonic crystal probed in the [111] direction has been reported previously.[122] With the refractive indices, volume fractions, and interlayer distance as the input, we used SWA to derive the expected diffraction peak intensity and normalized FWHM. Briefly, using Equation 1.2, we estimated the swelling ratio (d/d_0), where d and d_0 are spacing between FCC(111) layers in the swollen and compact hydrogel, from the spectroscopic swelling ratio (λ_b/λ_{b0}), where λ_b and λ_{b0} are the diffraction wavelengths for the swollen and compact

hydrogel. For the equation, the refractive index of the hydrogel (n_{gel}) was approximated by the published values for poly(HEMA) (n = 1.5119).[128] The refractive index values for the aqueous glucose buffers (n_{aq}) were measured by refractometry (Abbe-3L, Fisher Scientific).

To determine the effects of varying refractive index contrast and pore shrinkage on the reflection spectra, three simple models of hydrogel swelling were used. All three models assumed that the film swelled macroscopically in the sample normal direction by d/d_0 with aqueous solution at the given pH and glucose concentration; however, the FCC pores change dimensions in different ways (Fig. 3.19a). In the 0-D pore swelling model, the FCC pores maintain their shape and volume during hydrogel swelling, so the volume fraction of pores decreases. The new equilibrium volume fractions φ_{gel} and φ_{aq} for the hydrogel and pore phase respectively can then be recalculated, while the corresponding n_{gel} was approximated using effective medium approximation assuming that the hydrogel phase was swollen with a solution of n_{aq}. The new equilibrium refractive indices and volume fractions of the swollen hydrogel were then inputted into the SWA calculation of peak intensity and normalized FWHM. The process was repeated for the 1-D pore swelling model, except that the FCC pores swell by d/d_0 in the sample normal direction just like the bulk film, resulting in a constant pore volume fraction (~ 0.74) during hydrogel swelling. For the 2-D pore shrinkage model, the pores decrease in volume by d/d_0 while the hydrogel expand in the sample normal direction by d/d_0, causing the pores to effectively shrink in the directions parallel to the substrate. The SWA implementation was written with IDL 5.6 software (Research Systems, Inc., Boulder, CO). Hydrogel thickness values of 24 and 48 layer inverse opals were used for SWA (the experimentally

71

determined thickness corresponded to ~ 53 layers). For more details calculating diffraction peak parameters using different pore swelling models, please refer to Appendix A.

The transfer matrix (TMM) simulation[123,124] of the reflectance spectra of a hydrogel following a 0-D pore swelling model was performed using Translight, a freely available software written by A. L. Reynolds.[129] For ease of calculation, an inverse opal of 24 layers of pores was used for TMM. Once the theoretical reflectance spectra at different swelling ratios were calculated, the diffraction peak parameters were extracted using Origin 7.0 (OriginLab Co., Northampton, MA).

3.4 Results and Discussion: pH Sensor

3.4.1 Microscopy

SEM of the AA-functionalized inverse opal hydrogels polymerized in the presence of water revealed a highly ordered array of pores (Fig. 3.5); the average center to center spacing between nearest neighbors was 243 nm, which represents ~10% shrinkage compared with the nominal particle diameter (270 nm). The persistence of the periodic structure in vacuum and the moderate shrinkage suggest that the hydrogel is mechanically robust. Defects in the CC template such as vacancies, line defects, and drying cracks were completely infiltrated with the hydrogel, leading to regions containing excess hydrogel in the inverse FCC structure (Fig 3.5a).
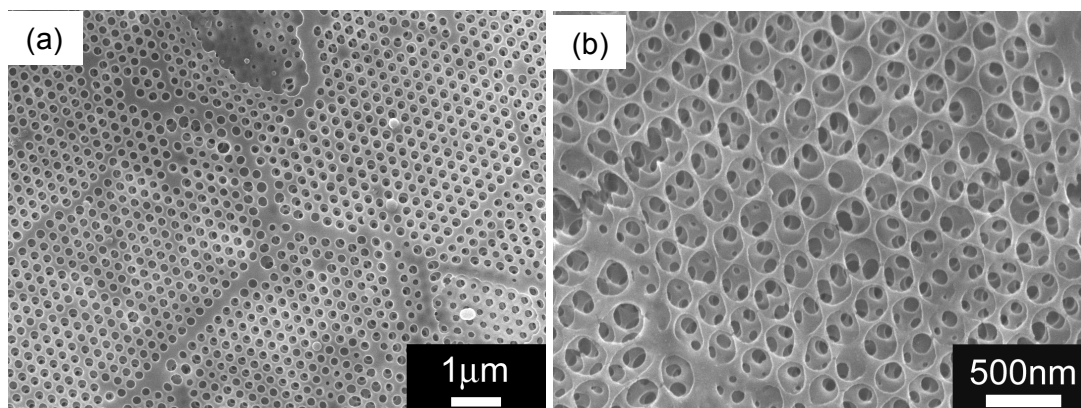
Figure 3.5: SEM of an AA-functionalized inverse opal hydrogel. (a) Low magnification view, showing good replication of defects in the colloidal crystal template with hydrogel (gray lines). (b) High magnication view, showing an interconnected array of FCC pores surrounded by hydrogel. The monomer mixture contained 20% v/v water.

Optical micrographs of the AA-functionalized inverse opal hydrogel in phosphate buffer (pH = 4) demonstrated Bragg reflection of green color (Fig. 3.6). Since the pK_a of AA is approximately 4.5 and increases in the polymer film due to close vicinity of AA moieties, the hydrogel should be mostly uncharged in the buffer. Indeed, the green color is consistent with the diffraction wavelength expected from an inverse FCC structure of a polymer (n = 1.51) in water (n = 1.33). In addition, dark regions representing hydrogel mesostructure with poor translational order and gray lines corresponding to drying cracks in the CC template are also seen (Fig. 3.6). Since the CC template diffracted a uniform color, the disorder observed in the hydrogel probably occurred during the polymerization and/or etching process, particularly during solvent exchange from $CHCl_3$ to ethanol to water, since (as we show later) ethanol causes significant swelling in hydrogel, possibly resulting in irreversible buckling and disorder.
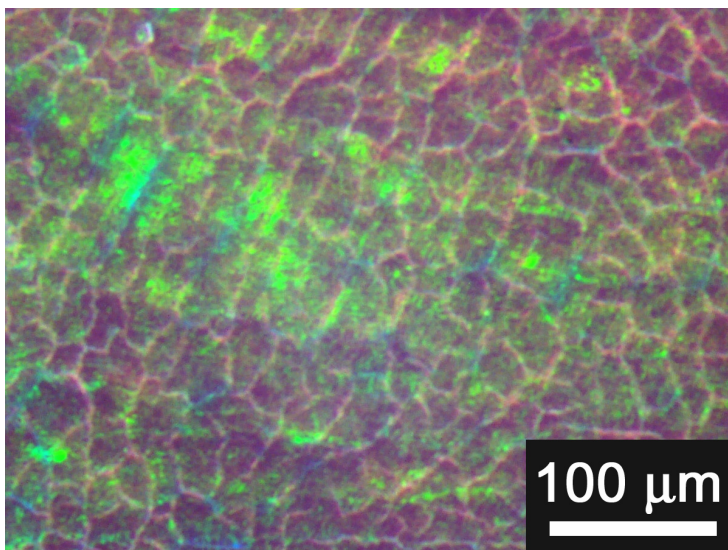
Figure 3.6: Optical micrograph of an AA-functionalized inverse opal hydrogel in pH 4 buffer. The reflection of green color is consistent with Bragg diffraction from a compact inverse FCC structure of crosslinked polymer in water. Regions with poor order (dark areas) and drying cracks (gray lines) are also clearly visible.

The optical response of inverse opal hydrogels functionalized with two different pH-sensitive groups as a function of pH is shown in Figure 3.7. These digital micrographs demonstrate that the long range translational order of the CC template was successfully replicated by the infiltrated hydrogel, as shown by the diffraction of nearly uniform color over an area of ~ 5 mm x 5 mm. Similar to the optical microscopy result, the 5% AA hydrogel polymerized with 20% v/v water diffracted green light in a phosphate buffer at pH = 4 (Fig 3.7a). As the phosphate buffer pH was increased to 7 and then 10, the hydrogel became transparent as the λ_b shifted to the infrared due to the swelling of the now-anionic hydrogel. The 5% DMAEMA hydrogel exhibited the opposite trend in diffracted color as a function of pH; as pH was decreased from 10 to 4, the diffraction red shifted from green to red/transparent (Fig 3.7b). Such a color change is consistent with the protonation of DMAEMA (pK_a ~ 9) to a cation as the pH is decreased. As a final example, a CC templated hydrogel which contains both 5% AA and 5% DMAEMA was transparent at pH = 4 and pH = 10 but diffracted an orange-red

74

color at pH = 7 (Fig 3.7c).   A possible explanation may be that neither the acid nor the base was fully charged at neutral pH.   However, the AA-only and DMAEMA-only hydrogel appear to be fully swollen as pH = 7, as shown by their diffraction of infrared light (Fig. 3.7a and 3.7b).   Thus, the oppositely charged AA and DMAEMA groups may partially neutralize each other, leading to a reduced Donnan potential inside the hydrogel and thus decreased swelling.
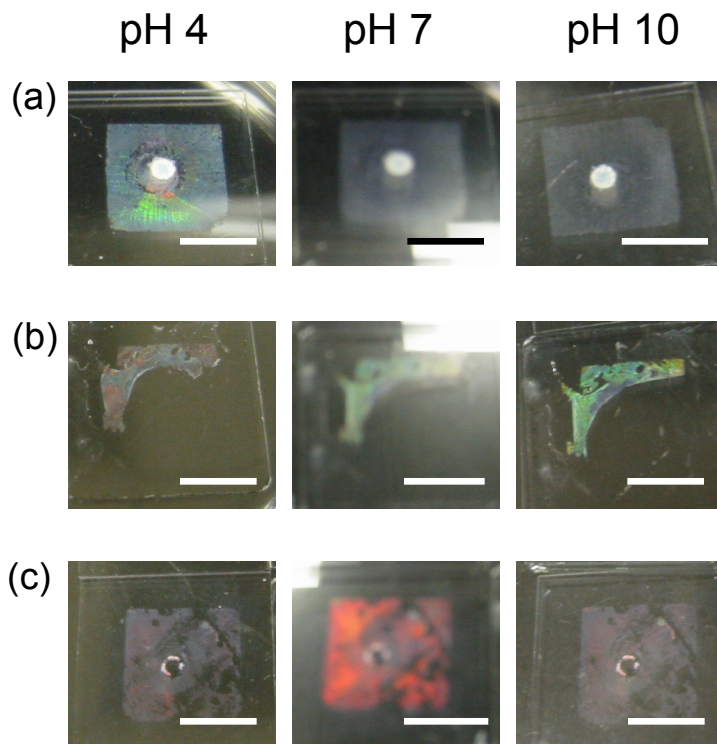
Figure 3.7: Digital photographs of acid and base-containing inverse opal hydrogels at different pH (a) 5% AA hydrogel (acid), showing a red shift in diffraction at high pH due to deprotonation of AA (b) 5% DMAEMA hydrogel (base), showing a red shift in diffraction at low pH due to protonation of DMAEMA (c) 5% AA + 5% DMAEMA, showing a reduced red shift in diffraction at pH = 7, possibly due to favorable interactions between AA and DMAEMA.

3.4.2 Microspectroscopy

3.4.2.1 Effect of AA Concentration

Figure 3.8 presents the pH dependence of diffraction for hydrogels containing various AA concentrations polymerized with 20% v/v water. At pH ≤ 4, the 5% AA hydrogel film diffracted 544 nm light, which was quite close to the value calculated by Bragg equation (547 nm), assuming an inverse opal of hydrogel (n = 1.51) in water which shrank by 10% during the solvent exchange process. As pH increases, the diffraction steadily red shifted until it reached 850 nm at pH 6.94. While the FWHM of the diffraction peak remains about the same during the red shift, the peak intensity (I_b) decreased from 60% at pH = 4 to 30% at pH = 7 (Fig 3.8a). This trend in diffraction peak as a function of hydrogel swelling is fully reversible and may be caused by a change in the refractive index contrast as the hydrogel swells with water and/or a change in the inverse opal mesostructure. λ_b/λ_{b0} for the film is equal to 1.56. In comparison, the 2.5% AA hydrogel diffraction red shifted from 517 nm to 652 nm at pH 7.01, a λ_b/λ_{b0} of 1.26. In other words, the 5% AA sample swelled about twice as much as the 2.5% AA sample. Because the normal reflectance spectra probe the spacing between FCC(111) planes, the linear relationship between the amount of swelling and the AA concentration suggests that the swelling is largely confined to the sample normal direction. Such behavior is reasonable because the hydrogel film is very thin (1.5 cm wide, 23 μm thick) and is anchored on one side to the substrate, and thus can only swell vertically. A control sample containing only HEMA exhibited a λ_b/λ_{b0} of 1.03, which can be explained by small quantities of acidic impurities in as-received HEMA.[130] When the direction of pH change was reversed, the diffraction of the AA containing films blue shifted until the

original diffraction wavelengths were recovered. Interestingly, an apparent hysteresis was present in the diffraction response for increasing and decreasing pH sweeps (Fig. 3.8b). As we demonstrate later, this hysteresis disappears after about 20 minutes and can most likely be attributed to the kinetics of counter diffusion.
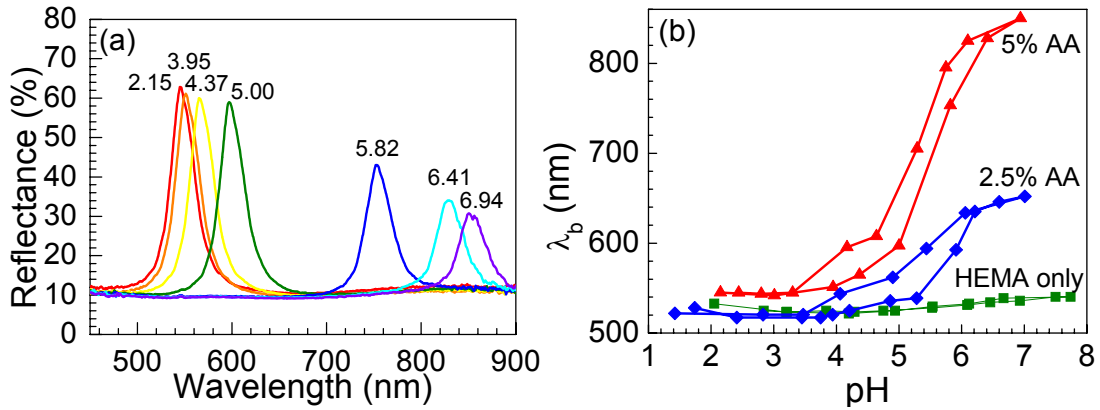
Figure 3.8: Diffraction response of AA-functionalized inverse opal hydrogel pH sensors. (a) Reflectance spectra of inverse opal hydrogel with 5% AA at different pH. (b) Diffraction response of inverse opal hydrogel films containing different concentrations of AA.

3.4.2.2 Effect of Ionic Strength

The magnitude of diffraction response for the inverse opal hydrogel pH sensor depended strongly on the ionic strength of the solution, as shown by varying KCl concentration in an unbuffered HCl (aq) solution (Fig. 3.9). When 5% AA hydrogel in unbuffered 1mM HCl/0.3M KCl (aq) solution was diluted with 1mM HCl (aq), its diffraction red shifted from 549nm to 565nm (Fig. 3.9b). Because the hydrogel was in its neutral state at this HCl concentration, the observed swelling (λ_b/λ_{b0} = 1.03) is most likely due to increasing nonspecific hydrophilic interactions between the hydrogel network and water molecules as KCl concentration decreases, also known as the "salting out" effect.[131] When KCl concentration was varied at 0.01 mM HCl, the 5% AA hydrogel, which was then negatively charged, exhibited reversible diffraction shift between 615 nm

at 300 mM KCl and 825 nm at 0.1 mM KCl (Fig. 3.9b). The reversible decrease in I_b as the diffraction peak red shifted was again observed (Fig 3.9a).
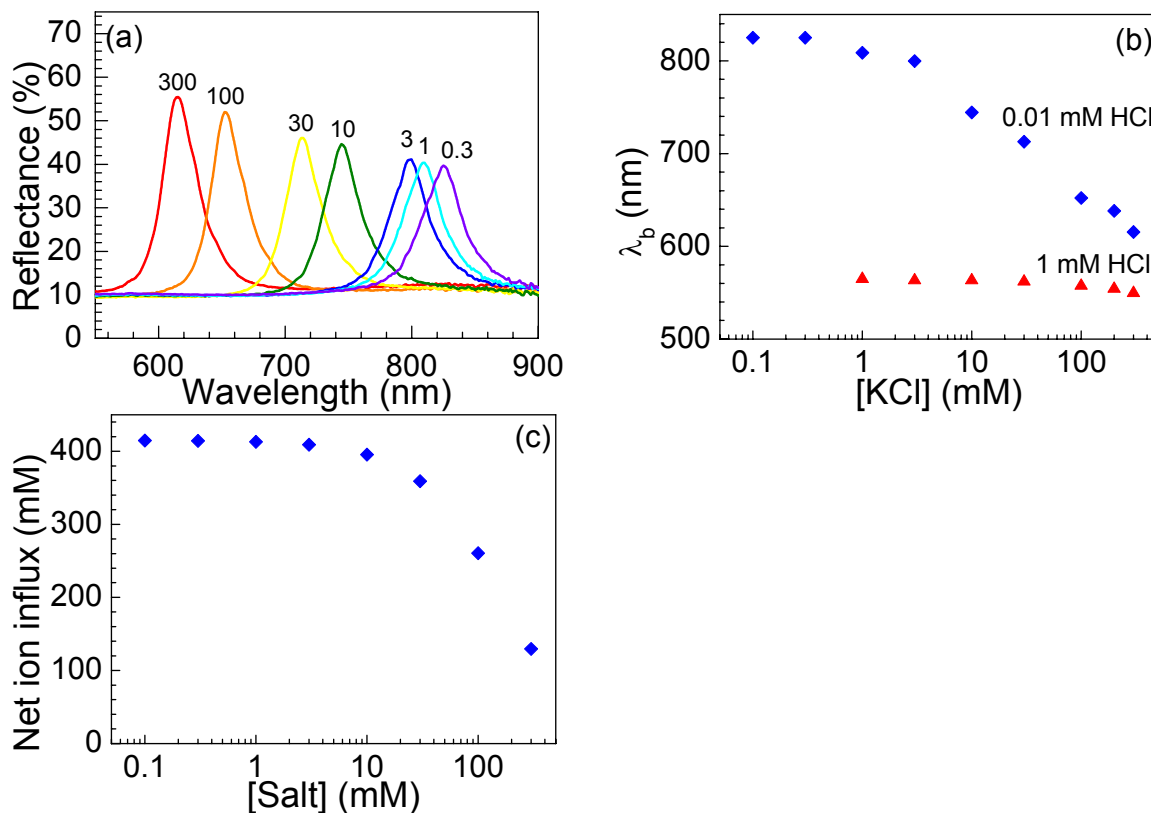
Figure 3.9: Effect of ionic strength on AA-functionalized inverse opal hydrogel pH sensors. (a) Reflectance spectra of inverse opal hydrogel with 5% AA in solution of 0.01 mM HCl and different concentrations of KCl (in mM) (b) Ionic strength dependence of 5% AA hydrogel in unbuffered 1mM and 0.01mM HCl (aq) solutions. (c) Calculated equilibrium net influx of ions into a fully charged 5% AA hydrogel at various salt concentrations.

The red shift in the diffraction wavelength as a ionic strength decreased agrees qualitatively with the amount of swelling induced by the Donnan potential inside polyelectrolyte networks and the subsequent influx of ions and solvent molecules to balance out the chemical potential between the hydrogel phase and the bulk solution. To calculate the expected amount of swelling caused by ionization of the hydrogel network, we use a simplified model where the chemical potential of the solution is equal to the product of ion concentrations, and further assume that the ions are generated from binary

salts (for example, KCl and HCl). At equilibrium, the chemical potential of the bulk solution (μ_0) equals the chemical potential of the hydrogel (μ_{gel}):

$$\mu_o = \mu_{gel} \tag{3.1}$$

Let c_a and C_a be the concentration of mobile anions inside the hydrogel and in the bulk solution, c_c and C_c be the concentration of mobile cations inside the hydrogel and in the bulk solution, and c_p be the concentration of immobile ionizable groups (in the case of AA-functionalized hydrogels, anions) on the hydrogel. Further, let C_a and C_c come from the same monovalent salt with concentration c, so that $C_a = C_p = c$. By assuming pH > pK_a so that ionizable groups are fully charged, and enforcing charge neutrality inside the hydrogel ($c_a + c_p = c_c$), Equation 3.1 can be rewritten as:

$$C_a C_c = c_a c_c = c_c^2 - c_c c_p = c^2 \tag{3.2}$$

Solving for c_c and taking the positive square root, we find:

$$c_c = \frac{c_p + \sqrt{c_p^2 + 4c^2}}{2} \tag{3.3}$$

and after substitution:

$$c_a = \frac{-c_p + \sqrt{c_p^2 + 4c^2}}{2} \tag{3.4}$$

Thus at equilibrium, a negatively charged hydrogel will be surrounded by an excess of cations and a low concentration of anions. The net ion influx during the equilibration can be defined as $c_a + c_p - 2c$. A plot of the net ion influx as a function of the monovalent salt concentration for a 5% AA hydrogel which is fully charged (c_p = 415 mM) is shown in Figure 3.9c. The ions collides with the hydrogel network and causes it to expand due to thermal motion; assuming that all ions causes the same amount of expansion, Figure

3.9c approximates the increase in hydrogel volume due to the high Donnan potential of a network with immobilized charge. The good qualitative agreement between Figure 3.9b and 3.9c suggests that the diffraction response of an AA-functionalized inverse opal hydrogel hydrogel to pH is due in large part to the influx of ions and solvent molecules after the ionization of the hydrogel network in order to balance the chemical potential of the hydrogel phase to that of the bulk solution.

3.4.2.3 Kinetics of Diffraction Response

The pH-sensitive hydrogel films were thin (23 μm) and contained an interconnected network of pores. As a result, pH-dependent diffraction shift kinetics on the order of minutes was observed. By making several simplifying assumptions, the kinetics of swelling for a charged polyelectrolyte network during pH change may be thought of as a hindered diffusion-limited process, where H^+ and OH^- ions, diffusing from the bulk solution into the gel phase due to a concentration gradient, are annihilated when they come into contact with immobilized deprotonated/protonated acid moieties on the network.[132] Thus, the effective diffusion coefficient is decreased by the local pH condition, and the time for hydrogel equilibration, τ, is on the order of:

$$\tau \approx \left(\frac{\lambda_b}{\lambda_{b0}}\right)^{\frac{2}{3}} l_0^2 \frac{\left(1 + \frac{c_p\left(\frac{\lambda_{b0}}{\lambda_b}\right)}{K_a}\right)}{D_0} \tag{3.5}$$

where l_0 is the thickness of the hydrogel corresponding to the rate-limiting diffusion process, K_a is the acid dissociation constant for the acidic moiety, and D_0 is the diffusivity of the analyte (in this case H^+ or OH^-) in water. One would initially assume

that diffusion of ions through the entire hydrogel film thickness represents the rate-limiting process. However, that would cause the top of the hydrogel to begin swelling at an earlier time, due to its proximity to the bulk solution. The coexistence of swollen and compact hydrogels should then significantly increase FWHM of the diffraction peak because of the superposition of peaks from templated hydrogels at different swelling ratios. In reality, the insensitivity of FWHM to the hydrogel swelling (Fig. 3.8a) suggests that the entire hydrogel film responded to the influx of H^+ or OH^- at about the same time. Thus, the rate-limiting step in the diffraction response kinetics is most likely the diffusion of analytes from the FCC pores into the dense inverse FCC hydrogel. The typical distance that the ions must diffuse through can be estimated by examining the void between three close-packed colloids, which would be filled with hydrogel following CC templating. A cross section through the center of the spheres reveals a hydrogel element that is approximately triangular in shape, and the distance from a vertex of the triangle to the center of the hydrogel element can be calculated using geometry to be D / 4. Thus, for a CC template with $D = 244$ nm, $l_0 \sim 60$ nm. Substituting l_0 and D_0 (~ 8 x 10^{-5} cm^2 / s) into Equation 3.5 yields a theoretical equilibration time (τ) of ~ 3 ms for analyte diffusion in water.

Figure 3.10a presents the diffraction shift kinetics of the 5% AA inverse opal hydrogel between pH 4 and 5.4. Increasing pH from 4.03 to 5.40 (diamonds) caused diffraction to slowly red shift from 557 nm at t = 0 s to 599 nm at t = 480 s, followed by a fast red shift to equilibration at 693 nm by t = 1200 s. Decreasing pH from 5.39 to 4.08 resulted in a similar behavior, where diffraction slowly blue shifted from 696 nm at t = 0 s to 682 nm at t = 320 s followed by a fast blue shift to equilibration at 562 nm by t =

1120s. Figure 3.10b shows the diffraction shift kinetics of the same hydrogel as pH increased from 5.42 to 6.81. Again, a delayed diffusion-limited diffraction shift was observed: the diffraction increased from 703 nm at t = 0 s to 705 nm at t = 60s, followed by a large red shift to 782 nm by t = 1120 s. We defined normalized diffraction shift as $(\lambda_b - \lambda_{bi}) / (\lambda_{bf} - \lambda_{bi})$, where λ_b is the diffraction wavelength at any given time and λ_{bi} and λ_{bf} are respectively the initial and final diffraction wavelengths at equilibrium. When the normalized diffraction shift is plotted versus the square root of elapsed time (Fig. 3.10c), we found linear relationships for all three pH changes at intermediate times ($t^{1/2}$ between 10 and 30), consistent with diffusion-limited kinetics. The slow initial diffraction shifts seemed random; in fact, later experiments on the diffraction response kinetics of all other functionalized hydrogels showed a simple diffusion-limited response which is linearly proportional to the square root of elapsed time over the entire duration of the experiment. Therefore, we believe that the complicated diffraction response kinetics is most likely explained by the fact that this experiment was performed prior to the optimization of the characterization protocol. A less likely possibility may be the presence of 20% v/v water during hydrogel polymerization, which has been shown (at higher concentration) to generate random voids in the crosslinked hydrogel due to phase separation during polymerization.[133,134] The microporous hydrogel structure may result in the coexistence of hydrogel elements with very different thickness values with different rates of swelling, which may help explain the complex diffraction response kinetics.
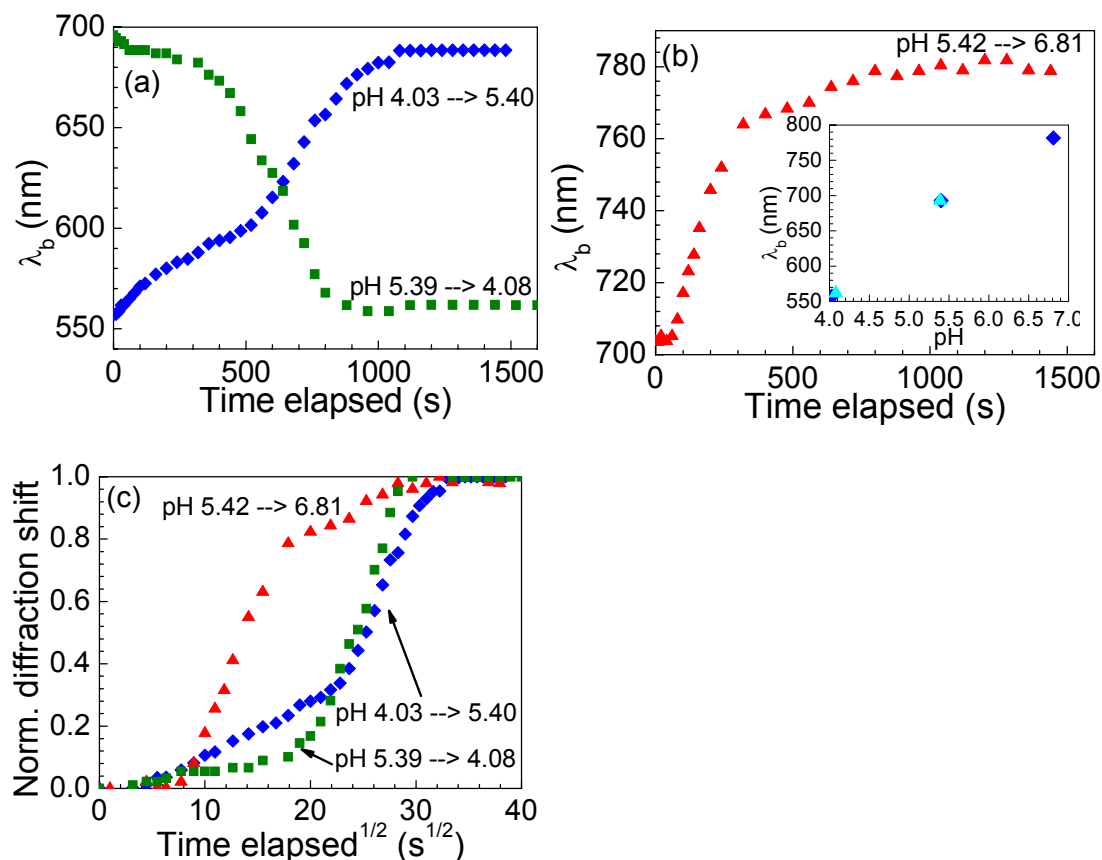
Figure 3.10: pH-dependent diffraction shift kinetics of the 5% AA inverse opal hydrogel film. (a) Diffraction shift kinetics during pH increase from 4.03 to 5.40 (diamonds) and during pH decrease from 5.39 to 4.08 (squares), showing full response at about ~ 1200 s with an initial time delay. (b) Kinetics of pH-induced diffraction shift as pH increased from 5.42 to 6.81. The initial time delay is smaller, while the overall equilibration time remains unchanged. Inset, final diffraction wavelengths of 5% AA hydrogel at various pH. When diffraction shifts are allowed to equilibrate, the diffraction wavelengths of the hydrogel as pH increased (diamonds) overlap those as pH decreased (triangles). (c) Normalized diffraction shift as a function of time$^{1/2}$. A linear relationship can be found for part of the diffraction shifts, suggesting diffusion-limited kinetics.

Several conclusions can be drawn from the diffraction shift kinetics. First, the similarity in the equilibration times and the slopes in Figure 3.10 suggest that the overall diffusion kinetics in the three cases is similar, although the variable initial slow shift regimes complicate the analysis. Second, the actual equilibration times are more than five orders of magnitude (4 x 10^5) greater than the calculated equilibration time ($\tau \sim 3$ ms), suggesting that the diffusion of analytes into a dense hydrogel is strongly retarded.

Our result is comparable to published reports on the diffusion of small probes through dense polymer films at different temperatures, which showed that as the temperature was decreased below the glass transition temperature (T_g) of the polymer, the translational diffusivity can also decrease by as much as six orders of magnitude due to the slowdown in polymer chain relaxation dynamics.[135,136]   Since crosslinked HEMA hydrogels have a T_g of ~ 95 °C,[137] it is not surprising that, at room temperature, the diffusivity of H^+ or OH^- through a compact inverse opal hydrogel would be five orders of magnitude smaller than D_0.   Finally, as Figure 3.10b inset shows, when the hydrogel swelling is allowed to equilibrate, the diffraction wavelengths of the hydrogel during the increasing pH sweep (diamonds) overlap those during the decreasing pH sweep (triangles), suggesting that the hysteresis in diffraction observed in Figure 3.9b is due to the short time allowed between pH steps (~ 400 s).

3.4.2.4 Effect of Monomer Concentration

The AA-functionalized inverse opal hydrogel polymerized without water exhibited diffraction response to pH that is qualitatively similar to the 20% v/v water sample (Fig. 3.11). In a citric acid-phosphate buffer at pH = 3.94, the 5% AA hydrogel showed a diffraction peak with λ_{b0} = 537 nm, within 2% of the value predicted for an inverse FCC polymer (n = 1.51) in water (n = 1.33) templated with a D = 244 nm CC (549 nm).   In other words, the inverse opal hydrogel polymerized from a water-free monomer mixture was less susceptible to shrinkage than a similar hydrogel polymerized from a 20% v/v water mixture. As the pH was increased to 6.71, the diffraction red shifted to 779 nm (Fig. 3.11b, squares). The maximum value for λ_b/λ_{b0} is 1.45, which is slightly smaller than spectroscopic swelling ratio observed for the 20% v/v hydrogel

(1.56). This may be attributed to the higher absolute concentration of crosslinkers in the water-free monomer mixture, since the recipes have the same ratio of crosslinker with respect to the monomer. By allowing sufficient time to elapse after a pH change (~ 30 minutes), the hysteresis in λ_b for increasing versus decreasing pH becomes very small (Fig. 3.11b). Again, we observed the reversible attenuation of I_b during the pH increase (from 39.7% to 15.1%), and the degree of the attenuation seems to be strongly correlated to be diffraction shift, and therefore to hydrogel swelling (Fig. 3.11b). The smaller absolute magnitude of I_b in the 5%AA water-free sample compared with Figure 3.8 is most likely due to the CC template thickness (12 μm) was about one half of the previous samples, leading to less efficient diffraction from a smaller number of FCC(111) layers. Finally, a weak negative correlation exists between the normalized FWHM ($FWHM/\lambda_b$) of the diffraction peak and pH (Fig. 3.11c). As we explain later, the decrease in $FWHM/\lambda_b$ as the hydrogel expands is qualitatively best described by shrinkage of the aqueous FCC pores. Figure 3.11d examines the diffraction response kinetics by showing the normalized diffraction shift as a function of the square root of elapsed time. The linear relationship again suggests that the diffraction response is most likely limited by the diffusion of ions. With the smaller initial sample thickness of 12 μm, τ is reduced to ~ 400 s, which is a factor of 3 smaller than the equilibration time for the 23 μm thick film of 5% AA hydrogel polymerized with 20% v/v water. This result contradicts the observation that the rate-limiting step of the diffraction response kinetics is the diffusion from the FCC pores into the inverse opal hydrogel, since l_0 should remain constant and thus τ should be independent of film thickness. Due to refinement of the characterization

85

technique, the diffraction response data in Figure 3.11 is probably less prone to error. In this case, the diffusivity of analyte (H^+ or OH^-) was reduced by 1.3×10^5 compared to D_0.
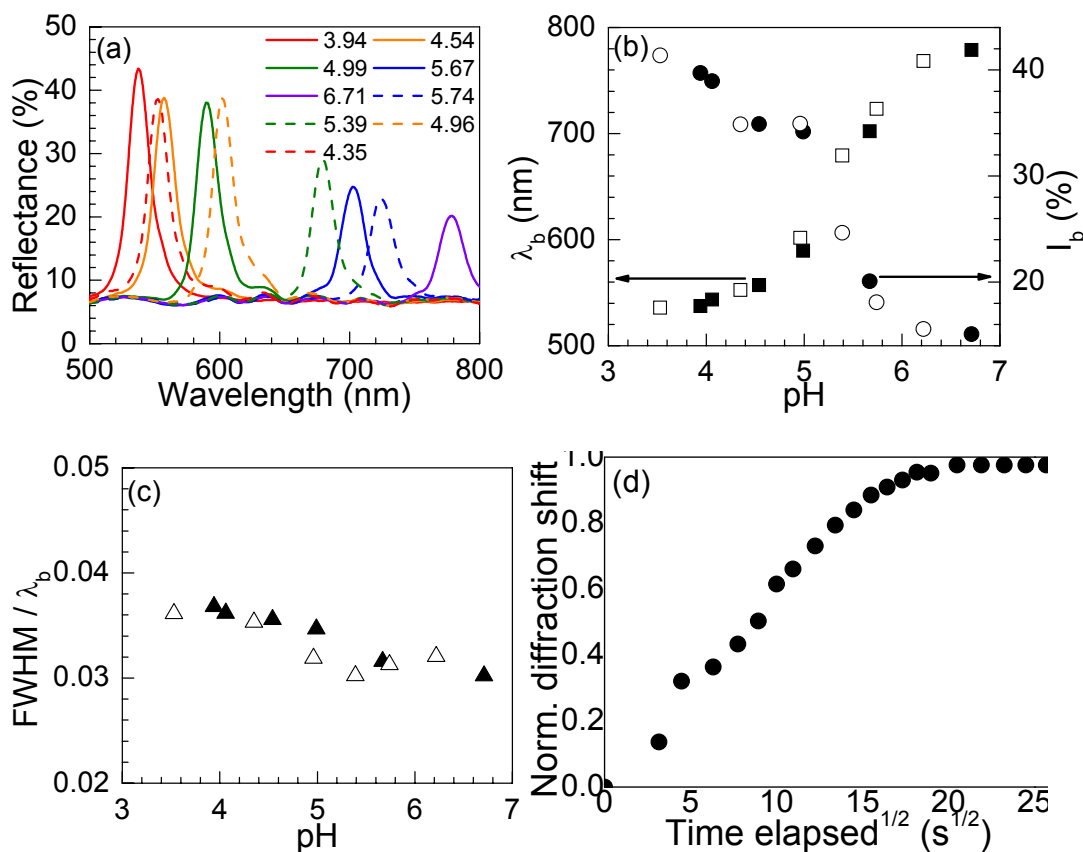
Figure 3.11: Diffraction response of AA-functionalized inverse hydrogel pH sensor polymerized without water. (a) Reflectance spectra of a 5% AA hydrogel at selected pH, showing a reversible red shift in diffraction as pH was increased. Solid (dashed) lines correspond to increasing (decreasing) pH. (b) λ_b (squares) and I_b (circles) of a 5% AA hydrogel as a function of pH. (c) *FWHM/λ_b* of a 5% AA hydrogel as a functional of pH. In all three plots, the overlap between the data taken for increasing and decreasing pH (solid and open symbols) demonstrated the reversibility of the Bragg diffraction response. (d) Normalized diffraction shift versus $t^{1/2}$ when pH was increased from 5.87 to 6.92, showing apparently diffusion limited kinetics.

3.4.2.5 Effect of Template Etching

To determine the effect of the CC template on the diffraction response, we fabricated a 5% AA hydrogel polymerized without water inside a CC template but did not perform the template etching. Like the inverse opal hydrogel, the hydrogel-CC composite exhibited a red shift in diffraction as pH was increased (Fig. 3.12). At pH $\leq$ 4,

the mesostructure exhibited λ_{b0} of 706 nm (Fig 3.12b), whereas Equation 1.2 predicts a value of 626 nm for a D = 244 nm polystyrene CC (n = 1.59) surrounded by a compact hydrogel (n = 1.51). In other words, the uncharged CC-hydrogel composite swelled by ~ 16% in the sample normal direction, possibly due to the hydrophilic interaction between HEMA and water. As pH was increased to 6.71, λ_b red shifted to 810 nm, for a spectroscopic swelling ratio of 1.15. This response is significantly smaller than that of the water-free inverse opal hydrogel (1.45), which is even more surprising considering that the hydrogel can no longer swell into the pores to minimize its free energy, which should in theory lead to a greater increase in the interlayer distance. Thus, the CC template is most likely hindering the full deformation of the hydrogel structure. More interestingly, the evolution of the diffraction peak for the CC-hydrogel composite during hydrogel expansion is qualitatively quite different when compared to the inverse opal analogue. For example, I_b increased from 37.8% at pH = 3.94 to 46.2% at pH = 6.71 (Fig. 3.12b, circles). At the same time, $FWHM/\lambda_b$ increased from 4.1% to 7.5% (Fig. 3.12c), which is also visible as a noticeable broadening of the peak shape in Figure 3.12a. Both trends are fully reversible, indicating that the hydrogel swelling is the primary cause for the trends in peak shape.
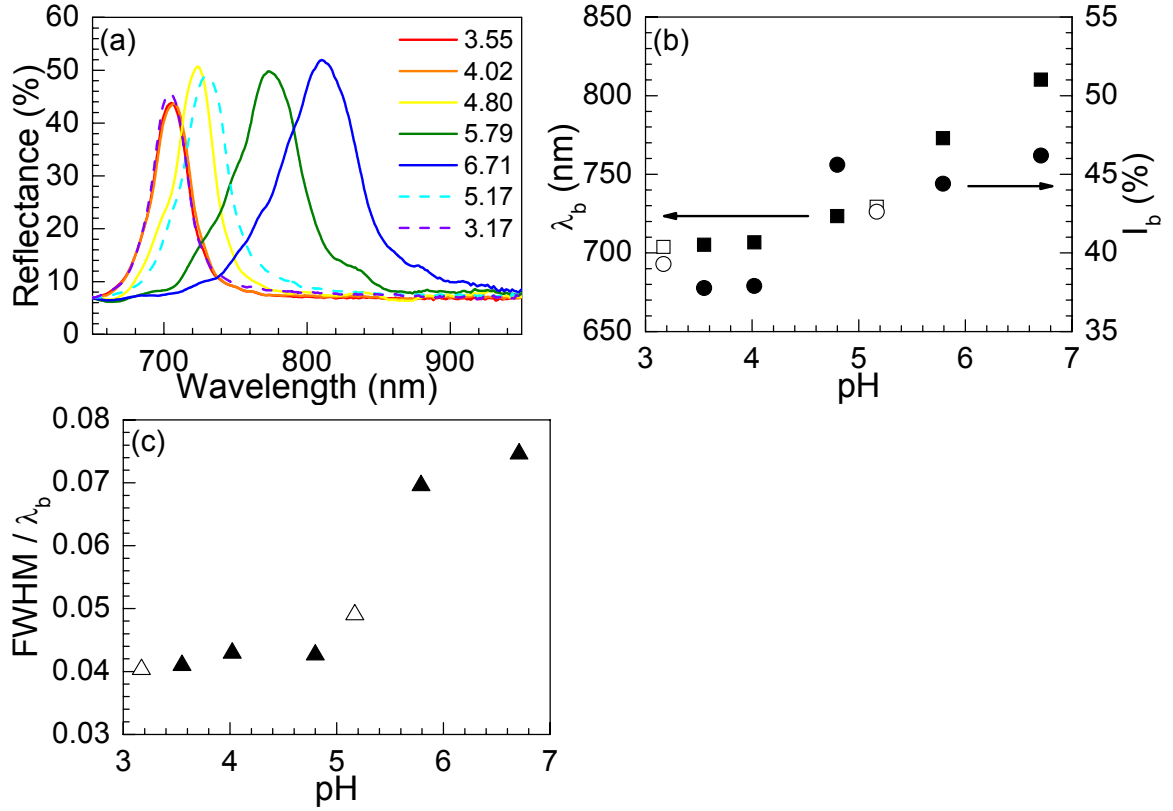
Figure 3.12: Diffraction response of CC-5% AA hydrogel composite to pH. (a) Reflectance spectra at selected pH, showing the expected red shift in diffraction as a function of pH. Solid (dashed) lines correspond to increasing (decreasing) pH. (b) λ_b (squares) and I_b (circles) of the CC-hydrogel composite as a function of pH. In contrast to the inverse opal system, I_b becomes stronger as the diffraction peak red shifts. (c) $FWHM/\lambda_b$ of the CC-hydrogel as a functional of pH. Solid (open) symbols are data collected while increasing (decrease) pH.

The deformation of a hydrogel inside a CC template differs in two major ways compared to an inverse opal hydrogel. First, the refractive index contrast between the polystyrene CC and the hydrogel phase increases as the hydrogel swells with water, whereas the opposite is true in an inverse opal hydrogel. Second, the presence of the CC template prevents the hydrogel from closing the FCC pores, thus maintaining a minimum index contrast regardless of the hydrogel swelling ratio. Both factors should contribute to the increase in I_b and $FWHM/\lambda_b$ for the CC-hydrogel composite, thus explaining the differences in the dependence of peak shape on hydrogel swelling.

3.4.2.6 Summary

In summary, we have demonstrated that CC templating of an acid/base functionalized hydrogel can successfully generate inverse opal mesostructures with a diffraction response that is tuned by pH. At the relative high ionic strength of ~ 0.15 M, the reversible red shift in the diffraction peak can be entirely attributed to the generation of a Donnan potential inside the ionized hydrogel, which in turn causes the net influx of counter ions and solvent molecules to expand the hydrogel phase. The magnitude of the diffraction response can be adjusted by varying parameters such the concentration of the acrylic acid functional group, the solution ionic strength, and composition of the monomer mixture. The kinetics of hydrogel expansion/contraction followed a delayed diffusion-limited process with equilibration time on the order of minutes. The large discrepancy between the apparent diffusivity of analytes in hydrogel versus water (10^5 smaller in hydrogel) can be explained by the slow chain relaxation dynamics of the compact hydrogel. Finally, the strong influence of hydrogel mesostructure on its optical properties is illustrated by comparing the pH-dependence of the diffraction response from an inverse opal hydrogel versus a CC-hydrogel composite. The effect of hydrogel swelling on the refractive index contrast and the pore morphology of the photonic mesostructure will be described in detail later in this chapter and also in Chapter 4.

3.5 Results and Discussion: Glucose Sensor

3.5.1 Microscopy

The mesostructure of the APBA-functionalized hydrogel was also well preserved in SEM (Fig. 3.13). In fact, because the APBA-containing monomer mixture was free of water, the resulting hydrogel exhibited almost no contraction in vacuum compared with

the dimension of the CC template (D = 244 nm).   However, the FCC pores were still

susceptible to collapse if the hydrogel was dried from an aqueous solution, and thus care

was taken to keep the inverse opal hydrogels submerged at all times.
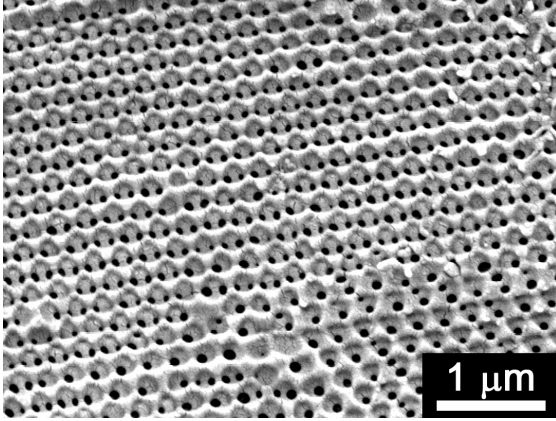
Figure 3.13: SEM of the 6.25% APBA hydrogel (top view), showing the expected FCC(111) inverse opal structure with a pitch of ~ 240 nm.

A optical reflection micrograph of the 6.25% APBA hydrogel in pH 6 phosphate

buffer is shown in Figure 3.14a. The templated film generally exhibited good single

color diffraction.   The better mesostructure uniformity compared with the AA-

functionalized hydrogel may be caused by the relatively hydrophobic APBA group,

which did not swell as much in ethanol during the solvent exchange process, thus

preserving the periodic mesostructure over a larger fraction of the film.   The expected

drying cracks in the original colloidal template are clearly visible as jagged lines

separating irregularly shaped single crystal domains with an average length of ~ 30 μm.

The corresponding reflection spectrum has an initial diffraction wavelength λ_{b0} of 539

nm. In deionized water, the 1.25% APBA hydrogels and a control hydrogel containing

no APBA also exhibited the same initial diffraction wavelength within ~ 5 nm (data not

shown). Substituting the value of λ_{b0} along with the refractive indices of DI water (n =

1.33) and hydrogel (n = 1.51) in an inverse FCC hydrogel structure into Equation 1.2

resulted in $D = 239$ nm, which was essentially the diameter of the colloid (244 ± 7 nm). Closer examination of the spectrum (Fig. 3.14c) revealed the presence of closely spaced Fabry-Perot interference fringes due to constructive interference of reflections from the top and bottom surfaces of the 3-D hydrogel structure. We calculated the thickness of the inverse opal from the wavelengths of the fringe maxima[122] and found the value to be 10.3 μm, or ~52 layers of FCC(111) water spheres in a polyHEMA matrix. The color of diffracted light changed from green to red when a 1 mM glucose in pH 9 CHES buffer was introduced (Fig. 3.14b), indicative of hydrogel swelling.
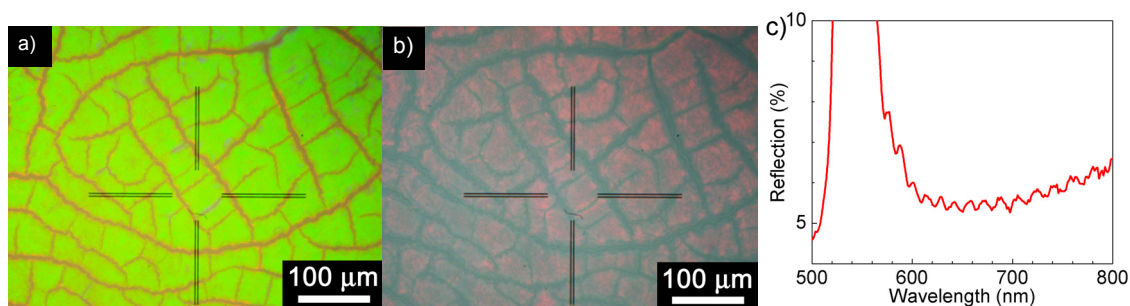
Figure 3.14: Optical properties of APBA-functionalized inverse opal hydrogels. (a) Optical reflection micrograph of a 6.25% APBA templated hydrogel in DI water. Strong diffraction of green light was generally observed, and opaque lines corresponding to drying cracks in the colloidal template were seen, indicating an average domain size of ~ 30 μm. Each reflection spectrum was collected from the region at the center of the crosshairs. (b) Optical reflection micrograph of the same hydrogel after exposure to 1 mM glucose in pH 9 buffer for ~ 20 minutes. (c) Reflection spectrum of a 6.25% APBA hydrogel in DI water, showing the Fabry-Perot fringes due to interfacial interference.

3.5.2 Microspectroscopy

3.5.2.1 Effect of APBA Concentration

The diffraction spectra of the 6.25% APBA hydrogel in buffer solutions of various glucose concentrations are plotted in Fig. 3.15a. As expected, the optical diffraction red shifted as glucose concentration increased (solid line), due to the increase in interlayer distance as the concentration of the anionic APBA-glucose complex increased. The diffraction wavelength then blue shifted when glucose concentration was

decreased (dashed line). To quantify the effect of glucose concentration on the swelling of the inverse opal hydrogels, the diffraction wavelengths for hydrogels containing 6.25%, 1.25%, and 0% APBA are shown in Figure 3.15b. As previously mentioned, the 6.25% APBA hydrogel diffracted 539 nm light when initially submerged in DI water (pH ~ 6). When a pH 9 buffer with an ionic strength of 150 mM was introduced, the diffraction wavelength increased to 599 nm due to deprotonation of the acid moieties. The increase in diffraction wavelength corresponds to a spectroscopic swelling ratio due to acid deprotonation $(\lambda_b/\lambda_{b0})_a$ of 1.111. Increasing the glucose concentration at pH 9 resulted in a gradual red shift of the diffraction wavelength until it reached 719 nm at 100 mM glucose, leading to a total shift (λ_b/λ_{b0}) of 1.334. The spectroscopic swelling ratio due to phenylboronic acid-glucose binding, $(\lambda_b/\lambda_{b0})_b$ is then equal to (λ_b/λ_{b0}) / $(\lambda_b/\lambda_{b0})_a$ = 1.201. The diffraction red shift was also easily perceptible to the naked eye, as the hydrogel film changed from a yellow-orange color at 0 mM glucose to clear (diffracting in the infrared) at 100 mM glucose. Thus, even at physiological ionic strength, the APBA-functionalized inverse opal hydrogel film exhibited sensitivity to glucose that was easily detected both spectroscopically and visually. The diffraction response of the 1.25% APBA hydrogel at different glucose concentrations is also shown in Figure 3.15b. A reversible red shift in diffraction wavelength was observed, going from 539 nm in DI water (not shown), to 575 nm in 0 mM glucose at pH 9, to 592 nm in 100 mM glucose at pH 9, leading to a $(\lambda_b/\lambda_{b0})_b$ of 1.030. In contrast, the control sample showed no sensitivity to glucose. Replacing DI water with pH 9 buffer caused the diffraction wavelength to red shift from 533 nm (not shown) to 566 nm (Fig. 3.15b), which may be explained by the presence of acrylic acid impurity in as-received HEMA.[130] The hypothesis is

supported by gas chromatography of as-received HEMA, which revealed the presence of acrylic acid at a concentration of ~ 0.15%. Increasing glucose concentration to 100 mM at pH 9 caused the diffraction wavelength of the control film to shift to 565 nm, which corresponds to a slight shrinkage of the hydrogel when the increase in refractive index from a 0 mM to 100 mM glucose solution (~1%) was taken in account. Thus, the diffraction red shift observed in APBA-functionalized hydrogels at pH 9 must be caused by complex formation between glucose and APBA.
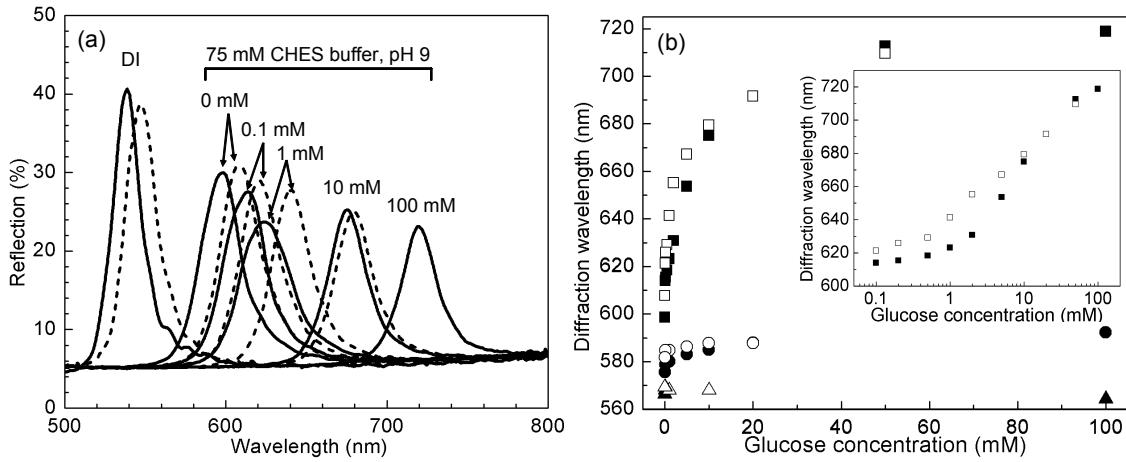
Figure 3.15: Diffraction response of APBA-functionalized hydrogels to glucose. (a) Reflection spectra of a 6.25% APBA hydrogel at selected glucose concentrations, showing a red shift in diffraction due to both change in pH (DI water to pH 9) and glucose concentration (0 mM to 100 mM). Solid lines correspond to increasing glucose concentration, and dashed lines correspond to decreasing glucose concentration. (b) Diffraction response dependence on glucose concentration for inverse opal hydrogels with different APBA concentrations. Solid symbols correspond to increasing glucose concentration, and open symbols correspond to decreasing glucose concentration. Squares, 6.25% APBA; circles, 1.25% APBA; triangles, 0% APBA (control film). Inset: Plot of diffraction wavelength vs. log of glucose concentration for 6.25% APBA hydrogel. The greatest response to glucose is at 1-10 mM, which is close to physiological concentrations (~ 5 mM).

Two interesting trends were observed in the optical response of the APBA-functionalized hydrogels to glucose. First, the diffraction peak intensity values decreased monotonically as the hydrogel swelled (Fig. 3.15a), with one exception that may be

caused by a small shift in sample spot during data collection. This behavior was observed in all samples (Table 3.3). The inverse relationship between diffraction peak intensity and λ_b/λ_{b0} for the hydrogel may be explained by a number of causes including a decrease in refractive index contrast during film swelling, an increasing presence of disorder in a swollen hydrogel, or partial pore closure during hydrogel expansion, which we will discuss in detail later. At the same time, the general shape of the peaks remains unchanged, suggesting that the overall layered mesostructure of the templated hydrogel was maintained during swelling. Second, while diffraction response appeared to reach steady state during the time frame of the experiment (~ 20 minutes between data points in Fig. 3.15b), the diffraction wavelengths during decreasing glucose concentration (open symbols) are red shifted versus their counterparts during increasing glucose concentration (solid symbols). This hysteresis completely disappeared after soaking the hydrogel film overnight, suggesting the existence of very slow diffusion in some portion of the inverse opal hydrogel.

Analyte	Solvent	[Analyte] (mM)	$\lambda_{b,inc}$[a] (nm)	$I_{b,inc}$[a] (%)	$\lambda_{b,dec}$[a] (nm)	$I_{b,dec}$[b] (%)
Glucose	DI water	0	539	35.7	548	33.2
	pH 9 buffer	0	599	24.4	608	25.5
	pH 9 buffer	100	719	17.1	-	-
Glucose	DI water	0	540	32.3	542	33.4
	pH 7.4 buffer	0	597	26.1	600	25.0
	pH 7.4 buffer	100	603	24.9	-	-
Glucose	DI water	0	531	20.4	540	19.3
	pH 9.5 buffer	0	666	9.5	673	8.6
	pH 9.5 buffer	100	718	5.4	-	-
Cis[c]	DI water	0	542	36.3	547	36.8
	pH 9 buffer	0	617	20.0	620	21.2
	pH 9 buffer	100	634	19.7	-	-

[a]Data collected during increasing analyte concentration.   [b]Data collected during decreasing analyte concentration. [c]cis-1,2-cyclohexanediol.

Table 3.3: Diffraction wavelength and peak intensity of 6.25% APBA hydrogel in various pH for increasing and decreasing analyte concentration.

3.5.2.2 Effect of pH and Analyte

Due to the pK_a of APBA, the pH of the glucose solution may significantly affect the degree of swelling of the APBA-functionalized hydrogel and therefore control the diffraction response. Indeed, when the pH of the buffer was adjusted to 7.4, the 6.25% APBA hydrogel became almost completely insensitive to glucose. Its diffraction wavelength changed from 597 nm in 0 mM glucose to 603 nm in 100 mM glucose (Table 3.3), equivalent to minimal swelling after accounting for the change in solution refractive index. A similar lack of response at physiological pH for the low ionic strength PCCA

glucose sensor was reported.[20] However, when the pH of the buffer was changed to 9.5, we found that the diffraction response of the hydrogel to glucose was diminished, but still detectable. The diffraction wavelength red shifted from 531 nm in DI water, to 666 nm in 0 mM glucose at pH 9.5, to 718 nm in 100 mM glucose at pH 9.5 (Table 1). The corresponding $(\lambda_b/\lambda_{b0})_b$ is 1.078. This behavior is different than the low ionic strength PCCA glucose sensor, which exhibited no response at pH 9.5.[20] The 6.25% APBA hydrogel was also responsive to cis-1,2-cyclohexanediol, an analogue of glucose which (unlike glucose) does not undergo mutarotation (cis-trans isomerization). The diffraction wavelength red shifted from 542 nm in DI water, to 617 nm in 0 mM cis-1,2-cyclohexanediol at pH 9, to 634 nm in 100 mM cis-1,2-cyclohexanediol at pH 9. The corresponding $(\lambda_b/\lambda_{b0})_b$ is 1.028, suggesting that APBA binding to cis-1,2-cyclohexanediol is less favorable than to glucose. Finally, a similar hysteresis in diffraction wavelength between decreasing and increasing analyte concentration was observed for all hydrogel samples that swelled.

3.5.2.3 Effect of Ionic Strength

By varying the concentration of NaCl in pH 9 CHES buffer solutions containing 10 mM glucose, the effect of ionic strength on diffraction response was studied and plotted in Fig. 3.16. The ionic strength of a 75 mM buffer solution of CHES ($pK_a = 9.3$) at pH = 9 was estimated to be 26 mM and was added to the NaCl concentration to calculate the total ionic strength.[127] As expected for a system where hydrogel swelling was caused by an increase in the Donnan potential due to ionization, the diffraction response of the 6.25% APBA hydrogel to 10 mM glucose became more pronounced as ionic strength was decreased. The diffraction wavelength red shifted from 634 nm at an

ionic strength of 326 mM to 698 nm at an ionic strength of 38 mM, after which it remained constant as the ionic strength decreased further to 26 mM (Fig. 3.16). When ionic strength was returned to 326 mM, the diffraction wavelength blue shifted to 628 nm. Thus, our inverse opal hydrogel exhibited diffractive optical response to glucose at physiological (~ 150 mM) and even greater ionic strengths, and ionic strength had little effect below ~ 40 mM. In comparison, the low ionic strength PCCA glucose sensor reported by Asher and co-workers, which employs the same phenylboronic acid based glucose sensing mechanism, demonstrated good sensitivity to glucose at ~ 2 mM ionic strength, but the diffraction response disappeared when ionic strength was increased above 10 mM.[20] We believe the ability of the inverse opal hydrogel to maintain sensitivity to glucose at high ionic strength may be attributed to the higher concentration of functional groups that can be attached to a dense hydrogel vs. the dilute hydrogel PCCA structure.
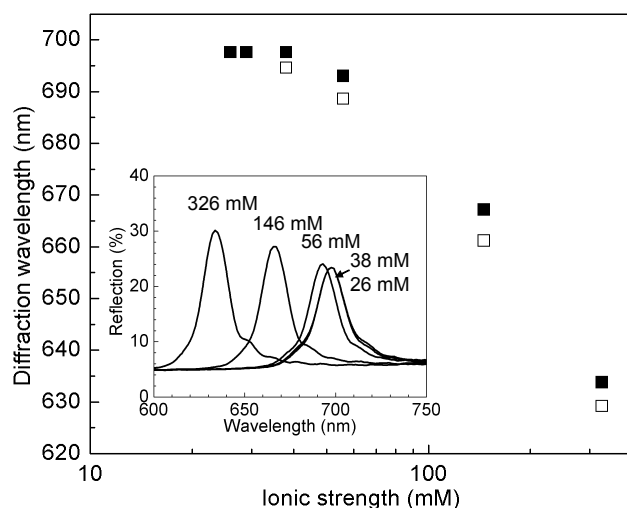
Figure 3.16: Effect of ionic strength on diffraction response of 6.25% APBA hydrogel in 10 mM glucose solution. A red shift of diffraction from 634 nm to 699 nm was observed when the ionic strength was reduced from 326 mM to 38 mM (solid squares), at which point the response became saturated. Increasing the ion concentration caused the diffraction wavelength to blue shift to 628 nm (open squares). Inset: reflection spectra of 6.25 % APBA hydrogel at several ionic strengths.

3.5.2.4 Kinetics of Diffraction Response

The kinetics of the diffraction shift due to phenylboronic acid-glucose binding was examined by studying the time evolution of diffraction wavelength inside a microfluidic flow cell. With flow cell dimensions of 1.8 cm x 1.8 cm x 170 μm, a flow rate of 2.5 μL/s is equivalent to a Reynolds number Re ~ 15.3,[138] so the flow of glucose solution above the inverse opal hydrogel was approximately laminar. By fluorescence microscopy with a rhodamine dye solution, we found that ~ 80 s is required for the solution front to be pumped from the syringe to the microfluidic flow cell, and this lag was subtracted from the recorded time to yield the actual elapsed time. The time evolution of diffraction wavelength was recorded for three stepwise changes in glucose concentration at pH 9: 0.1 mM to 1 mM, 1 mM to 10 mM, and 10 mM to 100 mM (Fig. 3.17a inset). For all three concentration increases, the diffraction wavelength red shifted minimally for ~ 20 s and then increased rapidly until it approached an equilibrium value. This initial dead time is consistent with the diffusion of glucose through the thickness of the flow cell (170 μm) to the solution/hydrogel interface. In all cases, when the flow was stopped, the diffraction wavelengths decreased ~ 2 nm to their final equilibrium value. To clarify the nature of the diffraction response kinetics, the diffraction wavelength values were normalized to their steady state values before the flow was stopped and plotted versus the square root of elapsed time t (Fig. 3.17a). In all three cases, a single straight line could be fit to the data for the majority of each experimental run, suggesting that the kinetics was proportional to $t^{1/2}$, which is characteristic of a diffusion limited process. For the two stepwise decreases in glucose concentration (100 mM to 10 mM and 10 mM to 1 mM), the diffraction shift kinetics followed the same $t^{1/2}$ relationship

(Fig. 3.17b). For the change from 0.1 mM to 1 mM glucose, the diffraction shift began to slow down at t ~1000 s but did not flatten completely during the time of the experiment, with an equilibration time of $\geq$ 1500 s. When glucose concentration was increased from 1 mM to 10 mM, a similar $t^{1/2}$ dependence was found (Fig. 4a, triangles). The diffraction shift began to slow at t ~ 500 s, and equilibrium was reached at t ~ 1100 s. For 10 mM to 100 mM, even faster kinetics was observed (Fig.4a, circles); the slow swelling regime was reached at t ~ 100 s, and by t ~ 250 s the diffraction wavelength had reached its equilibrium value. Decreasing glucose concentration resulted in diffraction blue shifts with slower rates than when glucose concentration was increased (Fig. 4b). For example, an equilibration time of ~ 1000 s was found for 100 mM to 10 mM, and the equilibration time was $\geq$ 2100 s when glucose concentration dropped from 10 mM to 1 mM. The apparent diffusivity of glucose in the dense hydrogel, D_{app}, can be estimated from pseudo 1-D diffusion, using the diffusion equation:

$$l_0^2 = 2D_{app}\tau \tag{3.6}$$

Since the FWHM of diffraction peaks did not significantly increase during hydrogel swelling (Fig. 3.15a), l_0 is once again approximately 60 nm, as glucose diffuses from the FCC pores into the surrounding hydrogel. From the equilibration time values, it was found that D_{app} ranged from 9 x 10^{-15} cm^2/s to 7 x 10^{-14} cm^2/s, which is much smaller than the diffusivity of glucose in water, 6.7 x 10^{-6} cm^2/s.[139] It should be noted that Equation 3.6 overestimates D_{app}, since glucose is consumed when it binds to the phenylboronic acid group, decreasing the actual flux of analyte to the functional group. However, since two binding equilibria exist for the glucose-phenylboronic acid system, an analogue to Equation 3.5 is more difficult to derive, and thus the simple 1-D diffusion

equation was used to qualitatively estimate the retardation of glucose diffusion by the dense hydrogel. Since the HEMA monomer mixture used in photopolymerization contained no water, the value of D_{app} is expected to be low initially and then increase as the volume fraction of water in the hydrogel phase increases due to glucose binding. Finally, the equilibration times of an APBA-functionalized hydrogel to glucose are much longer than that of an AA-functionalized hydrogel to pH (~ 400 s). However, as we show later, the diffraction response kinetics of an APBA-functionalized hydrogel to pH (Fig 3.21) is actually very similar to the AA-functionalized hydrogel (Fig. 3.11d). Thus, the relatively slow response time can be reasonably explained by the order-of-magnitude difference in the diffusivities of H^+ (8×10^{-5} cm^2/s) versus glucose in water.
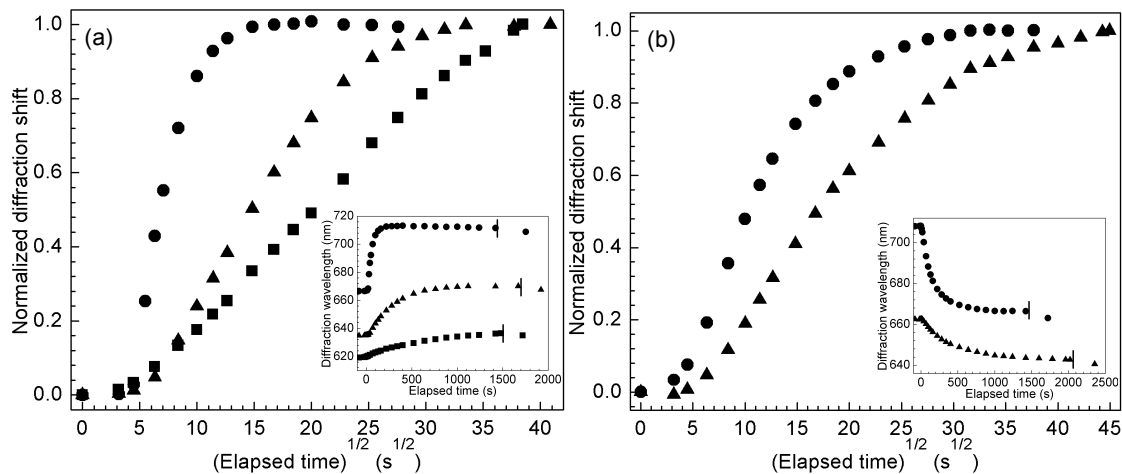
Figure 3.17: Kinetics of glucose sensing for 6.25% APBA hydrogel. (a) Normalized diffraction response for increasing glucose concentration. Squares, 0.1 mM to 1 mM; triangles, 1 mM to 10 mM; circles, 10 mM to 100 mM. (b) Normalized diffraction response for decreasing glucose concentration. Circles, 100 mM to 10 mM; triangles, 10 mM to 1 mM. Insets of both graphs: diffraction wavelength as a function of elapsed time. The vertical black line marks the time when the pump was turned off and flow stopped.

As mentioned, the diffraction response of the APBA-functionalized hydrogel follows a $t^{1/2}$ relationship over most of the swelling range, suggesting a diffusion limited kinetic response. Since pH remained constant while glucose was introduced to the

100

hydrogel, the concentration of H^+ should not impact kinetics. Thus, the diffusion of glucose to reactive APBA sites on the hydrogel is the most likely rate limiting factor during most of the swelling. The decrease in equilibration time as the hydrogel became more swollen is explained by the effect of expansion on the diffusivity of the hydrogel. It is well known that the diffusivity of an initially compact polymer to molecules may be increased by orders of magnitude when it swells in the presence of a good solvent.[131,140] Possible explanations for this phenomenon include the larger free volume for diffusion in a swollen hydrogel mesh[141] and faster chain relaxation dynamics and lower effective T_g for a swollen hydrogel.[140] Thus, as the hydrogel binds to glucose and becomes more swollen, the diffusivity of glucose will increase, and the equilibration time decreases. The general slowing of the kinetics towards the end of each run may be due to the slow rate of reaction between glucose and the sterically inaccessible APBA functional groups which are buried in the hydrogel structure. When the hydrogel becomes sufficiently swollen, these APBA groups may rotate or translate into configurations where they can bind glucose, leading to further red shift in diffraction. The dependence of diffusivity on the swelling ratio may also explain the relatively greater equilibration time and the larger regime of slow diffraction shift kinetics when glucose concentration was decreased. Since the glucose diffuses out of the top of the hydrogel film into the bulk solution first, this is the first region to contract, and since the contracted state has a lower diffusivity for glucose it could retard further outflow. The kinetically trapped interior regions reach equilibrium more slowly, explaining the apparent hysteresis in diffraction response observed over the time frame of our experiment (~30 minutes) which disappeared overnight.

3.5.2.5 Analysis of Diffraction Peak Evolution

Peak analysis was performed on the reflection spectra of the 6.25% APBA hydrogel in different glucose concentrations to determine effect of hydrogel swelling on the optical response, and if the templated hydrogel structure becomes disordered upon swelling. The best-fit I_b and *FWHM/λ_b* for the 6.25% APBA hydrogel were plotted against λ_b/λ_{b0} and displayed in Figure 3.18. The diffraction intensity decreased monotonically as the templated hydrogel swelled, going from 35% to 17% as the hydrogel expanded from $\lambda_b/\lambda_{b0} = 1$ (DI water) to $\lambda_b/\lambda_{b0} = 1.34$ (100 mM glucose). The normalized FWHM exhibited a complex behavior versus diffraction shift which seems to be sensitive to variations in the hydrogel mesostructure, as shown by the scatter in their values at different diffraction shifts (Fig. 3.18). In summary, the trend in diffraction intensity as a function of diffraction shift was consistent across multiple points on multiple samples, while the normalized FWHM had a less obvious relationship to diffraction shift.
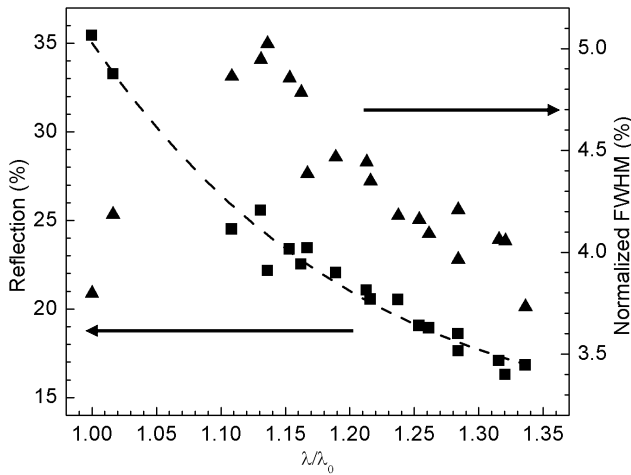
Figure 3.18: Curve fit data of reflection peak intensity (squares) and normalized FWHM (triangles) for the 6.25% APBA hydrogel versus spectroscopic swelling ratio (λ_b/λ_{b0}) due to pH change and glucose binding. The dashed line is a guide for the eye.

3.5.2.6 Comparison with SWA and TMM

Using the diffraction wavelength of the 6.25% APBA hydrogel as the starting point, we calculated the expected diffraction peak intensity and normalized FWHM values of an inverse opal hydrogel during swelling. The diffracted peak intensity and normalized FWHM values calculated from the three models using SWA are displayed in Fig. 3.19b and 3.19c; the TMM data are qualitatively similar for the 0-D pore swelling case and not shown (TMM simulations were not done for the 1-D pore swelling and 2-D pore shrinkage cases). Two observations can be made after comparing the calculated and experimental diffraction intensity values (Fig. 3.19b). First, depending on the swelling model used, the diffraction intensity may display drastically different trends. For example, for the 0-D pore swelling case (squares), the diffraction intensity increases slightly with swelling, while diffraction intensity decreased as the hydrogel swelled when using either the 1-D pore swelling (triangles) or the 2-D pore shrinkage model (circles). Second, the simulated diffraction intensity for all three models is much higher than the experimentally observed intensity (inverted triangles), suggesting that factors other than refractive index contrast and pore swelling influence the diffraction intensity of the inverse opal hydrogel. The same variability can be seen in the normalized FWHM data (Fig. 3.19b). While both the 0-D pore swelling model (squares) and the 1-D pore swelling model (triangles) showed relatively constant FWHM during swelling, the normalized FWHM for the 2-D pore shrinkage model (circles) decreased at high degrees of swelling, comparable to the experimental result (inverted triangles).
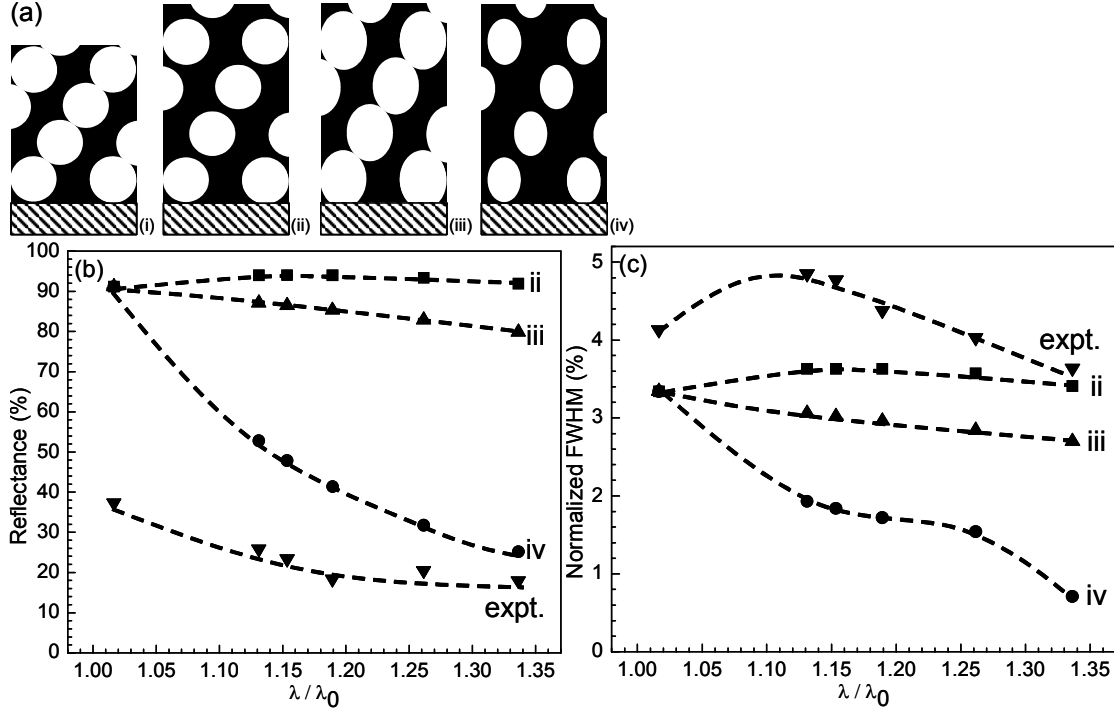
Figure 3.19: Comparison of experimental and calculated diffraction spectra of hydrogel swelling. (a) Schematic of the hydrogel swelling models. i. FCC{110} cross section of the fully contracted inverse opal hydrogel on the substrate. ii. 0-D pore swelling, with no change in pore volume or shape. iii. 1-D pore swelling, with pores expanding in the same fashion as the bulk hydrogel. iv. 2-D pore shrinkage, with pores contracting in the substrate normal directions. The overall swelling was assumed to be 1-D due to substrate pinning. (b) Diffraction intensity of 6.25% APBA hydrogel as a function of the total spectroscopic swelling ratio λ_b/λ_{b0}. Inverted triangles, experimental data; squares, 0-D pore swelling; triangles, 1-D pore swelling; circles, 2-D pore shrinkage. Dashed lines are guides for the eye. (c) Normalized FWHM of 6.25% APBA hydrogel as a function of λ_b/λ_{b0}. Same legend as (b). Calculations performed by Stephanie Pruzinsky.

As mentioned, a comparison of the experimental diffraction spectra versus the peak parameters simulated using SWA revealed a large difference in diffraction intensity (Fig. 3.19b) and normalized FWHM (Fig. 3.19c). Since the hydrogel swelling is accompanied by an influx of water and counter ions, the refractive index contrast between the hydrogel phase and the aqueous solution should decrease with swelling, which should in turn decrease the normalized FWHM of the diffraction peak for the swollen hydrogel. However the change in the shape of the pores should also be considered. Our 0-D pore swelling model accounted for the decreasing refractive index

104

contrast but not changes in pore dimensions. In this model, both calculated diffraction intensity and normalized FWHM increased and then decreased slightly as the spectroscopic swelling ratio increased (squares), whereas the experimental diffraction intensity (inverted triangles) decreased significantly as the hydrogel swelled.. Thus, variation in refractive index contrast alone was insufficient to predict the shape of a diffraction spectrum as a function of hydrogel swelling. The 1-D pore swelling model yielded diffraction spectra that are slightly more similar to the experimental data, but still qualitatively different. Over the entire range of hydrogel swelling, the diffraction intensity and the calculated normalized FWHM each decreased by ~10% versus their initial values (triangles). The 2-D pore shrinkage model, which is most physical in that it allows the hydrogel to expand into all available volumes, also seems to be qualitatively closest to the experimental data. For this model, the diffraction intensity decreased monotonically, with an intensity ~ 1/3 of its starting value at a diffraction shift of 1.34 (Fig. 3.19b, circles), which was similar to the experimental diffraction intensity decrease of ~ 1/2 (Fig. 3.19b, inverted triangles). Thus, the experimental trend in peak intensity can be partially explained by a combination of decreasing refractive index contrast and partial pore closure.

There are several variables not accounted for with our models and simulation methods. One factor is disorder of the inverse opal hydrogel due to drying cracks and crystal defects of the colloidal template. The presence of such disorder is clear, as shown by the reflection optical micrograph (Fig. 3.14a,b) as well as the SEM (Fig. 3.13). In addition, the well defined Fabry-Perot interference fringes disappeared as the hydrogel swelled (Fig. 3.15a), suggesting the flat interfaces at the top and bottom of the hydrogel

were disrupted, possibly due to inhomogeneous swelling. The disorder initially present in the templated hydrogel should result in lower diffraction intensity and higher FWHM due to interruption of the 3-D translational order. Since these defect sites are filled with hydrogel, they tend to swell more drastically as the rest of the hydrogel expands, which may cause the templated hydrogel to become increasingly disordered during swelling. The contributions of disorder may help explain the much lower initial diffraction intensity of the hydrogel film compared with its theoretical predictions (Fig. 3.19b), as well as the higher than predicted values for normalized FWHM (Fig. 3.19c). In addition, the higher swelling in the defect sites may create local stress points that can buckle the surrounding structure, resulting in a large scatter in the normalized FWHM values (Figs. 3.18 and 3.20).

Our microspectroscopy on the dried polystyrene-air colloidal crystal used as the template found the diffraction intensity was on the order of ~ 60%, when theory predicted that nearly 100% of the light should be reflected, given the higher refractive index contrast between polystyrene and air. Thus, improving the order of the colloidal template is important in optimizing the diffraction response of an inverse opal hydrogel sensor. Nevertheless, since our sensing mechanism depends on the change in diffraction wavelength rather than intensity, the current diffraction efficiency is probably sufficient for most sensing applications. Changes in the 3-D mesostructure must also be considered as a factor affecting the resulting reflection spectra. In order to fully understand the evolution of the diffraction peak of the inverse opal hydrogel during swelling, it may be beneficial to directly observe the change in the 3-D pore structure, perhaps through

optical microscopy. In addition, a more sophisticated model, such as finite element analysis of hydrogel swelling, may be beneficial.

3.5.2.7 Effect of Plasma Etching

SEM of the inverse opal hydrogels showed that some of the samples contained a ~1-2 μm thick overlayer of untemplated hydrogel. To elucidate the effect of the bulk hydrogel overlayer, to determine if the diffraction response is uniform across multiple points and multiple samples, we synthesized a 6.25% APBA hydrogel and used an oxygen plasma to remove any potential overlayer on the sample. Indeed, we overetched the sample by ~ 2 μm so as to ensure complete removal of a bulk film overlying any part of the sample, followed by the standard etching of the CC with CHCl$_3$. After solvent exchange, the 6.25% APBA inverse opal hydrogel exhibited λ_{b0} of 537 nm in DI water, in excellent agreement with the non-plasma treated sample. The evolution of diffraction intensity and normalized FWHM versus λ_b/λ_{b0} of the curve-fitted reflection spectra from a point on the plasma treated film is shown in Figure 3.20. The diffraction intensity for the plasma-treated film monotonically decreased from 27.5% to 10.3% as the hydrogel swelled to a λ_b/λ_{b0} of 1.40, which nearly matched the peak attenuation of the 2-D pore shrinkage model (Fig. 3.19b, circles). Also, it should be noted that the initial diffraction intensity of 27.5% is significantly lower than that of the untreated film (35.7%, Table 3.3), possibly because the oxygen plasma treatment decreased the number of layers of mesostructured hydrogels and/or damaged the hydrogel structure. In conclusion, there was good qualitative agreement between the equilibrium response for both the etched and unetched films in that both exhibited a monotonic decrease in the diffraction intensity, and there was not a clear trend in the FWHM as a function of swelling for either.
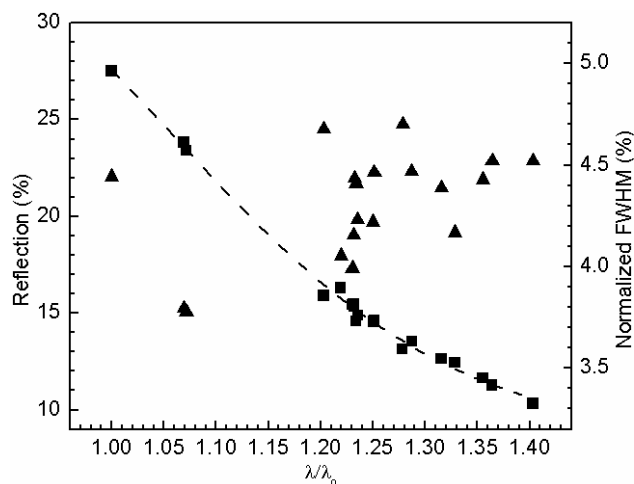
Figure 3.20: Curve fit data of reflection peak intensity (squares) and normalized FWHM (triangles) for the plasma-treated 6.25% APBA hydrogel versus spectroscopic swelling ratio (λ_b/λ_{b0}). The dashed line is a guide for the eye.

The diffraction response kinetics of the plasma-treated hydrogel to glucose (Fig. 3.21) shows an apparently diffusion limited behavior with equilibration times similar to the untreated hydrogel (Fig. 3.17). As the hydrogel became more swollen at higher glucose concentrations, the equilibration time decreased, going from ~ 1200 s at 0.1 mM glucose to ~ 240 s at 10 mM glucose. The slightly smaller equilibration times for the treated hydrogels may be partially due to the smaller final glucose concentrations in these experiments. In conclusion, since the diffraction response kinetic data of the etched film agrees (to within 10%) with that taken without plasma etching, one may gather that the film structure at the glass slide-hydrogel interface does not greatly impact the kinetics.
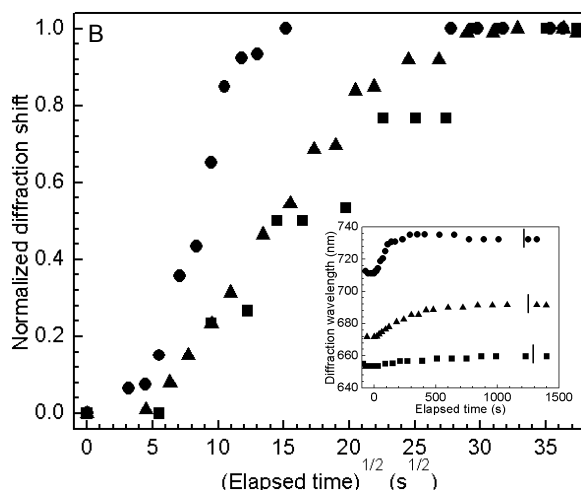
Figure 3.21: Glucose sensing kinetics for the plasma-treated hydrogel. Normalized diffraction response for increasing glucose concentration: squares are 0.1 mM to 0.3 mM; triangles are 1 mM to 3 mM; circles are 10 mM to 30 mM. Inset: diffraction wavelength as a function of elapsed time. (The vertical black lines mark the time when the pump was turned off and flow stopped).

Finally, the diffraction response of the 6.25% ABPA hydrogel to changing pH was examined in order to elucidate whether the slower equilibration times observed in glucose sensing could indeed be explained by the discrepancy in the analyte diffusivities. The diffraction shift kinetics from pH 6 to pH 9 shows that the response was essentially completed at t ~ 400 s (Fig. 3.22). After examining the all of the diffraction response data for the plasma etched hydrogel, it is clear that plasma treatment does not significantly improve the kinetics of diffraction response of an inverse opal hydrogel, while degrading the diffraction intensity of the CC templated mesostructure.
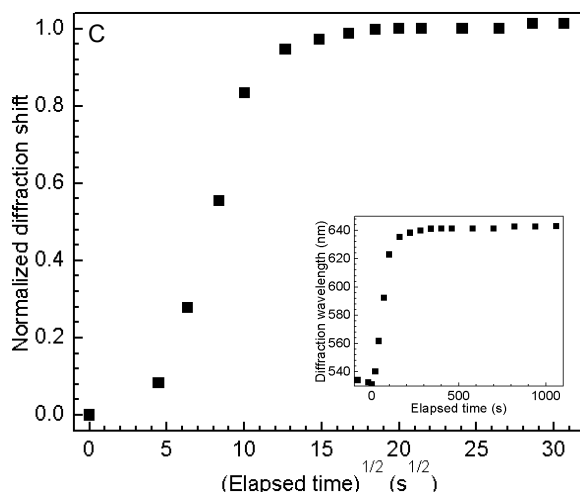
Figure 3.22: Kinetics of pH induced diffraction shift for the plasma treated glucose-sensitive hydrogel from pH 6 to pH 9.

3.5.2.8 Origin of Glucose Sensitivity at High Ionic Strength

The chemical mechanism for glucose sensing for our inverse opal APBA-functionalized hydrogel is essentially the same as for phenylboronic acid containing PCCA hydrogel glucose sensors.[20]   Specifically, formation of a charged complex between phenylboronic acid and glucose increases the degree of ionization on the hydrogel network, causing an influx of solvent and counter ions that swell the hydrogel, resulting in a red shift in optical diffraction.   However, the hydrogel mesostructures of these two systems are quite different from each other.   In our case, infiltration of the dried colloidal crystal with HEMA-APBA mixtures followed by template removal resulted in a dense functionalized mesostructure, whereas the PCCA utilized polymerization of a relatively dilute polyacrylamide hydrogel inside a charge stabilized colloidal crystal which was then functionalized with phenylboronic acid moieties.   We believe that the persistence of glucose sensitivity for the inverse opal hydrogel at high ionic strength (Fig. 3.15b and Fig. 3.16) is a direct result of the dense hydrogel structure, which can carry a high concentration of APBA groups.   For example, the 6.25% APBA content contained

110

an estimated phenylboronic acid concentration of 515 mM. In comparison, a complete

conversion of acrylamide groups in the PCCA into phenylboronic acid moieties would

yield a concentration of 14 mM. Thus, even when the anionic APBA-glucose complex is

electrically screened at high ionic strength, the larger concentration of ionizable groups in

the inverse opal hydrogel allows the mesostructure to swell sufficiently to generate an

optical response. The glucose sensitivity of the inverse opal hydrogel at pH 9.5 (Table

3.3) may also be explained by the higher concentration of APBA groups. Even though a

large fraction of the APBA groups are deprotonated at pH 9.5, there is still enough

protonated APBA so that complex formation with glucose leads to a significant increase

in the equilibrium degree of ionization on the hydrogel. Here, the high solution ionic

strength causes the film to remain partially swollen even at pH 9.5, so that the glucose

binding could cause a further red shift of diffraction. Based on the glucose sensing data

and our previous pH sensing results,[19] we propose that the dense inverse opal hydrogel

structure may be especially well suited for detection of analytes at high ionic strength

using spectroscopic methods.

3.5.2.9 Dimensionality of Swelling

Previously, work on a variety of unpinned PCCA hydrogels found that their

swelling was 3-D as expected; i.e. the dimensionless change in volume $\Delta V/V_0$, was found

to be proportional to $(\Delta\lambda_b/\lambda_{b0})^3$. Since $\Delta V/V_0$ should be directly proportional to the

concentration of ionizable groups on the hydrogel at low degrees of ionization, we

compared the calculated $(\lambda_b/\lambda_{b0})_b$ values for the 6.25% APBA and the 1.25% APBA

hydrogel. We found that the diffraction from the 6.25% APBA hydrogel shifted about 7

times more than the 1.25% APBA hydrogel at the same glucose concentration; in other

words, a 5-fold increase in ionizable groups led to a 7-fold increase in optical response. This result implies that the charged inverse opal hydrogel does not swell in 3-D but rather mostly in the sample normal direction, which is similar to the behavior of our pH sensitive hydrogels.[19] Again, this is almost certainly because the hydrogel was covalently attached to the glass substrate and thus could not macroscopically swell in 3-D without delaminating from the substrate.

3.5.2.10 Error Analysis

In Fig. 3.17 and Fig. 3.18, curve fitting was performed on the experimental diffraction spectra to quantitatively study the kinetics and equilibrium peak shapes, respectively. The error bars for diffraction wavelength, peak intensity, and normalized FWHM generated by the least square peak fit were very small and thus were not plotted. For example, the average for the normalized error (error divided by the data value) for diffraction wavelength, diffraction intensity, and normalized FWHM in Fig. 3.17a and 3.17b were 6.2×10^{-5}, 6×10^{-3}, and 6×10^{-3}, respectively. The average normalized errors for the corresponding parameters in Fig. 3.18 were 4×10^{-5}, 4×10^{-3} and 3×10^{-3}. It is clear that the peak fitting algorithm is more proficient at fitting the diffraction wavelength than the other two peak parameters, as shown by its significantly smaller error. This may explain why the data points in Fig. 3.17a and 3.17b, which plotted the diffraction wavelength, formed a smoother line than the data in Fig. 3.18 dealing with the peak intensity and normalized FWHM. In addition, the diffraction spectra in Fig. 3.17a and 3.17b contained higher errors when compared with corresponding values generated from Fig. 3.18. This may be explained because the kinetics data in Fig. 3.17a and 3.17b were acquired over a shorter time interval than the steady state data in Fig. 3.18 (1 s vs. 7.5 s),

which reduced the signal-to-noise ratio of each spectrum. Finally, the signal resolution of the diffraction spectrum is limited by the diffraction grating spectrophotometer, which contains 512 elements arrayed over the range 290 nm to 1100 nm. Thus, all peaks have a minimum uncertainty of 1.6 nm.

3.5.3 Summary

In conclusion, by utilizing dried colloidal crystals as templates, we synthesized phenylboronic acid-functionalized inverse opal hydrogels within microfluidic flow cells for glucose sensing. The diffraction response was characterized with a maximum diffraction shift due to glucose binding of 1.201 for 6.25% APBA hydrogel at 100 mM glucose. The dependence of swelling on the concentration of APBA functional group and the lack of delamination from the substrate suggested that the templated hydrogel preferentially swelled in the substrate normal direction. Detectable diffraction response was observed for ionic strengths as high as 326 mM; the ability to sense glucose at physiological and higher ionic strengths may be attributed to a higher concentration of APBA groups in a dense hydrogel than is achievable by previous PCCA techniques. Diffraction response kinetics followed a $t^{1/2}$ relationship, with an equilibration time of $\sim$ 1100 s for physiological ionic strength and glucose concentrations, suggesting slow diffusion-limited kinetics. At equilibrium, the diffraction peak intensity decreased monotonically with swelling, with a maximum intensity reduction of $\sim 1/2$ at a diffraction shift of 1.34, while the normalized FWHM remained at $\sim$ 4-5% with a large degree of scatter. Comparison to simulated reflection spectra suggested that a combination of refractive index contrast decrease and pore deformation partially explains the trend in diffraction intensity as a function of swelling. In addition, sample disorder and/or

changes in the 3-D mesostructure due to pore deformation may contribute to the discrepancy between simulated and experimental values of diffraction intensity and normalized FWHM.

3.6 Results and Discussion: Ethanol Sensor

3.6.1 Microspectroscopy

CC templated HEMA hydrogels without additional functional groups exhibited tunable Bragg diffraction to many moderately polar molecules, due to favorable interactions between the side group –OH on HEMA and the molecule. For example, an inverse opal HEMA hydrogel exhibited red shifts in diffraction depending on the concentration of ethanol in an aqueous solution (Fig. 3.23). In DI water, the HEMA-only exhibited a λ_{b0} of 589 nm (Fig. 3.23b). As the ethanol concentration in the solution was increased, λ_b increased almost linearly to a value of 846 nm at 30% v/v ethanol (Fig 3.23b), for a spectroscopic swelling ratio of 1.44. The diffraction response is fully reversible and showed essentially zero hysteresis, as demonstrated by the overlap in the reflectance spectra for data collected while increasing and decreasing ethanol concentration (solid and dashed, Fig. 3.23a). Examination of λ_b as a function of ethanol concentration suggests that the hydrogel film is capable of further swelling if the ethanol concentration was further increased; however, no further increase in ethanol concentration was performed due to the tendency of the inverse opal hydrogel to delaminate from the substrate within the time required for diffraction response equilibration when λ_b/λ_{b0} goes above ~ 1.6. Due to the large swelling of HEMA in the presence of ethanol, it is reasonable to conclude that the solvent exchange procedure post CC etching (submerging the inverse opal hydrogel in pure ethanol for 30 s) may

introduce disorder in the hydrogel mesostructure due to local buckling. Indeed, two-photon fluorescence imaging of an inverse opal hydrogel (Chapter 4) revealed regions inside the hydrogel with disordered pores, especially in the swollen state. As is the case for all other inverse opal hydrogel sensors that we studied, the red shift in diffraction is accompanied by attenuation in the diffraction peak intensity; I_b decreased from 18.0% to 3.4% as the ethanol concentration was increased from 0% v/v to 30% v/v (Fig. 3.23b).
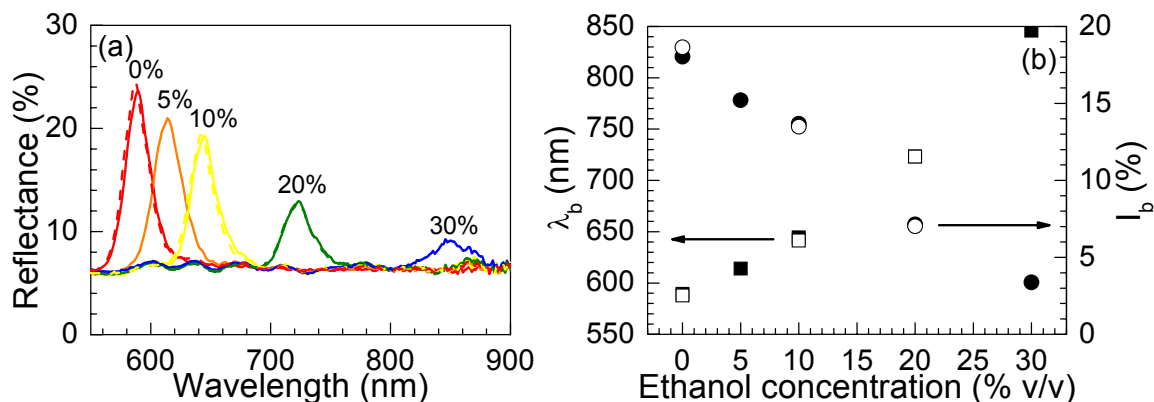
Figure 3.23: Diffraction response of a HEMA-only inverse opal hydrogel to ethanol. (a) Reflectance spectra in solutions of different % v/v ethanol in water, showing a red shift and attenuation in Bragg diffraction as the ethanol concentration was increased. Solid (dashed) lines correspond to increasing (decreasing) ethanol concentration. (b) λ_b (squares) and I_b (circles) of the inverse opal hydrogel as a function of ethanol concentration. λ_b increases almost linearly as a function of ethanol concentration, while I_b decreases in a similar fashion. The excellent overlap λ_b and I_b for increasing (solid) and decreasing (open) ethanol concentration demonstrate that there is no hysteresis in the diffraction response.

The diffraction response kinetics for a HEMA-only inverse opal hydrogel sensor to ethanol followed the same apparently diffusion-limited behavior, although with significant smaller equilibration times compared with the pH and glucose sensors (Fig. 3.24). For example, changing the ethanol concentration from 0% v/v to 5% v/v induced a diffraction shift which was complete at $\tau \sim 100$ s. Using Equation 3.6 and assuming the same value for l_0, a D_{app} of $\sim 1.8 \times 10^{-13}$ cm^2/s is calculated for the diffusion of ethanol into the hydrogel (Fig 3.24b). The diffraction response during a ethanol concentration

increase from 10% v/v to 20% v/v exhibited about the same rate of response, while the kinetics for the corresponding decrease in ethanol concentration was noticeably faster, with $\tau \sim 60$ s and $D_{app} \sim 3 \times 10^{-13}$ cm^2/s (Fig. 3.24b). The relatively faster response for decreasing (Fig. 3.24b, circles) versus increasing (Fig. 3.24b, triangles) analyte concentration is similar to behavior of the APBA-functionalized glucose sensor (Fig. 3.16 and 3.17), and can be explained by the higher diffusivity of ethanol through a hydrogel with a higher initial swelling ratio. However, D_{app} of ethanol through the HEMA-only inverse opal hydrogel was reduced by a factor of $\sim 5 \times 10^7$ compared to the diffusivity of ethanol in water (1.24 x 10^{-5} cm^2/s),[139] while D_{app} of glucose through the APBA-functionalized inverse opal hydrogel was reduced by a factor of $\sim 4 \times 10^8$ with the hydrogel in the compact state. A possible explanation for the smaller diffusivity reduction for ethanol may be the smaller hydrodynamic radius of ethanol compared to glucose. Experimental studies have found that the diffusivity of a particle through a polymer coil decreases exponentially as a function of its hydrodynamic radius, if the hydrodynamic radius is similar to the polymer mesh size.[142,143] Thus, even a small discrepancy in size between ethanol and glucose can significantly enhance the diffusivity of ethanol through the dense hydrogel. Also, in contrast to glucose, which may be bound to phenylboronic acid at any given time, ethanol is free to diffuse throughout the hydrogel network, which may also contribute to the higher D_{app} value for a CC templated hydrogel ethanol sensor.
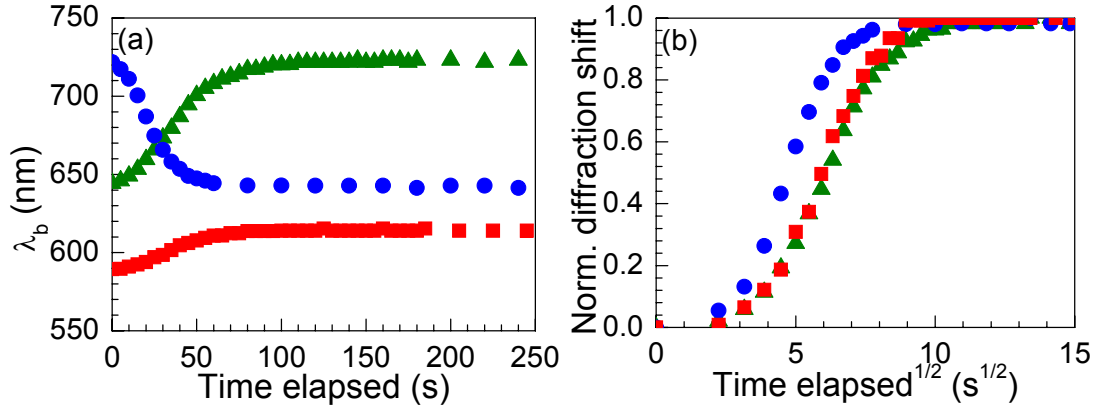
Figure 3.24: Diffraction response kinetics of a HEMA-only inverse opal hydrogel to ethanol. (a) Evolution in λ_b as a function of time for three ethanol concentration changes (% v/v): 0 to 5 (squares), 10 to 20 (triangles), 20 to 10 (circles). (b) Normalized diffraction shift as a function of $t^{1/2}$, with the same set of symbols. The diffusion limited diffraction response is completed in ~ 60 s for 20% v/v to 10% v/v ethanol, and within 100 s for the other experiments.

3.6.2 Laser Diffraction

When an inverse opal hydrogel synthesized in a large CC template ($D = 1250$ nm) was illuminated with a visible laser ($\lambda = 532$ nm), the mesostructured hydrogel essentially acts as a 2-D Bragg grating (Fig. 3.25) with a grating pitch λ_G determined by diameter of the CC template. The diffraction angle α can be predicted with the following equation:

$$\sin\alpha = \frac{m\lambda}{n\lambda_G} \tag{3.7}$$

where m is a positive integer representing the order of diffraction and n is the refractive index that the diffracted light travels through. Two common characteristic distances for a layer of close-packed spheres are shown in Figure 3.25b. An ordered monolayer of close-packed colloids exhibits six-fold symmetry and thus should have an expected diffraction pattern of six spots equidistant from the central undiffracted beam. However, it has been shown that the ABC stacking of an FCC colloidal crystal enhances the intensity of three of those diffraction spots, and a defect-free FCC CC with low refractive

index contrast should exhibit a three-spot diffraction pattern.[144] Thus, laser diffraction can be used to simultaneously detect deformations in the sample parallel direction and probe the degree of order in the CC templated hydrogel.
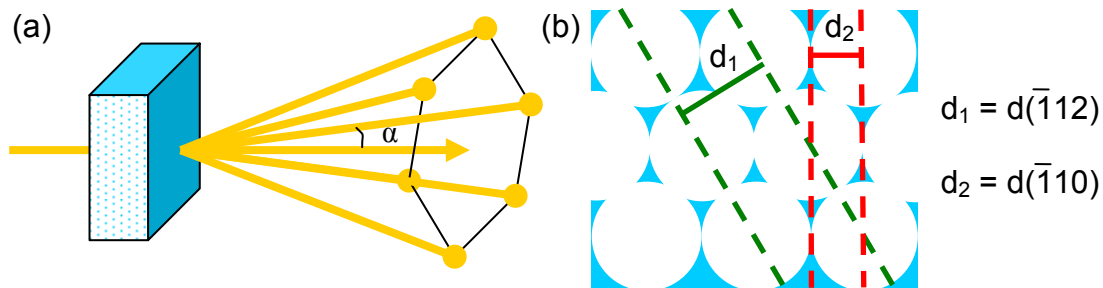
Figure 3.25: Laser diffraction by an inverse opal hydrogel. (a) Schematic of laser diffraction. (b) Two common characteristic distances probed by laser diffraction, with $d_1 = (\sqrt{3}/2)D$ and $d_2 = 0.5D$.

The diffraction patterns of an HEMA-only inverse opal hydrogel in different solvents exhibited the expected six spots (Fig. 3.26), indicating that within the area illuminated by the laser (spot size = 2mm), the inverse opal hydrogel consisted of a single domain of ordered pores, or multiple domains all oriented in the same direction.   In CHCl$_3$ (n = 1.448), a set of six bright diffraction spots ~ 4 mm away from the central beam can be easily seen (Fig. 3.26a). A slightly dimmer set of six spots ~ 8.5 mm away from the central beam and offset by 30° can also be detected. Finally, several faints spots ~ 10 mm away from the central beam are barely visible. The diffraction pattern of the same hydrogel film in water-ethanol mixtures is more difficult to pick out due to a larger amount of light scattering from the refractive index contrast between the hydrogel and the water-ethanol mixture (Fig. 3.26b-f). A quick examination of the six diffraction spots closest to the central beam shows that three spots are clearly brighter than the other three. This strongly suggests that the pores possessed mostly FCC symmetry, potentially with some twinning defects that led to nonzero intensity of the second set of three spots.

Using a distance of 11 mm between the hydrogel and the paper onto which the diffraction pattern is projected, and approximating the refractive index of the ethanol solutions using effective medium theory, the characteristic spacings corresponding to the diffraction spots were calculated and shown in Table 3.4. Several conclusions can be drawn from the calculated characteristic spacings. First, the characteristic spacings calculated from the diffraction pattern of the inverse opal are equal to the values calculated from the diameter of the CC template. This suggests that the hydrogel is a direct replica of the CC template, with a minimal deformation after the CC was removed. Second, the characteristic spacings remained relatively unchanged regardless of the ethanol concentration; since the laser diffraction probes periodicity along the sample parallel direction, this indicate that the change in the characteristic interlayer spacing was limited to the sample normal direction, corroborating the microspectroscopy data. In the future, experiments such as laser diffraction from a sample placed at a nonperpendicular angle and direct counting of the diffracted light intensity for each of the six diffraction spots will assist in characterizing other structural properties of the CC templated hydrogel, such as the exact dimensionality of swelling and the long range translational order of the hydrogel and the original CC template.
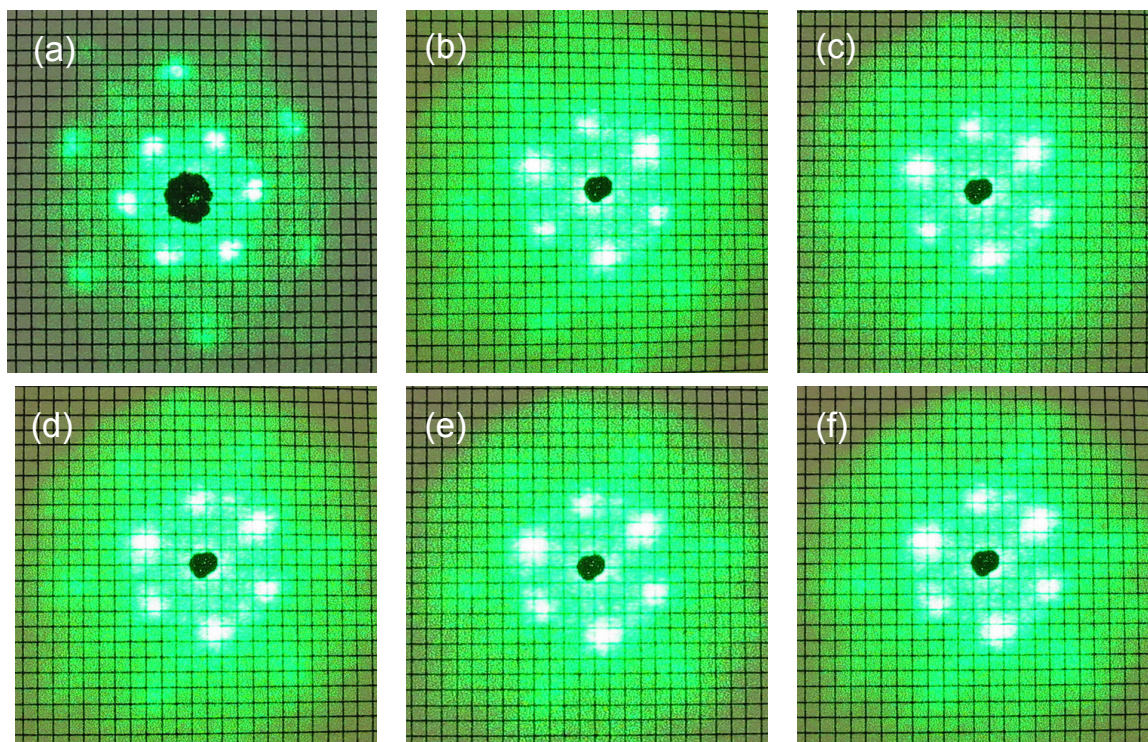
Figure 3.26: Laser diffraction patterns of a HEMA-only inverse opal hydrogel in different solvents. (a) $CHCl_3$. (b) Water. (c) 5% v/v ethanol (aq.). (d) 10% v/v ethanol (aq.). (e) 20% v/v ethanol (aq.). (f) 30% v/v ethanol (aq.). Grid = 1 mm.

Condition	n	φ_1 (°)	d_1 (nm)	φ_2 (°)	d_2 (nm)
$CHCl_3$	1.448	20.8	1037.1	37.6	603.1
water	1.333	21.3	1096.8	38.5	641.5
5% ethanol	1.334	21.5	1085.7	37.6	653.3
10% ethanol	1.336	21.5	1088.3	37.7	651.6
20% ethanol	1.339	21.3	1093.8	37.1	659.5
30% ethanol	1.341	21.4	1087.0	36.5	667.3
Predicted			1082.5		625.0

Table 3.4: Characteristic spacings along the surface of an inverse opal hydrogel calculated from the diffraction pattern. There is good agreement between the calculated characteristic distances and values predicted from the diameter of the CC template. In addition, the characteristic spacing did not change drastically when the ethanol concentration was increased.

3.6.3 Summary

By polymerizing a standard monomer mixture with no additional functional groups inside CC templates, inverse opal hydrogel sensors can be fabricated that exhibit a red shift in diffraction when exposed to increasing concentrations of ethanol. The

magnitude of the diffraction response appeared to be linearly proportional to ethanol concentration, and was not yet saturated at 30% v/v ethanol. The diffraction shift was completed in ~ 100 s, which is significantly faster than the kinetics of either pH or glucose sensors, even accounting for the higher diffusivity of ethanol in water compared to glucose. Laser diffraction of a HEMA-only inverse opal hydrogel in $CHCl_3$ and different ethanol-water mixtures revealed that the hydrogel periodicity matched well with the periodicity of the CC template, suggesting that the hydrogel is mechanically robust. In addition, the diffraction pattern remained largely unchanged at different ethanol concentrations, confirming that the swelling in the interlayer distance only occurs in the sample normal direction.

3.7 Results and Discussion: Crosslinker Sensor

The BAC-functionalized inverse opal hydrogel contained a crosslinker with disulfide linkage. Such crosslinking can be easily broken through reduction of the disulfide bond into two thiol groups, and reactivated with an oxidizing agent. A reversible crosslinking system involving the reducing agent DTT and the oxidizing agent sodium bromate is schematically shown in Figure 3.27. Using such a system, we found that the BAC-functionalized inverse opal hydrogel showed a small red shift in diffraction when reduced, which can be reversed by oxidation (Fig. 3.28). With a total crosslinker concentration of 2.0 mol%, the BAC-functionalized hydrogel diffracted 625 nm light in water, indicating that it was slightly swollen from an inverse FCC mesostructure, perhaps because the acrylamide group on BAC is more hydrophilic than HEMA. When the hydrogel was submerged in 1 mM DTT, λ_b red shifted by a small but noticeable amount over ~ 20 minutes to 640 nm (Fig. 6.28b). The amount of red shift cannot be accounted

121

for by the increase in refractive index from the addition of DTT. Instead, it is most likely caused by a reduction of crosslinker density toward the value of the nonreactive crosslinker EGDM (0.4 mol%). It should be noted that since no ionizable group was in the monomer mixture, the relatively weak hydrophilic interaction between HEMA and water is the main driving force for hydrogel swelling, and thus the diffraction response should be small. The presence of oxygen in the atmosphere may also attenuate the diffraction red shift during chemical reduction, since oxygen is known to cause disulfide bond formation and therefore partially offset the cleavage of disulfide bonds by DTT.[145] Replacing 1 mM DTT with 1 mM sodium bromate resulted in a partial recovery of λ_b over ~ 20 minutes to 630 nm, which is reasonable since not all thiol groups can be expected to recombine with each other, especially given the large excess in the concentration of BAC in the hydrogel (~ 0.13 M) compared with the concentration of sodium bromate (1 mM). When the experiment is repeated with higher concentrations of DTT and the sodium bromate, the diffraction response were slightly enhanced, red shifting to 645 nm in 0.1 M DTT and back to 629 nm in 0.1 M sodium bromate.
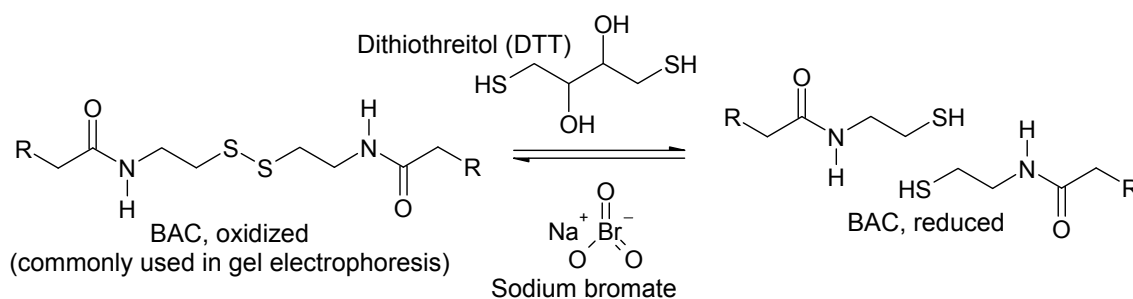
Figure 3.27: Schematic reactions for the activation of a reversible crosslinker (BAC) with mild reduction with DTT and mild oxidation with sodium bromate.
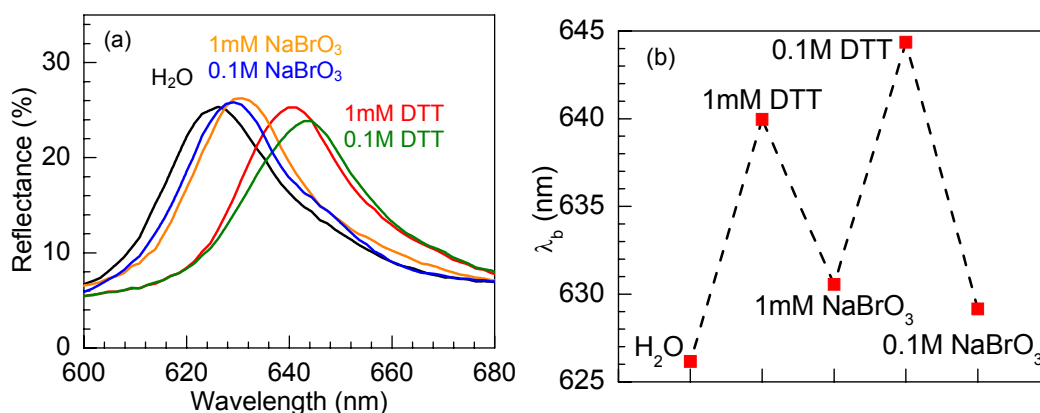
Figure 3.28: Diffraction response of a BAC-functionalized inverse opal hydrogel to DTT and sodium bromate. (a) Reflectance spectra of the hydrogel in various aqueous solutions. (b) λ_b evolution after exposure to DTT and sodium bromate.

There are many future experiments that can be carried out to fine tune the diffraction response of inverse opal hydrogels utilizing switchable crosslinkers. First, the magnitude of the diffraction response may be enhanced through variations such as testing the BAC-functionalized hydrogel in a controlled atmosphere, copolymerization of ionizable groups, incorporation of a separate expansion/contraction mechanism (e.g. adding alcohol) after changing the crosslinker density, and the use of other types of reactive crosslinkers. Once optimized, such reversible crosslinker systems may function as sensors to various molecules which can cleave/reform the crosslinker moiety. In conclusion, through copolymerization with BAC, inverse opal hydrogels have been synthesized which exhibit reversible diffraction shifts in the presence of mild reducing and oxidizing agents. The currently modest diffraction response is primarily caused by weak hydrophilic interactions between HEMA and water, and may be improved with a different combination of monomers, oxidizing/reducing agents, and other experimental parameters.

3.8 Summary

Inverse opal hydrogel sensors with Bragg diffraction tuned by interactions with specific analyte molecules have been synthesized using CC templating and characterized both structurally and spectroscopically. The UV-polymerization of precursor mixtures containing 2-hydroxyethyl methacrylate (monomer), ethylene glycol dimethacrylate (crosslinker), Irgacure® 651 (photoinitiator), an appropriate polymerizable functional group, and up to 20% v/v water inside dried polystyrene CCs, followed by $CHCl_3$ etching of the CC template, resulted in mechanically robust inverse opal hydrogels with narrow bandwidth Bragg diffraction from planes of FCC(111) pores surrounded by the responsive hydrogels. By taking advantage of the significant volumetric change that accompanies the ionization of a crosslinked hydrogel, we have fabricated acid/base functionalized hydrogels as a diffraction-based pH sensor, as well as a 3-acrylamidophenylboronic acid functionalized hydrogel as a diffraction-based glucose sensor which operate at the physiological ionic strength of ~ 0.15 M. The spectroscopic swelling ratio of acrylic acid-functionalized hydrogels can be as high as ~ 1.5 going when pH was increased from 4 to 7, while the spectroscopic swelling ratio of APBA-functionalized hydrogels to glucose was ~ 1.2 at 100 mM glucose in pH 9 buffer. The magnitude of the diffraction response was controlled by varying parameters such as functional group concentration, solution ionic strength, concentration of HEMA monolayer (through dilution with water). The diffraction shift and the corresponding swelling of ionized hydrogels were qualitatively consistent with the influx of ions and solvent molecules due to the higher Donnan potential inside the hydrogel phase. The kinetics of Bragg diffraction response for the pH and glucose sensors were on the order

of several hundred seconds and were dependent on the initial swelling ratio of the hydrogel. The relatively slow diffraction response kinetics was explained in terms of hindered diffusion of the analyte molecules through a dense hydrogel mesh. Finally, interesting features in the diffraction spectra of inverse opal hydrogels, most noticeably the attenuation in diffraction peak intensity as the hydrogel swelled, were compared to predictions from computational techniques such as scalar wave approximation and transfer matrix method, which found the peak parameter evolution to be most consistent with a decrease in the volume fraction of the FCC pores as the inverse opal hydrogels expanded.

We also demonstrated the diffraction response of inverse opal hydrogels composed of only HEMA, which showed a large red shift in diffraction when submerged in aqueous solutions of increasing ethanol concentration, with a spectroscopic swelling ratio of 1.44 at 30% v/v ethanol. The large magnitude of diffraction response, as well as the fast response time of 100 s, was explained by the relatively small size of ethanol molecules and their free diffusion through the hydrogel network. By probing a HEMA-only inverse opal hydrogel templated using a large diameter CC ($D = 1250\ nm$) with the monochromatic light from a Nd:YAG laser ($\lambda = 532$ nm), we obtained diffraction patterns which corroborate earlier evidence suggesting that the change in the characteristic distance between layers of poress in the hydrogels occurred almost exclusively in the sample normal direction. Finally, through copolymerization of a crosslinker containing disulfide linkage, an inverse opal hydrogel was fabricated which exhibited reversible red shifts in diffraction when the disulfide linkage was broken and reformed through the addition of mild reducing and oxidizing agents. In conclusion, CC templating of

125

functionalized hydrogels has been shown to be a versatile technique for the synthesis of functional materials exhibiting tunable Bragg diffraction through several different mechanisms.

CHAPTER 4

MESOSTRUCTURE OF CC TEMPLATED HYDROGELS

4.1 Introduction

In Chapter 3, we demonstrated the polymerization of functionalized hydrogels infiltrated inside dried colloidal crystal templates, which after template etching yielded a robust inverse opal mesostructure. We found these mesostructured hydrogels to exhibit a strong first order Bragg diffraction peak that can be tuned by adjusting solution parameters such as pH, ionic strength, glucose concentration, ethanol concentration, and crosslinker density, depending on the functional group incorporated. While examining the UV-vis reflectance spectra, we noticed several interesting trends in the swelling behavior of these hydrogel sensors. First, as diffraction wavelength λ_b red shifted due to hydrogel swelling, the diffraction peak intensity I_b monotonically decreased.[19,21] We compared this reversible trend in I_b to analytical predictions using a scalar wave approximation (SWA) method[122] and found the result to be consistent with a decrease in the volume fraction of the FCC pores and/or an increase in disorder during hydrogel swelling.[21] Second, we found the relative magnitude of the diffraction shift $\Delta\lambda_b/\lambda_{b0}$ at various analyte concentrations (where λ_{b0} is the diffraction wavelength of the hydrogel in the compact state) was linearly proportional to the concentration of the functional group.[19,21] Since our spectroscopy geometry only probed dimensional changes in the sample normal direction,[21] the linear concentration dependence implies that the increase in the interlayer distance of the inverse opal hydrogels is limited to the sample normal direction. Third, the hydrogel responded more quickly to a change in the analyte concentration when the initial swelling ratio was higher,[21] suggesting that the hydrogel

127

swelling ratio may significant impact its mesostructure. To fully characterize the mesostructure evolution of inverse opal hydrogel sensors during swelling, we decided to directly image a Rhodamine B (RhoB) labeled inverse opal hydrogel pH sensor using two-photon laser scanning fluorescence microscopy.

Florescence techniques are frequently used to determine the physical properties of linear and crosslinked polymers, especially to quantify the diffusion of fluorescent probes in aqueous polymer solutions. Khoury and co-workers measured the diffusion coefficient of several fluorescein-labeled proteins in untemplated hydrogels with chemical compositions similar to our pH sensor, using the technique of fluorescence recovery after photobleaching (FRAP).[146] By changing only the hydrogel crosslinker density and measuring the diffusion coefficient at a constant pH of 7, they found that the diffusion of bovine serum albumin (BSA) approached the dilute solution limit as the hydrogel swelled to 5 times its original volume, indicating that the mesh size of the compact hydrogel was much smaller than the hydrodynamic radius of BSA (3.4 nm). They also discovered that as the solution pH increased, the diffusion coefficient of the BSA decreased, which they attributed to the repulsive electrostatic interactions between the deprotonated acid group on the hydrogel and BSA (isoelectric point pI = 4.2). In contrast, the protein lysozyme showed essentially zero diffusion inside the AA-functionalized hydrogels at pH of 7 and 10, possibly because of the attractive interaction between the hydrogel and lysozyme (pI = 11). FRAP was also used to characterize the diffusion coefficient of hydrophobic probes in a system of polyacrylic acid grafted onto a amphiphilic triblock copolymer of polyethylene oxide and polypropylene oxide, which showed a marked decrease in

diffusion coefficient at ~ 30 °C due to gelation of the copolymer and subsequent trapping of the fluorophor in the hydrophobic core of the gel.[147]

Multiphoton excitation of fluorophors is an attractive technique for studying the 3-D diffusion of dyes inside polymers and for nondestructive fluorescence imaging through the interior of a 3-D sample. In the multiphoton process, the dye is simultaneously excited by two or more photons of lower energy; as a result, the number of dye molecules excited (N) is related to the incident light power (P) by the following equation:

$$N \propto P^a \tag{4.1}$$

where a is the number of photons involved per multiphoton excitation process. If a focused light of an appropriate power is used, then the excitation process can be confined to the focal volume of the incident light, leading to selective fluorescence and/or photobleaching from a diffraction limited spot. By using a multiphoton FRAP process, Brown and co-workers examined the full 3-D mobility of fluorescent probes in cells with a resolution of several microns.[148] The same technique was later used to study the diffusion of dye in polyvinyl alcohol samples containing various amounts of glycerin plasticizer.[149] Multiphoton excitation combined with rastering of the light source allows for fluorescence imaging of 2-D cross sections; through software analysis of the 2-D slices, the 3-D mesostructure of the sample can be reconstructed. For example, this procedure was utilized to reconstruct the structure of a colloidal crystal formed by sedimentation on a patterned substrate.[55] Recently, the microstructure of polyvinyl alcohol hydrogels, formed in solution by freezing induced phase separation, was also examined by two-photon fluorescence microscopy.[150]

The choice of fluorescent dye strongly influences the image quality and resolution that can be achieved, especially in an index mismatched system such as our pH-sensitive hydrogel (n = 1.51) in water (n = 1.333). Fortunately, through multiphoton imaging, we can minimize negative effects such as photobleaching of the entire sampling area and scattering induced loss of depth resolution.[151] We selected Rhodamine B as the dye for imaging an AA-functionalized inverse opal hydrogel since RhoB exhibits a good two-photon cross section using a 780 nm Ti:sapphire laser[149,152] and its fluorescence is not strongly affected by pH. After scanning a series of horizontal 2-D images with a known vertical displacement between each slice, the fluorescence image data can be reconstructed by software to yield a full 3-D view of the mesostructure.

Using two-photon excitation, fluorescence cross sections of an AA-functionalized inverse opal hydrogel in buffers with pH ranging from 3 to 7 were collected on a laser scanning confocal microscope. The 3-D mesostructure of the hydrogel at different swelling ratios were reconstructed from the images with commercial software to examine the evolution of the FCC pore morphology during hydrogel swelling. Parameters such as the normalized interlayer distance (d/d_0), where d is the interlayer distance of the swollen hydrogel and d_0 is the initial interlayer distance, were calculated from the fluorescence data. d/d_0 values at different pHs were compared to the normalized spectroscopic swelling ratios (λ_b/λ_{b0}) from microspectroscopy. The 3-D hydrogel mesostructure from two-photon imaging were also compared to analytical predictions from finite element calculations.[153] The initial inverse opal structure was approximated by a finite element model with experimentally determined viscoeleastic properties as reported by other groups.[154] A thermal strain was applied to the mesh to simulate the effect of swelling

on the mesostructure of the elastomer. The two sets of data were matched to determine if the experimentally observed mesostructure is the thermodynamically favored configuration.

4.2 Synthesis

4.2.1 Colloidal Crystal Formation

Only the procedure for making the CC template for two-photon fluorescence imaging will be described here; please see Chapter 3 for a complete description on fabricating CC templates for microspectroscopy and other experiments. An aqueous suspension of monodisperse polystyrene colloids ($D = 3 \pm 0.087$ μm) was purchased from Interfacial Dynamics Co., Portland, OR. The CC templates were formed in the same way as described in Chapter 3.2.1, using 22 mm x 22 mm cover slips (No. 1, Corning) as the substrates. To ensure an adequate number of layers for a CC with $D = 3$ μm, a thick flow cell was made by stacking two Mylar® gaskets on top of each other, which was then submerged in a 0.05% v/v polystyrene colloidal suspension in water for 30 seconds. The cell was assembled by clamping together a glass slide, a 25 mm x 25 mm x 12 μm Mylar® film (as a shock absorbing layer), a cover slip substrate, a double-thickness colloid decorated gasket, and a top slide/reservoir. After flowing a 2% v/v aqueous PS colloidal suspension through the flow cell for 24 hours under damped, the cell was removed from the sonicator, excess colloidal suspension was decanted, the rubber bulb was placed back on, and the cell was allowed to dry overnight under an inverted crystallization dish.

4.2.2 Inverse Opal Hydrogel Synthesis

Rhodamine B isothiocyanate (RhoB-ITN) (Sigma-Aldrich) and 2-aminoethylmethacrylate hydrochloride (AEMA) (Acros) were used as received. The hydrogel composition used to fabricate the inverse opal pH sensor was essentially identical to that of the AA-functionalized hydrogel polymerized without water (Table 3.1), except that a polymerizable acrylated RhoB was added to the monomer mixture to enable fluorescence imaging. Acrylated RhoB was synthesized by dissolving RhoB-ITN (9.4 mg, 17.5 μmol) and AEMA (2.9 mg, 17.5 μmol) in water (1.75 mL), and the pH was adjusted to ~ 6 by adding 1M NaOH (aq.) (~ 50 μL). The solution was stirred for 2 hours at RT to complete the reaction and was used without further purification. AA (13.9 mg, 193 μmol), EGDM (5.0 mg, 25.2 μmol), and IR-651 (10.5 mg, 40.3 μmol) were dissolved in HEMA (0.471 g, 3.62 mmol). Then, 1 μL of the RhoB solution (10 mM) was diluted with 10 μL of the monomer mixture; 4 μL of the resulting product was mixed with 400 μL of the monomer mixture to yield a RhoB concentration of ~ 10 μM. This mixture was then infiltrated into a dry CC (D = 3 μm). ~ 300 μL of the fluorescent monomer mixture was pipetted into the injection tube, which was then capped with a rubber bulb. Once the colloidal crystal became translucent, indicating successful infiltration, excess precursor was removed from the injection tube, and the remaining mixture was photopolymerized at 365 nm for 50 minutes using a high intensity UV lamp (B-100A, UVP, Inc., Upland, CA). The top slide and the bottom substrate were separated and then placed in chloroform for at least 24 hours to fully dissolve the polystyrene colloids. Each inverse opal hydrogel was solvent exchanged by submerging the sample

in pure CHCl$_3$ for 30 seconds, in ethanol for 30 seconds, in water for 30 seconds, and finally placed in 1mM HCl (aq.) for storage.

4.3 Characterization

4.3.1 Two-photon Fluorescence Microscopy

The mesostructure of the RhoB-labeled inverse opal hydrogel sensor was imaged by two-photon fluorescence microscopy using a laser scanning confocal microscope (LSCM) (SP2, Leica). A mode locked Ti:sapphire laser at 780 nm (Spectra-Physics) was used as the excitation source. A 63x oil immersion objective was used to collect the reflectance and fluorescence signal. The hydrogel sample was assembled inside an imaging flow cell designed by Carla Heitzman of our group. First, the hydrogel film was placed on an aluminum substrate with a hole machined in the center to allow for imaging with the oil immersion objective through the cover slip. A Viton o-ring was placed on top of the sample to act as a gasket, and a machined polycarbonate piece was placed above the o-ring and secured to the aluminum substrate via through screws to seal the flow cell. pH buffers were flown into the cell via 2 Luer lock adapters through the top of the polycarbonate piece. Once the flow cell was placed on top of the mechanized translation/tilt stage of the LSCM, the sample was aligned so that it rests in a perfectly horizontal position, and the image was focused at the hydrogel/cover slip interface using the reflectance mode of the LSCM. For fluorescence scans, a diffraction grating monochromator limited the collection wavelength range from 550 nm to 700 nm. Care was taken to reduce the laser intensity to minimize photobleaching and hydrogel damage. A series of horizontal scans with 1024 x 1024 pixels were performed with a full field view of 60 μm x 60 μm. Each horizontal scan was separated by a vertical displacement

133

of 203.5 nm. Thus, the raw 3-D voxel size is 58.5 nm x 58.5 nm x 203.5 nm. The orientation of the horizontal scans corresponded to the imaging of FCC(111) planes. pH was adjusted by flushing the cell with an excess of the new pH buffer, and the resulting pH was determined by measuring the effluent pH. A series of horizontal fluorescence scans was performed for each pH. Reconstructions of cross sections along other crystallographic orientations were performed via commercial software (Analyze, Mayo Clinic). From the vertical cross sections, d for each pH was determined and used to calculate the ratio d/d_0.

4.3.2 Finite Element Modeling of Mesostructure Deformation

A parabolic tetrahedral mesh with a maximum element size of 30 nm was applied to an inverse opal structure representing the hydrogel. The symmetry of the inverse opal structure was exploited, and an irreducible triangular prismatic unit cell model was created, with three layers, representing the ABC stacking of the FCC(111) planes. To approximate the real structure of the colloidal template (slight sintering at the contact points), spherical FCC voids with diameter of 256 nm and center to center distance of 250 nm were used. The Arruda-Boyce material model[153] was used since only uniaxial tensile test data were available. The pH dependent mechanical properties of the AA-functionalized hydrogel were adopted from literature.[154] Symmetry boundary conditions were applied to the sides of the triangular prism, while the hydrogel/substrate interface was fixed. A uniform bulk strain was applied to the mesh by applying a thermal strain to the entire model. Bulk strain corresponding to the observed vertical strain was applied to determine the equilibrium pore mesostructure of the hydrogel. The

ABAQUS/Standard geometric non-linear solver was used to solve the finite element model.

4.4 Results and Discussion

4.4.1 Imaging of Hydrogel Mesostructure Deformation

The fluorescence cross section images illustrate the dramatic change in pore morphology as pH was increased and the inverse opal hydrogel swelled. For example, the FCC(111) cross sections for layers not adjacent to the hydrogel/substrate interface showed significant pore shrinkage and deformation as the pH was raised from 3.4 to 6.6 (Fig. 4.1a). As a result of hydrogel swelling, the darker regions corresponding to the water filled pores accounted for a smaller fraction of the total area, suggesting that the pore volume fraction shrinks, as predicted by SWA theory.[21] In addition, the pore cross sections transformed dramatically from a slightly distorted circle at pH = 3.5 to a triangle at pH = 5.0 and finally to a three-pointed star at pH = 6.6 (Fig. 4.1a). We believe that the end points of each three pointed star corresponding to the interconnects between each pore and its three nearest neighbors in the next FCC(111) layer. The interconnects did not fully collapse, probably because there was insufficient hydrogel around these interconnects to swell into the available volume. As we show later, the interconnects also appear to exhibit the highest compressive stress, making them less likely to close. In contrast, the FCC(111) cross section for the layer closest to the interface exhibited much smaller deformation as pH was increased (Fig. 4.1b); at pH = 6.6, the cross section was triangular. The diminished deformation may be a result of substrate pinning due to the covalent linkage between the substrate and the hydrogel and the much higher stiffness of

the glass substrate. Substrate pinning would restrict the swelling of the hydrogel in the

immediate vicinity, thus leading to a smaller magnitude of deformation.
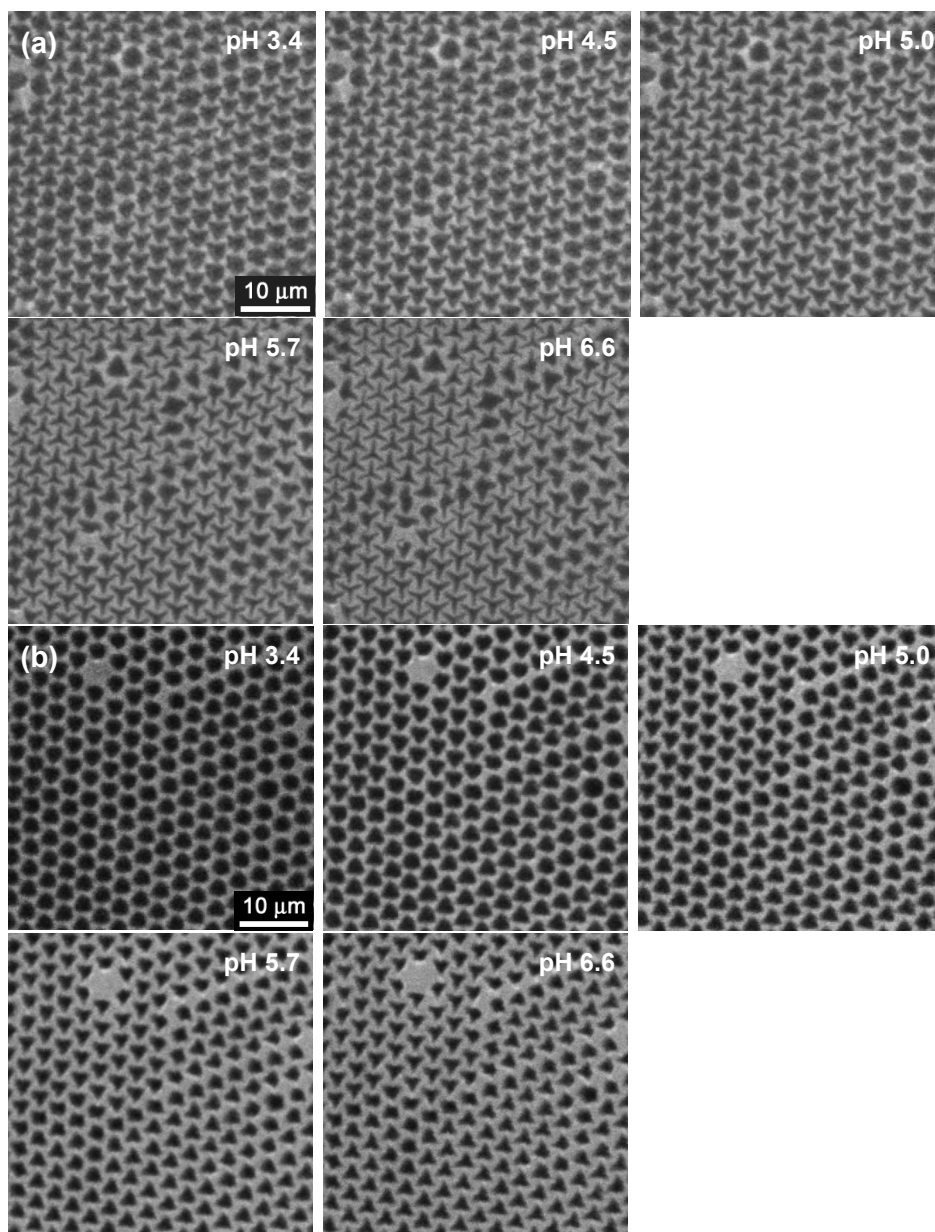
Figure 4.1: pH-induced mesostructure evolution for a 5% AA inverse opal hydrogel imaged with two-photon fluorescence microscopy. (a) FCC(111) cross sections of the hydrogel for the second layer above the hydrogel/cover slip interface at different pH, showing dramatic deformation of pore morphology from a circular cross section at pH = 3.4 to a three pointed star at pH = 6.6. (b) FCC(111) cross sections of the hydrogel for the first layer, showing smaller pore deformation with increasing pH due to substrate pinning. Images acquired by Carla Heitzman.

As the pores deformed from a circular to a triangular cross section during hydrogel swelling, they also developed an orientation which may indicate a change in the crystallographic symmetry. Most significantly, the orientation of the deformed pores alternated as one moves up through the layers of the hydrogel. This is illustrated in Figure 4.2a, which shows the FCC(111) cross sections at pH = 6.5 for the bottom layer and 3 consecutive layers above it. The alternation of pore orientation during hydrogel swelling may correspond to the transformation of the aqueous pores from ABCABC stacking (FCC lattice) to something akin to ABCA'B'C' stacking ($L1_1$ lattice). This lattice transformation is reasonable when examining the spatial distribution of strain within a swollen hydrogel, as shown conceptually in Figure 4.2b. When the pores adopt a $L1_1$ symmetry, the hydrogel deformation is relatively uniform, as illustrated by the schematic diagram in Figure 4.2b, which shows a large number of shared pore boundaries with uniform width when the orientation of the pores alternative between layers. In comparison, if the pores maintained a FCC symmetry while deforming into a triangular cross section, the thickness of the surrounding hydrogel may vary greatly (Fig. 4.2b), suggesting that parts of the swollen hydrogel is under high strain (thick elements), while other parts may be essentially unstrained (thin elements). This difference in strain would result in a spatially varying osmotic pressure inside the hydrogel, causing the regions with positive osmotic pressure (near interconnects) to expand and the regions with negative osmotic pressure (far from interconnects) to contract until the osmotic pressure equaled zero for the entire hydrogel. In other words, the deformation of the FCC pores inside a templated hydrogel and the alternation of their layer-by-layer orientation are qualitatively consistent with the volume expansion in a bulk hydrogel. Finally, the

potential change in crystallographic symmetry induced by hydrogel swelling may also modify the photonic band structure; possible effects on the diffraction response are currently under investigation.

Figure 4.2: Evolution of pore orientation in the swollen inverse opal hydrogel imaged with two-photon fluorescence microscopy. (a) FCC(111) cross sections of the swollen hydrogel at pH 6.6 at increasing layer numbers above the substrate, showing an alternating pore orientation. (b) Schematic of crystallographic transformation from FCC to $L1_1$ (CuPt) symmetry. Images acquired by Carla Heitzman.

Two-photon fluorescence imaging of the inverse opal hydrogels at various swelling ratios also revealed other interesting feature which may help explain the previously observed trends in diffraction peak shape as the diffraction wavelength red shifted. For example, the fluorescence cross sections revealed that disorder became more prominent as the mesostructured hydrogel swelled. At pH = 6.6, more than half of the pores in a 5% AA hydrogel two layers away from the hydrogel/substrate interface exhibited a cross section which appeared irregular (Fig. 4.3a), possibly caused by local buckling of the surrounding hydrogel from inhomogeneous swelling. In addition, the irregularly shaped pores appear with greater frequency near defects and drying cracks of

the original CC template (Fig. 4.1a). Such a result is expected, since the excess hydrogel present near the defects may locally increase swelling, leading to a higher probability of buckling. The effect of the local pore buckling on the uniformity of the interlayer distance (and therefore the diffraction peak intensity I_b) is unclear. However, since diffraction peak parameters are sensitive to the volume fractions of the aqueous pores (Fig.3.19), the local variations in pore volume fraction may impact the ability of the mesostructure to diffract light especially at higher swelling ratios, contributing to the attenuation in I_b as the Bragg diffraction red shifted (Fig. 3.11b). Fluorescence cross sections also revealed that within the same FCC(111) layer, the highly swollen hydrogel also exhibited alternating orientations in pore mesostructure (Fig. 4.3b). Interestingly, defects in the CC template, particularly the line defects, appear to form the boundaries for single domains of inverse opal hydrogel containing the same pore orientation (Fig. 4.3b). These may be analogous to the domain walls and/or antiphase boundaries observed in many materials.[155-158] Thus, drying cracks in the CC template influenced the pore morphology evolution during hydrogel expansion, especially at high swelling ratios.
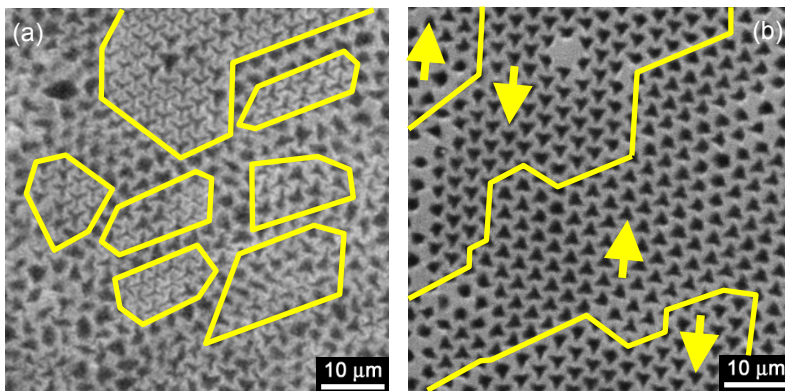
Figure 4.3: Details of mesostructure deformation for a 5% AA hydrogel imaged with two-photon fluorescence microscopy. (a) Increasing predominance of defects in a highly swollen hydrogel (pH = 6.6, layer 3). (b) Development of domain walls in a highly swollen hydrogel (pH = 6.6, layer 1), apparently along line defects in the CC template.

Through software reconstruction, the mesostructure evolution of the swelling hydrogel can be examined in other cryallographic directions. Figure 4.4a shows FCC(-110) cross sections of the inverse opal hydrogel. At pH = 3.4, the expected ABC stacking of spherical pores was observed, consistent with FCC symmetry. As pH was increased, the pores elongated along the sample normal direction, increasing d. At the same time, the pores shrank in the sample parallel direction for layer > 1, indicating that hydrogel was swelling into the pores (Fig. 4.4a). At pH = 6.6, a typical pore did not fully collapse but appeared to have a twisted, elongated rectangular cross section. The FCC(-110) cross sections further reinforces the observation that the pores did not shrink uniformly as the hydrogel around them swelled. Instead, the hydrogel expansion was maximized in regions far away from the interconnects (upper left and lower right corners of each pore in Fg 4.4a), such shape is consistent with the anchoring of the pores by the interconnects, presumably located at the endpoints of each rectangle. Note that as the hydrogel swelled with water as the pH was increased, the depth resolution of the two-photon imaging became enhanced due to decreased refractive index contrast. Also, the center-to-center distance between pores along the sample parallel direction remained essentially unchanged, comparing values from layer 1 to layer 4 as well as varying pH from 3.4 to 6.6 (Fig. 4.4a). In other words, the fluorescence cross sections corroborate the conclusion from microspectroscopy that the increase in interlayer spacing occurred only in the sample normal direction as the hydrogel swelled.
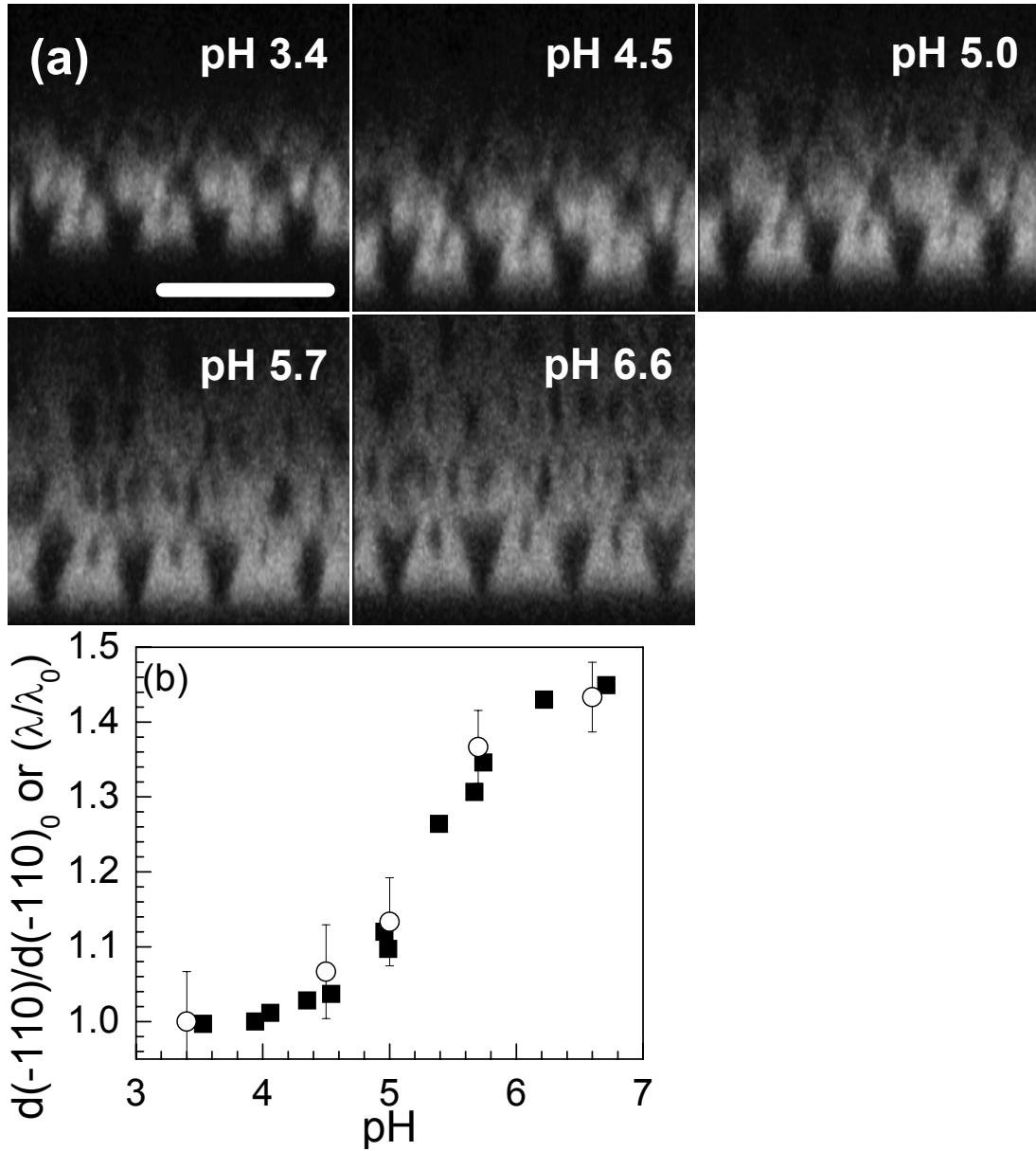
Figure 4.4: pH-induced mesostructure evolution for a 5% AA inverse opal hydrogel reconstructed from two-photon fluorescence microscopy. a) Reconstructed FCC(-110) cross section of the hydrogel at different pH. Scale bar, 10 μm. (b) pH dependence of normalized d(-110) from confocal (circles) and normalized diffraction shift (λ_b/λ_{b0}) (squares), showing essentially identical trends. This suggests that the diffraction response is almost completely due to the change in interlayer distance in the sample normal direction. Images acquired by Carla Heitzman.

To calculate d/d_0 from fluorescence microscopy data, we directly measured the distance between neighboring FCC (-110) layers, d(-110), from Figure 4.4a and normalized with respect to its value at pH = 3.4, d(-110)$_0$. As a side note, it is reassuring

to find that $d(-110)_0 = 3.0$ μm, since the initial interlayer spacing between FCC(-110) planes should be equal to the colloid diameter. After normalization, the ratios calculated from the fluorescence data can be directly compared to λ/λ_0 from microspectroscopy. When plotted as a function of pH, both sets of data essentially overlap each other (Fig. 4.4b), suggesting that the diffraction shift in microspectroscopy is almost entirely a consequence of the increase in interlayer distance due to hydrogel swelling. Also, a maximum $d(-110)/d(-110)_0$ of 1.45 was calculated from the fluorescence micrographs of the hydrogel in pH = 6.6 buffer (Fig. 4.4b). For comparison, untemplated 5% AA hydrogels were infiltrated into glass capillaries ($D \sim 140$ nm) and UV-polymerized, and the glass capillaries were etched with 5% v/v hydrofluoric acid (aq.) for 24 h. The cylinders of 5% AA hydrogel were then placed in a Petri dish containing a phosphate pH buffer. When the pH of the buffer was increased from 3 to 7, the untemplated hydrogel exhibited a swelling ratio of 1.22 in diameter, corresponding to an expansion to 1.83 times its original volume. Assuming that the CC-templated hydrogel increased in volume by the same amount, the maximum $d(-110)/d(-110)_0$ of 1.45 indicated that the inverse opal hydrogel expansion was not limited to increasing interlayer distance, but also contributed to other processes such as swelling into the pores. Assuming the discrepancy between the two values is solely due to the swelling of hydrogel into the pores, a back of the envelope calculation suggested that at pH = 6.6, the FCC pores decreased to 25.4% of its original volume, which is approximately $(1.45)^{-3}$. In other words, the fluorescence microscopy data suggests that the 3-D pore shrinkage model, when used as the input in the scalar wave approximation method, should yield calculated diffraction peak wavelengths (Fig. 3.19b, circles) and normalized FWHMs (Fig. 3.19c, circles) that most

closely match the microspectroscopy results. As Figure 3.19 shows, the 3-D pore shrinkage model gives the best qualitative match in diffraction peak parameters compared to the experimental results, and the quantitative discrepancies may now be attributed to factors such as the deformation of pore morphology and the increase in disorder during hydrogel swelling which were observed by multiphoton fluorescence microscopy.

4.4.2 Comparison with Finite Element Modeling

Applying a thermal expansive bulk strain to the inverse opal hydrogel mesh and constraining the model to expand in the normal direction resulted in pore mesostructure that looked significantly different compared to the fluorescence images. For example, the pore morphology at a strain of ~ 50% in the sample normal direction showed an almost undeformed FCC(111) cross section (Fig. 4.5a). In the FCC(-110) cross section, the pores appeared elongated and twisted, but the finite element model again exhibited little contraction in the sample parallel directions (Fig. 4.5b), indicating that the hydrogel did not swell significantly into the pores at this large bulk strain (equivalent to pH ~ 7). Closer examination showed that the interconnects exhibited very high stresses (red color) compared with other parts of the hydrogel mesostructure. Thus, it is possible that the experimental hydrogel sample actually consisted of two stress states: the interconnects at high stress and minimal swelling, and the rest of the pores at low stress and large swelling. Thus, the true swelling may be a non-linear function of stress, local feature size, and pH, rather than pH alone. Another explanation for the difference between the experiment and the simulation may be that the materials model used for the hydrogel was incorrect. For example, the porous hydrogel mesostructure may decrease Young's modulus compared with the value for the bulk hydrogel which was used in the finite

element simulation.[154]   Also, previous research have found that certain microporous materials are auxetic, where they expand both transversely and along the direction of an applied tensile force.[159-162]   In other words, such materials will exhibit a negative Poisson's ratio.   Since the inverse opal hydrogel contained an array of ordered mesopores, it may also be auxetic, which may cause significant deviations in its mechanical properties compared to the bulk hydrogel.   The material properties may also differ from the bulk material properties in regions where the local feature size is comparable to the molecular characteristic length, such as the hydrogel adjacent to the interconnects between the pores.   Due to these considerations, it may be necessary to directly measure the viscoelastic properties of a CC templated hydrogel to achieve good agreement between the fluorescence micrographs and finite element results.   Finally, the constraints placed on the hydrogel expansion in finite element modeling may cause the simulated mesostructure to deviate significant from the experimental situation.   To force the expansion of the characteristic interlayer distance in the sample normal direction, we placed mirror boundary conditions on the vertical faces of the triangular prismatic unit cell, enforced zero strain at the bottom face (hydrogel/substrate interface), and allowed free expansion at the top face (hydrogel/solution interface).   However, if the hydrogel expansion is such that significant twisting and distortions occur, especially along the vertical faces, then the boundary conditions may no longer be valid.   The small size of the prism relative to the diameter of the FCC pore (Fig. 4.5) may also cause the simulated mesostructure to deviate from the experimental system, although the same simulation performed with a larger unit cell, consisting of four prismatic unit cells stacked so that they form a rhombus when viewed from the top, yielded essentially identical results.

Finally, the parabolic tetrahedral mesh applied to the finite element model may be too coarse-grained to capture the deformation of a hydrogel, even with the large FCC pores. We are currently refining the finite element model in order to more fully capture the buckling behavior of mesostructured hydrogels during swelling.
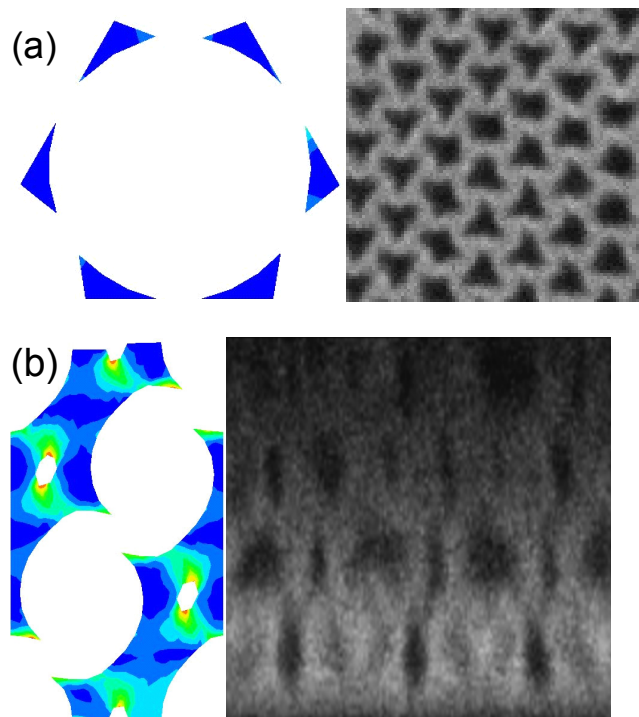
Figure 4.5: Comparison between finite element predictions and fluorescence cross sections of a swollen inverse opal hydrogel. (a) FCC(111) cross section of the deformed inverse opal structure with a strain of 0.5 in the sample normal direction predicted by finite element analysis, compared to the experimental sample with $d/d_0 = 1.45$. Blue (red) regions in the finite element cross sections indicate regions with low (high) compressive stress. (b) FCC(-110) cross section of the deformed hydrogel from finite element analysis, compared to the experimental data. Finite element modeling performed by Walter Frei.

4.5 Summary

We performed two-photon fluorescence imaging on a RhoB-labeled inverse opal hydrogel pH sensor using a LSCM to characterize the pore mesostructure evolution as a function of hydrogel swelling and to compare with trends in the diffraction response using microspectroscopy. From two different cross sections of the distorted FCC

structure, we found that the pores appear to both elongate along the sample normal direction and collapse along the sample parallel directions, consistent with 1-D swelling of the interlayer distance. The interconnects seem to serve as anchor points with little deformation, while the other regions of the hydrogel swelled significantly into the pores. The presence of interconnects may have caused a change of the hydrogel lattice symmetry during deformation, from a FCC ABC packing to possibly a $L1_1$ lattice with ABCA'B'C' packing. Reconstructed FCC(-110) cross sections confirmed that a 1-D increase in the interlayer distance along the sample normal direction was responsible for essentially all of the diffraction response of the hydrogel sensor. Comparison with predictions from finite element analysis showed that the experimental mesostructure was significantly more deformed than the calculated data, indicating that the swollen hydrogel may exhibit multiple stress states or that the viscoelastic and mechanical properties of a periodically mesoporous hydrogel may be significantly different than its untemplated counterpart.

CHAPTER 5

EFFECT OF NUMERICAL APERTURE ON CC DIFFRACTION

Significant components of this chapter were published as "Diffraction from colloidal crystals: effect of numerical aperture", Y.-J. Lee, S. A. Pruzinsky, and P. V. Braun, *Optics Letters*, in press.

5.1 Introduction

The Bragg diffraction of colloidal crystals (CCs) and CC templated materials is often characterized by the specular reflection of incident light in the sample normal direction, both because the experiment is simple to set up and because the FCC(111) crystallographic orientation of CCs on planar substrate results in a large incomplete gap in the ΓL direction in the photonic band structure, even for low refractive index contrast systems. However, since self-organized mesostructures such as CCs always contain point and line defects as well as drying cracks, it is often advantageous to study the Bragg diffraction spectra from a small sampling region of a CC to minimize the effect of the crystallographic defects. We collected the reflection spectra of the inverse opal hydrogels from a circular region with a diameter of ~ 16 μm by focusing the incident light with a microscope objective (in this case, 10x) and coupling the reflected light, collected by the same objective, to a diffraction grating spectrometer through an optical fiber. The diameter of the fiber (~ 400 μm) and the magnification of the objective removes most of the light reflected from outside the region of interest, allowing us to examine the Bragg diffraction from a nominally defect free region of a photonic mesostructure. Such microspectrometer has also been used by others to study single domains of CCs and other photonic crystals,[57,163] and CC-templated

hydrogels.[14,15,19,21]   Vlasov and co-workers studied silica CCs formed by evaporation from ethanol using a microspectrometer and found reflection spectra which matched almost perfectly with calculations, including the peak positions and (to a lesser extent) the intensities of all Fabry-Perot interference fringes.[163] Galisteo-Lopez and co-workers examined PS CCs formed by evaporation from water and was able to distinguish subtle optical features such as the difference in peak shape of CCs deposited on silica versus Si wafers and compare the results to theoretical calculations.[57] Microspectroscopy appears to be an excellent technique for quantifying the Bragg response of CCs which eliminates negative contributions from defects and drying cracks.

In the previous reports examining the Bragg diffraction of CCs using microspectroscopy, the experimental data were compared to theoretical calculations which assumed a perfectly collimated beam of light striking the CC at normal incidence or other well defined angles.[57,163]   In contrast, the focused light used in microspectroscopy causes the CC to be probed with a cone of light with a distribution of angles and a nonzero NA, defined as:

$$NA \; = \; \sin \psi_{max} = \sin \left(\tan^{-1} \left(\frac{d_c}{2h} \right) \right) \tag{5.1}$$

where ψ_{max} is the maximum half-angle of the cone of light, and d_c is the diameter of the cone measured at a distance h away from the focal plane. For example, the experimental reflectance spectra of the inverse opal hydrogels (Chapter 3) were collected with an NA of 0.25. The excellent agreement between the experimental and calculated spectra in the earlier reports suggests that at small NAs, the effect of focusing the light on the Bragg response of CCs is negligible.[57,163]   On the other hand, when the incident light impinges on the sample at a direction which is sufficiently different from the sample

148

normal, the reflection spectra of the CC changes drastically; indeed, one of the aforementioned papers also studied the effect of tilting the sample on the Bragg diffraction of the CC.[57,163] Therefore, it would be beneficial to determine the exact effect of incident and collection light NA on the shape of the Bragg diffraction peak, and to determine if such an effect can be directly compared to calculations.   To this end, we studied the optical response of a PS CC formed by evaporative self-assembly using a microspectrometer where the objective contains a adjustable diaphragm to control NA.

5.2 Synthesis

We formed the PS CC via evaporative self-assembly using a room temperature dip-coating process from Gu and co-workers.[30] We first cut silica glass slides into 12 mm x 38 mm pieces from standard microscope slides (Fisher). The slides were cleaned with hot piranha mixture of 3 parts by volume of H_2SO_4 to1 part by volume of 30% H_2O_2 (aq.) at ~ 100 ºC for ~ 1 hour). The glass pieces were then rinsed thoroughly with water and dried with a N_2 stream. One end of the small glass slide (12 mm x 38 mm) was attached by masking tape to a syringe pump resting in the vertical position (KDS100, KDS). The small glass slide was vertically suspended in a 2% v/v aqueous suspension of 244 ± 7 nm sulfonated PS colloids (Interfacial Dynamics, Co.) in a glass vial (diameter ~ 20 mm) and then withdrawn at a rate of 0.2 μm/s for ~ 16 h, until the slide completely lifted clear of the colloidal suspension. No special care was taken to maintain a constant room temperature or relative humidity.   At the end of the dip coating process, an opalescent CC was formed on the portion of the glass slide that was originally submerged in the suspension. A reasonably uniform CC thickness of ~ 24 layers was achieved, in good agreement with the earlier report.[30]

5.3 Characterization

5.3.1 Microspectroscopy at Different NA

We characterized the Bragg diffraction of the polystyrene (PS) CC as a function of NA by collecting its normal incidence reflectance spectra using the visible-near IR microspectrometer as described in detail in Chapter 3. Briefly, light reflected from the sample was collected by an inverted optical microscope (Axiovert 135, Zeiss) and coupled to an diffraction grating spectrometer (Control Development, Inc.) by an optical fiber (D = 400 μm). The optical fiber acts effectively as a pinhole by collecting only the reflected light that falls within its diameter. Reflectance spectra were collected using two objectives (Acroplan 5x 0.12 NA and Neofluar 20x 0.5 NA, Zeiss), corresponding to sampling spot diameters of 32 and 8 μm, respectively. All reflectance spectra were normalized to a front-silvered mirror (Edmund) for 100% reflectance and to air for 0% reflectance. The NA was controlled by mounting a calibrated iris diaphragm (Thorlabs) below each objective and varying the iris diameter from 8 mm to 1 mm in 1-mm increments. The effective NA values for each iris diameter were determined following Eq. 6.1 by focusing on a 400 μm pinhole and measuring the dimensions of the transmitted cone. We also examined the diameters of the diaphragm that were initially mounted at the back of the 5x and 20x objectives (10 mm and 8mm respectively) and correlating them with the stated NA values (0.12 and 0.50 respectively) to determine h for each objective. When the values of h were used to calculate the expected NAs at different iris diaphragm diameters, we found that the measured and expected NA values differed by less than 10%.

From the reflectance spectra of the PS CC at different NAs, several parameters of the strong peak corresponding to first order Bragg diffraction were determined. Peak intensity (I_b) was normalized by subtracting a constant background intensity I_{bg} from the reflectance spectra and dividing the resulting maximum reflectance by $(1 - I_{bg})$. The wavelength corresponding to I_b was selected as the diffraction wavelength (λ_b). The wavelengths at $I_b / 2$ were identified in order to calculate the normalized full width at half maximum ($FWHM/\lambda_b$). Peak asymmetry (A_b), defined as $[(\lambda_{max} - \lambda_b) / FWHM - 0.5]$, where λ_{max} is the wavelength at half maximum on the longer wavelength side of the peak, was also calculated. We also used the Fabry-Perot interference fringes visible from reflectance spectra with NA < 0.3 to calculate the CC thickness using a published procedure.[56] By plotting the maxima of these interferences fringes and inputting the refractive indices of PS (n = 1.592) and air (n = 1), we determined the CC thickness to be 4.8 μm, or ~ 24 layers of colloids. Finally, reflectance optical micrographs were captured with an optical microscope (DMR, Leica) equipped with a digital camera.

5.3.2 Theoretical Calculation of NA Dependence

To determine the effect of NA on the theoretical diffraction response of the PS CC, we first calculated the reflectance spectra from perfectly collimated light at specific incident angles ψ. We used the layered Korringa-Kohn-Rostoker (KKR) method,[164] which approximates the CC as a Bragg stack with spherical scattering conditions. For the calculation, a 20-layer stack of PS spheres (n = 1.592) in air on a silica substrate (n = 1.51) and ψ values between 0° and 30° at 0.5° increments were used. To construct the effective theoretical reflectance spectra for each NA, we used a weighed summation of the individual reflectance spectra for the angles enclosed in the cone of light

corresponding to the NA. Specifically, we multiplied the spectra for each ψ by its corresponding normalized solid angle and then summed up the weighted spectra. This weighing scheme is described below in greater detail.

We first modeled the light reflected from a focused spot on a substrate as a cone of light with constant intensity I for all angles. Assuming we have a cone with the focal point at the origin and spreading out in the positive z direction, the total flux of light Φ passing through this cone of light then is equal to $I\Omega$. In this case, Ω is the solid angle, or the normalized surface area of an imaginary sphere that the cone of focused light cuts through, with the focal point at the center of the sphere. We then calculated Φ as:

$$\Phi = I\Omega = I\iint_S \frac{\hat{n} \cdot da}{r^2} = I\iint_S (\sin\phi)d\theta d\phi \qquad (5.2)$$

Here, n is the normal unit vector pointing from the origin, da is the differential area of a small patch on the surface, r is the distance from the origin (focal point) to the patch. Eq. 5.2 is expressed in spherical coordinates where ϕ is the polar angle (angle from the z-axis), and θ is the azimuth (the longitude). By substituting ψ_{max} for ϕ, we get:

$$\Phi = I \int_0^{\psi_{max}} \int_0^{2\pi} (\sin\phi)d\theta d\phi = -2\pi I(\cos\psi_{max} - \cos(0)) = 2\pi I(1 - \cos\psi_{max}) \qquad (5.3)$$

Thus, if the above assumption of constant light intensity at all incident angles is valid, the total flux (counts) of light should be a linear function of $(1 - \cos \psi_{max})$, which is indeed the case, as shown by Fig. 5.1.
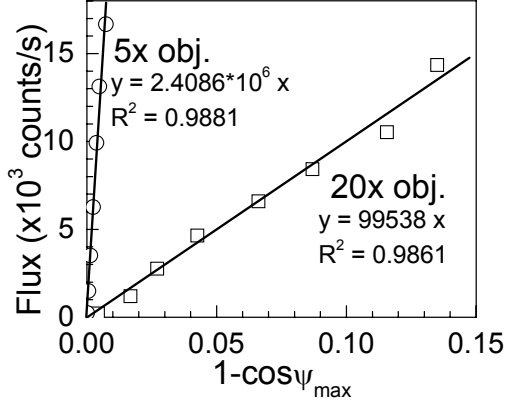
Figure 5.1: Relationship between the background-subtracted flux reflected from a front-silvered mirror and $(1 - \cos \psi_{max})$ using 20x (squares) and 5x (circles) objectives. The lines are least square for linear fits of the data going through the origin. The linear relationship between total flux and $(1 - \cos \psi_{max})$ suggests that the light intensity is constant as a function of ψ, allowing us to use the weighing scheme described in the text.

As mentioned previously, using the layered KKR method, we calculated the reflectance $r = I / I_0$ for each angle ψ, where I and I_0 are the reflected and incident intensities at angle ψ, respectively. To calculate the reflectance $R = \Phi / \Phi_0$ for a cone of light, we multiplied the contribution from each intensity by its corresponding slice of the solid angle and then summed up all the contributing fluxes. Finally, we need to divide the total reflected flux by the total incident flux. For every i^{th} angle ψ_i where we have calculated a reflectance spectra by layered KKR, the minimum angle that define the corresponding solid angle can be approximated by using the midpoint of ψ_i and the next smaller angle ψ_{i-1}. Similarly, the maximum angle of the corresponding solid angle is the midpoint between ψ_i and ψ_{i+1}. Then R was calculated as:

$$R = \frac{\int I d\Omega}{\int I_0 d\Omega} = \frac{\int r d\Omega}{\Omega} \cong \frac{\sum_i r_i \Delta\Omega_i}{\Omega} = \frac{\sum_i r_i \left(\cos\left(\frac{\psi_i + \psi_{i-1}}{2} \right) - \cos\left(\frac{\psi_i + \psi_{i+1}}{2} \right) \right)}{1 - \cos\psi_{max}} \quad (5.4)$$

There are two special cases to this approximation. For $\psi_{max} = 0°$, R diverges according to Eq. 4. In this case, we set R to be the reflectance value calculated from layered KKR at ψ

= 0°. Second, for the reflectance spectra calculated at the minimum (maximum) $\psi = 0°$ (30°), the angle itself is used in Eq. 4 to calculate the contribution to the solid angle, since no smaller (larger) angle exists for finding the midpoint. In other words, contributions from the reflectance spectra at $\psi = 0°$ and 30° will count roughly half as much as would be expected. Thus, by using this averaging scheme, R for each ψ_{max} (and thus NA) was reconstructed from the individual reflectance spectra calculated from KKR. The peak parameters as a function of NA were extracted from these calculated and weighed reflectance spectra in the same way as described for the experimental data.

5.4 Results and Discussion

Under a reflected optical microscope, the PS CC exhibited an orange-yellow color due to Bragg diffraction of light from planes of colloids (Fig. 5.2a) Drying cracks are clearly visible as dark lines, which divided the CC into domains of ~ 15 μm x 15 μm. There were also slight variations in the coloration of the CC, suggesting that other crystallographic defects exist within the CC (Fig. 5.2a). The reflectance of the PS CC shows a strong main peak, (Fig. 5.2b) and the diffraction wavelength λ_b of ~ 580 nm matched well with the color observed in the optical micrograph. As the NA increased, the diffraction peak gradually increased in intensity and blue shifted in position. At the highest NA of 0.5, the peak also broadened in shape while the intensity decreased slightly. For NA < 0.3, periodic oscillations in reflectance intensity were evident (Fig. 5.2b), and were attributed to Fabry-Perot interference fringes of light reflected from the top and bottom interfaces of the CC.[56] The Fabry-Perot interference fringes disappeared at high NA, presumably because the large spread of incident light angles smears out the constructive interference conditions at individual angles.
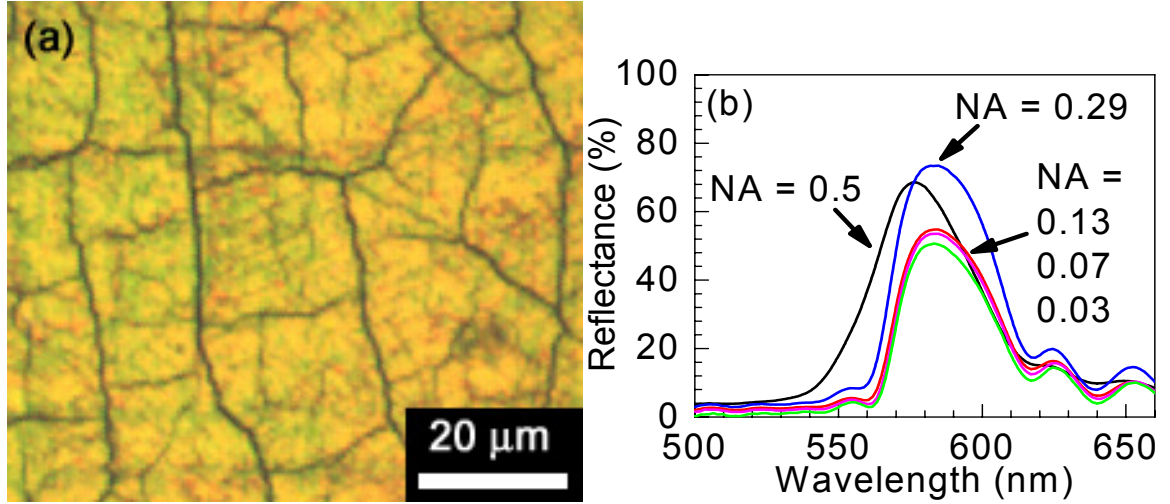
Figure 5.2: Visual and spectroscopic properties of a PS CC. (a) Reflection micrograph of a PS CC (D = 244 nm) in air. Bragg diffraction from FCC(111) planes leads to reflection of yellow-orange light (NA = 0.13). (b) Experimental reflectance spectra of the CC at various NA.

The theoretical reflectance spectra of the CC calculated using the layered KKR method are plotted in Figure 5.3a for values of ψ of 0° to 30° at 5° increments. The rounded tophat shape of the peaks and nearly unity I_b indicate that a perfectly ordered 20-layer CC is an efficient Bragg reflector. After the weighed summation, the effective theoretical reflectance spectra (Fig. 5.3b) exhibited qualitatively similar peak shapes and NA dependence to the experimental data (Fig. 5.2b), broadening and blue shifting as the NA increased. In contrast to the experimental spectra, the theoretical Bragg diffraction exhibited high I_b values even at the NA = 0.03. Also, the Fabry-Perot interference fringes became significantly less pronounced at high NA, although they did not completely disappear as was the case for the experimental spectra. Finally, the photonic band structure of an infinite CC was calculated in the ΓL direction (corresponding to FCC <111>) with a plane wave expansion method (PWE) (Fig. 5.3c).[28] The width of the partial gap in photonic band structure can be compared to the FWHM of the both the experimental and theoretical reflectance peak at the lowest NA.

155
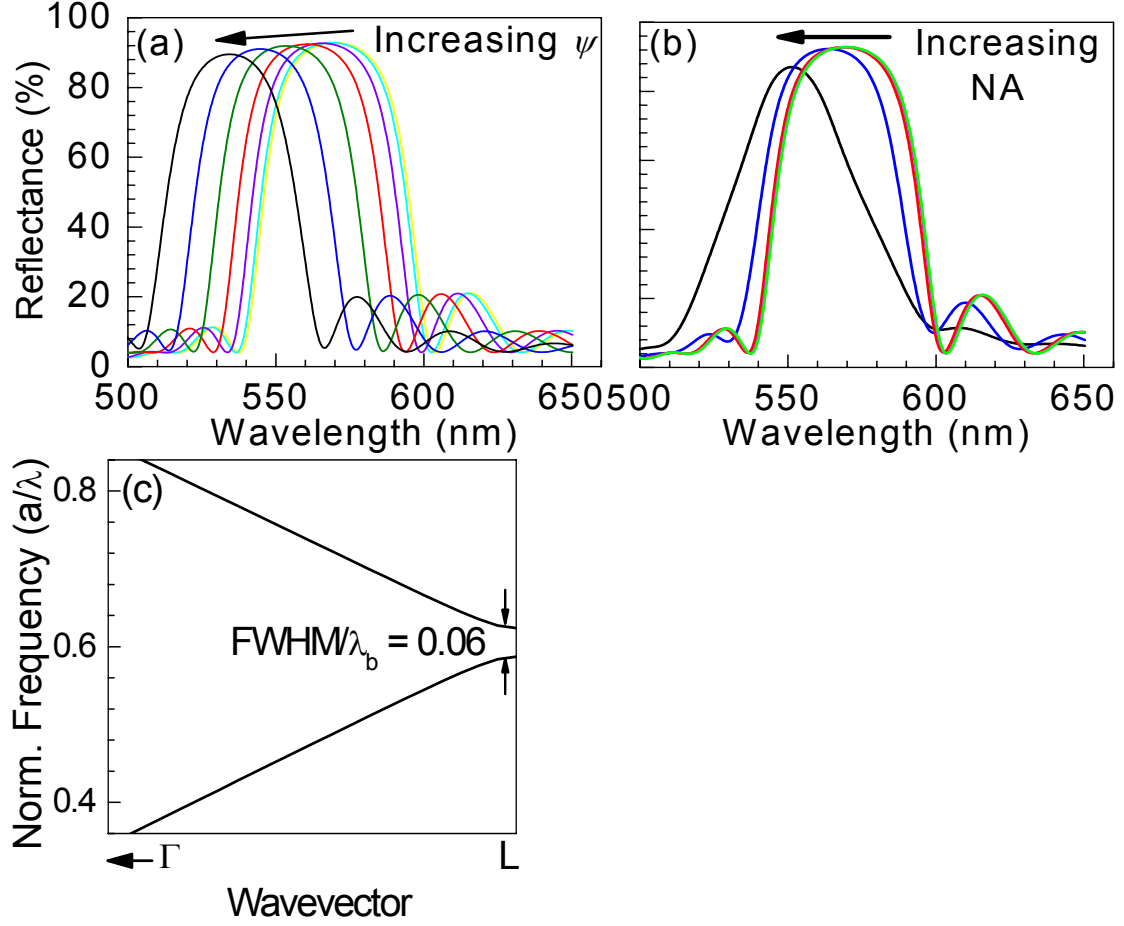
Figure 5.3: Calculated reflectance spectra and photonic band structure of the PS CC. (a) Theoretical reflectance spectra of the CC from layered KKR for $\psi = 0°$ to 30° displayed for 5° increments. (b) Effective reflectance spectra after weighting, with the same NAs as in Fig. 1b. (c) Partial photonic band structure of an infinite CC from PWE, with $FWHM/\lambda_b$ extracted from the width of the stop band. KKR calculations performed by Stephanie Pruzinsky.

The diffraction peak parameters generally exhibited a weak dependence on NA that became stronger for NA > 0.3. As shown in Figure 5.4a, the experimental λ_b essentially remained constant for NA < 0.3, and then blue shifted at higher NA (Fig. 5.4a, squares). This trend qualitatively agrees with theory, both from the layered KKR (Fig. 5.4a, circles) and from applying the same weighting scheme to Eq. 1 to predict λ_b (Fig. 5.4a, triangles). From the frequency at the center of the ΓL stop band (Fig. 5.3c), we found the normal incidence λ_b from PWE to be 570 nm, very close to that determined

from layered KKR (Fig. 5.4a, circles), and within ~ 2% of the experimental value. The predicted $FWHM/\lambda_b$ also remained approximately constant for NA < 0.3 and displayed good qualitative agreement with the experimental results (Fig. 5.4b). $FWHM/\lambda_b$ from PWE (0.06) matched closely with the experimental value for the smallest NA of 0.017 (0.062, Fig. 5.4b). There was a greater discrepancy between the experimental and theoretical NA dependence for I_b and A_b. While both experimental and theoretical I_b decreased for NA > 0.3, only the experimental I_b decreased at low NA (Fig. 5.4c, solid squares). The experimental peak shape was asymmetric throughout the entire NA range (Fig. 3d, squares). In contrast, the KKR-derived peaks were nearly symmetric (A_b = 0.02) for NA < 0.3 and became slightly more asymmetric as NA was increased (Fig. 5.4d, circles).

The discrepancies between experimental and theoretical peak parameters may be attributed to factors such as defects in the CC, drying cracks, and limitations in computational methods. Theoretical methods such as KKR and PWE generally assume a perfect CC, while the real sample contains point and line defects, stacking faults, and drying cracks (Fig. 5.2a). Since λ_b corresponds to the characteristic spacing between planes of colloids, it is relatively insensitive to local disorder, leading to the quantitative agreement in Figure 3a. We found that $FWHM/\lambda_b$ for several different spots on the CC were identical within experimental error, similar to other reports,[57] suggesting that local variations in packing also do not significantly impact $FWHM/\lambda_b$. Although experimental and KKR-derived $FWHM/\lambda_b$ agree qualitatively in their dependence on NA, their values differ quantitatively (Fig. 5.4b). This may suggest that the approximation in KKR of a CC as a dielectric stack with spherical scattering[164] may not capture the

behavior of a CC as completely as the PWE method (Fig. 5.3c). The qualitative

agreement in the NA trends, however, suggests that KKR gives a reasonable

approximation for the Bragg response of a low photonic strength CC.
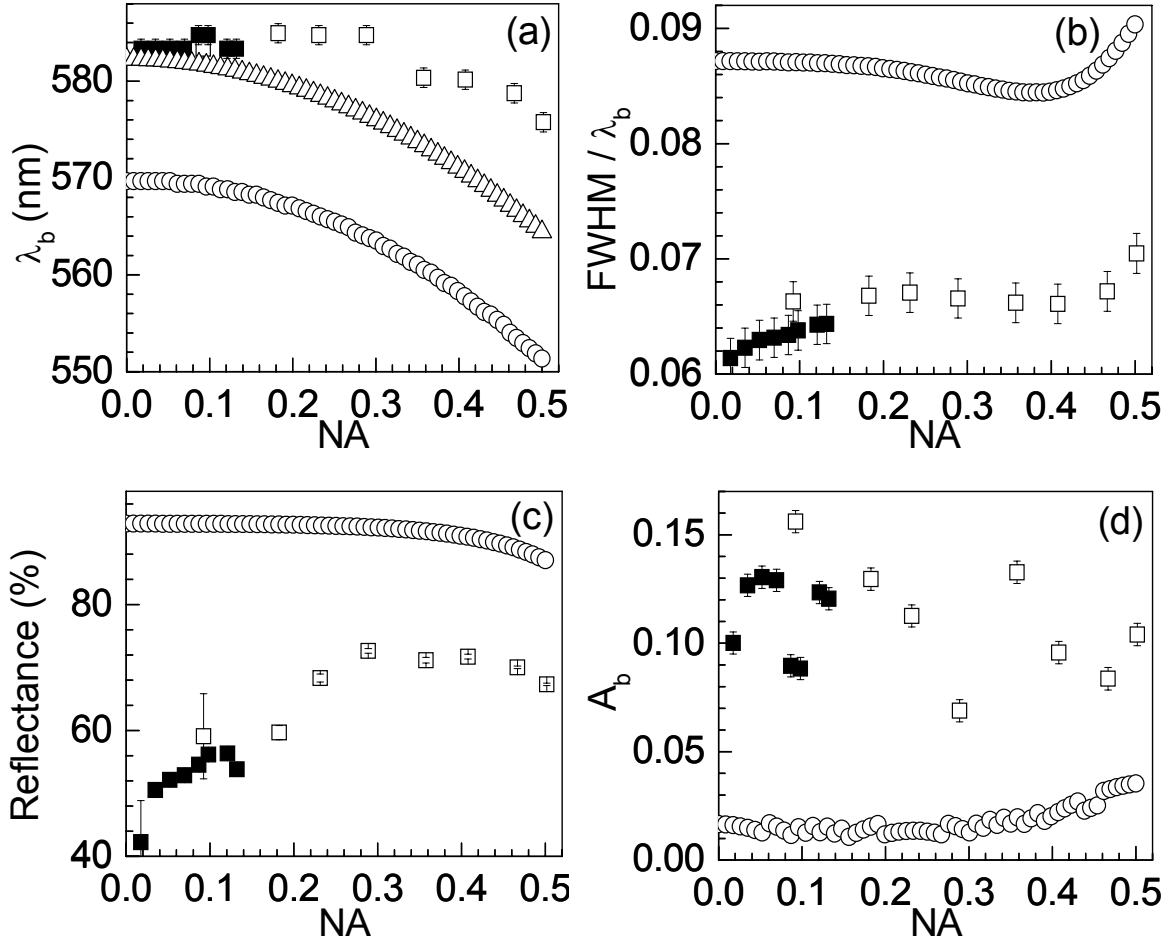
Figure 5.4: NA dependence of diffraction peak parameters from the PS CC (squares), layered KKR calculation (circles), and Bragg equation (triangles). (a) Diffraction wavelength. (b) Normalized FWHM. (c) Peak intensity. (d) Peak asymmetry. Open (solid) experimental data were collected with 20x (5x) objective.

It is well known that I_b values of real CCs are universally lower than theoretical

predictions, presumably due to disorder.[57,163,165] Recently, Koenderink and Vos

reported that disorder in real photonic crystals causes the diffracted light to propagate in a

range of angles around the direction of specular reflection.[59] Since our illumination

and collection NA are the same, some of the light reflected from the CC may not be

collected, possibly explaining the attenuation in experimental I_b at low NA (Fig. 5.4c). Scattering from drying cracks may also decrease I_b for the lower NA data collected with the 5x objective (Figs. 5.4c, solid squares), since the corresponding spot size (32 μm) was larger than the average domain size. Finally, in contrast to the nearly symmetric shape of the KKR-derived peaks for any ψ (Fig. 5.3a), the experimental spectra are asymmetric even for the lowest NA, corresponding to $\psi_{max} \sim 1°$ (Fig. 3d, solid square). We do not yet completely understand the asymmetry, and plan to investigate this further.

5.5 Summary

Microspectroscopy of small sampling spots on photonic crystals can circumvent issues such as defects and irregularities that may arise during the fabrication of the periodic mesostructures, which was an significant problem for self-assembled CCs and materials templated from CCs. The Bragg response could be collected from single domains of well-ordered regions, allowing the characterization of only the response of the PCs and also quantitative comparison of their quality with theoretical predictions. However, it was unclear if the focused nature of the probe light complicates the interpretation of the spectroscopic data, due to the dependence of the PC response on the incident angle. Thus, we studied the experimental Bragg diffraction of a PS colloidal crystal probed with a cone of light via an microscope objective and compared it with theoretical results calculated with layered KKR and PWE. Good qualitative agreement was found between the experimental and theoretical NA trends, especially for the peak position and normalized FWHM. The blue shift in the peak position and the broadening of the peak shape as NA was increased from 0.03 to 0.5 were observed both in the experimental reflectance spectra and the reconstructed theoretical reflectance spectra. In

addition, the Fabry-Perot interference fringes were attenuated as the spread of incident angles increased. Such agreement shows that a low refractive index contrast photonic crystal probed with a cone of light exhibits a Bragg response that can be approximated as the weighed sum of the calculated Bragg response from individual angles, up to a maximum angle of at least 30º (NA = 0.5). Quantitative discrepancies in the peak intensity and the peak asymmetry may be attributed to defects, drying cracks, and limitations in the computational methods. For example, scattering of the incident light from real, imperfect colloidal crystals may cause a decrease in the light reflected from the CC that can be sense by the detector, potentially explaining the attenuation of the experimental peak intensity, especially at very small NA values. As a whole, we found that the Bragg diffraction response was relatively insensitive to NA < 0.3 and can thus be directly compared to normal incidence calculations. As a result, microspectroscopy is an attractive technique with high spatial resolution and good signal-to-noise for the characterization of CCs and other low photonic strength mesostructures.

CHAPTER 6

CC TEMPLATING OF METALS

6.1 Introduction

3-D metallic photonic crystals have attracted research interest due to their interesting and sometimes unique PBG properties. Interactions between photons and mesostructured metals can lead to interesting phenomena such as absorption/emission of selective frequencies,[42,166,167] surface plasmon resonance,[168-170] and negative refractive index,[171] potentially enabling new applications for metallic PCs. Theoretical calculations have predicted that 3-D metallic PCs may exhibit larger PBGs compared to dielectric PCs.[172,173] In particular, Sigalas and co-workers suggested that 3-D metallic PCs consisting of isolated metallic scatterers embedded in a dielectric medium should behave like dielectric PCs, while continuous metallic PCs should exhibit PBG behavior above a certain cutoff frequency.[172] Moroz later indicated that an ordered array of metallic nanoparticles inside a dielectric medium (e.g. CC self-organized from monodisperse Au-SiO$_2$ core-shell colloids) may exhibit full PBG between the second and third bands at visible wavelengths due to surface plasmon resonance.[174,175] Fan and co-workers simulated the optical response of Au spheres embedded in Teflon and discovered a partial PBG if the Au array was FCC and a full PBG if the Au array was diamond cubic.[173] Earlier experimental reports utilized lithography and micromachining to generate a variety of 3-D metallic PCs including Au in Teflon,[176] wire meshes[166], woodpiles[177], and arrays of metallic cubes.[178] All of these PCs exhibited attenuation in transmittance in good agreement with simulations. In several reports, the wavelength range of attenuation was tuned by varying parameters such as the

dimensions of the metallic elements[178] and inclusion of defects.[177] However, most of the earlier 3-D metallic PCs operated in the microwave region due to limitations in fabrication techniques. More recently, researchers at Sandia fabricated woodpile structures of W in air with characteristic dimensions on the order of 1-5 μm using lithography and demonstrated a large PBG in the infrared region.[42] The W PCs also exhibited strong absorption at selective wavelengths that was attributed to an enhanced photonic density of state in the metallic mesostructure at the corresponding frequencies, and this effect has been utilized to induce emission of narrow bandwidth blackbody radiation[167] and to fabricate higher efficiency IR photovoltaic cells[179] using 3-D metallic PCs. They also modeled the transmission and reflectance spectra of the woodpile metallic PCs with different rod thicknesses and found excellent agreement between theoretical predictions and experimental results.[180] Thus, lithographically fabricated metallic PCs have successfully demonstrated the existence of PBGs as well as interesting optical effects due to dispersion and absorption of light by metals.[181]

3-D metallic mesostructures can also be fabricated using colloidal crystal templating. The metal can be deposited using a variety of techniques, including electroless plating inside CC seeded with the appropriate metal nanoparticles,[182,183] high temperature calcination of metal oxalate salts in a H_2 atmosphere,[184] direct infiltration of metal nanoparticles into CCs during self-assembly,[185,186], chemical vapor deposition,[187] and electrodeposition inside CCs and/or inverse opals.[188-193] The CC templated metals exhibit several interesting physical and optical properties. Inverse opal metals synthesized from electroless deposition and high temperature calcinations exhibited high specific surface areas (10-100 cm^2/g),[182,184] making them

potentially attractive as catalytic materials with large accessible pores. Arrays of Au nanoparticles packed inside CCs during CC formation increased the sensitivity to a model organic molecule during surface-enhanced Raman spectroscopy (trans-1,2-bis(4-pyridyl)ethylene) by a factor 10^4 over uncoated glass substrates and by a factor of 10 over randomly distributed Au nanoparticles on glass, due to the order of the FCC pores and the high surface area of the close-packed nanoparticles.[186] FCC arrays of Ni electrodeposited inside a polymethyl methacrylate inverse opal exhibited higher magnetic coercivity values than bulk Ni.[192]

In contrast, the PBG properties of CC templated metals were generally not studied in detail until recently. Bartlett and co-workers examined the optical properties of CC templated films of Pt, Au, and Ag (D = 700 nm) with thicknesses less than one monolayer of colloids and found a characteristic dip in reflectance at a wavelength just below D, which they attributed to surface plasmon grating-like behavior.[193] In addition, they found periodic dips in reflectance for films thickness than 1/4 of a monolayer that corresponded to Fabry-Perot interference of light reflected from the top of the film and the light reflected from within the partial spherical cavities.[193] Very recently, von Freymann and co-workers studied the optical properties of inverse opal W films grown via chemical vapor deposition where the thickness of the W shell was varied by adjusting the reaction time.[187] They discovered that, as the W shell thickness increased, the visible-near IR reflection spectra quickly shifted from a strong single peak due to Bragg diffraction of the bare CC, to Fabry-Perot interference fringes at intermediate W shell thickness, to an essentially featureless spectra with a single small dip due to surface plasmon resonance when the inverse FCC voids were completely filled

with W. They attributed the disappearance of the Bragg diffraction features to the high absorbance of W at visible and near-IR wavelengths.[187]. In comparison, the woodpile W PC used by the Sandia group exhibited PBG at ~ 5 μm,[42,167,179,180] where the reflectance of W is greater than 90%.[181] Thus, for the fabrication of CC templated metallic PCs where the light interacts with the entire mesostructure, one must carefully control parameters such as CC diameter, thickness of the metal infiltrated into the inverse FCC regions, roughness of the metal film, and the optical constants of the metal at the wavelengths of interest. To generate solid metallic films of controlled thickness and good surface roughness, we utilized electrodeposition to infiltrate metals into CC templates. Au, Cu, and Ni were selected as candidates for CC template, because they generally exhibit high reflectance in the visible and near-IR wavelengths.[181] In addition, all three metals have melting point T_m of > 1200K.

The flux of radiation (Φ) emitted from a black body at a temperature (T) is calculated by the well-known Stefan-Boltzmann law:

$$\Phi \cong \varepsilon \sigma T^4 \tag{6.1}$$

where ε is the emissivity of the blackbody and σ is the Stefan-Boltzmann constant. The emission curve of this blackbody reaches a maximum value at a wavelength (λ_{max}) which can be predicted by Wien's Displacement Law:[194]

$$\lambda_{\max} T \cong 2.898 \times 10^{-3} \, \mathrm{m} \cdot \mathrm{K} \tag{6.2}$$

Thus, to maximize the flux of light emitted from metallic PC at a specific wavelength λ, T should be increased. To further maximize the efficiency of emission, the dimensions of the metallic PC should be controlled so that $\lambda \sim \lambda_{max}$. Therefore, to maintain the

mechanical stability at the high temperatures required, high T_m is an attractive feature for CC templated metal films.

6.2 Synthesis

6.2.1 Colloidal Crystal Formation

PS CCs with values of D on the order 1 μm were fabricated on two types of conducting substrates via evaporative assembly.[56] ITO on glass substrates (ITO thickness = 100 nm, Delta Technologies) were cut into 25 mm x 8 mm pieces, cleaned by submerging them in 20% v/v ethanolamine (Acros) in DI water (Millipore) at 80 °C for 30 minutes, and dried under flowing N_2. Thin films of Au (100 nm) on Cr (10 nm) were thermally evaporated on 1 mm thick glass slides (Fisher) using a commercial vacuum evaporator (DV-502A, Denton). The Au-coated slides were also cut into 25 mm x 8 mm pieces, cleaned with ethanol rinse, and dried under N_2. We found that when the Au slides were placed in colloidal suspensions, there was no CC formation because water did not wet the Au surface. Therefore, the 25mm x 8 mm Au slides were treated in 2 mM mercaptopropionic acid in ethanol for 30 minutes to render them more hydrophilic, cleaned with ethanol rinse, and dried under N_2. A ITO or Au slide was placed against the side wall of a 20 mL scintillation vial filled with ~ 5 mL of 0.4% v/v PS colloidal suspension in water (Interfacial Dynamics), with the conducting sides facing toward the center of the vial. The scintillation vial was then inserted in a dry bath incubator (Isotemp 125D, Fisher) filled with sand and heated to 55 °C. The scintillation vial (and slide) rested either vertically or at ~ 45° to vertical (conducting side facing up). After water was evaporated over about 24 h, opalescent CCs of 10 to 20 layers in thickness were formed on the ITO and Au slides. We found the average thickness of a CC was

inversely proportional to D, similar to previous reports,[56] and CCs with $D \leq 1.5$ μm can be formed via the evaporative process. To improve their mechanical stability, CCs were sintered at 85 °C for 2 hrs inside a glassware oven.

6.2.2 Electrodeposition of Metals

6.2.2.1 Nickel

Ni films were electrodeposited through the CC templates using published procedure.[192] A commercial nickel sulfamate solution (Techni S RTU, Technic) was used for all Ni electrodeposition. A 20 mL scintillation vial was filled with the Techni S solution. One end of the CC-containing slide was covered with Cu tape (3M) to improve current conduction. To prevent the CC from flaking off due to the high surface tension of water, the CC-containing slide was dipped in ethanol for ~ 1 minute, in water for ~ 1 minute, and then in the electroplating solution. Using a potentiostat/galvanostat (263A-2, Princeton Applied Research) Ni was electrodeposited galvanostatically at 0.8 mA / cm^2 for 4 hours, with a Pt flag (area = 1 cm^2) as the counter electrode. No agitation of the electroplating solution was performed to prevent delamination of the CC from the substrate. The total charge density of 3000 mC / cm^2 should yield a dense film of 1 μm thickness, or a 4 μm inverse opal film, assuming 100% coulombic efficiency. After electrodeposition, the electrode was removed from the electroplating solution, gently rinsed with water to remove undeposited metal ions, and then submerged in tetrahydrofuran (Acros) overnight to dissolve the PS CC template.

6.2.2.2 Copper

Cu films were electrodeposited galvanostatically on CC on Au using a CuSO$_4$ solution. The Cu electroplating solution were prepared by mixing CuSO$_4$·5H$_2$O (4 g, Fisher),

H$_2$SO$_4$ (11 mL, Mallinkrodt), HCl (25 μL, Fisher), a commercial stabilizer (0.75 mL, Cu 2300 Carrier, Technic), and water (60 mL). We found that the H$_2$SO$_4$-containing electroplating solution dissolved ITO, and thus only CC/Au substrates were used for Cu deposition. Many current densities were tried based on recommendations from the manufacturer. We found that a current density of 3 mA / cm^2 generated an inverse opal film with the most uniform thickness (see section 6.4.3 for details). All other electrodeposition details were identical to the Ni process.

6.2.2.3 Gold

Au films were electrodeposited galvanostatically on CC on Au using a commercial HAuSO$_4$ electroplating solution (Gold 25 RTU, Technic). Au deposited on CC on ITO showed poor adhesion to ITO and lifted the CC template off the ITO substrate, and thus CC on ITO was not used for electrodeposition of Au. A current density of 0.5 mA / cm^2 was used, and a total charge density of 2000 mC / cm^2 should yield a dense film of 1 μm thickness, or a 4 μm inverse opal film, assuming 100% coulombic efficiency. All other electrodeposition details were identical to the Ni process.

6.2.3 Wet Chemical Etching of Inverse Opal Ni

The mesostructure of inverse opal Ni films were modified after electrodeposition through wet chemical etching with a commercial Ni etchant (Nickel TFG, Transene). We diluted the etchant by a factor of 4 and performed the etching at room temperature to reduce the etching rate to ~ 1 A / s. The inverse opal Ni was submerged for up to 30 minutes with no stirring or gentle stirring at 300 rpm on a stir plate (Fisher).

6.3 Characterization

6.3.1 Scanning Electron Microscopy

The mesostructure of electrodeposited and etched inverse opal metal films was examined directly with a standard scanning electron microscope (6060LV, Jeol) at an accelerating voltage of 30 kV.

6.3.2 Optical Microscopy

Optical micrographs of the inverse opal metals in reflection were captured on an inverted optical microscope (DMR, Leica) equipped with a digital camera using a 50x objective (Leica).

6.3.3 Microspectroscopy

The standard visible-near IR microspectrometer was described in detail in Chapter 3. Briefly, light reflected from the sample at normal incidence was collected by an inverted optical microscope (Axiovert 135, Zeiss) and coupled to an diffraction grating spectrometer (Control Development, Inc.) by an optical fiber (D = 400 μm). The objective used (Acroplan 10x, Zeiss) and the fiber diameter limited the analysis spot size to a circle with D = 16 μm.

6.3.4 FT-IR Microspectroscopy

The FT-IR reflectance microspectrometer consisted of a standard FT-IR spectrometer (Nicolet Nexus 6700, Thermo Electron) with the light input port coupled to a homemade IR microscope mounted on a micrometer stage on top of an optical table (Fig. 6.1). In the normal reflectance mode, the blackbody radiation of a light source was focused by an Au-coated off-axis parabolic mirror (90º, D = 25.4 mm, f = 50.8 mm, Janos Technologies) and reflected from a beamsplitter to the intermediate image plane

(pinhole, Fig. 6.1). The light was then focused by the IR objective into a spot on the sample, and the reflected light was collected by the same objective and sent to the FT-IR spectrometer. Fine focus is achieved by turning the knob on the manual micrometer stage. The sample stage itself was mounted on a two-axis mechanized micrometer stage (Zaber), resulting in full 3-D translation of the objective with respect to the sample. Transmission microspectroscopy can be perfomed by moving the location of the light source, but was not done because the metal film thickness (~ 10 μm of inverse opal) resulted in essentially 0% transmittance. To maximize the collection of normal reflectance light at the expense of resolution and larger aberrations, we replaced the standard reflective objective with a simple refractive IR objective consisting of a planoconvex ZnSe lens (D = 12.7 mm, f = 25.4 mm, ISP Optics) mounted inside a lens tube, with a magnification of 5.0x. We discovered that the Al pinhole resulted in significant stray reflection of the incident light, and thus sample spot size was controlled by using a microspot MCT (mercury cadmium telluride) detector with a built-in 500 μm pinhole, corresponding to a sample spot diameter of ~ 900 μm. Depending on the wavelength range being probed, a different set of light source and beamsplitters, both external and inside the FT-IR spectrometer, was used. For λ = 1 – 4 μm ("near IR"), the setup consisted of a tungsten lamp (Thermo Electron), a quartz internal beamspliiter (Thermo Electron), and a CaF_2 external beamsplitter (ISP Optics). For λ = 2 – 10 μm ("mid IR"), it was a globar light source (Thermo Electron), a Ge-coated KBr internal beamspliiter (Thermo Electron), and a double polished Ge wafer as an external beamsplitter.
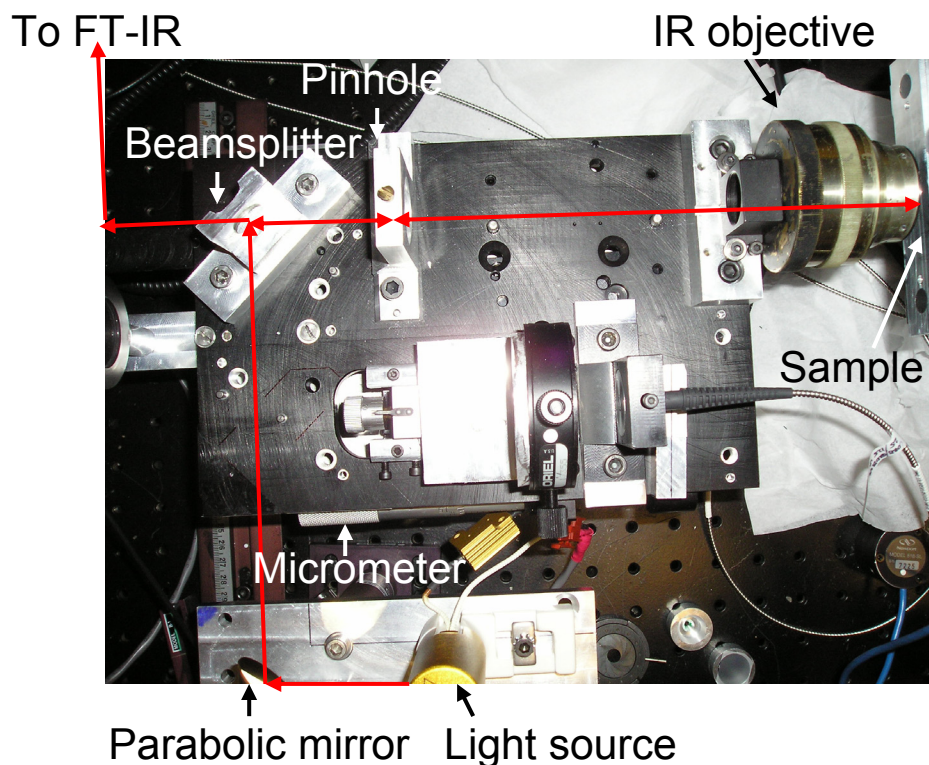
Figure 6.1: FT-IR microspectrometer in reflection mode. It consists of a homemade FT-IR microscope mounted on a micrometer stage with the light output coupled into a standard FT-IR spectrometer. The light path for normal incidence reflectance spectroscopy is shown in red.

For FT-IR microspectroscopy, an inverse opal metal film was mounted on the sample stage, which was then moved via software until an opalescent spot was illuminated. Light was focused on the sample until the IR signal detected by the FT-IR spectrometer approached a maximum value. The reflectance spectra was then collected over the appropriate wavelength range, a process that typically takes ~ 5 minutes to acquire acceptable signal to noise ratios. A 20 mL scintillation vial containing the diluted metal etchant was raised on an adjustable height lab stand (LabJack) until the metal film was submerged. The sample was then etched for a known period of time. Immediately following etching, the lab stand was lowered, and the exposed metal film was submerged in a container of DI for ~ 30 s to remove any remaining etchant, and dried under a gentle

N_2 stream. The spectra collection procedure was then repeated. All reflectance values were normalized to an Al mirror (Edmund).

6.4 Results and Discussion

6.4.1 Mesostructure of Inverse Opal Ni

Ni films deposited through CC on ITO (D = 1250 nm) exhibited the expected inverse opal structure with a high degree of smoothness (Fig. 6.2). The replication of the CC template structure by the electrodeposited Ni film was excellent, as shown by the full infilling of the CC template defects (Fig. 6.2a) and the interconnected pore structure corresponding to the FCC CC template (Fig. 6.2b). Not surprisingly, the CC templated Ni film exhibited zero shrinkage compared with the CC template diameter (Fig. 6.2b), due to the stiffness of the metallic mesostructure. Ni film electrodeposited outside the CC template exhibited a larger surface roughness, suggesting that, similar to the case of CC templated conducting polymers, the CC acted as a leveling agent during the electrodeposition process. Ni films deposited inside another CC (D = 880 nm) revealed essentially identical mesostructures.

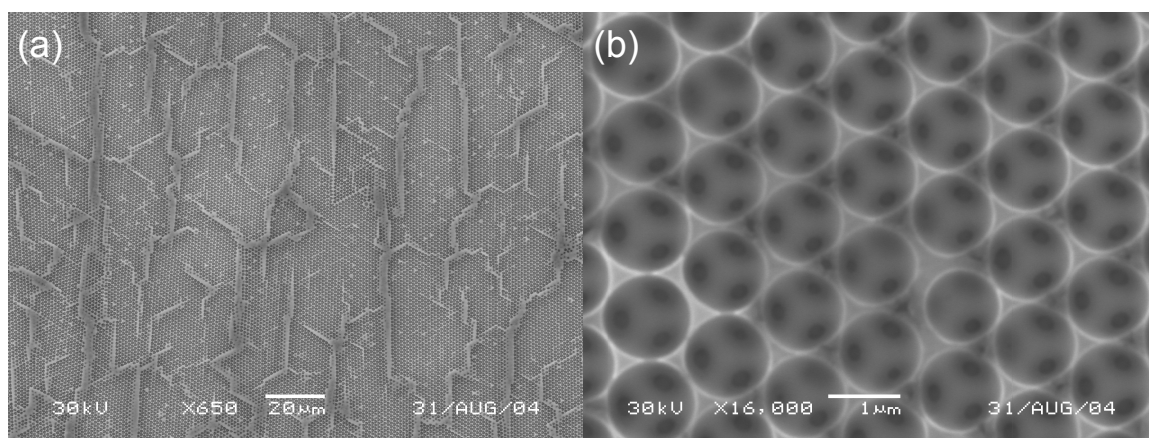**Figure 6.2:** SEM images of inverse opal Ni films electrodeposited at 0.8 mA / cm^2 through a CC template (D = 1250 nm). (a) Low magnification view, showing replication of all features of the CC template, including defects and drying cracks. (b) High magnification view, showing the interconnected FCC pore mesostructure. Electrodeposition and SEM performed by Xindi Yu.

We also discovered that the coulombic efficiency of Ni electrodeposition in CC was rather low. Assuming 100% coulombic efficiency and an inverse FCC volume fraction of 0.26, our electrodeposition charge density of 3000 mC / cm^2 should have resulted in a film 4 μm in thickness. A cross sectional view of the inverse opal Ni film revealed that the actual thickness was ~ 1.6 μm, equivalent to a coulombic efficiency of 0.4. The coulombic efficiency remained constant at different CC diameters (466 nm, 880 nm). In contrast, Ni films electrodeposited in an inverse FCC mesostructure had a coulombic efficiency of 0.94.[192] There are several possible reasons for this discrepancy. First, a significant fraction of the ITO electrode was not covered with CC and would be expected to experience a larger flux of Ni^{2+} ions due to its open nature. Second, the unequal flux of Ni^{2+} ions to the CC templated versus untemplated regions was possibly exacerbated by our decision to not stir the electroplating solution during electrodeposition. Fortunately, the low coulombic efficiency is consistent for all Ni electrodeposition experiments and does not seem to adversely affect the quality of the electrodeposited film. Thus, through galvanostatic electrodeposition, we have fabricated inverse opal Ni films with good crystallographic order and sample smoothness, which may be important in the usefulness of these mesostructured films as 3-D photonic crystals.

The mesostructure of inverse opal Ni films were significantly modified with wet chemical etching, and the final film morphology was dependent on the stirring of the etchant solution (Fig. 6.3 and 6.4). For example, an inverse Ni film (D = 1250 nm) after 25 minutes of etching with no stirring exhibited larger interconnect size (Fig. 6.3) compared with the unetched film (Fig. 6.2), indicating that Ni was being removed.

However, the etched film was also significantly rougher, both along the top surface (Fig. 6.3a) and within the pores (Fig. 6.3b), suggesting that the etching was not uniform. In contrast, inverse opal Ni films etched under nearly identical conditions but with gentle stirring (300 rpm) for 29 minutes exhibited significantly smoother mesostructure (Fig 6.4). First, stirring increased the etch rate of Ni, as shown by the thinner side walls and larger interconnects compared with Figure 6.3. Second, stirring resulted in an uniform etch, as shown by smoothness of the Ni film after etching (Fig. 6.4a) and the uniformity of the etched mesostructure through the bulk of the film (Fig. 6.4b). Finally, the amount of Ni film etched is of the same magnitude as that predicted from the product literature (170 nm ~ 1 A / s * 29 minutes). Thus, through proper control of the etching conditions, we can create uniform and open mesostructures from inverse opal Ni films which may allow light to interact more strongly with the 3-D metallic mesostructure.

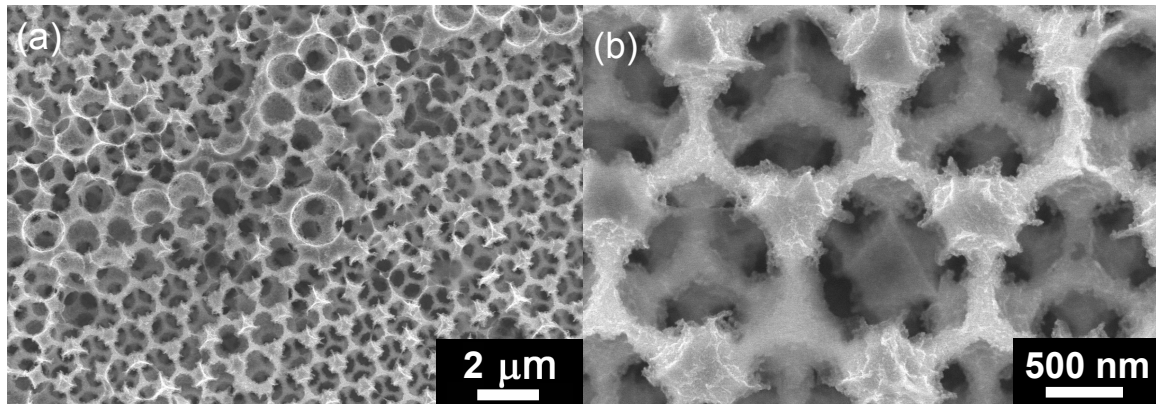**Figure 6.3:** SEM of a CC templated (D = 880 nm) Ni film after 24 minutes of etching with no stirring. (a) Low magnification view, showing non-uniform etching and increasing film roughness. (b) High magnification view, with significant removal of Ni as shown by the larger interconnect size, but also displaying a high degree of roughness.
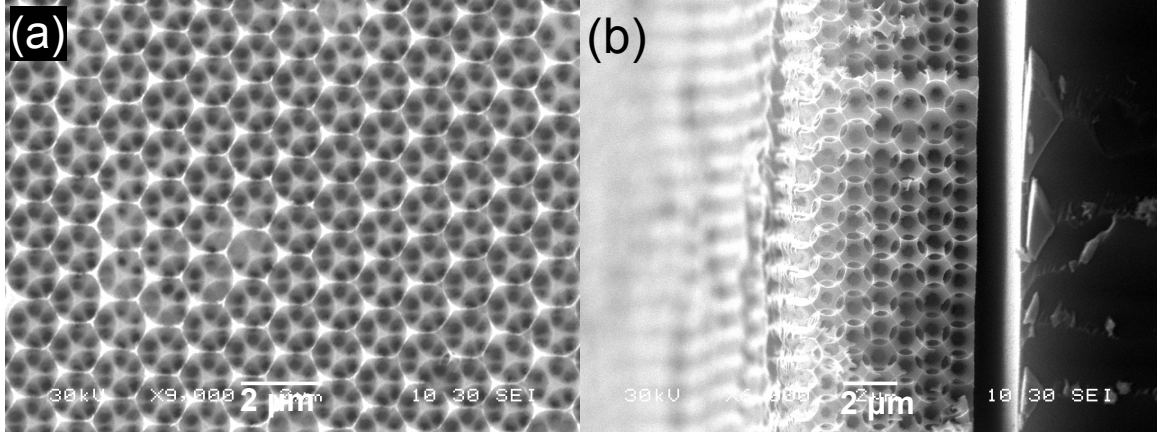
Figure 6.4: SEM of a CC templated (*D* = 1250 nm) Ni film after 29 minutes of etching with stirring. (a) Top view, showing smooth film with a degree of etching. (b) Side view, showing uniform etching through the bulk of the Ni film. Etching and SEM performed by Xindi Yu.

6.4.2 Optical Properties of Inverse Opal Ni

Electrodeposited inverse opal Ni films exhibited visible opalescence that varied according to the diameter of the CC template, as shown in Figure 6.5. Although the whole templated region appeared to be opalescent to the naked eye, examination with an optical microscope revealed that certain regions exhibited bright colors while other regions remained dark (Fig. 6.5). When reflectance spectra were collected from the bright regions, we discovered oscillations in reflectance indicative of interference fringes (Fig. 6.6a). However, due to the opaque nature of metallic films, the constructive interference probably resulted from the reflection from the top of the film and reflection from the surface one layer into the film (Fig. 6.6b), a mechanism that was previously used to explain interference fringes from inverse opal W films made by CVD.[187] When the reflectance spectra was plotted against the energy of the photon, the periodic maxima should be separated according to the following equation:[187]

$$\Delta E = \frac{hc}{2D} \qquad (6.3)$$

where $\varDelta E$ is the energy difference between fringe maxima, h is Planck's constant, c is velocity of light in vacuum, and D is the colloid diameter. The experimentally observed peak separation (Fig 6.6a) matched reasonably well to values calculated from Equation 6.3 ($\varDelta E$ = 0.49 eV for D = 1250 nm, $\varDelta E$ = 0.70 eV for D = 880 nm). The dark regions also exhibited interference fringes, but the maxima were significantly weaker. In other words, the visible opalescence most mostly corresponds to interference fringes from the surface of the mesostructure Ni film, which is sensitive to factors such as sample roughness.
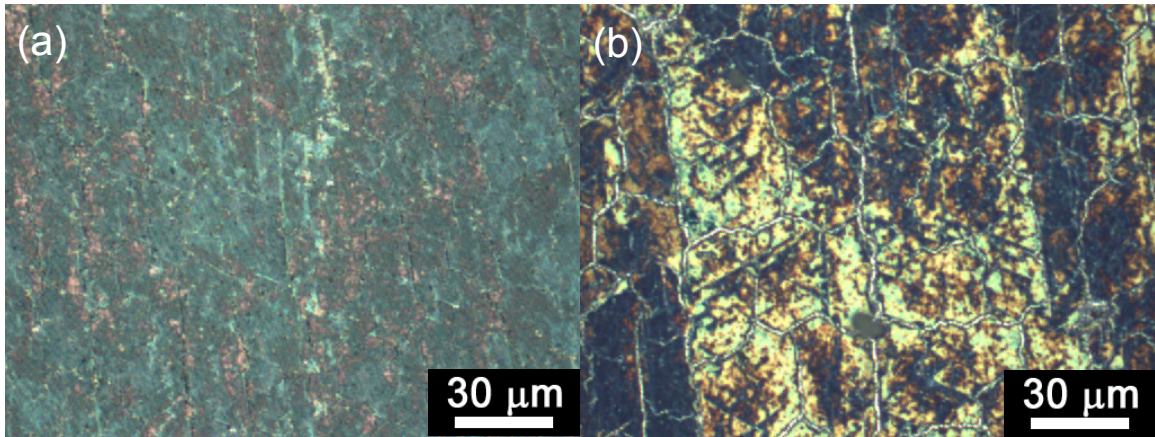

Figure 6.5: Reflectance optical micrograph of CC templated Ni films in air. (a) D = 1250 nm. (b) D = 880 nm. The inverse opal Ni films reflected different colors depending on CC template diameter, with certain dark regions possibly due to variation in film thickness.
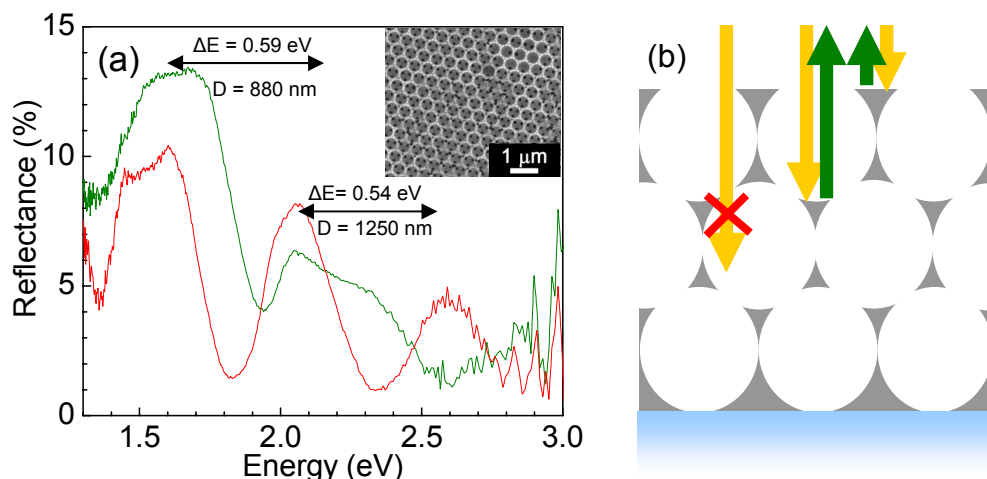
Figure 6.6: Interference fringes from inverse opal Ni films. (a) Reflectance spectra of inverse opal Ni film as a function of photon energy, showing regularly spaced peaks in reflectance. Green (red) spectra are from inverse opal Ni with $D = 880$ nm (1250 nm). (b) Proposed mechanism for the development of the interference fringes due to reflections from two surfaces separated by D. There is no contribution from reflection off of surfaces deeper into the sample due to opaqueness of Ni, which explains the low intensity of the interference fringe maxima.

FT-IR reflectance microspectroscopy of the CC templated Ni films did not show the interference fringes, possibly because the larger spot size (900 μm) averaged out the reflectance from bright and dark regions. On the other hand, we discovered other optical features which depended strongly on etching. Figure 6.7 shows the FT-IR reflectance spectra of an inverse opal Ni film ($D = 1250$ nm) as a functioning of etching time with stirring. Prior to etching, a reflectance peak at 1.43 μm was visible. As the etching time was increased above ~ 10 minutes, the peak began to red shift, to a final position of 1.85 μm at 29 minutes of etching (Fig. 6.7). Since the sampling spot throughout etching was the same, the red shift in peak position most likely corresponded to the change in the mesostructure from an inverse opal to a more open mesh. A weak peak also existed at 1.1 μm and became attenuated without shifting as the etching time increased (Fig. 6.7). Interestingly, inverse opal Ni fabricated from a smaller CC (D = 880 nm) contained only the peak at 1.1 μm (Fig. 6.8), although the lack of a reflectance peak that was sensitive to

176

etching may be explained by the slightly non-uniform etch of the Ni film as shown by its increased roughness when examined with SEM (Fig 6.8, inset). Determination of the exact origin of the peak shift for an etched inverse opal Ni film is also complicated by the fact that Ni is magnetic, and therefore the refractive index is a function of both its dielectric permittivity and magnetic permeability. We are currently exploring several options on the analysis of the relationship between the mesostructure and the optical response of these CC templated Ni films.
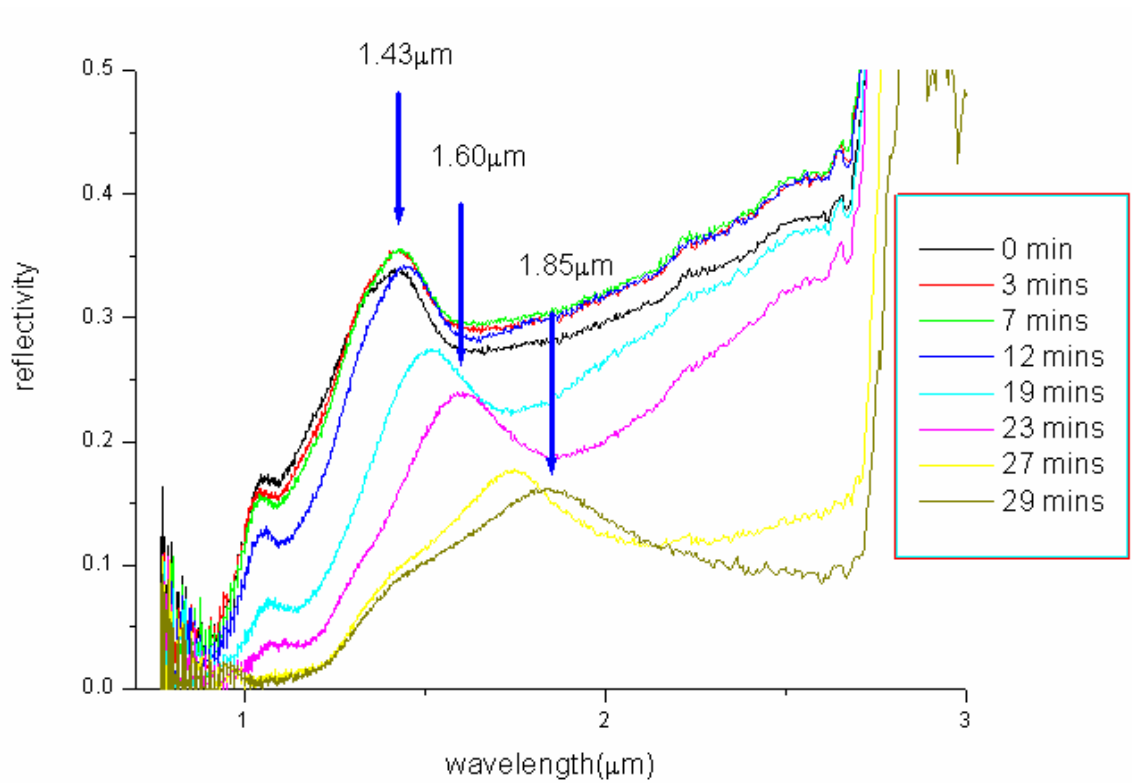

Figure 6.7: FT-IR reflectance spectra of a CC templated (D = 1250 nm) Ni film in air as a function of etching time. As the etching time increased, the characteristic peak red shifted from 1.43 μm to 1.85 μm, possibly corresponding to the change in film mesostructure. A weak peak at 1.1 μm is also observed who does not shift as a function of etching time. Spectra collected by Xindi Yu.
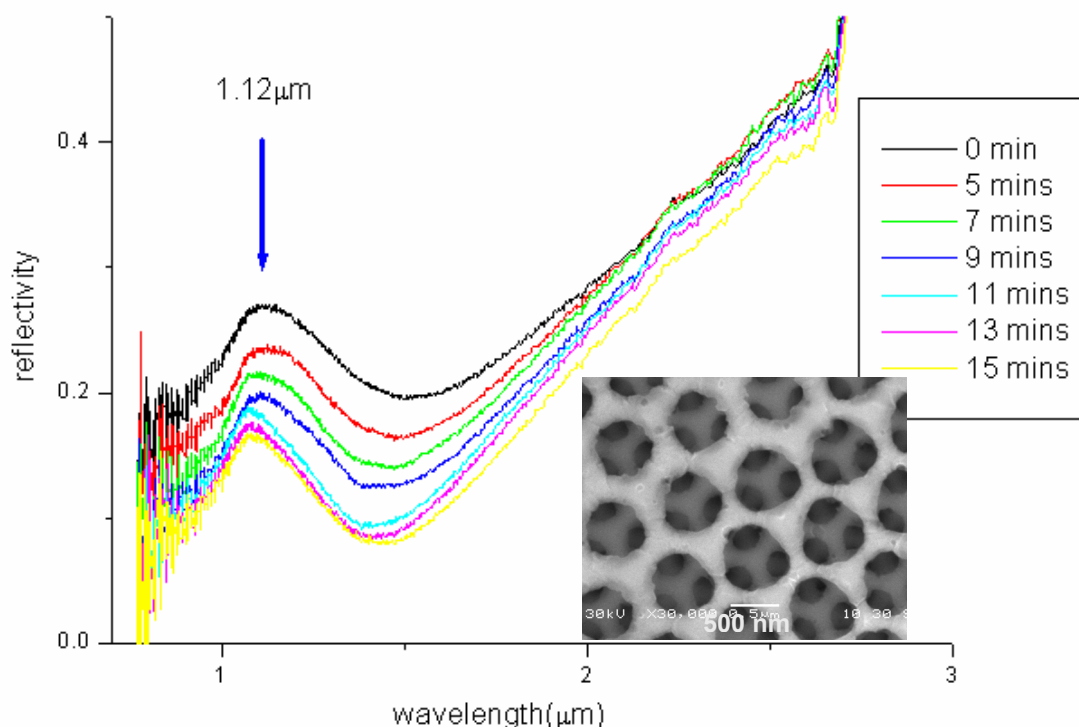
Figure 6.8: FT-IR reflectance spectra of a CC templated (D = 880 nm) Ni film in air as a function of etching time. The peak at 1.1 μm remained, while the shifting peak at higher wavelength disappeared. Inset: SEM of the inverse opal Ni film after 15 minutes of etching, showing a smaller degree of etching and an increased roughness compared with Figure 6.4. Spectra collected by Xindi Yu.

6.4.3 Mesostructure of Other Inverse Opal Metals

Cu and Au were also electrodeposited through CC templates on Au coated glass slides. However, the success of templating was strongly influenced by the electrodeposition conditions, specifically the current density. For Cu, if the current density was too high or too low, the electrodeposited the film exhibited significant variations in film thickness (Fig. 6.9a). In addition, the electrodeposition process caused the CC template to detach from the electrode, as shown by the layer of untemplated Cu deposited underneath the templated region (Fig. 6.9b). On the other hand, at a current density of 3 mA / cm^2, the inverse opal Cu film exhibited comparable roughness to the Ni

film and remained templated all the way to the film/electrode interface (Fig. 6.10). The thickness of the CC templated Cu film (10 μm) corresponds to a coulombic efficiency of 100% for the electrodeposition.
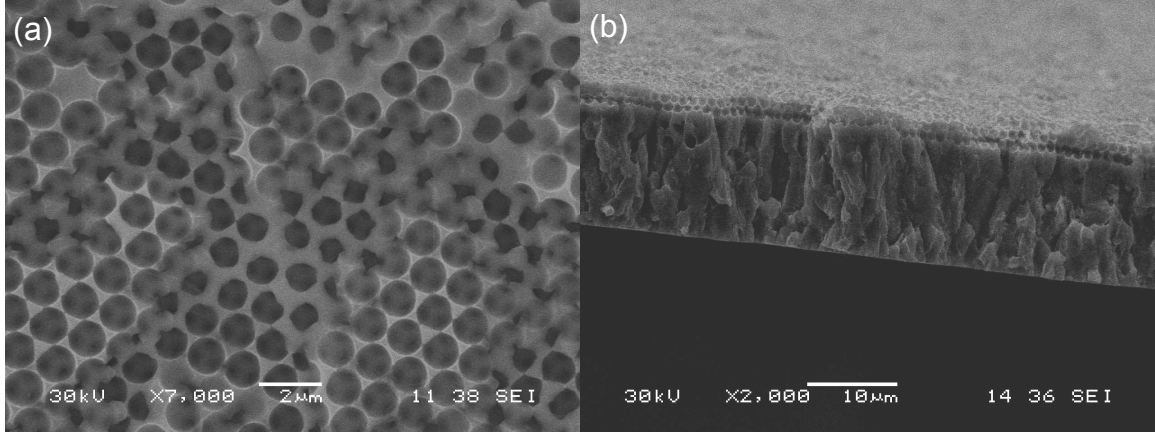
Figure 6.9: SEM of a CC templated ($D = 1250$ nm) Cu film electrodeposited at 1.5 mA / cm^2. (a) Top view, showing significant variations in film thickness. (b) Side view, showing a thick untemplated Cu film underneath the templated region, suggesting that the CC detached from the electrode. Electrodeposition and SEM performed by Xindi Yu.
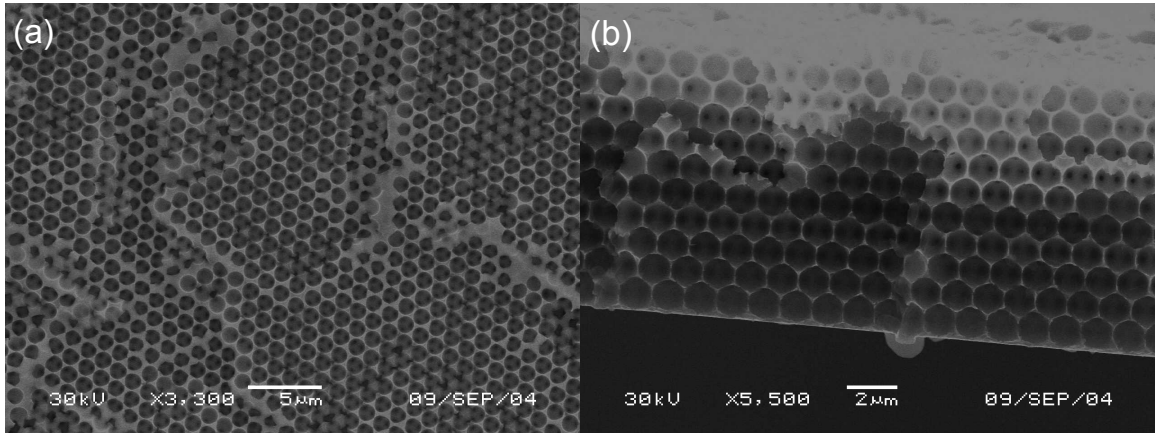
Figure 6.10: SEM of a CC templated ($D = 1250$ nm) Cu film electrodeposited at 3 mA / cm^2. (a) Top view. (b) Side view, with full templating to the film/electrode interface. Electrodeposition and SEM performed by Xindi Yu.

The current density of electrodeposition also influenced the quality of CC templated Au films. At high current density values, CC detachment was observed, similar to the case of Cu. However, at a current density of 0.5 mA / cm^2, we observed good CC templating of the electrodeposited Au film and a high degree of smoothness

(Fig 6.11a and 6.11b). The thickness of the inverse opal film in the CC templated region was 2 μm, and the coulombic efficiency was 40% (Fig. 6.11c). In contrast, the thick solid film electrodeposited at the untemplated electrode equaled a coulombic efficiency of ~ 100% (Fig. 6.11d). Once again, the presence of the CC template hindered the diffusion of Au^+ ions to the electrode, leading to a decreased coulombic efficiency. Work is underway to determine the optical response of the inverse opal Au films.
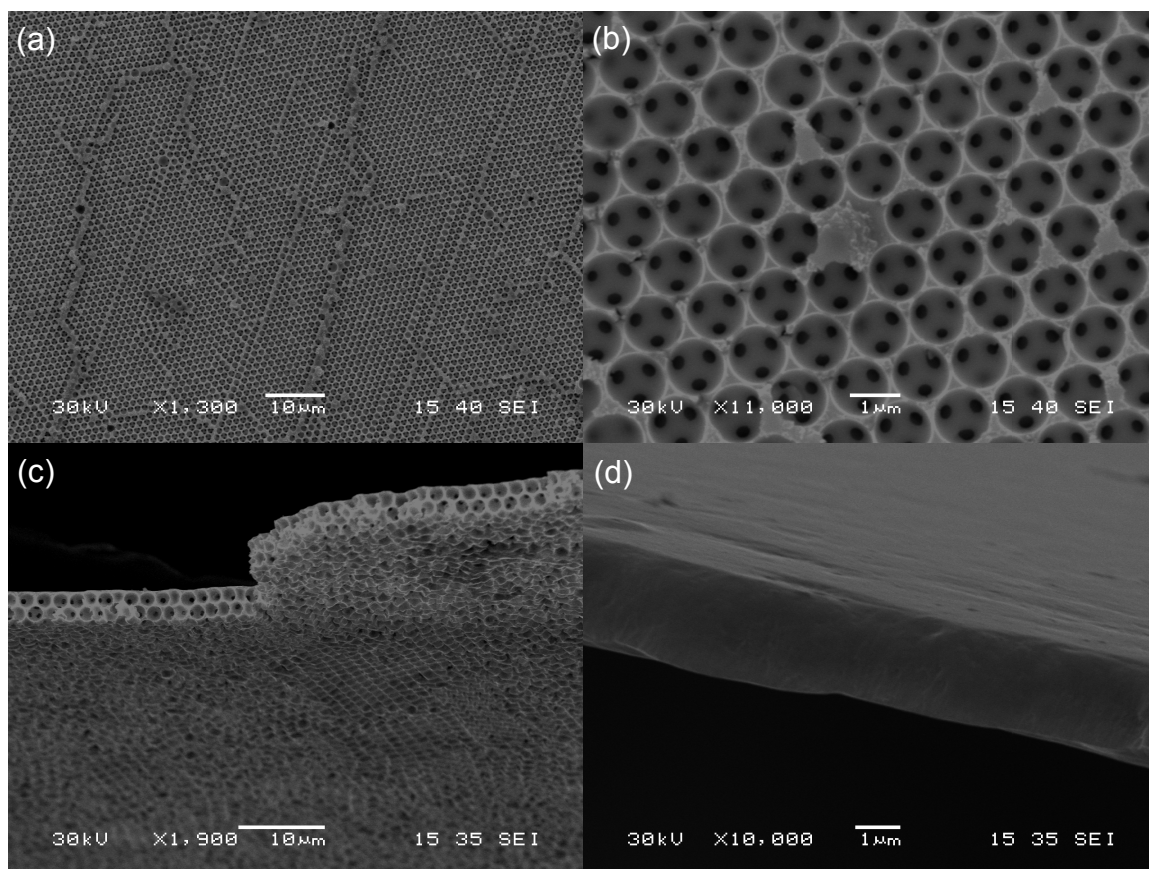
Figure 6.11: SEM of a CC templated ($D = 1250$ nm) Au film electrodeposited at 0.5 mA / cm^2. (a) Top view, low magnification. (b) Top view, high magnification, showing direct CC templating with good film smoothness. (c) Side view of the templated region, showing a bilayer. (d) Side view of the untemplated region, showing a thick dense film, indicating a much higher coulombic efficiency.

6.5 Summary

Ni, Cu, and Au films of controlled thickness were successfully electrodeposited through PS CC templates under galvanostatic conditions from commercial electroplating

solutions, followed by template removal with THF. When the current density was optimized, the resulting inverse opal metal films exhibited uniform thickness and excellent smoothness. A coulombic efficiency of ~ 40% was observed for electrodeposition of Ni and Au inside CC, while preliminary data on Cu showed a near unity coulombic efficiency. Interestingly, the corresponding decrease in diffusion of metal ions to the CC templated electrode seemed to assist in creating a more level film. Opalescence from selected regions of inverse opal Ni was explained by interference fringes of reflections from metallic surfaces separated by the colloidal diameter. Wet chemical etching of inverse opal Ni films using a commercial etchant were also demonstrated, and we found that with gentle stirring (300 rpm), the rate and uniformity of etching can both be improved, yielding open inverse opal meshes of Ni. FT-IR microspectroscopy of a CC templated (D = 1250 nm) Ni film in air as a function of etching time revealed the presence of a reflectance peak at 1.43 μm that red shifted by ~ 0.4 μm as the Ni film was etched. In contrast, a Ni film grown inside a smaller CC template (D = 880 nm) did not exhibit a similar mesostructure-dependent peak shift. Efforts are now underway to model the optical response of inverse opal Ni films with variable mesostructure and to determine the optical properties of inverse opal Au films to test their applicability as CC templated 3-D metallic photonic crystals.

CHAPTER 7

CONCLUSIONS

Colloidal crystal templating is increasingly utilized for the fabrication of 3-D mesostructures with novel and interesting chemical, physical, and optical properties using a variety of materials. Colloidal crystals were fabricated by the self-organization of monodisperse spherical microparticles. The periodic modulation of dielectric constant in these colloidal crystals may result in a variety of interesting optical phenomena, the most accessible of which is the first order Bragg diffraction of light due to constructive interference of reflection from the planes of colloids. By molding functional materials around the 3-D periodicity of colloidal crystals, tunable inverse opal mesostructures have been generated with potential applications as electrochemical elements, sensors, flow control devices, and novel photonic band gap materials. In the general colloidal crystal templating scheme, a colloidal crystal was first formed using a variety of techniques including evaporation and packing inside flow cells. A second material was then grown inside the interstitial space of the colloidal crystal templates via electrodeposition, photopolymerization, and other methods. The template was then chemically etched, yielding an inverse opal of the functional material. Various characterization techniques were then employed to determine the structures and properties of these mesostructures.

Using colloidal crystal templating, inverse opal conducting polymer films were fabricated by electropolymerization. Examination with scanning electron microscopy revealed that the film microstructure was smoother and more compact than the untemplated films, possibly due to interconnectivity of the face centered cubic mesopores. These structural differences were reflected in the larger electrochemical

response detected using cyclic voltammetry. Finally, as the oxidation state of the conducting polymer varied during electrochemical cycling, the inverse opal conducting polymer films exhibited shifts in the Bragg diffraction peaks in microspectroscopy, which may be explained by the change in the spacing between conducting polymer chains due to counter ion intercalation, as well as the variation in the refractive index of the conducting polymer due to changes in oxidation state.

Mesostructured functionalized hydrogels were also templated inside colloidal crystals to take advantage of the reversible volumetric changes of these hydrogel to tune the Bragg diffraction of the photonic structure. By infiltrating colloidal crystals with 2-hydroxyethyl methacrylate monomer, crosslinker, photoinitiator, and appropripate functional groups, followed by UV polymerization and template etching, mechnically robust inverse opal hydrogel thin films were synthesized. These films exhibited reversible shifts in Bragg diffraction based on changes in parameters such as solvent (ethanol), pH, ionic strength, crosslink density, and glucose concentration, caused by the expansion and contraction of the hydrogel film due to changes in the local Donnan potential. The diffraction response was observed both visually and by microspectroscopy, demonstrating the versatility of using tunable Bragg diffraction for sensing applications. The linear relationship between the magnitude of diffraction response and functional group concentration for the pH and glucose sensors implies that the macroscopic hydrogel swelling occurred primarily in the sample normal direction. The diffraction response for the ionizable CC templated hydrogels were explained by the increase in Donnan potential during hydrogel ionization, which caused an influx of excess counter ions that expanded the hydrogel network. The kinetics of the diffraction

response was also studied and was shown to correspond to the square root of elapsed time, suggesting that the response rate was limited by the diffusion of analytes from the FCC pores into the surrounding dense hydrogel.

In comparison to other 3-D periodic hydrogels where the colloidal crystal template was not etched, the diffraction response of the inverse opal hydrogel exhibited several interesting trends. For example, as the diffraction wavelength red shifted, the peak intensity decreased, regardless of the functional group used. Also, when the initial diffraction wavelength was higher, the kinetics of further diffraction shifts became faster. Thus, we studied the structural evolution of Bragg diffracting inverse opal hydrogel sensors during swelling by laser scanning multiphoton fluorescence microscopy. A fluorescently labeled pH-sensitive hydrogel was UV-polymerized in a dried polystyrene colloidal crystal template, and the inverse opal mesostructure was facricated following template removal. Examination of the pH induced 3-D deformation of the FCC pore structure using two photon fluorescence imaging revealed that as the hydrogel swelled, the characteristic distance between layers of pores in the sample normal direction increased. In addition, the pore volume fraction decreased significantly, while the pore shape deformed from an ellipsoid in the compact state to a twisted cylinder at high swelling ratios. The confocal results are consistent with the trends in UV-vis microspectroscopy, and suggest a change in pore symmetry. Hydrogel deformation was simulated using finite element analysis in which an isotropic bulk strain was applied to a model on a thin film inverse opal elastomer structure. The resulting dependence of pore structure to hydrogel swelling deviated significantly from the experimental data, suggesting that the inverse opal hydrogel swelling may induce local internal buckling at

high stress points, leading to greater disorder at high degree of swelling, similar to experimental observations. Finally, the expected diffraction response of a swollen hydrogel was simulated using scalar wave approximation, which indicated that the large attenuation in diffraction peak intensity was achieved only with a large decrease in the pore volume fraction, corresponding very well with the fluorescence imaging results.

Microspectroscopy represents an excellent method to study the Bragg diffraction response of photonic mesostructures within a single crystalline domain; a collection spot size of ~ 20 μm minimizes the detrimental effects of disorder and drying cracks. However, since both the incident and reflected light beams were focused using a microscope objective, the numerical aperture (NA) is nonzero, which may significantly affect angle dependent optical phenomena such as Bragg diffraction. Thus, we studied the quantitative effect of NA on the Bragg diffraction response of a polystyrene colloidal crystal both experimentally and theoretically. Using microspectroscopy, we found that the diffraction peak parameters changed noticeably as the NA was increased from 0.017 to 0.5. For example, the diffraction wavelength blue shifted 1.4% from 584 nm to 576 nm, and the normalized FWHM increased from 6.2% to 7.0%. These shifts were in qualitative agreement with results predicted using a layered Korringa-Kohn-Rostoker method. Both experiment and theory showed that the peak parameter changes mostly occurred for NA > 0.3. Thus, by using focusing optics with a NA below 0.3, the experimental first order Bragg diffraction of low photonic strength mesostructures may be directly compared to normal incidence calculations.

We also fabricated and characterized inverse opal metallic films as potentially novel photonic mesostructures. Through electrodeposition of metals inside colloidal

crystals with micron sized diameters, the inverse opal mesostructures may cause enhanced absorption and emission at specific wavelengths due to enhancement of the photonic density of state. We have synthesized inverse opals of nickel and copper and are currently characterizing their reflectance and emission properties using an FT-IR microscope. We have also shown that the film mesostructure can be carefully altered by chemical etching of the metal, and are determining if corresponding changes in photonic band structure and optical properties may also exist.

Colloidal crystal templated mesostructures can be made from a variety of materials using various infiltration techniques. Through careful material selection, mesostructures with a wide range of interesting chemical, physical, and optical properties may be created. Through experimental techniques such as cyclic voltammetry, electron and light microscopy, microspectroscopy, laser diffraction, and fluorescence imaging, the response of these functionalized 3-D periodic films were quantified and correlated to evolution of the mesostructure. When compared with theoretical methods to predict the optical response and changes in mesostructure, these experiments allow for a more complete understanding of the structure-property relationship for these tunable photonic mesostructures.

REFERENCES

1. Sakoda, K. *Optical Properties of Photonic Crystals*; Springer-Verlag: Berlin, 2001.

2. Johnson, S. G., Joannopoulos, J. D. *Photonic Crystals: The Road from Theory to Practice*; Kluwer Academic Publishers: Boston, 2002.

3. Lopez, C. *Adv. Mater.* **2003**, *15*, 1679-1704.

4. Lin, S. Y., Fleming, J. G., Hetherington, D. L., Smith, B. K., Biswas, R., Ho, K. M., Sigalas, M. M., Zubrzycki, W., Kurtz, S. R., Bur, J. *Nature* **1998**, *394*, 251-253.

5. Chow, E., Lin, S. Y., Johnson, S. G., Villeneuve, P. R., Joannopoulos, J. D., Wendt, J. R., Vawter, G. A., Zubrzycki, W., Hou, H., Alleman, A. *Nature* **2000**, *407*, 983-986.

6. Noda, S., Tomoda, K., Yamamoto, N., Chutinan, A. *Science* **2000**, *289*, 604-606.

7. Blanco, A., Chomski, E., Grabtchak, S., Ibisate, M., John, S., Leonard, S. W., Lopez, C., Meseguer, F., Miguez, H., Mondia, J. P., Ozin, G. A., Toader, O., van Driel, H. M. *Nature* **2000**, *405*, 437-440.

8. Vlasov, Y. A., Bo, X. Z., Sturm, J. C., Norris, D. J. *Nature* **2001**, *414*, 289-293.

9. Noda, S., Chutinan, A., Imada, M. *Nature* **2000**, *407*, 608-610.

10. Akahane, Y., Asano, T., Song, B. S., Noda, S. *Nature* **2003**, *425*, 944-947.

11. Subramania, G., Lin, S. Y., Wendt, J. R., Rivera, J. M. *Appl. Phys. Lett* **2003**, *83*, 4491-4493.

12. Qi, M. H., Lidorikis, E., Rakich, P. T., Johnson, S. G., Joannopoulos, J. D., Ippen, E. P., Smith, H. I. *Nature* **2004**, *429*, 538-542.

13. Ogawa, S. P., Imada, M., Yoshimoto, S., Okano, M., Noda, S. *Science* **2004**, *305*, 227-229.

14. Holtz, J. H., Asher, S. A. *Nature* **1997**, *389*, 829-832.

15. Holtz, J. H., Holtz, J. S. W., Munro, C. H., Asher, S. A. *Anal. Chem.* **1998**, *70*, 780-791.

16. Lee, K., Asher, S. A. *J. Am. Chem. Soc.* **2000**, *122*, 9534-9537.

17. Takeoka, Y., Watanabe, M. *Langmuir* **2002**, *18*, 5977-5980.

18. Debord, J. D., Eustis, S., Debord, S. B., Lofye, M. T., Lyon, L. A. *Adv. Mater.* **2002**, *14*, 658-662.

19. Lee, Y.-J., Braun, P. V. *Adv. Mater.* **2003**, *15*, 563-566.

20. Asher, S. A., Alexeev, V. L., Goponenko, A. V., Sharma, A. C., Lednev, I. K., Wilcox, C. S., Finegold, D. N. *J. Am. Chem. Soc.* **2003**, *125*, 3322-3329.

21. Lee, Y.-J., Pruzinsky, S. A., Braun, P. V. *Langmuir* **2004**, *20*, 3096-3106.

22. Cassagneau, T., Caruso, F. *Adv. Mater.* **2002**, *14*, 34-38.

23. Cassagneau, T., Caruso, F. *Adv. Mater.* **2002**, *14*, 1837-1841.

24. Pan, G. S., Kesavamoorthy, R., Asher, S. A. *Phys. Rev. Lett.* **1997**, *78*, 3860-3863.

25. Pan, G. S., Kesavamoorthy, R., Asher, S. A. *J. Am. Chem. Soc.* **1998**, *120*, 6525-6530.

26. Garcia-Santamaria, F. "Photonic Crystals Based on Silica Microspheres", *Materials Science*; Universidad Autonoma de Madrid: Madrid, 2003.

27. Foll, H. *Semiconductors*, 2004; http://www.techfak.uni-kiel.de/matwis/amat/semi_en/kap_2/backbone/r2_1_5.html.

28. Johnson, S. G., Joannopoulos, J. D. *Opt. Expr.* **2001**, *8*, 173-190.

29. Hiltner, P. A., Krieger, I. M. *J. Phys. Chem.* **1969**, *73*, 2386-2389.

30. Gu, Z. Z., Fujishima, A., Sato, O. *Chem. Mater.* **2002**, *14*, 760-765.

31. Soljacic, M., Joannopoulos, J. D. *Nat. Mater.* **2004**, *3*, 211-219.

32. Kosaka, H., Kawashima, T., Tomita, A., Notomi, M., Tamamura, T., Sato, T., Kawakami, S. *Phys. Rev. B* **1998**, *58*, 10096-10099.

33. Wu, L. J., Mazilu, M., Karle, T., Krauss, T. F. *IEEE J. Quantum Electron* **2002**, *38*, 915-918.

34. Prasad, T., Colvin, V., Mittleman, D. *Phys. Rev. B* **2003**, *67*.

35. Kosaka, H., Kawashima, T., Tomita, A., Notomi, M., Tamamura, T., Sato, T., Kawakami, S. *Appl. Phys. Lett* **1999**, *74*, 1370-1372.

36. Kosaka, H., Kawashima, T., Tomita, A., Notomi, M., Tamamura, T., Sato, T., Kawakami, S. *Appl. Phys. Lett* **1999**, *74*, 1212-1214.

37. Russell, P. *Science* **2003**, *299*, 358-362.

38. Fink, Y., Winn, J. N., Fan, S. H., Chen, C. P., Michel, J., Joannopoulos, J. D., Thomas, E. L. *Science* **1998**, *282*, 1679-1682.

39. Ibanescu, M., Fink, Y., Fan, S., Thomas, E. L., Joannopoulos, J. D. *Science* **2000**, *289*, 415-419.

40. Bayindir, M., Sorin, F., Abouraddy, A. F., Viens, J., Hart, S. D., Joannopoulos, J. D., Fink, Y. *Nature* **2004**, *431*, 826-829.

41. Noda, S., Yamamoto, N., Sasaki, A. *Jpn. J. Appl. Phys. Part 2* **1996**, *35*, L 909-L 912.

42. Fleming, J. G., Lin, S. Y., El-Kady, I., Biswas, R., Ho, K. M. *Nature* **2002**, *417*, 52-55.

43. Campbell, M., Sharp, D. N., Harrison, M. T., Denning, R. G., Turberfield, A. J. *Nature* **2000**, *404*, 53-56.

44. Yang, S., Megens, M., Aizenberg, J., Wiltzius, P., Chaikin, P. M., Russel, W. B. *Chem. Mater.* **2002**, *14*, 2831-+.

45. Xia, Y. N., Gates, B., Li, Z. Y. *Adv. Mater.* **2001**, *13*, 409-413.

46. Garcia-Santamaria, F., Lopez, C., Meseguer, F., Lopez-Tejeira, F., Sanchez-Dehesa, J., Miyazaki, H. T. *Appl. Phys. Lett* **2001**, *79*, 2309-2311.

47. Garcia-Santamaria, F., Miyazaki, H. T., Urquia, A., Ibisate, M., Belmonte, M., Shinya, N., Meseguer, F., Lopez, C. *Adv. Mater.* **2002**, *14*, 1144-1147.

48. Lee, W. M., Pruzinsky, S. A., Braun, P. V. *Adv. Mater.* **2002**, *14*, 19.

49. Sozuer, H. S., Haus, J. W., Inguva, R. *Phys. Rev. B* **1992**, *45*, 13962-13972.

50. Garcia-Santamaria, F., Ibisate, M., Rodriguez, I., Meseguer, F., Lopez, C. *Adv. Mater.* **2003**, *15*, 788-+.

51. Asher, S. A.; US Patent No. 4627689: Crystalline Colloidal Narrow Band Radiation Filter, 1986.

52. Yablonovitch, E. *Phys. Rev. Lett.* **1987**, *58*, 2059-2062.

53. John, S. *Phys. Rev. Lett.* **1987**, *58*, 2486-2489.

54.   Lin, S. Y., Moreno, J., Fleming, J. G. *Appl. Phys. Lett* **2003**, *83*, 380-382.

55.   van Blaaderen, A., Ruel, R., Wiltzius, P. *Nature* **1997**, *385*, 321-324.

56.   Jiang, P., Bertone, J. F., Hwang, K. S., Colvin, V. L. *Chem. Mater.* **1999**, *11*, 2132-2140.

57.   Galisteo-Lopez, J. F., Palacios-Lidon, E., Castillo-Martinez, E., Lopez, C. *Phys. Rev. B* **2003**, *68*.

58.   Lu, Y., Yin, Y. D., Gates, B., Xia, Y. N. *Langmuir* **2001**, *17*, 6344-6350.

59.   Koenderink, A. F., Vos, W. L. *Phys. Rev. Lett.* **2003**, *91*, 213902.

60.   Tohver, V., Smay, J. E., Braem, A., Braun, P. V., Lewis, J. A. *Proc. Natl. Acad. Sci.* **2001**, *98*, 8950-8954.

61.   Lee, W., Chan, A., Bevan, M. A., Lewis, J. A., Braun, P. V. *Langmuir* **2004**, *20*, 5262-5270.

62.   Chiang, C. K., Fincher, C. R., Park, Y. W., Heeger, A. J., Shirakawa, H., Louis, E. J., Gau, S. C., MacDiarmid, A. G. *Phys. Rev. Lett.* **1977**, *39*, 1098-1101.

63.   Baughman, R. H. *Synth. Met.* **1996**, *78*, 339-353.

64.   Madden, J. D., Cush, R. A., Kanigan, T. S., Brenan, C. J., Hunter, I. W. *Synth. Met.* **1999**, *105*, 61-64.

65.   Xia, Y. N., Rogers, J. A., Paul, K. E., Whitesides, G. M. *Chem. Rev.* **1999**, *99*, 1823-1848.

66.   Bao, Z., Rogers, J. A., Katz, H. E. *J. Mat. Chem.* **1999**, *9*, 1895-1904.

67.   Groenendaal, L., Jonas, F., Freitag, D., Pielartzik, H., Reynolds, J. R. *Adv. Mater.* **2000**, *12*, 481-494.

68.   Albert, K. J., Lewis, N. S., Schauer, C. L., Sotzing, G. A., Stitzel, S. E., Vaid, T. P., Walt, D. R. *Chem. Rev.* **2000**, *100*, 2595-2626.

69.   McQuade, D. T., Pullen, A. E., Swager, T. M. *Chem. Rev.* **2000**, *100*, 2537-2574.

70.   Ghosh, S., Inganas, O. *Adv. Mater.* **1999**, *11*, 1214-1218.

71.   Hughes, M., Shaffer, M. S. P., Renouf, A. C., Singh, C., Chen, G. Z., Fray, J., Windle, A. H. *Adv. Mater.* **2002**, *14*, 382-385.

72. Hulvat, J. F., Stupp, S. I. *Angew. Chem. Int. Ed.* **2003**, *42*, 778-781.

73. Bartlett, P. N., Birkin, P. R., Ghanem, M. A., Toh, C. S. *J. Mat. Chem.* **2001**, *11*, 849-853.

74. Satoh, S., Kajii, H., Kawagishi, Y., Fujii, A., Ozaki, M., Yoshino, K. *Jpn. J. Appl. Phys. Part 2* **1999**, *38*, L1475-L1477.

75. Satoh, S., Kajii, H., Kawagishi, Y., Tamura, T., Fujii, A., Ozaki, M., McCullough, R. D., Yoshino, K. *Synth. Met.* **2001**, *121*, 1503-1504.

76. Deutsch, M., Vlasov, Y. A., Norris, D. J. *Adv. Mater.* **2000**, *12*, 1176-1180.

77. Yamaura, M., Sato, K., Hagiwara, T. *Synth. Met.* **1990**, *39*, 43-60.

78. Sakmeche, N., Aeiyach, S., Aaron, J.-J., Jouini, M., Lacroix, J. C., Lacaze, P.-C. *Langmuir* **1999**, *15*, 2566-2574.

79. Bobacka, J., Lewenstam, A., Ivaska, A. *J. Electroanal. Chem.* **2000**, *489*, 17-27.

80. Bard, A. J., Faulkner, L. R. *Electrochemical Methods: Fundamentals and Applications*; 2nd ed.; John Wiley & Sons: New York, 2001.

81. Li, G. C., Pickup, P. G. *PCCP Phys. Chem. Chem. Phys.* **2000**, *2*, 1255-1260.

82. Tanaka, T., Fillmore, D., Sun, S.-T., Nishio, I., Swislow, G., Shah, A. *Phys. Rev. Lett.* **1980**, *45*, 1636-1639.

83. Katayama, S., Hirokawa, Y., Tanaka, T. *Macromolecules* **1984**, *17*, 2643-2645.

84. Ilavsky, M., Hrouz, J., Ulbrich, K. *Polym. Bull.* **1982**, *7*, 107-113.

85. Hirotsu, S. *J. Chem. Phys.* **1988**, *88*, 427-431.

86. English, A. E., Tanaka, T., Edelman, E. R. *J. Chem. Phys.* **1997**, *107*, 1645-1654.

87. Kikuchi, A., Suzuki, K., Okabayashi, O., Hoshino, H., Kataoka, K., Sakurai, Y., Okano, T. *Anal. Chem.* **1996**, *68*, 823-828.

88. Miyata, T., Asami, N., Uragami, T. *Nature* **1999**, *399*, 766-769.

89. Watanabe, M., Akahoshi, T., Tabata, Y., Nakayama, D. *J. Am. Chem. Soc.* **1998**, *120*, 5577-5578.

90. Anastase-Ravion, S., Ding, Z., Pelle, A., Hoffman, A. S., Letourneur, D. *J. Chromatogr. B* **2001**, *761*, 247-254.

91. Braun, P. V., Zehner, R. W., White, C. A., Weldon, M. K., Kloc, C., Patel, S. S., Wiltzius, P. *Adv. Mater.* **2001**, *13*, 721-724.

92. Asher, S. A., Holtz, J., Liu, L., Wu, Z. J. *J. Am. Chem. Soc.* **1994**, *116*, 4997-4998.

93. Xia, Y. N., Gates, B., Yin, Y. D., Lu, Y. *Adv. Mater.* **2000**, *12*, 693-713.

94. Park, S. H., Xia, Y. N. *Adv. Mater.* **1998**, *10*, 1045-1049.

95. Jiang, P., Hwang, K. S., Mittleman, D. M., Bertone, J. F., Colvin, V. L. *J. Am. Chem. Soc.* **1999**, *121*, 11630-11637.

96. Yoshino, K., Satoh, S., Shimoda, Y., Kajii, H., Tamura, T., Kawagishi, Y., Matsui, T., Hidayat, R., Fujii, A., Ozaki, M. *Synth. Met.* **2001**, *121*, 1459-1462.

97. Fudouzi, H., Xia, Y. N. *Adv. Mater.* **2003**, *15*, 892-+.

98. Tanaka, T. *Sci. Am.* **1981**, *244*, 124-138.

99. Beebe, D. J., Moore, J. S., Bauer, J. M., Yu, Q., Liu, R. H., Devadoss, C., Jo, B. H. *Nature* **2000**, *404*, 588-590.

100. Yu, Q., Bauer, J. M., Moore, J. S., Beebe, D. J. *Appl. Phys. Lett* **2001**, *78*, 2589-2591.

101. Suzuki, A., Tanaka, T. *Nature* **1990**, *346*, 345-347.

102. Tanaka, T., Nishio, I., Sun, S. T., Uenonishio, S. *Science* **1982**, *218*, 467-469.

103. Osada, Y., Hasebe, M. *Chem. Lett.* **1985**, 1285-1288.

104. Liu, Z. S., Calvert, P. *Adv. Mater.* **2000**, *12*, 288-291.

105. James, T. D., Shinkai, S. *Top. Curr. Chem.* **2002**, *218*, 159-200.

106. Lorand, J. P., Edwards, J. O. *J. Org. Chem.* **1959**, *24*, 769-774.

107. Yoon, J., Czarnik, A. W. *J. Am. Chem. Soc.* **1992**, *114*, 5874-5875.

108. James, T. D., Sandanayake, K. R. A. S., Shinkai, S. *Angew. Chem. Int. Ed.* **1994**, *33*, 2207-2209.

109. Barker, S. A., Chopra, A. K., Hatt, B. W., Somers, P. J. *Carb. Res.* **1973**, *26*, 33-40.

110. Kataoka, K., Miyazaki, H., Bunya, M., Okano, T., Sakurai, Y. *J. Am. Chem. Soc.* **1998**, *120*, 12694-12695.

111. Elmas, B., Onur, M. A., Senel, S., Tuncel, A. *Colloid Polym. Sci.* **2002**, *280*, 1137-1146.

112. Foulger, S. H., Jiang, P., Lattam, A. C., Smith, D. W., Ballato, J. *Langmuir* **2001**, *17*, 6023-6026.

113. Asher, S. A., Peteu, S. F., Reese, C. E., Lin, M. X., Finegold, D. *Anal. Bioanal. Chem.* **2002**, *373*, 632-638.

114. Alexeev, V. L., Sharma, A. C., Goponenko, A. V., Das, S., Lednev, I. K., Wilcox, C. S., Finegold, D. N., Asher, S. A. *Anal. Chem.* **2003**, *75*, 2316-2323.

115. Flory, P. J. *Principles of Polymer Chemistry*; Cornell University Press: Ithaca, NY, 1953.

116. Liu, L., Li, P. S., Asher, S. A. *Nature* **1999**, *397*, 141-144.

117. Liu, L., Li, P., Asher, S. A. *J. Am. Chem. Soc.* **1999**, *121*, 4040-4046.

118. Weissman, J. M., Sunkara, H. B., Tse, A. S., Asher, S. A. *Science* **1996**, *274*, 959-960.

119. Debord, J. D., Lyon, L. A. *J. Phys. Chem. B* **2000**, *104*, 6327-6331.

120. Hu, Z. B., Lu, X. H., Gao, J. *Adv. Mater.* **2001**, *13*, 1708-1712.

121. Takeoka, Y., Watanabe, M. *Adv. Mater.* **2003**, *15*, 199-201.

122. Mittleman, D. M., Bertone, J. F., Jiang, P., Hwang, K. S., Colvin, V. L. *J. Chem. Phys.* **1999**, *111*, 345-354.

123. Pendry, J. B., Mackinnon, A. *Phys. Rev. Lett.* **1992**, *69*, 2772-2775.

124. Bell, P. M., Pendry, J. B., Moreno, L. M., Ward, A. J. *Comput. Phys. Commun.* **1995**, *85*, 306-322.

125. Kitano, S., Koyama, Y., Kataoka, K., Okano, T., Sakurai, Y. *J. Control. Rel.* **1992**, *19*, 161-170.

126. McDonald, J. C., Whitesides, G. M. *Acc. Chem. Res.* **2002**, *35*, 491-499.

127. Perrin, D. D., Dempsey, B. *Buffer for pH and Metal Ion Control*; Chapman and Hall Ltd.: London, 1974.

128. Brandrup, J., Immergut, E. H., Grulke, E. *Polymer Handbook*; Wiley: New York, 1999.

129. Reynolds, A. L., Arnold, J. M.; http://www.elec.gla.ac.uk/groups/opto/photoniccrystal/Software/SoftwareMain.htm.

130. Mayes, A. G., Blyth, J., Millington, R. B., Lowe, C. R. *Anal. Chem.* **2002**, *74*, 3649-3657.

131. Gehrke, S. H. *Adv. Poly. Sci.* **1993**, *110*, 81-144.

132. Mafe, S., Manzanares, J. A., English, A. E., Tanaka, T. *Phys. Rev. Lett.* **1997**, *79*, 3086-3089.

133. Chirila, T. V., Chen, Y. C., Griffin, B. J., Constable, I. J. *Polym. Int.* **1993**, *32*, 221-232.

134. Dalton, P. D., Flynn, L., Shoichet, M. S. *Biomaterials* **2002**, *23*, 3843-3851.

135. Hall, D. B., Deppe, D. D., Hamilton, K. E., Dhinojwala, A., Torkelson, J. M. *J. Non-Cryst. Sol.* **1998**, *235-237*, 48-56.

136. Hall, D. B., Torkelson, J. M. *Macromolecules* **1998**, *31*, 8817-8825.

137. Seidel, J. M., Malmonge, S. M. *Mat. Res.* **2000**, *3*, 79-83.

138. Bird, R. B., Stewart, W. E., Lightfoot, E. N. *Transport Phenomena*; John Wiley and Sons: New York, 1960.

139. *CRC Handbook of Chemistry and Physics*; 74th ed.; CRC Press, 1993.

140. Graves-Abe, T., Pschenitzka, F., Sturm, J. C. *Mat. Res. Soc. Symp. Proc.* **2002**, *725*, P311-P316.

141. Yasuda, H., Peterlin, A., Colton, C. K., Smith, K. A., Merrill, E. W. *Makromol. Chem.* **1969**, *126*, 177.

142. Tong, P., Ye, X., Ackerson, B. J., Fetters, L. J. *Phys. Rev. Lett.* **1997**, *79*, 2363-2366.

143. Cheng, Y., Prud'homme, R. K., Thomas, J. L. *Macromolecules* **2002**, *35*, 8111-8121.

144. Amos, R. M., Rarity, J. G., Tapster, P. R., Shepherd, T. J., Kitson, S. C. *Phys. Rev. E* **2000**, *61*, 2929-2935.

145. Lai, M. C., Topp, E. M. *J. Pharm. Sci.* **1999**, *88*, 489-500.

146. Khoury, C., Adalsteinsson, T., Johnson, B., Crone, W. C., Beebe, D. J. *Biomed. Microdevices* **2003**, *5*, 35-45.

147. Ho, A. K., Bromberg, L. E., O'Connor, A. J., Perera, J. M., Stevens, G. W., Hatton, T. A. *Langmuir* **2001**, *17*, 3538-3544.

148. Brown, E. B., Wu, E. S., Zipfel, W., Webb, W. W. *Biophys. J.* **1999**, *77*, 2837-2849.

149. Van Keuren, E., Schrof, W. *Macromolecules* **2003**, *36*, 5002-5007.

150. Fergg, F., Keil, F. J., Quader, H. *Colloid Polym. Sci.* **2001**, *279*, 61-67.

151. Booth, M. J., Wilson, T. *J. Biomed. Opt.* **2001**, *6*, 266-272.

152. Wakebe, T., Van Keuren, E. *Jpn. J. Appl. Phys. Part 1* **1999**, *38*, 3556-3561.

153. Arruda, E. M., Boyce, M. C. *J. Mech. Phys. Solids* **1993**, *41*, 389-412.

154. Johnson, B., Bauer, J. M., Niedermaier, D. J., Crone, W. C., Beebe, D. J. *Exp. Mech.* **2004**, *44*, 21-28.

155. Finel, A., Mazauric, V., Ducastelle, F. *Phys. Rev. Lett.* **1990**, *65*, 1016-1019.

156. Itchkawitz, B. S., McEllistrem, M., Grube, H., Boland, J. J. *Surf. Sci.* **1997**, *385*, 281-293.

157. Song, Z. Y., Hida, M., Sakakibara, A., Takemoto, Y. *Scr. Mater.* **1997**, *37*, 1617-1622.

158. Wu, J. S., Jia, C. L., Urban, K., Hao, J. H., Xi, X. X. *J. Appl. Phys.* **2001**, *89*, 5653-5656.

159. Lakes, R. *Science* **1987**, *235*, 1038-1040.

160. Caddock, B. D., Evans, K. E. *J. Phys. D-Appl. Phys.* **1989**, *22*, 1877-1882.

161. Evans, K. E., Nkansah, M. A., Hutchinson, I. J., Rogers, S. C. *Nature* **1991**, *353*, 124-124.

162. Chen, C. P., Lakes, R. S. *J. Mater. Sci.* **1991**, *26*, 5397-5402.

163. Vlasov, Y. A., Deutsch, M., Norris, D. J. *Appl. Phys. Lett* **2000**, *76*, 1627-1629.

164. Stefanou, N., Yannopapas, V., Modinos, A. *Comput. Phys. Commun.* **1998**, *113*, 49-77.

165. Astratov, V. N., Adawi, A. M., Fricker, S., Skolnick, M. S., Whittaker, D. M., Pusey, P. N. *Phys. Rev. B* **2002**, *66*, 165215.

166. Sievenpiper, D. F., Sickmiller, M. E., Yablonovitch, E. *Phys. Rev. Lett.* **1996**, *76*, 2480-2483.

167. Lin, S. Y., Fleming, J. G., El-Kady, I. *Appl. Phys. Lett* **2003**, *83*, 593-595.

168. Wang, W., Asher, S. A. *J. Am. Chem. Soc.* **2001**, *123*, 12528-12535.

169. Sun, Y. G., Mayers, B. T., Xia, Y. N. *Nano Lett.* **2002**, *2*, 481-485.

170. Cassagneau, T., Caruso, F. *Advanced Materials.* **2002**, *14*, 732-+.

171. Pendry, J. B. *Phys. Rev. Lett.* **2000**, *85*, 3966-3969.

172. Sigalas, M. M., Chan, C. T., Ho, K. M., Soukoulis, C. M. *Phys. Rev. B* **1995**, *52*, 11744-11751.

173. Fan, S. H., Villeneuve, P. R., Joannopoulos, J. D. *Phys. Rev. B* **1996**, *54*, 11245-11251.

174. Moroz, A. *Phys. Rev. Lett.* **1999**, *83*, 5274-5277.

175. Moroz, A. *Phys. Rev. B* **2002**, *66*.

176. Brown, E. R., McMahon, O. B. *Appl. Phys. Lett* **1995**, *67*, 2138-2140.

177. Ozbay, E., Temelkuran, B., Sigalas, M., Tuttle, G., Soukoulis, C. M., Ho, K. M. *Appl. Phys. Lett* **1996**, *69*, 3797-3799.

178. McIntosh, K. A., Mahoney, L. J., Molvar, K. M., McMahon, O. B., Verghese, S., Rothschild, M., Brown, E. R. *Appl. Phys. Lett* **1997**, *70*, 2937-2939.

179. Lin, S. Y., Fleming, J. G., El-Kady, I. *Opt. Lett.* **2003**, *28*, 1683-1685.

180. Li, Z. Y., El-Kady, I., Ho, K. M., Lin, S. Y., Fleming, J. G. *J. Appl. Phys.* **2003**, *93*, 38-42.

181. Weber, M. J. *Handbook of Optical Materials*; CRC Press LLC, 2000; http://www.engnetbase.com/books/818/3512_fm.pdf.

182. Jiang, P., Cizeron, J., Bertone, J. F., Colvin, V. L. *J. Am. Chem. Soc.* **1999**, *121*, 7957-7958.

183. Kulinowski, K. M., Jiang, P., Vaswani, H., Colvin, V. L. *Adv. Mater.* **2000**, *12*, 833-838.

184. Yang, H. W., Blanford, C. F., Lytle, J. C., Carter, C. B., Smyrl, W. H., Stein, A. *Chem. Mater.* **2001**, *13*, 4314-4321.

185. Velev, O. D., Tessier, P. M., Lenhoff, A. M., Kaler, E. W. *Nature* **1999**, *401*, 548-548.

186. Tessier, P. M., Velev, O. D., Kalambur, A. T., Rabolt, J. F., Lenhoff, A. M., Kaler, E. W. *J. Am. Chem. Soc.* **2000**, *122*, 9554-9555.

187. von Freymann, G., John, S., Schulz-Dobrick, M., Vekris, E., Tetreault, N., Wong, S., Kitaev, V., Ozin, G. A. *Appl. Phys. Lett* **2004**, *84*, 224-226.

188. Bartlett, P. N., Birkin, P. R., Ghanem, M. A. *Chem. Commun* **2000**, 1671-1672.

189. Wijnhoven, J., Zevenhuizen, S. J. M., Hendriks, M. A., Vanmaekelbergh, D., Kelly, J. J., Vos, W. L. *Adv. Mater.* **2000**, *12*, 888-890.

190. Bartlett, P. N., Baumberg, J. J., Birkin, P. R., Ghanem, M. A., Netti, M. C. *Chem. Mater.* **2002**, *14*, 2199-2208.

191. Sumida, T., Wada, Y., Kitamura, T., Yanagida, S. *Langmuir* **2002**, *18*, 3886-3894.

192. Xu, L. B., Tung, L. D., Spinu, L., Zakhidov, A. A., Baughman, R. H., Wiley, J. B. *Adv. Mater.* **2003**, *15*, 1562-+.

193. Bartlett, P. N., Baumberg, J. J., Coyle, S., Abdelsalam, M. E. *Faraday Discuss.* **2004**, *125*, 117-132.

194. Hecht, E. *Optics*; 4th ed.; Addison-Wesley: San Francisco, 2002.

APPENDIX A

HYDROGEL SWELLING MODEL

Significant components of this section were published as supplemental information to "Glucose-sensitive inverse opal hydrogels: analysis of optical diffraction response", Y.-J. Lee, S. A. Pruzinsky, and P. V. Braun, *Langmuir* **2004**, *20*, 3096-3106.

Appendix A is subdivided into two sections. In the first, an expression is developed in order to compare the experimentally measurable optical diffraction shift with the swelling ratio. In the second, a simple model is developed that allows the definition of various dimensionalities of pore shrinking or swelling in order to compare and contrast the impact of various possible pore responses to bulk one-dimensional swelling on the predicted reflection spectra. The theoretical and experimental spectra can then be compared to elucidate the nature of the pore response.

Section 1: Swelling Ratio

We begin by defining a dimensionless swelling ratio as the ratio of the final (swollen) to initial (compact) volumes of the overall inverse opal hydrogel film. As noted in the paper, it was experimentally suggested that the overall swelling of the film was most likely one-dimensional. In the case of one-dimensional swelling in the direction normal to the substrate, this is equivalent to the ratio of the interlayer spacing of the planes parallel to the substrate, which, in this case are the FCC (111) planes. Note that γ does not account for swelling into the templated pores.

$$\gamma = \frac{v}{v_0} = \frac{d\_111}{d\_111_0} \tag{1}$$

We can then use Bragg's law and a dielectric mixing model for the effective index (Eq. 1.2), although, here v = volume and Φ = volume fraction) to determine d_111_0. (Alternatively, one could express d_111_0 in terms of the diameter of the colloids, d, where $d\_111_0 = d * 6^{1/2} / 3$.)

$$\lambda_0 = 2 \cdot n\_eff_0 \cdot d\_111_0 \tag{2}$$

$$n\_eff_0 = \sqrt{\phi_0 \cdot \left(n\_aq_0\right)^2 + \left(1 - \phi_0\right) \cdot n\_poly^2} \tag{3}$$

$$d\_111_0 = \frac{\lambda_0}{2 \cdot \sqrt{\phi_0 \cdot \left(n\_aq_0\right)^2 + \left(1 - \phi_0\right) \cdot n\_poly^2}} \tag{4}$$

Where the volume fraction of the FCC phase, Φ_0, equals 0.74.

This can similarly be done for d_111, remembering that the volume of the polymer phase is conserved and that the change in volume of the hydrogel during swelling is solely due to influx of the aqueous solution. Note that there is a distinction between the initial and current index of refraction of the FCC aqueous phase; this is because the composition (pH and concentration of glucose) of the aqueous phase is changed in order to induce swelling and this affects the index of refraction.

$$\lambda = 2 \cdot n\_eff \cdot d\_111 \tag{5}$$

$$n\_eff = \sqrt{\frac{\left[v - \left(1 - \phi_0\right) \cdot v_0\right] \cdot n\_aq^2 + \left(1 - \phi_0\right) \cdot v_0 \cdot n\_poly^2}{v}} \tag{6}$$

One can then use the definition of the swelling parameter to substitute for v, equation 4 to substitute for d_111_0, and then plug this into the Bragg equation. After

simplification, the result is the following equation with five convenient inputs (n_aq, n_poly, Φ_0, λ_0, λ) which can then be solved for its one unknown, d111.

$$\lambda = 2 \cdot d\_111 \cdot \sqrt{n\_aq^2 + \left(n\_poly^2 - n\_aq^2\right) \cdot \frac{(1 - \phi_0)}{d\_111} \cdot \left[\frac{\lambda_0}{2 \cdot \sqrt{\phi_0 \cdot \left(n\_aq_0\right)^2 + (1 - \phi_0) \cdot n\_poly^2}}\right]} \qquad (7)$$

This now allows one to determine the swelling ratio, γ, which could now be compared with the experimentally measurable optical diffraction shift, λ / λ_0.

Section 2: Pore Shrinking/Swelling Models

To perform simulations for comparison with the thermodynamic swelling experiments, we will further develop this model to incorporate information about the pore swelling or shrinking dimensionalities. This will then allow the definition of the parameters needed to carryout scalar wave approximation (SWA) calculations of theoretical spectra for comparison with experiment. We begin by defining a pore swelling factor, α, with components both in the unconfined direction of the bulk swelling ($\alpha_{perpendicular}$) and in the transverse directions in which the film is confined ($\alpha_{parallel}$). The component pore swelling factors are between -1 and 1 indicating the degree of shrinking or swelling of the pore in that direction relative to the bulk one-dimensional swelling ratio, γ. So, if the magnitude of the pore swelling in a certain dimension is the same as γ, the pore swelling factor for that dimension would equal 1; if it shrunk in that dimension, the factor would equal -1; likewise, if the pore didn't change size in that dimension, the factor would equal 0.

$$\alpha = \alpha_{perpendicular} + 2 \cdot \alpha_{parallel} \qquad (8)$$

200

The pore volume change can then be expressed in terms of the bulk swelling ratio to the sum of the pore swelling factors for three dimensions.

$$\frac{v\_fcc}{v\_fcc_0} = \gamma^\alpha \tag{9}$$

We can now define the volumes and volume fractions of the component phases.

$$v\_fcc_0 = \phi_0 \cdot v_0 \tag{10}$$

$$v\_fcc = v\_fcc_0 \cdot \gamma^\alpha = \phi_0 \cdot v_0 \cdot \gamma^\alpha \tag{11}$$

$$\phi = \frac{v\_fcc}{v} = \frac{\phi_0 \cdot v_0 \cdot \gamma^\alpha}{v_0 \cdot \gamma} = \phi_0 \cdot \gamma^{\alpha-1} \tag{12}$$

$$v\_inv_0 = (1 - \phi_0) \cdot v_0 \tag{13}$$

$$v\_inv = v - v\_fcc = \gamma \cdot v_0 - \phi_0 \cdot v_0 \cdot \gamma^\alpha \tag{14}$$

Recall the assumption is that the original state is that of a completely compact inverse opal hydrogel in which case the FCC phase consists of aqueous solution and the inverse-FCC phase consists of polymer. The final or swollen state is composed of an

$$v\_inv\_poly = v\_inv\_poly_0 = v\_inv_0 = (1 - \phi_0) \cdot v_0 \tag{15}$$

$$v\_inv\_aq_0 = 0 \tag{16}$$

$$v\_inv\_aq = v\_inv - v\_inv\_poly = \gamma \cdot v_0 - \phi_0 \cdot v_0 \cdot \gamma^\alpha - (1 - \phi_0) \cdot v_0 \tag{17}$$

aqueous FCC phase and an inverse-FCC phase which contains the original amount of polymer in addition to some aqueous solution with which the hydrogel has swollen. It is therefore useful to break down the volume of the inverse-FCC phase into the volumes of its components: polymer and aqueous solution.

Now that we know the volumes of all the components of the phases, we can write expressions for the effective indices of the phases using the dielectric mixing model where necessary:

$$n\_fcc = n\_aq \tag{18}$$

$$n\_inv = \sqrt{\frac{n\_poly^2 \cdot v\_inv\_poly + n\_aq^2 \cdot v\_inv\_aq}{v\_inv}} = \sqrt{\left(n\_poly^2 - n\_aq^2\right) \cdot \frac{\left(1 - \phi_0\right)}{\left(\gamma - \phi_0 \cdot \gamma^\alpha\right)} + n\_aq^2} \tag{19}$$

We can now perform the desired SWA calculations now that we have determined: Φ, n_fcc, n_inv, and d_111.

AUTHOR'S BIOGRAPHY

Yun-Ju Lee ████████████████████████████████████ and moved to the United States at the age of 12. He graduated from Massachusetts Institute of Technology with a S. B. in materials science and engineering. He then moved to Urbana, Illinois, to pursue graduate study in materials science and engineering. Following completion of his Ph. D., Lee will begin work as a postdoctoral fellow at Sandia National Laboratories in the Material & Process Science division.